



TECHNISCHE
UNIVERSITÄT
WIEN

DISSERTATION

Evaluation of the Radiation Environment of the LHCb Experiment

ausgeführt zum Zwecke der Erlangung des akademischen Grades eines Doktors der
technischen Naturwissenschaften

unter der Leitung von

Em.Univ.Prof. O.Univ.Prof. Dipl.-Ing. Dr.techn. Hannes Aiginger

E141, Atominstitut

und

Dott. Gloria Corti

CERN

eingereicht an der Technischen Universität Wien
Fakultät für Physik

von

Dipl.-Ing. Matthias Karacson

Matrikelnummer: 0026233

Schützengasse 1, 2700 Wr. Neustadt

Wien, November 2016

Acknowledgements

There have been bets on if this thesis was ever going to be finished. I hope I didn't disappoint too many people. Six years are likely a bit above average, but I am honestly happy that I was able to spend this time in one of the most amazing, welcoming, inspiring and exciting work places that exist on this planet. The knowledge and experience I accumulated over the years thanks to colleagues and friends on and off work are absolutely invaluable, and I appreciate every single day I was allowed to participate in this giant scientific laboratory and social experiment called CERN. In conclusion to this part of my life that I am hereby finally able to wrap up, I want to offer sincere thanks to the following people and to many more whom I might not mention here in name, but to whom I certainly will express my gratitude in person.

Thank you Prof. Hannes Aiginger and Dr. Karin Poljanc for your continuing support over the years and your patience in waiting for the final book. Thank you as well for your valuable help in dealing with administrative issues over a distance of a thousand kilometers while I was trying to figuratively acquire "Permit A38" in best Gaulish tradition. Thank you Prof. Helmut Vincke for providing support and helpful advice even after your supervision of my diploma thesis ended, and for trusting me with operating your Alanine and RPL readout equipment when I needed to. Also, thank you and Prof. Peter Kindl very much for agreeing to review this thesis on short notice. Thank you Gloria Corti for your extremely helpful and patient supervision, for sharing so much of your valuable time even when you barely had any time to spare, and for your guidance that helped me to progress and that allowed me to write this thesis in the first place. I also especially thank the whole LHCb infrastructure team for welcoming me, for allowing me to participate and hopefully successfully contribute. And thank you Rolf, Eric, Laurent, Heinrich and Gloria in particular for providing me with enough breathing space lately to enable me to finally finish this thesis.

Thank you to the LHCb collaboration for providing such an awesome and welcoming work environment and for making me feel useful. Thank you Barbara Obryk for always collaborating with us in the most helpful way and for welcoming us in Krakow so cordially. Thank you Luis Granado Cardoso for always being helpful and efficient anytime I just impolitely rush into your office with another request concerning our FLUKA computing farm setup or our active sensor interface. Thank you Federico Ravotti for generously providing us with your active sensors and for always having an open ear and some advice when I was having difficulties understanding them. Thank you as well for trusting me with the BPW readout in your laboratory. Thank you Stefan Roesler for establishing contact with LHCb and therefore giving me the opportunity to start working here so many years ago. Thank you Chris Theis for your patient and expedient answering of my mostly FLUKA related questions over so many lunches, and for providing your very useful tools that brought so much color to the plots of this thesis. Thank you Fernando Leite Pereira for your patient technical support which significantly facilitated performing the first large-scale simulations on my own small virtual COFLU cluster during my first years at LHCb.

I also thank all my friends in and from Austria, France, Switzerland, Germany, Portugal, Italy and elsewhere and those who seem to be always on the move, some of whom I already mentioned, some of whom I will acknowledge in person, for their friendship, support and understanding, even though I sometimes made myself scarce to some of you over the years. Last but certainly not least I want to thank my family, my parents and my brother, who always supported me in everything I needed over the years without ever losing hope that I might finally get this done.

Finally, I apologize for these in my view rather short acknowledgements and for leaving out so many individual names by just mentioning the larger group. Given the time I already spent as doctoral student and the average amount of time I seem to require for writing a single paragraph, I certainly wanted to avoid missing this last deadline at all costs.

Abstract

The unprecedented radiation levels of the Large Hadron Collider (LHC) during high-energy proton-proton collisions will have an impact on the operation of its experiments' detectors and electronics. LHCb, one of the 4 major LHC experiments, has started operation in 2009 and from 2011 onward it has been collecting data at and above its design luminosity. Detectors and associated detector electronics are prone to damage if the radiation levels exceed the expected values. It is essential to monitor the radiation environment of the experimental area and compare it with predictions obtained from simulation studies in order to assess the situation and take corrective action in case of need. Understanding the existing radiation environment will also provide important input to the planning of maintenance and for operation at upgrade luminosity. A set of radiation detectors has been installed in the LHCb experimental area to measure different aspects of its radiation environment. Passive dosimeters including Thermo-Luminescence-Dosimeters, Radio-Photoluminescence-Dosimeters and Polymer-Alanine-Dosimeters are distributed throughout the detector to cover the wide range of radiation levels expected. Many of these sensors, widely used for the measurements of radiation fields, are applied in the unprecedented radiation environment that is being produced in the experiment. Active radiation monitors, consisting of small printed-circuit-boards with multiple radiation sensitive field-effect-transistor and diode sensors have been installed close to passive sensor positions to allow for the monitoring of both peak and long term radiation levels. They can be read out online and the data stored in a database.

The thesis involves studying the radiation environments of the experiment in all of its aspects. Measurements collected by the active and passive sensors are analyzed and converted from raw data to physical quantities. Cross calibrations are performed between the two systems and the measurements are correlated with the evolving running conditions. Another important element of the project is the comparison of the measurements with simulation estimates. Many aspects of the radiation environment of the LHCb experiment have been numerically evaluated in the past assuming 14 TeV center of mass (CM) collision energy and nominal LHCb luminosity. In order to better compare the expectation with the measurements, new simulation studies reflecting the run conditions in 2010-2013 with 7 and 8 TeV CM collision energy are performed. These simulation studies to evaluate the various aspects of the radiation environment of LHCb are carried out with FLUKA, a state of the art program for the simulation of high energy particle transport and interaction with matter. The results are reviewed, also in regard to integrating changes in the experimental setup if needed. Establishing the reliability of the simulation is essential, as it is needed to provide important input for technical choices in view of the planned upgrade of the experiment for operation at higher luminosity.

Kurzfassung

Aufgrund der von hochenergetischen Proton-Proton Kollisionen im LHC erzeugten einzigartigen Strahlungsfelder ist mit Auswirkungen auf die Detektoren der LHC Experimente und deren Elektronik zu rechnen. Das LHCb Experiment, eines der vier grossen LHC Experimente, hat im Jahr 2009 den Betrieb aufgenommen und sammelt seit 2011 Daten mit der ursprünglich geplanten und später auch mit einer dieser gegenüber erhöhten Kollisionsrate. Die Detektoren und die mit diesen verbundene Elektronik sind bei Überschreitung der zu erwartenden Strahlungswerte dem Risiko von Beschädigungen ausgesetzt. Um die Situation ausreichend beurteilen und gegebenenfalls korrektive Massnahmen ergreifen zu können, ist es notwendig, die Strahlungsumgebung des Experimentbereichs zu überwachen und die Messwerte mit den Voraussagen von Simulationen zu vergleichen. Ein grundsätzliches Verständnis der existierenden Strahlungsumgebung gewährt wertvolle Einsichten für die Planung von Wartungsarbeiten sowie für den Betrieb mit erhöhter Luminosität nach dem geplanten Upgrade des Experiments. Eine Zusammenstellung von Strahlungsmessgeräten wurde im Experimentalbereich von LHCb installiert um verschiedene Aspekte der Strahlungsumgebung zu untersuchen. Passive Dosimeter, inklusive Thermo-Lumineszenz-, Radio-Photoluminescence- und Polymer-Alanine-Dosimeter, wurden um und innerhalb des Detektors verteilt um die je nach Messort stark variierenden Strahlungsniveaus abzudecken. Viele dieser teils bereits über Jahre erprobten und in verschiedensten Situationen eingesetzten Sensortypen werden nun in dem im Experiment produzierten neuartigen Strahlenfeld eingesetzt. Aktiv betriebene Monitore, bestehend aus einer Leiterplatte mit mehreren Feldeffekt-Transistoren und Dioden als Sensoren, wurden in der Nähe der passiven Sensorpositionen installiert um sowohl Spitzen- als auch Langzeitwerte des Strahlenfeldes zu messen. Diese aktiven Sensoren können online ausgelesen und deren Messwerte in einer Datenbank gespeichert werden.

Die Dissertation beschäftigt sich mit dem Studium des Strahlenfeldes des Experiments in all seinen Aspekten. Messungen von aktiven und passiven Sensoren werden analysiert und von Rohdaten in physikalische Messgrössen konvertiert. Vergleichende Analysen zwischen den beiden Systemen werden durchgeführt und die Messwerte werden mit den sich ändernden Betriebsbedingungen des Experiments korreliert. Viele Aspekte der Strahlungsumgebung des LHCb Experiments wurden in der Vergangenheit mittels Simulation unter der Annahme von 14 TeV center of mass (CM) Kollisionsenergie und nomineller LHCb Luminosität evaluiert. Um derartige Erwartungswerte besser mit den tatsächlichen Messwerten vergleichen zu können, werden neue Simulationsstudien durchgeführt, in denen die jeweiligen Betriebsparameter der Jahre 2010 bis 2013 mit 7 bzw. 8 TeV CM Kollisionsenergie nachempfunden werden. Für die Realisierung dieser Studien wird das Monte Carlo Programm FLUKA benutzt, das eine realistische Simulation des Transports von Teilchen und deren Interaktion mit Materie ermöglicht. Die Ergebnisse dieser Studien werden begutachtet und es werden Rückschlüsse auf potentielle Verbesserungsmöglichkeiten des experimentellen Aufbaus gezogen. Die Evaluierung des Verlässlichkeitsgrades der Simulation ist essentiell, da die daraus resultierenden Abschätzungen eine wichtige Informationsgrundlage darstellen, um technische Entscheidungen bezüglich des geplanten Upgrades des Experiments für einen Betrieb mit höherer Luminosität zu fällen.

Contents

1	Introduction.....	11
1.1	CERN and the LHC.....	12
1.2	The LHCb Experiment.....	14
1.3	General Layout of the LHCb Experiment.....	14
1.4	Operation of the LHCb Experiment.....	17
1.5	Radiation Produced by High Energy Particle Accelerators.....	20
1.5.1	Definitions.....	20
1.5.1.1	Particle Fluence.....	21
1.5.1.2	1 MeV Neutron Fluence Equivalent.....	21
1.5.1.3	Dose (Energy).....	21
1.5.2	Interactions of Light Electromagnetic Particles.....	22
1.5.3	Heavy Charged Particles.....	23
1.5.4	Neutron Interactions.....	24
1.5.5	Other Particles of Interest.....	25
1.5.6	High Energy Particle Cascades.....	26
1.5.6.1	Hadronic Cascade.....	26
1.5.6.2	Electromagnetic Cascade.....	26
1.6	Radiation Effects on the Equipment.....	27
1.6.1	Cumulative Effects:.....	27
1.6.2	Single Event Effects:.....	28
2	Dosimetry.....	29
2.1	Dosimeters and Fluence Sensors used in LHCb.....	29
2.2	Passive Dosimeters.....	30
2.2.1	Polymer-Alanine-Dosimeters.....	30
2.2.2	Radio-Photo-Luminescence Dosimeters.....	32
2.2.3	Thermo-Luminescent Dosimeters.....	33
2.3	Active Sensors.....	36
2.3.1	Types of Active Sensors in LHCb.....	37

2.3.1.1	Radiation-sensing Field Effect Transistors	37
2.3.1.2	High-resistivity Forward-based PiN diodes	39
3	Monte Carlo Simulation.....	41
3.1	FLUKA: A Multiparticle Transport Code	41
3.1.1	Geometry Description.....	41
3.1.2	Materials	42
3.1.3	Lattice	42
3.1.4	Beam and Source	43
3.1.5	User Routines.....	43
3.1.6	Use of Magnetic Field Maps	43
3.1.7	Scoring	44
4	Estimating the LHCb Prompt Radiation Field using FLUKA MC Simulation	45
4.1	Simulation Geometry	46
4.1.1.1	Upstream of the Interaction Point.....	47
4.1.1.2	VELO.....	50
4.1.1.3	Inner and Outer Tracker.....	51
4.1.1.4	Calorimeters.....	51
4.1.1.5	Cavern	53
4.1.2	Materials	54
4.1.3	Beam Source Parameters and Thresholds	54
4.1.4	Scoring Approach	56
4.2	Comparison of a First Stable Build with Results from 2003	57
4.3	Simulation Predictions	60
4.3.1	FLUKA Simulations of LHCb.....	60
4.3.2	Fluence Maps.....	62
4.3.2.1	Neutron Fluence	63
4.3.2.2	Proton Fluence	65
4.3.2.3	Photon Fluence	66
4.3.2.4	Electron & Positron Fluence.....	67

4.3.2.5	Charged Hadron Fluence.....	69
4.3.2.6	Fluence of Hadrons > 20 MeV.....	70
4.3.3	Integrated Estimators.....	71
4.3.3.1	1 MeV Neutron Fluence Equivalent.....	71
4.3.3.2	Total Ionizing Dose.....	73
4.3.3.3	Influence from the LHC Tunnel.....	74
4.3.3.4	Differential Fluence Scoring.....	76
5	Evaluation of Dosimeters.....	79
5.1	Evaluation of Passive Monitors based on Calorimeter Measurements.....	79
5.1.1	Measurement Setup.....	80
5.1.2	Simulation Predictions.....	85
5.1.3	Specific Properties of RPL Dosimeters used until LS1.....	88
5.1.3.1	RPL Sensor Deficiencies (Crystal Damage).....	90
5.1.4	Measurement Results.....	95
5.1.4.1	HCAL Backside.....	98
5.1.4.2	HCAL Front.....	101
5.1.4.3	ECAL Front.....	103
5.1.4.4	SPD Front.....	104
5.1.4.5	ECAL Test Modules.....	106
5.1.4.6	Calorimeter Electronics.....	107
5.1.5	Characterization of Specific Dosimeter Properties.....	109
5.1.5.1	MCP Linearity above 1 Gy.....	110
5.1.5.2	MTS Linearity above 100 Gy.....	115
5.1.6	Simulation and Measurement Comparisons.....	117
5.1.6.1	MCP versus Simulation.....	117
5.1.6.2	Alanine versus Simulation.....	121
5.1.7	Differences in Measurements between 7 TeV CM and 8 TeV CM.....	125
5.2	Evaluation of Passive 1 MeV Neutron Fluence Equivalent Sensors.....	128
5.2.1	Readout.....	129

5.2.2	Results.....	130
5.3	Evaluation of Active Dosimeters	136
5.3.1	Measurement Setup	137
5.3.2	Signal Corrections	140
5.3.2.1	Temperature and Offset Corrections	140
5.3.2.2	Readout Current (“Jumps”) Correction.....	142
5.3.2.3	Drift Correction and Luminosity.....	143
5.3.2.4	Spikes and Noise Correction	144
5.3.3	Inside the Experiment: Muon Station M1.....	146
5.3.3.1	Locations	146
5.3.3.2	Measurements and Comparison with Simulation.....	148
5.3.3.3	Comparisons of TID between Active and Passive Sensors and Simulation	150
5.3.3.4	Comparisons of 1 MeV Neutron Fluence Equivalent between Active and Passive Sensors and Simulation	156
5.3.4	Highly Exposed Radiation Areas	158
5.3.4.1	Total Ionizing Dose Values	160
5.3.4.2	1 MeV Neutron Fluence Equivalent Values.....	164
5.3.5	Around the Experiment’s Electronics	167
5.3.5.1	Measurement Results (Total Ionizing Dose)	168
5.3.5.2	Measurement Results (1 MeV Neutron Fluence Equivalent).....	183
5.3.5.3	Summary of Measurements around Electronics.....	186
5.3.6	LAAS Calibration Efforts	188
6	Conclusions	193
7	References	201
8	Appendix.....	205
8.1	Measurement Result Tables	205
8.1.1	HCAL backside.....	205
8.1.2	HCAL front.....	207
8.1.3	ECAL front	208

8.1.4	SPD front	210
8.1.5	ECAL Test Modules	211
8.1.6	Calorimeter Electronics.....	212
8.1.7	Summary tables of Reliable Measurements	213

The CERN Large Hadron Collider (LHC) located in Geneva in Switzerland is able to provide collisions of record-breaking energies to four large underground experiments located in dedicated caverns along the accelerator. These collisions lead to unprecedented radiation fields in the experiments themselves, impacting the operation of their detectors and electronics. If expected radiation levels are exceeded, the equipment is put at risk. Understanding the existing radiation environment will provide valuable input to the planning of future operation at nominal beam energy and later at upgrade luminosity. In order to measure different aspects of the radiation environment, a network of radiation monitors has been installed in the LHCb experimental area. These include passively used dosimeters and 1 MeV neutron fluence equivalent sensors as well as actively used sensors measuring the same quantities, which are controlled electronically and are capable of retaining a detailed history of measurements over time. While at least some of these sensor types have been previously examined in mixed radiation fields, all of them are now exposed to an unprecedented radiation environment in LHCb.

The aim of this thesis is to characterize the radiation environment of the LHCb experiment by investigating multiple aspects. Measurements collected by active and passive sensors are converted from raw data to physical quantities and analyzed for this purpose. Cross-checks are performed between systems and the measurements are correlated with the evolving running conditions. Monte Carlo simulations are performed reproducing the running conditions between 2010 and 2013 and compared to the corresponding measurements.

During construction of the LHCb detector some of the design choices, in particular for electronics components, were still being taken. First simulation studies from 2003 aimed to predict parameters of the prompt radiation field at the experiment for the originally intended collision energy, which is roughly double the amount the experiment was actually exposed to during the period in the scope of this thesis. Nonetheless, these first estimations showed that the complex radiation field in and around the experiment exhibits dose and fluence levels which span several orders of magnitude. Therefore it is necessary to use a variety of different sensor types for the whole experiment, as none of the available devices is able to cover the full range of values between different locations by itself. Even though the sensor network around the LHCb experiment includes a very large number of individual sensors, it is impossible to cover all of the locations in and around the detector with them. Some parts of the detector simply do not have room for any additional sensors and lack accessibility, but the main reason for most locations is to minimize interference with the experiment's main purpose: the taking of data aiming to make precision measurements and to search for new physics. As a consequence, simulation studies recreating running conditions are used to fill in the gaps of knowledge and provide estimations for locations which cannot be monitored otherwise. Part of the scope of this thesis is to revise, update and evaluate the validity of the simulation by comparing it to reliable measurements, enabling a characterization of the radiation environment for the whole area of interest.

An overview over the various sensor types used in LHCb is provided in section 2 and an introduction of the Monte Carlo application used for simulating the LHCb radiation field is given in section 3. Some results of the Monte Carlo simulations performed covering the LHCb experiment are explained in section 4. In section 5 these estimations are used in conjunction with the various measurements to analyze the behavior of the different sensor types. Individual measurements are compared to each other as well as to estimates yielded by the simulation. Due to the large amount of sensors and the large variety of sensor types applied at LHCb, this section is split into smaller subsections based on the location of sensors in order to characterize specific dosimeter's properties in the most appropriate way. In a first step, passive sensors are evaluated on a subset comprising about 75% of all passive sensors in LHCb. The reliability of different passive sensor types in various scenarios is determined. Subsequently, the outcome of these studies is used to evaluate the behavior of the various active sensor types distributed in and around the experiment, based on measurements from distinct

locations with various levels of exposure to radiation. At the same time, discrepancies between measurements and simulation estimates are analyzed and conclusions for the reliability of the simulation are drawn.

1.1 CERN AND THE LHC

Founded in 1952, at a time when pure physics research was still concentrated on understanding the inside of an atom, the “Conseil Européen pour la Recherche Nucléaire” had a mandate of establishing a world-class fundamental research organization in Europe. Based on this mandate, a laboratory planned astride the Franco-Swiss border near Geneva was built in 1954, constituting the foundation of what has developed over decades into a successful European Laboratory currently supported by 22 member states and cooperating with many more institutes and universities from all around the world. The acronym CERN was derived from its original French denomination and retained as a common and recognizable identifier until this day.

The understanding of matter has come a long way since the middle of the last century, and as a consequence, also CERN’s main area of research has shifted from nuclear physics to particle physics, which means the studying of the fundamental constituents of matter and the forces acting between them.

The instruments that are used at CERN to perform such studies are purpose-built particle accelerators, the biggest of them at this time being the Large Hadron Collider (LHC), and detectors of various shapes and functions.

These detectors are at the foundation of seven experiments that make direct use of the LHC and of many more at other accelerators and facilities on CERN laboratory grounds. Of the seven LHC experiments, four are making use of their own dedicated underground caverns where the LHC beams are forced to collide. The biggest two, ATLAS and CMS, use general-purpose detectors to investigate the largest range of physics that they can cover. Their independent designs help in cross-confirming any new discoveries. Using their own underground caverns as well, ALICE and LHCb are specialized experiments that focus on the study of specific phenomena. The remaining three LHC experiments are TOTEM, LHCf and MoEDAL, utilizing small spaces at and around the locations of the bigger experiments to focus on highly energetic “forward particles” at very small angles to the beam line, as well as hypothetical particles.

The declared main mission of CERN is to push forward the frontiers of knowledge. This undertaking is set to bring about possible insights into the fundamental science of particles of nowadays as well as within the first moments of our universes’ existence. In order to achieve the stated goal, new technologies in connection with accelerators and detectors have to be developed at CERN, contributing to even more broadly composed fields of science than just accelerator development. These contributions include many improvements and new ventures in medicinal diagnosis and therapy, like Positron Emission Tomography (PET), or particle accelerator-based hadron and ion therapy for the treatment of cancer patients. Experiments performed at the CERN facility ISOLDE are paving the way for advances in nuclear and atomic physics, solid-state physics, materials and life sciences. Implications of galactic cosmic rays for Earths’ climate are the focus of the CLOUD experiment. Significant progress has also been accomplished in information technology, by establishing fundamental groundwork of today’s World Wide Web, or by operating large distributed computing systems like the GRID. Future scientists and engineers have to be trained at CERN to enable this innovation to take place. By offering a plethora of education and training programs integrated into the scientific routine of the laboratory to participants from the international community, CERN also manages to perform an important job of uniting people from different countries, cultures and backgrounds by motivating them to achieve a common purpose.

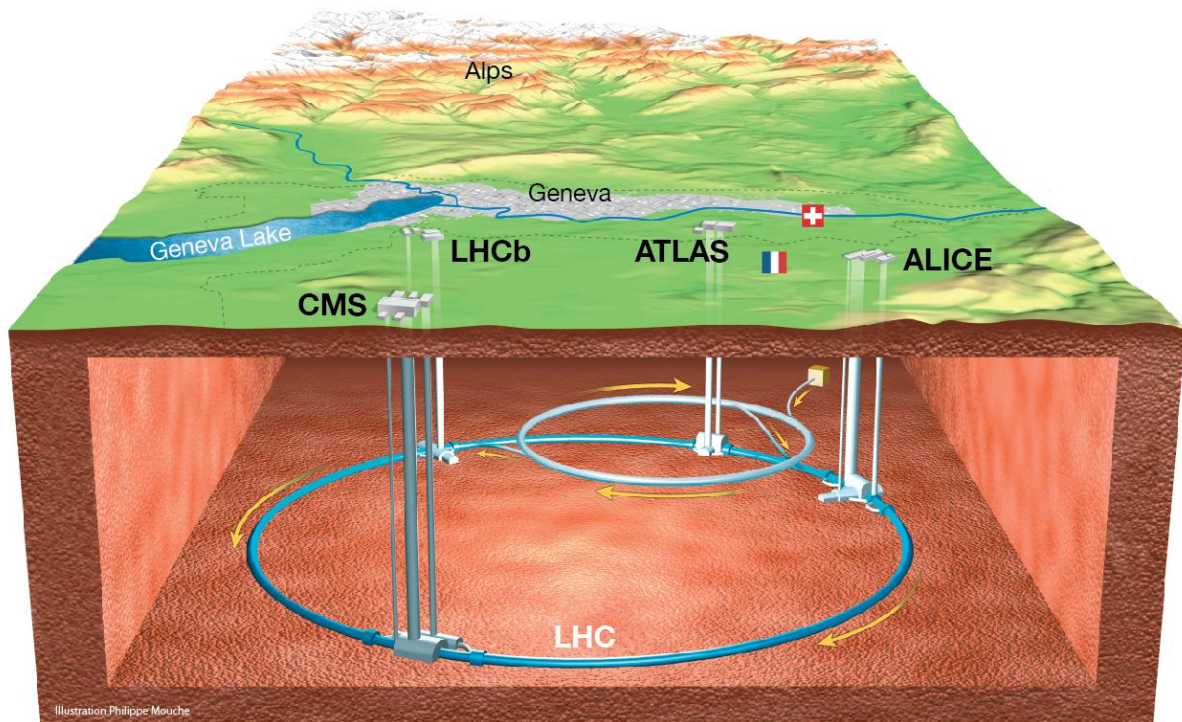


Figure 1: Sketch view of the 4 large underground experimental installations connected via the LHC tunnel [1].

The Large Hadron Collider (LHC) is a two-ring superconducting hadron accelerator and collider. It was installed in the existing underground tunnel constructed for the CERN Large Electron Positron (LEP) Collider. The tunnel stretches out between the Léman Lake and the Jura and measures 26.7 km in circumference. Situated between 45 and 170 meters below the surface, the tunnel is made of 8 arcs and 8 straight sections on a plane inclined at 1.4% sloping towards the lake. Existing structures have been used as much as possible when constructing the LHC, but many like the underground and surface at ATLAS and CMS had to be built from scratch. ALICE and LHCb were able to make use of available sites. The injection chain could be reutilized as well. This cost-effective planning influenced the decision-making process that finalized in the building of the LHC at CERN. A sketch view of the experimental underground facilities connected by the LHC can be seen in figure 1.

The LHC has two rings to guide counter-rotating beams, unlike particle-antiparticle colliders where both beams can share the same phase space in a single ring. Although there are heavy space constraints in the LHC tunnel, which is less than 4 meters wide, it was possible to keep the rings separate by relying on a magnetically coupled twin-bore super-conducting magnet design. The main purpose of the machine is to accelerate and transport protons in both rings for proton-proton (pp) collisions most of the time, but during shorter periods also lead ions are accelerated for p-Pb and Pb-Pb collisions. Instead of using all available 8 crossing points from the LEP structure, the LHC only has 4 interaction regions. Located around these interaction points are the four largest experiments at CERN: ATLAS, CMS, ALICE and the main object of interest for this thesis, the LHCb experiment [2].

1.2 THE LHCb EXPERIMENT

The LHCb detector [3] is a single-arm forward spectrometer covering the pseudorapidity range $2 < \eta < 5$. It was designed for precise measurements of particles containing b or c quarks. The LHCb abbreviation stands for Large Hadron Collider beauty experiment. It was named with the initial physics aims of the experiment in mind, which was to study characteristics of particles that contain the beauty (or “bottom”) quark. Although it was designed as a special purpose experiment dedicated to precision measurements on B mesons, as soon data taking started, it was used for much more diverse studies probing all kinds of hadrons containing the b- and the c-quark, performing very precise studies of charm physics, rare Kaon decays and much more.

1.3 GENERAL LAYOUT OF THE LHCb EXPERIMENT

Being an experiment built for a special purpose, LHCb also features a very unique layout. In accelerator-based particle physics, the parameter of pseudorapidity η is a commonly used coordinate to describe the angle of a moving particle in relation to the beam axis. LHCb is designed to cover the range of $2 < \eta < 5$ within its acceptance, which translates into a forward-directed cone around the beam line originating in the collision point. This well-defined area of interest influenced the shape of the detector displayed in figure 2. The collision point is located inside the Vertex Locator, and the subdetectors line up along the beam pipe after that point. The earlier mentioned single-arm geometry implies that only half of the forward directed particles within the experiment’s acceptance which are created in a collision are examined with the experiment’s detectors.

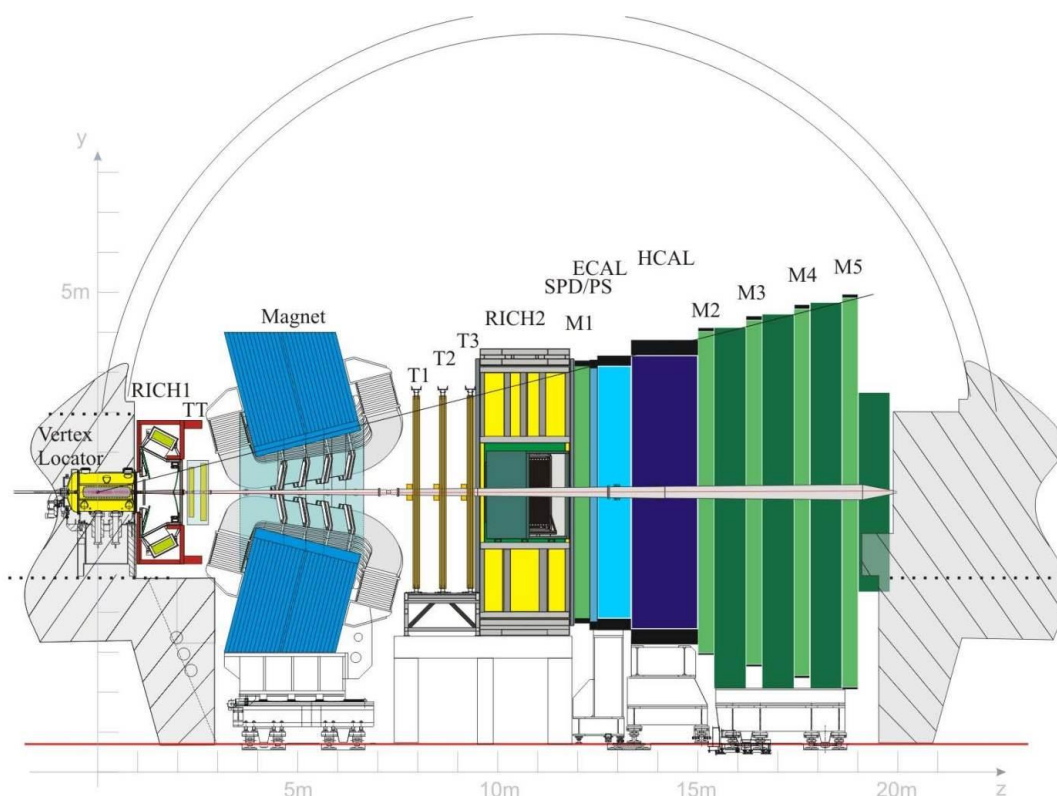


Figure 2: Layout of the LHCb experiment. The beams, moving inside the beam pipe in the center of the structure, are set to collide within the Vertex Locator of the left of the image. From there, several subdetectors measure the properties of particles created by the collision on their way through the detector. A large dipole is situated in between particle-tracking subdetectors in order to extract detailed information about particle momenta and discriminate their charges [2].

Although the shape of the experiment differs strongly from the usual cylindrical shape of the LHCs general purpose detectors CMS and ATLAS, all detectors share a lot of similarities regarding their architecture. All experiments feature tracking detectors close to the interaction point (IP) where the beams are colliding, a large magnet for bending charged particle trajectories, Calorimeters to measure energy deposition by absorption of most particle cascade products, and several layers of muon detectors downstream. In addition to those, LHCb uses Ring Imaging Cherenkov detectors for particle identification. However since LHCb covers a smaller acceptance than the general purpose cylindrical detectors, the segmentation of subdetectors and the allocation of connected electronics and support structures can be solved in a much more practical way. As a consequence, each LHCb subdetector can split in half along the vertical, and each half can be moved completely outside the acceptance for maintenance operations. This also simplifies the access to most of the sensors described in this thesis.

The subdetectors which are mostly labelled with abbreviations in figure 2 are briefly described in the following paragraphs, starting on the left side of the picture:

Built directly around the IP, the Vertex Locator (VELO) consists of a series of silicon sensors placed inside a vacuum vessel on opposite sides along the beam line which overlap along the vertical axis when the detector is closed. These provide precise measurements of the r and φ coordinates of particle tracks which are very close to the interaction region. The whole detector including most of its electronics is located in a small alcove, which is referred to as the VELO alcove, indicated by the grey striped area on the left side of figure 2. This extension of the LHCb underground cavern is separated from the LHC tunnel by a concrete wall upstream of the IP, with the exception of a small hole through which the LHC beam pipe passes. It however shares similarities to the shape of the adjacent LHC underground tunnel, including a generally lower ceiling.

Downstream along the beam line directly attached to the VELO follows the first of two Ring-Imaging-Cherenkov (RICH) detectors, referred to as RICH1. Inside, Aerogel and C4F10 radiators are used to generate Cherenkov light. This light is then redirected via mirrors to the Hybrid Photon Detectors (HPDs) placed just outside the acceptance above and below the beam line. The detector is surrounded by a heavy metallic shielding protecting it from the influence of the nearby large dipole magnet. In addition, individual HPDs of both RICH detectors are still placed in MuMetal cylinders to permit high performance operation in magnetic fields up to 50 mT.

One of the single largest objects of the detector is the dipole magnet, which is located very close to RICH1 in between more tracking stations. In order to match the required detector acceptance, it was designed with sloping poles and saddle-shaped coils in a window-frame iron yoke weighing more than 1500 tons. It was required to minimize the field inside the envelopes of the RICH detectors, while maintaining a very high integrated magnetic field of 4 Tm over tracks of 10 m length. LHCb collects half of its data with the direction of the magnetic field upwards and the other half with the field pointing downwards.

Apart from the VELO, the LHCb tracking system consists of four planar tracking stations, of which the Trigger Tracker, or Tracker Turicensis (TT) is the only one upstream of the dipole magnet. Downstream of the magnet, three tracking stations (T1-T3) are made of individual Inner Tracker (IT) and Outer Tracker (OT) stations. Both TT and IT use silicon-microstrip detectors for enhanced precision in the region close to the beam. While the TT is 150 cm wide and 130 cm high, the IT boxes only cover a cross-shaped 120 cm wide and 40 cm high area in the center of the stations. The OT detectors are utilizing straw tubes to cover the remaining area up to the outer edge of the acceptance for the three stations.

RICH2 is located downstream of the magnet after the tracking stations and much larger than RICH1 in order to cover the increased cone of acceptance at this position. The RICH2 gas enclosure alone has a volume of around 95 m³. In contrast to RICH1, the HPDs are placed in separate magnetic shield boxes on the horizontal sides of the detector, but still outside of the acceptance.

The first out of five muon detectors (M1) is positioned quite far upstream of its counterparts, directly behind RICH2. The individual muon detectors themselves are rectangular multi-wire proportional chambers, providing a binary information on space point measurements of particle tracks. Their spatial resolution varies depending on their vicinity to the beam and to the IP. They are mounted in an overlapping fashion on both sides of a thin support wall made of an aluminum wrapped honeycomb structure.

A lot of effort was made to minimize the number of interactions of particles coming from the IP in the LHCb detector until they arrive at the calorimeter detectors, which start directly after M1. The calorimeter detectors are the first detectors intendedly introducing heavy materials inside the acceptance of the experiment. The first subdetectors downstream of M1 are the very thin Scintillating Pad Detector (SPD) and the PreShower (PS) detector, which sandwich around a 1.2 cm thick lead plate. The particle showers induced by interactions of particles coming from the collision with this lead plate are subsequently arriving at the more massive Electromagnetic Calorimeter (ECAL), painted in light blue in figure 2. The ECAL detector is made of laterally segmented stacks of modules of different sizes which allow for a higher resolution around the central regions of the detector. Each of the modules consists of thin stacked layers of lead and scintillating material along the direction of the beam. The scintillating light is transported via fibers to the downstream side of the detector, where the signals are measured with photomultiplier tubes mounted on the back of the ECAL. The largest of the calorimeter subdetectors is the Hadron Calorimeter (HCAL). Although it uses the same basic concept of stacked layers of metal and plastic scintillators as the ECAL, there are some key differences: the absorber material is iron instead of lead, and the tiles are segmented into square cells, running parallel to the beam axis in a checkerboard style. Individual modules are much larger than those of ECAL, as the whole HCAL is built of 26 modules for each half of the detector. Extending about 1.65 m along the beam axis, these modules are absorbing the full hadronic showers coming from the direction of the initial collisions.

Downstream of the calorimeter structure, the remaining four muon detectors M2-M5 are interleaved with 80 cm thick iron shielding walls, displayed in dark green in figure 2. Their function is to shield the detector chambers from everything except penetrating muons. Behind M5, an iron shielding of reduced size is separating the experimental cavern from the RB86 downstream LHC tunnel section.

A more detailed description of the individual detector components can be found in [3].

The LHCb coordinate system used throughout this document defines the origin $(x,y,z)=(0,0,0)$ at the nominal collision point inside the VELO [4]. As this reference point is fixed, actual collision points during operation usually differ slightly from this definition. The z axis lies in the center of the beam pipe along the nominal beam line and points from the IP inside the VELO downstream in the direction of the muon detectors. The x-axis points horizontally from the origin towards the direction of the PZ shaft on the Accessible side (A-side), and away from the cryogenic area on the other side of the experiment (C-side). The y-axis leads upwards along the vertical. An illustration of the experiment where the coordinate system is indicated is shown in figure 3. Any coordinates and positions given in this document will refer to this coordinate system.

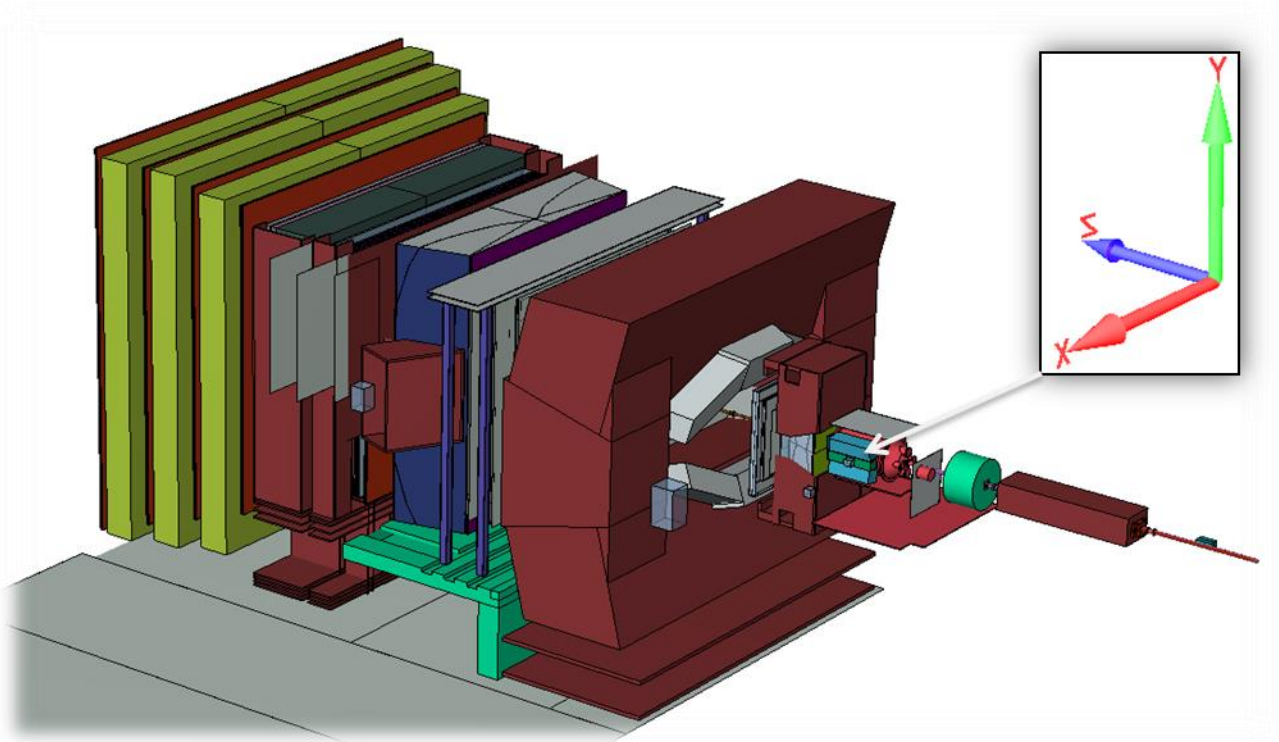


Figure 3: 3D sketch view of the Monte Carlo simulation geometry of the LHCb experiment used in this thesis, indicating the directions of the x, y and z axis in relation to the detector, as well as the position of the origin at (0,0,0) inside the VELO detector at the tip of the gray arrow. The beam line divides the experimental cavern into an A-side along the positive x-axis, and a C-side along the negative x-axis.

1.4 OPERATION OF THE LHCb EXPERIMENT

All 4 large LHC experiments make use of colliding proton and heavy ion beams provided by the LHC to confirm known and potentially discover new physics. When using collisions instead of fixed targets for single beams, more energy is available for the production of new effects. Little to no energy is lost in the Center of Mass (CM) system, which is why particle colliders like the LHC are considered apt to discover those effects.

Apart from the energy of the colliding beams, the performance of a particle collider is usually quantified by the term luminosity (\mathcal{L}) [5], which is directly correlated to the number of (useful) interactions, or events, being produced within a certain timeframe.

$$\frac{dR}{dt} = \mathcal{L} * \sigma_p \quad (1)$$

Luminosity is a proportionality factor, which links the number of events per second dR/dt to the production cross section σ_p as shown in formula (1). It has the unit $[\text{cm}^{-2} \text{s}^{-1}]$.

Exact predictions for the cross section of proton-proton collisions at the energy level of the LHC were not available at the start of operation. Therefore, the LHC experiments used purely experimental methods to determine luminosity values during operation. One approach is the “van der Meer scan” method, which was first developed at the world’s first hadron collider, the Intersecting Storage Rings (ISR) at CERN. The overlap of the beams is measured while the interaction rate is monitored in order to determine \mathcal{L} . This method is used by all experiments at the LHC and requires a special period of data taking operation. Using a different technique,

LHCb physicist M. Ferro-Luzzi proposed the Beam-Gas Imaging (BGI) method, which takes advantage of the excellent precision of the LHCb Vertex Locator (VELO) to reconstruct vertices of interactions between beam particles and residual gas nuclei inside the vacuum of the beam pipe. This data provides information on the angles, positions and shapes of the individual beams without interference. The combination of both methods enabled a combined relative precision of the luminosity calibration of 1.16%, when applied to the full data set before LS1. This represents the most precise luminosity measurement achieved so far at a bunched-beam hadron collider [6].

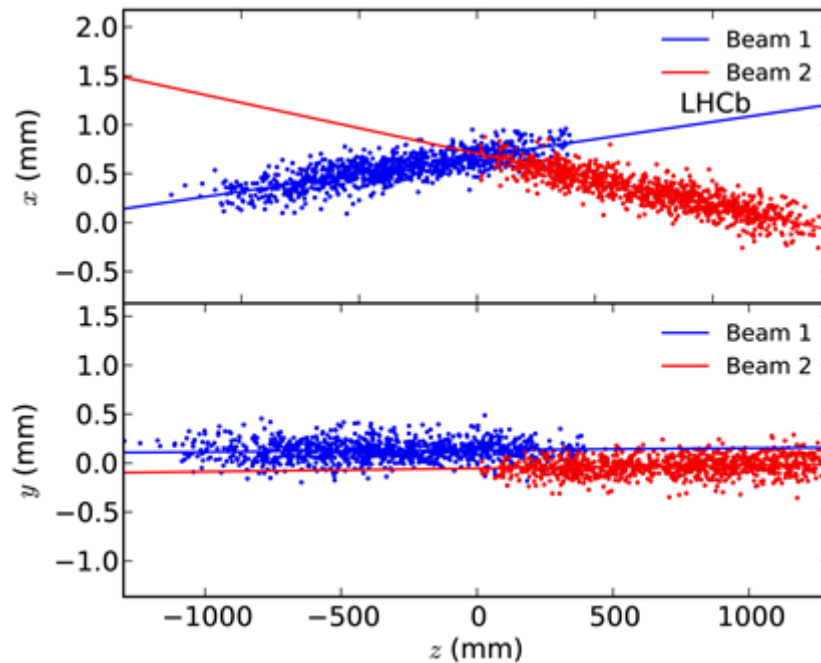


Figure 4: Reconstructed positions of proton-beam-gas collision points. Bunches are crossing at an angle horizontally to ensure that no unwanted collisions between bunches happen outside of the interaction point [6] [7].

An illustration of colliding bunches of protons at the interaction point of LHCb, according to reconstruction methods as described in [6], is shown in figure 4. The beam bunches are usually made to cross at an angle in at least one directional plane, in order to ensure that no unwanted collisions between bunches take place outside of the interaction region.

The main irradiation of the experiment takes place during the data-taking phase for particle physics studies. These phases consist of separate fills, which usually last for several hours until the beams are dumped. For a fill the LHC ring is loaded up with proton bunches going in both directions from the accelerator chain. After the beams have reached their target energy in the LHC, they are made to collide at the experiments.

At LHCb, a special mechanism called luminosity leveling [8] has been implemented and used during routine operation. The overlapping section of the colliding beams is constantly readjusted during a fill of the LHC, in order to reduce the initial number of collisions and keep a stable luminosity value during data taking. Since in LHCb about 1 to 3 pp collisions are needed to perform its measurements most efficiently, the experiment already runs at a lower luminosity level than what the LHC can deliver and what is used at the general purpose experiments. The luminosity leveling maximizes the number of events collected in these stabilized conditions and consequently helps to simplify triggering and event reconstruction on the LHCb online computing farm.

In the short breaks between fills no collisions take place. When maintenance operations become necessary either in the LHC or in one of its experiments, they are performed in those breaks, which sometimes results in longer downtimes between fills. Over the course of a year, longer breaks usually lasting a week for planned interventions and maintenance are foreseen, which are called technical stops (TS). The longest breaks between the start of the experiment in 2010 and the beginning of Long Shutdown 1 (LS1) are called Year End Technical Stops (YETS), and are lasting for a few months at a time beginning December. These provide extended predictable time to perform larger adjustments or repair campaigns to various detector equipment as well as the experimental infrastructure.

Maintenance operations during YETS always involves opening several subdetectors, including the calorimeters, the tracking stations and the muon detectors. In cooperation with the different subdetector teams, the planned opening procedures provided an occasion to access, recuperate and exchange some dosimeters used for this thesis who are otherwise not reachable during the year. The yearly readout interval for the sensors analyzed in this thesis is based on this circumstance. Coincidentally, the pp operating conditions of the LHC usually also happen to change with the end of a YETS, which allowed to investigate how these changes influenced the radiation field using passive sensors. Heavy ion runs are often scheduled before the beginning of a YETS, but they are not relevant for this thesis due to the extremely low collision rates of these at LHCb.

During the first 3 years of operation, the LHC delivered proton beams with individual energies of 3.5 TeV in 2010 and 2011, and increased to 4 TeV per proton in 2012. Hence these beams collided at the experiments with 7 TeV CM (Center of Mass) and 8 TeV CM energy, respectively. The operation until LS1 including operating conditions at both energies is referred to as Run1. While Run2 has officially started with the machine delivering collisions at 13 TeV CM since the end of LS1, this thesis only covers the time up to LS1, i.e. Run1.

An overview of the integrated luminosity values taken from LHCb operations plots for proton-proton collisions until LS1 is shown in figure 5. There is a notable difference between the delivered luminosity, a value which is provided by the LHC operators, and the recorded luminosity, which correlates with the amount of data which was collected and recorded at the experiment. The error on each data point is larger than 10%, as they were not prepared with the sophisticated methods described in [6]. Any references to luminosity values mentioned in this thesis are always referring to the delivered luminosity value.

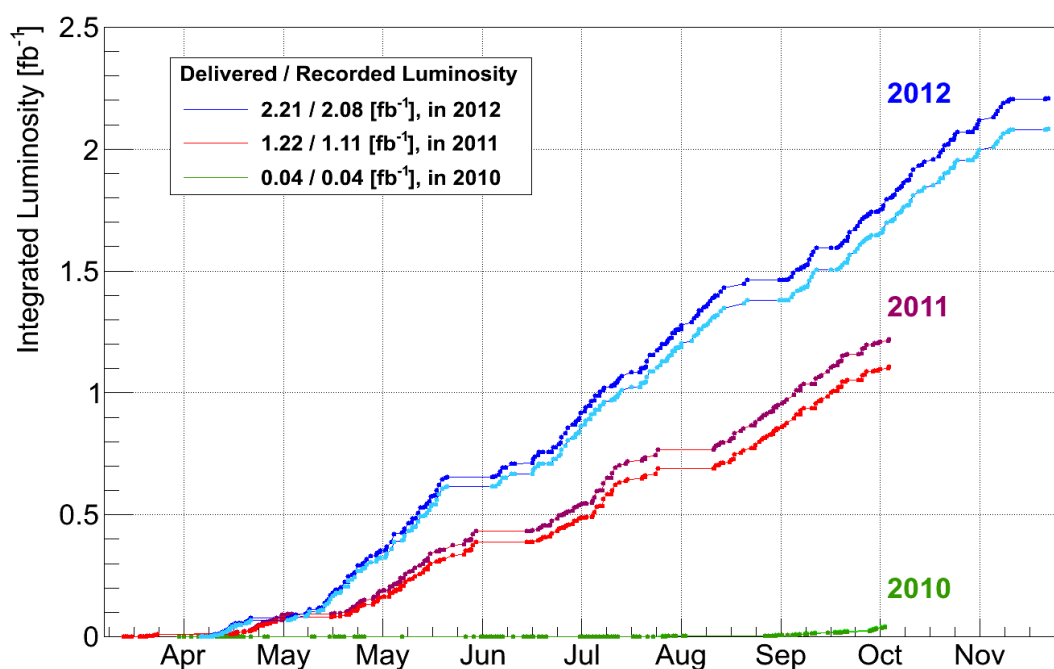


Figure 5: Overview of the integrated luminosity values in fb^{-1} over the course of Run1, until the start of LS1 [9].

The step-like structure of the integrated luminosity curves in figure 5 indicates periods of operation. While the ascending segments are concurrent with collisions taking place at the experiment, they are interrupted by technical stops followed by machine development lasting up to one or two weeks, where no collisions take place and therefore \mathcal{L} remains constant.

During the data taking of 2013, just before the official start of LS1, a campaign to produce collisions between protons and heavy ions was undertaken at the LHC. The LHCb experiment took part, but was only exposed to a minuscule amount of proton-ion collisions, which was negligible compared to the number of collisions during the previous years of proton-proton operation. These proton-ion collisions represented less than one millionth of the total integrated luminosity of 2012, and therefore had no recognizable influence on the radiation levels. As a consequence, the effects of these collisions are not considered in this thesis [10].

1.5 RADIATION PRODUCED BY HIGH ENERGY PARTICLE ACCELERATORS

1.5.1 DEFINITIONS

When compared to radiation facilities like nuclear reactors, electron beam accelerators or facilities using strong radioactive sources, a high-energy Hadron Collider produces radiation fields which are substantially different. The characterization of the radiation fields created by its collisions necessitates the use of special quantities that are best fit to describe its properties of interest. The following paragraphs explain some of the definitions of those quantities as used in this thesis.

1.5.1.1 PARTICLE FLUENCE

The fluence ϕ is defined as the ratio between the amount of incident particles on a spherical surface dN and the cross sectional area of the sphere da , and it has the unit [m^{-2}].

$$\Phi = \frac{dN}{da} \quad (2)$$

In Monte Carlo Simulations, and specifically in FLUKA, which is used for this thesis and will be described in section 3, fluence is often expressed using the sum of particle track lengths dl through a volume dV [11].

$$\Phi = \frac{dl}{dV} \quad (3)$$

The energy distribution of a particle fluence, labeled as differential fluence Φ_E , is defined as fluence per energy interval $[E, E + dE]$. In this thesis, this term will be used to describe particle spectra calculated via Monte Carlo simulation.

$$\Phi_E = \frac{d\Phi}{dE} \quad (4)$$

The unit of the differential fluence is [$\text{J}^{-1}\text{m}^{-2}$]. Fluence values in FLUKA simulations are based on track length of a given set of particles passing through a user-defined volume.

1.5.1.2 1 MEV NEUTRON FLUENCE EQUIVALENT

The origins of the 1 MeV neutron fluence equivalent are connected to the discovery of radiation damage effects in silicon-based electronics. The fluence of fast neutrons in crystalline structures like silicon is linked to the occurrence of bulk defects related to the displacements of lattice atoms. However, also other types of particles with varying energies are able to produce the same effects.

Displacement damage is proportional to the Non-Ionizing Energy Loss (NIEL) of an incident particle. It is described with an energy-dependent damage function $D(E)$ [12]. This function is used to characterize the damage efficiency of any particle for a given energy, and its values are normalized to that of neutrons with an energy of 1 MeV [13]. This means that the damage effects of an arbitrary mixed-particle irradiation on a material, can be expressed as the equivalent of a 1 MeV neutron beam having the same effect. The NIEL hypothesis describes the proportionality between the fluence of particles and the resulting damage. In this thesis, the term 1 MeV neutron fluence equivalent will always be calculated for silicon, which is the most used material when electronic devices are concerned. The unit is the same as that of a standard particle fluence [cm^{-2}].

1.5.1.3 DOSE (ENERGY)

One of the basic quantities in radiation physics is the energy dose D , which is able to cause permanent damage to exposed equipment if deposited in large enough quantities. It describes the average energy $d\bar{E}$ deposited by ionizing radiation within matter of the mass dm .

$$D = \frac{d\bar{E}}{dm} \quad (5)$$

This quantity is measured in [Gy], which can be expressed as [J kg^{-1}].

1.5.2 INTERACTIONS OF LIGHT ELECTROMAGNETIC PARTICLES

When passing through matter, electrons and positrons lose energy via two main processes: either by ionization via collisions, or by the production of Bremsstrahlung, which is electromagnetic radiation emitted during deceleration of charged particles when they are deflected by other charged particles or nuclei. Formula (6) describes the loss of energy as a sum of both processes.

$$\left(\frac{dE}{dx}\right)_{tot} = \left(\frac{dE}{dx}\right)_{col} + \left(\frac{dE}{dx}\right)_{rad} \quad (6)$$

The energy at which these two loss mechanisms are equal is defined as critical energy E_c . At energies above E_c , losses via radiation are more frequent, whereas ionization processes dominate at lower energies. As an example, E_c in iron lies around 20 MeV [14]. Positrons annihilate with electrons at the end of their flight paths, most of the time by transforming into two photons with 511 keV each, which equals the rest energy of an electron or positron.

Photon behavior is different from that of electrons as they cannot interact by continuous ionization along their path. Photon interactions can be narrowed down to three principal mechanisms: Photoelectric effect, which is most prevalent at low photon energies, Compton Scattering and Pair Production.

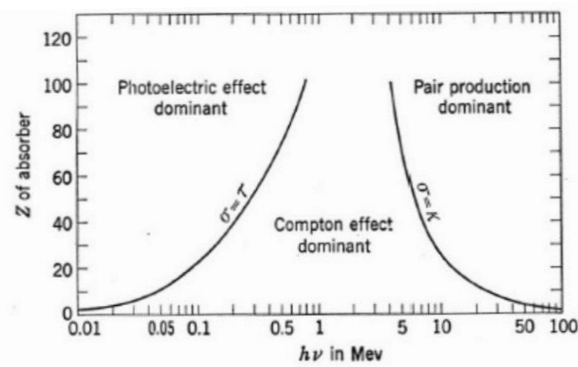


Figure 6: Illustration of dominant effects of photo-absorption for different Z values vs. the incident energy of the photon [15].

An illustration of the dominant effects for the absorption of photons, which mainly depend on the energy of the photon and the type of the absorbing element (based on its Z number), is shown in figure 6. According to the plot, photons with lower energies are depositing energy preferably via Photoelectric and Compton effects, while high energy photons are mainly attenuated via pair production even within relatively light materials. Cross sections for the pair production mechanism within various materials remain quite stable at high energies above 100 MeV. In figure 7 the absorption length over the energy of the incident photon is shown for different elements. While this property is visibly volatile and distinct for different elements at lower energies, it becomes stable above 100 MeV for all of them.

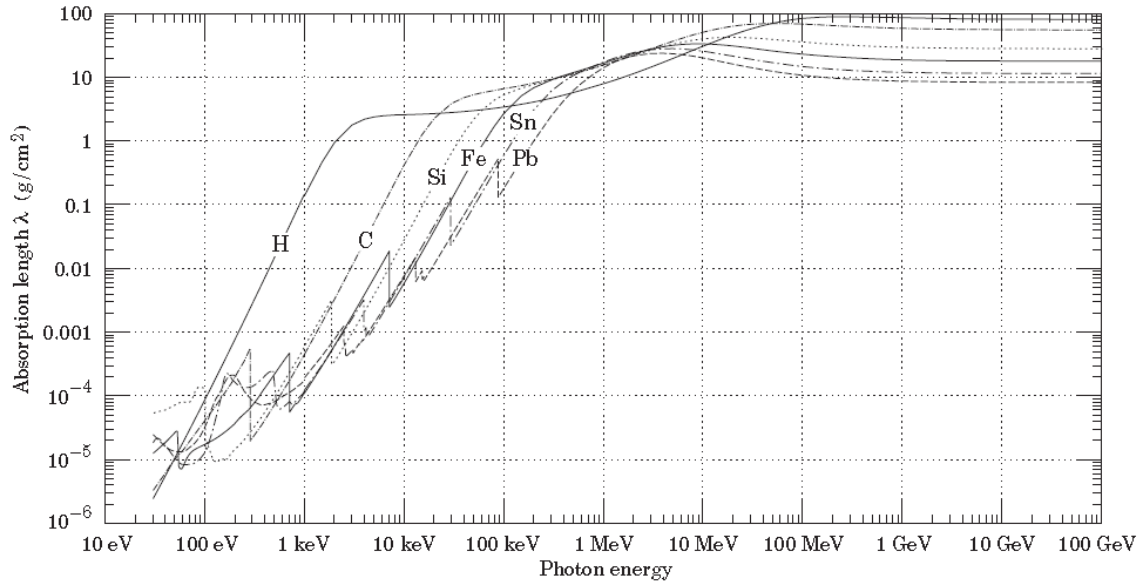


Figure 7: Absorption length per incident photon energy for various elements [14].

Electromagnetic interactions in LHCb will comprise the whole spectrum of possibilities described above, as particles continuously lose energy on their way through the detector. However due to the very high incident energy of particles created in the collisions in the Interaction Point, pair production for photons and Bremsstrahlung for electrons and positrons do play a relatively large role in distributing the energy through electromagnetic cascades. A parameter often used in this regard is the radiation length. The radiation length X_0 is defined as the mean distance that an electron or positron with high energy crosses until its energy is reduced to a fraction of $1/e$ of its initial value by Bremsstrahlung. It also characterizes the mean free path for pair production λ_{pp} in a material for energies larger than the critical energy E_0 : X_0 is $7/9$ of λ_{pp} [14].

1.5.3 HEAVY CHARGED PARTICLES

Protons and heavier particles such as the alpha particle primarily interact with matter through Coulomb forces. In most cases, this means interactions between the incident particle and the orbital electrons of the absorbing matter. While interactions with nuclei are possible, they normally occur at a much less significant rate. [15].

As the heavy charged particle passes through the absorber, some of its impulse is transferred via Coulomb force to the orbital electrons. Depending on the circumstance of the encounter, the impulse may either excite the electron to a higher shell, or completely remove it from the atom by ionization. The velocity of the incident particle is continuously decreased as a consequence of this process until it comes to a stop. Since only a small fraction of energy can be transferred from the heavy particle onto the electron in a single collision, a lot of interactions of this kind are taking place during the passage of a particle through matter.

When they only interact with the Coulomb field of the absorber, heavy charged particles usually go along a rather straight path during deceleration, because each encounter with an electron only deflects the incoming particle by a tiny amount. Hence, they can be attributed a range in a given absorber material, representing the maximum distance they can pass. When the velocity of a moving heavy charged particle is reduced, the momentum transmission to the surrounding atoms increases, and at the end of its path, most of its remaining energy is almost deposited on the spot. This leads to the formation of a so called Bragg peak in the deposited dose. The location of this peak depends on the type and the initial energy of the particle and the irradiated

material. This effect occurs in hadron calorimetry, although the hadrons in the detector are mainly stopped by hadronic interactions that induce a much higher loss of energy. It is also used as a more widespread application in accelerator facilities for medicinal ion-therapy against forms of cancer which are otherwise difficult to access.

In practice however, only a very tiny amount of heavy particles starting above energies of 1 GeV will ever reach this maximum range, because of inelastic hadronic interactions which are able to stop them faster in their tracks than the continuous electromagnetic interaction is able to. Materials with a high density and high atomic number Z provide the largest stopping power for both effects, but inelastic interactions also depend on the specific cross sections between the incident particle and the absorber material.

1.5.4 NEUTRON INTERACTIONS

The operation of high energy ion accelerators is always accompanied by large emissions of neutrons. These neutrons are generated by primary beam losses as well as highly energetic secondary radiation interacting with the material of the machine and the experiments.

Neutrons are uncharged particles which ionize matter indirectly, and they only interact with the nuclei by means of absorption, elastic and inelastic scattering or spallation. The deposition of energy on matter is primarily propagated by heavy charged secondary particles like pions or protons and particles of the electromagnetic cascade (electrons, positrons and photons).

Scattering leaves the number of neutrons and protons of the nuclei intact. Elastic scattering changes the direction of the incoming neutron when it is deflected off the surface of a nucleus, while imparting kinetic energy via recoil. Whereas during inelastic scattering, the neutron is actually captured for a very short amount of time, and is transferring some of its energy to the other nucleons before it is re-emitted. In some cases, other nucleons are emitted as a reaction of the inelastic scattering process.

Absorption of a neutron transforms the absorbing nucleus into an excited quasi-bound, so-called compound nucleus. In order to release the excess energy and reach a stable state, different reactions like the emission of gammas or single nucleons may take place. The impinging neutron can also cause the disintegration of nuclei above energies of several tens of MeV, resulting in the creation and emission of high-energy particles such as protons or pions. This is referred to as spallation and it is frequently followed by a de-excitation process of the nucleus, which is called evaporation. Another possible reaction is nuclear fission, which is mainly being triggered when heavy elements capture neutrons. The nuclei then split into two or more fragments plus several neutrons.

Cross sections of interactions of neutrons with matter depend strongly on the energy of the incident particle. Neutron capture followed by subsequent emission of gammas (n,γ) or, less frequently, protons (n,p) are the dominating process below 1 eV. The probability of interaction in this energy region rises with the duration of stay of the neutron in the vicinity of a nucleus, and therefore the cross section is inversely proportional to the velocity of the neutron. Above this so-called thermal region, the total cross section stays relatively constant up to several MeV depending on the nuclei, with elastic scattering accounting for most of the interactions. Typically, different materials exhibit a very particular resonance structure in their neutron cross sections, which is caused by the potential excited states of nucleons as well as collective excited states of the nucleus. At higher energies up to 20 MeV, the probability for inelastic scattering and the emission of heavier secondary particles, for example deuterium (n,d) or alpha particles (n,α), increases. Relativistic neutrons with energies above 20 MeV are mainly responsible for spallation and evaporation processes [15] [16] [17].

1.5.5 OTHER PARTICLES OF INTEREST

High energy collisions between nuclei produce a large number of particles including pions, kaons, other nucleons, as well as fragments of the nuclei involved in the collision. When their production becomes energetically possible, the presence of pions becomes more noticeable at higher energies of primary protons. At very high energies, pions are usually the dominant particles produced in collisions at the LHC. As an example, a Monte Carlo simulation of a lethargy spectra of the main particle distributions in the LHCb cavern about 2 m from the IP and at 15 cm distance to the beam line is shown in figure 8. In this case, pions are clearly the dominant particles at energies of several 100 MeV and upwards. Within the acceptance of the LHCb experiment, this dominance at the highest energies will remain until the particle showers reach the calorimeter subdetectors. The absorption lengths of pions are comparable in magnitude with those of protons. Charged pions mostly decay into muons, which have long ionization ranges, providing a path for energy to escape a hadronic cascade. Given the extraordinary energies at the LHC, many pions and even kaons are able to reach the calorimeter detectors in LHCb.

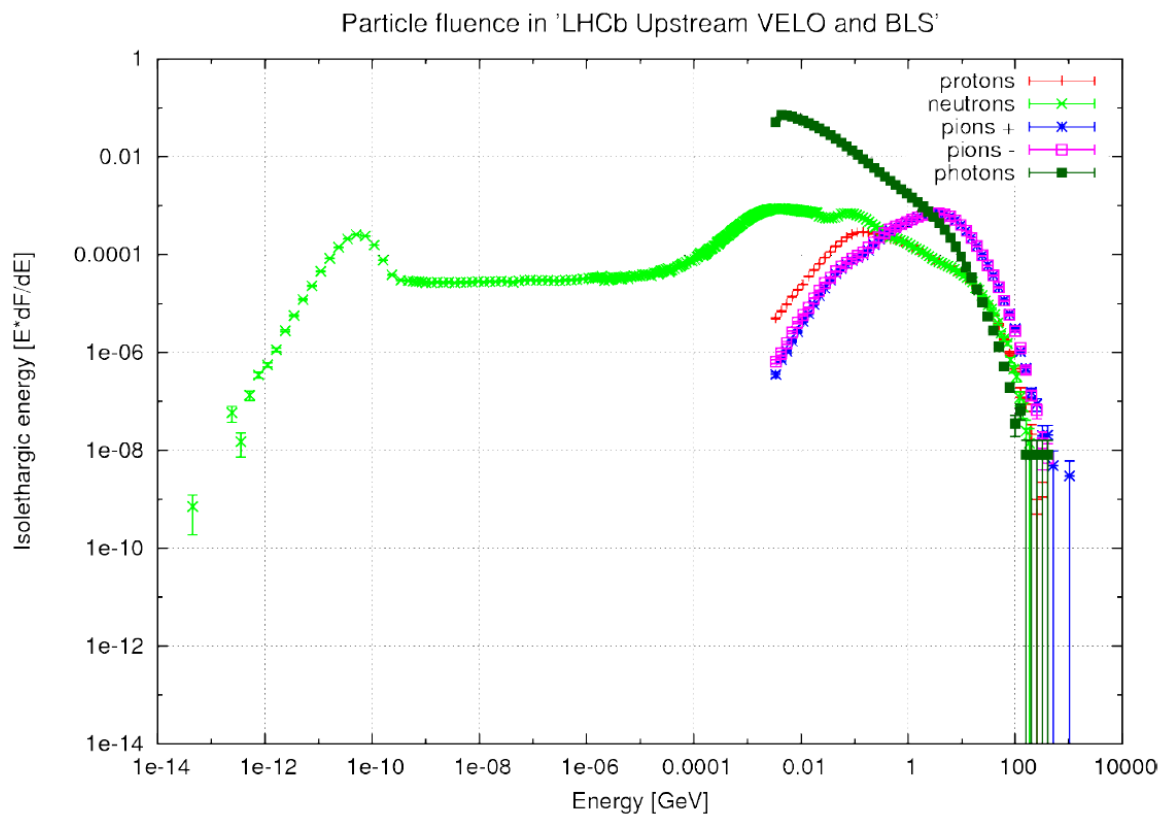


Figure 8: Lethargy plot of various particle fluences simulated at the upstream wall of the VELO alcove in the LHCb cavern, at about 15 cm distance from the beam line. Within most of the acceptance of the LHCb experiment, pions are clearly the dominating particle at higher energies [18].

Kaons in general have a very short half-life, and they are generated in comparably low numbers in LHC collisions. Therefore they are only of small relevance for most radiation field parameters.

Muons on the other hand do have a significant impact on the radiation field at high-energy accelerators. Due to their very high kinetic energies at the time of production, they are able to traverse large fractions of very dense material before they pass on enough energy and decay themselves. In fact, one of the reasons for the LHC being built underground is a consequence of the implications of muons for radiation protection because of their range. They are generated either by a form of pair-production very similar to the one related to electrons and positrons, or by decay processes from other short lived particles such as pions or kaons [19].

1.5.6 HIGH ENERGY PARTICLE CASCADES

A wide variety of particles is created when protons collide with high energy at the LHC, similar to the impact of cosmic radiation on earth's atmosphere. Many of those have sufficient energy to produce several generations of secondary particles, initiating a particle cascade. The total amount of secondaries depends on the energy of the primary particle. At an LHC experiment which is based on high-energy proton or ion collisions, two main types of cascades propagate the energy of the original collision through the detector: the hadronic and the electromagnetic cascade.

1.5.6.1 HADRONIC CASCADE

A cascade made of hadronic particles grows in size as long as the energy of its secondary particles is still high enough to produce further generations of secondary hadrons. The development of the hadronic shower involves the production of new hadrons via collision with nuclei, the decay of particles like pions and nuclear de-excitation processes. If the average energy of the hadrons in the cascade falls below a certain threshold, an attenuation process takes over the build-up. The extension of the cascade is defined by the primary hadron energy and by the material it passes through, which determines the hadronic interaction length λ , also called the mean free path. A notable property of λ is that within heavy materials it is considerably longer than the radiation length X_0 , which is the defining parameter for electromagnetic cascades. This means that hadronic showers start later than electromagnetic showers, explaining the reasoning behind the construction of calorimeter detectors with the electromagnetic detector placed before the hadronic [14].

The hadronic cascade is able to transfer energy to an electromagnetic cascade via different mechanisms, of which the π^0 particle plays the most important role, if the primary particle energy exceeds some tens of GeV. This very short lived hadron has a mean lifetime of $8.4 \cdot 10^{-17}$ seconds. With a probability of around 99%, it decays into 2 photons with an energy of at least 135 MeV, which is the rest mass of the neutral pion. These photons have sufficient energy to initiate a cascade themselves, transforming most of the initial hadron energy into an electromagnetic shower.

1.5.6.2 ELECTROMAGNETIC CASCADE

High energy electrons, positrons and photons interacting with matter are able to initiate cascades made of electromagnetic secondary particles by Bremsstrahlung and pair production, respectively. The size of the cascade depends on the energy of the primary particle, where the number of daughter particles per generation t develops with 2^t due to the nature of the processes involved, as shown in figure 9. This number is much more correlated to the initial energy of the particle than for hadronic cascades, where the nature of the involved processes results in a much more fluctuating number of secondaries. In the electromagnetic cascade, the build-up continues as long as the energy of the current generation of particles is still high enough to favor pair production over other photon interaction mechanisms.

As with hadronic cascades, the material composition has an influence on the spatial extension of the cascade, but the defining parameter for electromagnetic particles is the radiation length X_0 , which defines mean distances for high-energy electrons and positrons and mean free paths of high-energy photons as described in 1.5.2. A transfer of energy from an electromagnetic into a nuclear cascade is possible by means of photo-nuclear reactions.

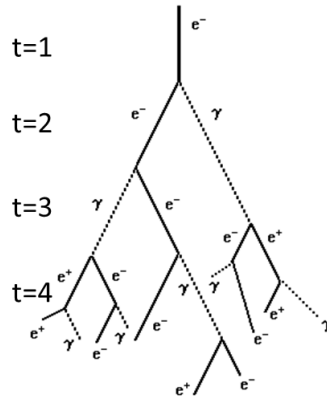


Figure 9: Sketch of processes during an electromagnetic cascade. Each generation t , 2^t particles are created until the critical energy E_c is reached [20].

1.6 RADIATION EFFECTS ON THE EQUIPMENT

In the LHC and its experiments, all detector components need to tolerate some amount of radiation dose induced by all kinds of particles at energies ranging from meV to TeV, which are generated during proton-proton collisions. Since front-end electronics of each subdetector are located either within or very close to the detector acceptance, its parts and modules have been custom developed to handle large-scale signal processing in an environment with elevated radiation levels. These components had to undergo extensive radiation tests to verify correct behavior during and after radiation exposure. Nonetheless, systems exposed to the mixed radiation fields present at the experiment are experiencing different forms of damage due to radiation during their lifetime. Most relevant among these are: displacement damage caused by Non Ionizing Energy Loss (NIEL), Single Event Effects (SEEs) and damage from Total Ionizing Dose (TID).

1.6.1 CUMULATIVE EFFECTS:

Total Ionizing dose (TID) (1.5.1.3), which is measured in Gy, can gradually damage components of the LHCb detector in several ways. As an example, energy deposited from particles passing through silicon-based electronic devices can induce space-charges which might lead to a degradation through micro-discharges inside the device. TID is also responsible for reducing the transparency of light-transmitting fibers, which are used to transfer scintillation light from detectors to the signal amplifying photomultipliers. Of course also many types of scintillators themselves suffer from this effect. Extremely high dose may even damage splices or isolations made of synthetic materials, depending on their sensitivity to radiation. If the deposited dose reaches high enough levels in the kGy to MGy range, it can even lead to degradation or structural damage of supporting components like glue, insulation or composite materials in general [21].

Another form of cumulative damage which is mostly correlated with damage to electronics, is caused by particles displacing atoms from a crystal lattice like silicon. If these atoms and the created vacancies do not immediately recombine and instead start migrating through the crystal, they may lead to point defects in the lattice through recombination with impurities. This effect is referred to as displacement damage and it can lead to a degradation of the performance of semiconductor devices over time. The threshold for these bulk damage effects in silicon lies around 100 keV [22]. The corresponding damage produced by different particles

with different energies can be scaled according to the NIEL hypothesis and expressed in terms of the 1 MeV neutron fluence equivalent (1.5.1.2) [12].

1.6.2 SINGLE EVENT EFFECTS:

In contrast to cumulative effects, the impact of Single Event Effects (SEE) is very acute. This term is used mainly in connection with specific interactions of high energy hadrons (HEH) (>20 MeV) with electronic devices. As an example, local charges induced by incident hadrons can sometimes change the content of individual logic components like memory cells, triggers or switches. HEHs and heavy ions are capable of inducing very high space-charges in a very narrowly defined spot. If the effect is only temporary and non-destructive, it is called Single Event Upset (SEU). Concerning the operation of a device, the consequence of a SEU can range from having almost no effect, if only some data path is affected, to shutting it down because of a critical upset in the control path. In some cases, a large enough localized energy deposition can also lead to permanent damage of a device. Strong misguided currents may destroy parts of the equipment due to induced charges lowering the impedance in critical regions. This is referred to as Single Event Latchup (SEL). If the current exceeds a certain level, the latch-up can evolve into an even more destructive burn-out (SEB). Depending on the sensitivity of devices to such SEEs, their probability of occurrence can be linked to fluence values of HEHs [23].

2.1 DOSIMETERS AND FLUENCE SENSORS USED IN LHCb

The radiation-monitored locations of the LHCb experimental area can be loosely sorted into groups, which will be described in detail in the later sections: the largest cluster of sensors is distributed in between the calorimeter detectors, including positions very close to the beam pipe as well as close to the edge of the detectors. The other relevant accumulation of sensors inside the experiment's acceptance is located on the front of the M1 muon detector. Most of the more easily accessible locations around the experiment cavern are at the edge of the experiment, close to the control systems and other electronics of the detectors themselves. A last group of sensors is located in the nearby tunnel upstream of the experimental cavern. All measurement positions are equipped with groups of different passive sensors. A sample holder box made of polyethylene [24], shown in figure 10, houses the different types of sensors, in order to facilitate their placement and bookkeeping. The dosimeter set consists of Polymer Alanine Dosimeters (Alanine) and Radio-Photo-Luminescence (RPL) crystals for High Level Dosimetry, a small plastic slide with 4 different Thermo-Luminescent Dosimeters (TLDs) measuring in the low as well as a high dose range, and a passive PiN diode for estimating 1 MeV neutron equivalent fluences. The latter is not sensitive to the fluences experienced in LHCb until LS1 in most of the positions. A detailed description of these sensors will be given in the following pages. A view of the interior of a filled sensor housing can be seen in figure 11.

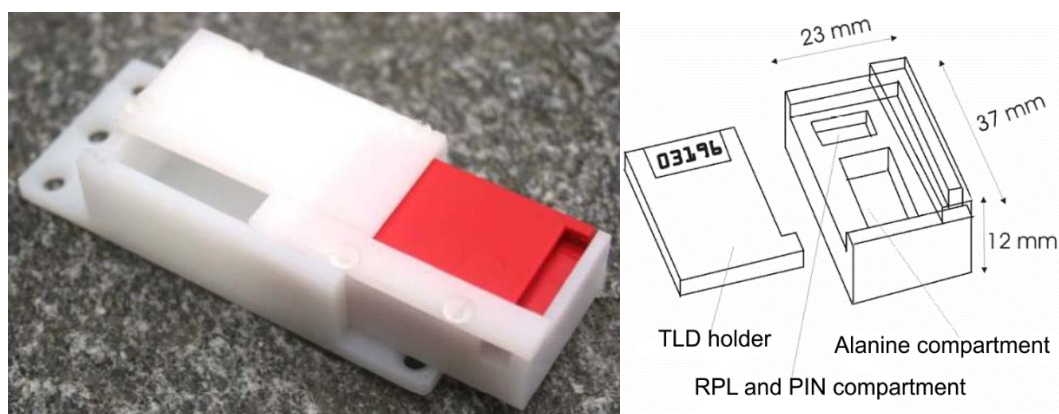


Figure 10: Photo (left) and sketch of the passive detector box which is used at LHCb. The TLD holder acts as a cover for the smaller compartments housing Alanine, RPL and PiN sensors.

Two main collection campaigns were conducted for the passive dosimeter boxes for most locations in the aforementioned groups. The first campaign was carried out during the YETS at the end of 2011 and the second at the beginning of LS1 in 2013. All of the sensors in the collected boxes have been measured each time. Some sensor boxes, which are placed in areas with lower radiation exposure next to electronic racks at the top of the calorimeter support structure and at the outer edges on top and bottom of the PS and SPD, were collected and measured during LS1 for the first time since their installation in 2009.

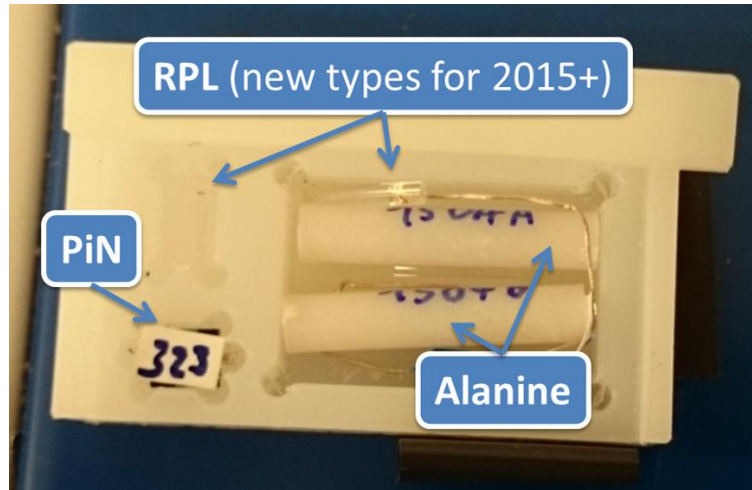


Figure 11: Inside look of a passive dosimeter housing filled for use after LS1. Contents include Alanine, a PiN diode and two different types of RPL. Alanine sticks represent the largest sensors inside the compartment.

Acquiring measurement results at the aforementioned times was decided upon because of two main reasons. Firstly, the maintenance operations during shutdown were conveniently timed, which made it possible to access and replace the dosimeters with a reasonable effort despite a very tight schedule. More importantly, being able to compare measurements taken during operation at a collision energy of 7 TeV CM in 2011 versus an energy of 8 TeV CM in 2012 allows for a more detailed analysis of the behavior of the radiation field as well as the sensors themselves.

At the end of 2010 during the first YETS, a handful of sensor boxes around the edges of the experiment including the ones on the front of M1 have been measured and replaced for the first time. Since they only accumulated dose corresponding to an integrated luminosity of about 0.04 fb^{-1} , compared to 1.22 fb^{-1} during 2011, most of the sensors were not able to measure any significant amount of dose or fluence. For a few sensors in the center of M1 and on the wall upstream of the VELO, the reduction of the measurement of around 3% for some of the replaced sensors in 2011 was considered negligible.

2.2 PASSIVE DOSIMETERS

2.2.1 POLYMER-ALANINE-DOSIMETERS

Alanine is an amino acid showing a chemical composition (L- α -alanine: $\text{CH}_3 \cdot \text{CH}(\text{NH}_2) \cdot \text{COOH}$) that is close to human tissue. Therefore it is mostly used in Radiation Protection to estimate equivalent dose values after converting the energy dose measured by the dosimeter. However, the dose range of Alanine measurements matches the range of radiation tolerance for many types of equipment used at the experiment. Combined with its compact form factor and simple handling, it proved to be very suitable to measure dose to equipment at CERN in general. Alanine dosimeters provided by DGS-RP have been widely tested and used at CERN for several years, and have therefore been chosen for use in the LHCb experiment [25].

When Alanine is exposed to ionizing radiation, radicals are generated which can be measured using electron spin resonance (ESR) spectrometers. The concentration of radicals measured is directly related to the dose absorbed by the dosimeter. At CERN, Alanine is used as Polymer Alanine Dosimeter (PAD), where the polymer acts as a binder to give them a compact cylindrical form of 20 mm in length and 4 mm in diameter. These Alanine sticks are provided by CERN DGS-RP.

The method used to read the Alanine dosimeters at the end of 2011 is not entirely clear, because the readout was handled at the time by an external contractor employed by the CERN Radiation Protection group. He presumably used an EMS 104 EPR Analyzer from Bruker [26].

For measuring the dosimeters collected at the beginning of LS1, a Miniscope MS 400 spectrometer, shown in figure 12 together with control software by Aérial was made available to the author by the Radiation Protection group. This second set of measurements was instead performed by the author, using calibration curves provided by the Radiation Protection group.

The readout equipment that was used to measure the sensors collected during the YETS of 2011 only gave meaningful results down to a minimum dose of about 3 to 5 Gy according to the contractor. The new equipment that is used to read out Alanine sensors exposed in 2012 is considered to be reliable down to a minimum dose of 1 Gy. The upper limit of the Miniscope S400 is quoted at 120 kGy. The equipment has been calibrated by the CERN Radiation Protection group with samples that were irradiated with a ^{60}Co source. One of the calibration dosimeters was measured before and after each batch of measurements, to correct for eventual spectrometer response variations over time. The software automatically chooses the best polynomial fit for the curve. All analysis results are stored into an internal database of the software to enable reliable access to the data itself and its linked measurement parameters.

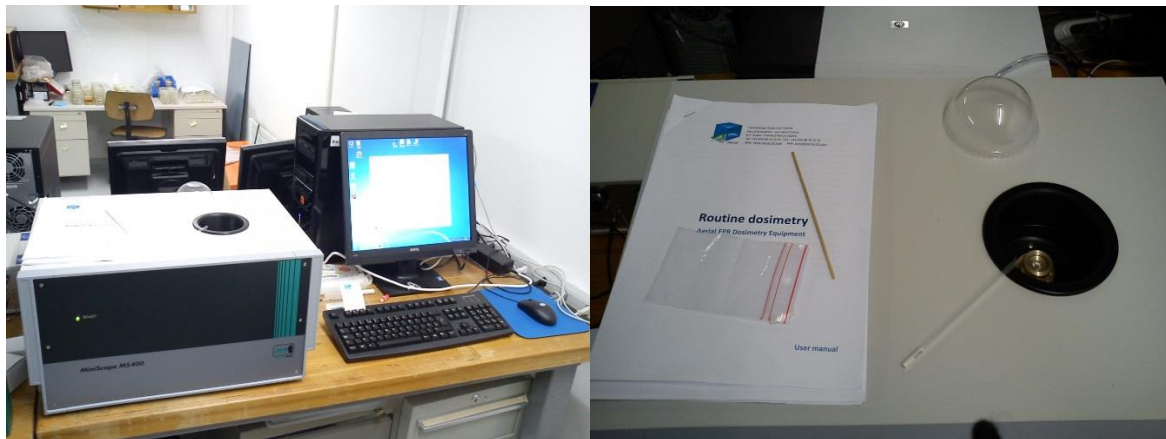


Figure 12: Miniscope MS 400 on the left. Dosimeters are carefully inserted from above via a glass tube visible on the right in between magnetic coils used for the measurement.

Dosimeters usually respond differently to different types of radiation, for example hadrons, which are omnipresent in most of the central areas of the LHCb experiment. First calibration efforts with proton beams at the IRRAD1 facility at CERN have shown that the response of RPL and Alanine is higher to protons than to photons [27]. Based on the results and the methods cited, it is however very difficult to deduce a general behavior of Alanine dosimeters within a complex mixed field where not only the hadron type but also the hadron energy can vary.

Another study undertaken at the CERN-EC High-Energy Reference field Facility (CERF-field) compared the response of Alanine that is exposed to mixed high-energy (up to a few GeV) particle fields to FLUKA Monte Carlo simulations. At applied doses between 130 Gy and 1 kGy, Alanine dosimeters showed little to no deviation from the simulated dose in air [28].

Taking into account the elevated energies and dose, as well as differing compositions of high-energy particle fields at the LHCb experiment, the author considers Alanine to be the most reliable dosimeter system at the moment for dose >3 Gy and <120 kGy for data collected in 2011 and dose >1 Gy due to the change of readout equipment in 2012. The fact that the calibration curve is based on ^{60}Co radiation is taken into account for this statement. We conclude that Alanine measurements are fully reliable in this dose range, considering the fact

that they have been tested and evaluated at a range of up to 100 kGy by the CERN Radiation Protection group, among others, for several years.

2.2.2 RADIO-PHOTO-LUMINESCENCE DOSIMETERS

Radio-Photo-Luminescence (RPL) dosimetry is currently deployed by the Radiation Protection group at CERN and subsequently used by the LHCb experiment as the only passive dosimetry system for dose measurements exceeding 120 kGy. At the moment, no reliable alternative dosimeter for this dose range has been considered for use by the Radiation Protection group nor LHCb. The CERN RP group provides dosimeter crystals made of silver-activated aluminophosphate glass, which emits light when exposed to UV light. The amount of emitted light from the crystal, which is measured using photomultipliers, correlates to the amount of radiation absorbed in the glass.

RPL sensors were added to the passive dosimeter boxes of the calorimeter for the first time during the YETS of 2011. Up to that point, only Alanine, TLD and Pin diodes were present in the calorimeters. Although Alanine dosimeters did cover the high dose range for all calorimeter sensor positions, it was considered useful by the author to add an additional measurement method, which was already used at other locations in the LHCb experiment. The additional sensors were intended to help with the characterization of the utilized dosimeter types within the mixed field. The RPL dosimeters provided to us by the Radiation Protection group were mostly reused from previous measurement campaigns at CERN, because the manufacturing of this type of crystals was discontinued years ago.

In general, we observed that RPL sensors' measurements are in good agreement with those of the Alanine. Unfortunately, a large number of RPL sensors that had been installed have been found to be damaged on the surface to various degrees. A wide variety of cracked and splintered surfaces has been observed, an example between many is shown in figure 13 and figure 14. This kind of damage is influencing the readout process. During the readout, the crystals are illuminated using ultraviolet LEDs in order to stimulate the emission of light that corresponds to a dose value. Due to the geometry of the proprietary measurement setup, cracked or bent surfaces can influence the amount of light that reaches the photomultiplier by reflection. Also, small variations in volume have been registered with some crystals, which had an influence on the measurement when compared to the more stable Alanine results.

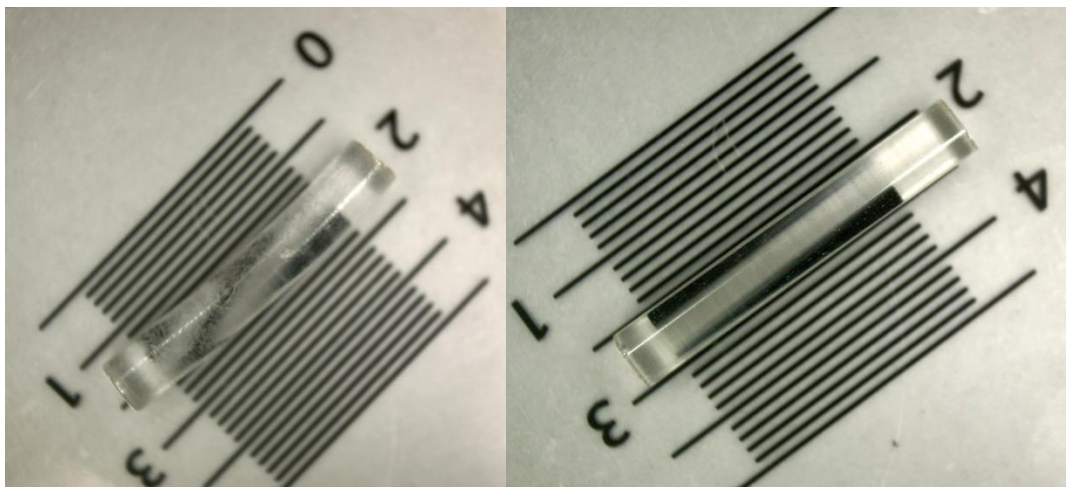


Figure 13: A damaged and bent out of shape RPL crystal collected during LS1 on the left compared to an intact RPL crystal with a smooth surface on the right. The rough surface as well as the bent shape can influence the amount of light reaching the photomultiplier and therefore the measurement.



Figure 14: Comparison of the top surface of a damaged crystal (left) versus an intact crystal with a smooth surface (right). Dents and cracks like these influence the readout of the crystals through reflection and dispersion mechanisms that cannot be adjusted for. More varieties of damage can be found on other RPL dosimeters from this measurement campaign.

Due to this reason, many of the RPL measurements needed to be discarded. Most of the RPL measurements between those retained have been found to deviate from the Alanine readouts up to $\pm 30\%$. It should be pointed out, that some crystals that are visibly broken exhibit much higher discrepancies. Since the specific dose range of RPLs is largely covered by Alanine sensors, which are deemed to be reliable and less prone to damage, only the measurements performed with Alanine and TLD sensors, which cover high and low dose ranges respectively, will be presented in this thesis.

Based on this experience, it was realized in collaboration with the RP group that to obtain reliable results with RPL dosimeters, strict quality control is necessary. New Japanese RPL crystals of a slightly bigger size and flawless surface are currently being used for High Level Dosimetry by the RP group at CERN, and they have been installed in LHCb for dose assessment in Run2.

2.2.3 THERMO-LUMINESCENT DOSIMETERS

Thermo-Luminescent Dosimeters (TLD) are made of inorganic crystal structures which have the ability to trap electrons in an energy-band-gap between valence and conduction band. Electrons are elevated from the valence to the conduction band by incident ionizing radiation, and instead of returning to their initial state, are trapped in the gap between bands. The number of accumulated trapped electrons corresponds to the number of electron-hole pairs that were created during irradiation. Measurements are made by heating the material to elevate the electrons again into the conduction band, and then using a photomultiplier to capture the emitted light from the trapped electrons as they recombine with positive holes. This procedure yields a “glow curve”, where the number of photons is recorded as a function of the temperature, which is used to calculate the deposited dose.

The TLDs that are used in LHCb are provided by the Institute of Nuclear Physics (IFJ) in Krakow (Poland). After collection, they are sent to the Institute for readout. It was chosen to use a small variety of types of TLD compositions for the measurements. The characteristics of each type should differ in a way that would make it possible to perform cross-checks with other data from measurements and simulation.

Of the 4 different types of TLDs that were provided, 2 have been used to measure the total ionizing dose: those referred to as MCP(7) (LiF: Mg, Cu, P) and MTS(7) (LiF: Mg, Ti, sintered) detectors. Both are based on lithium fluoride with ^7Li , hence the nomenclature MCP-7 and MTS-7 in the tables in this thesis. However, because of their distinct dopant composition, they differ in some aspects of their dosimetric properties, like sensitivity, non-linearity of dose response and efficiency when measuring dose by hadrons [29].

MTS crystals have been used for standard dosimetry for many decades. Above a registered dose value of about 1 Gy, their response to γ -radiation becomes supra-linear and has to be corrected accordingly in order to obtain a correct measurement. MCP dosimeters were developed later, and they exhibit a higher sensitivity to γ -radiation by a few orders of magnitude, with the drawback of having lower sensitivity for heavy charged particles. In contrast to MTS detectors, their response becomes sub-linear above a dose of 1 Gy, which similarly calls for a correction factor when converting signal to dose [29].

The other 2 types of TLDs, named MCP-N and MTS-N, feature a “natural” component of ^6Li , which makes the material sensitive to thermal neutron radiation. TLDs using ^7Li only do not interact with low-energy neutrons in a significant way. In a mixed radiation field with a thermal neutron component, sensors with ^6Li will measure higher dose than sensors with only ^7Li . As expected, an increase of the measured dose for type-N TLDs compared to type-7 could be observed in measurements from most places in the LHCb experiment. This difference in dose can be used to obtain a neutron fluence value by using Burgkhardt coefficients, which take into account calibration efforts with a thermal neutron reference field at GeNF. [30] However, the thermal neutron component of the prompt radiation field at LHCb is relatively small in comparison to the overall neutron radiation. At LHCb, neutrons reach very high energies due to the hadron radiation coming from the LHC’s proton-proton collisions, showing intensity peaks at 1 MeV and 100 MeV and recognizable quantities up to several hundred GeV. Unfortunately, the neutron cross section of ^6Li quickly decreases with higher energies; with the difference in sensitivity for thermal neutrons vs. 1 MeV neutrons already spanning several orders of magnitude [31]. The neutron cross sections for ^7Li and ^6Li are shown in figure 15. Considering that a very large component of neutron radiation within and close to the experiment consists of neutrons with energies around and greater than 1 MeV, this behavior does not allow an accurate measurement of neutron fluence at the experiment with these types of sensors. As a consequence, results from N-type sensors have been omitted in this document.

Efforts have been made by scientists at IFJ in Krakow to extend the measuring range of the TL dosimeters to a few orders of magnitude above their traditional maximum limit [32]. They demonstrated that, with appropriate corrections, the main luminosity peaks of the readout of MTS detectors can be used to measure dose up to a maximum of about 1 kGy. TLD MTS sensors that are exposed to a dose of more than 1000 Gy saturate and are considered to be outside of their sensitive range.

While the response of both types of TLD sensors is considered to be linear up to a dose of 1 Gy, all measurements exceeding this value have to be corrected for a deviation in the linearity of said response [33]. The sub-linear (MCP) and supra-linear (MTS) correction factors have been determined for each dosimeter type based on a calibration with γ -rays from a ^{60}Co source, but as it was already mentioned, the collisions at LHCb produce a complex mixed field with varying properties which strongly depend on the position within the detector. Due to the different responses of TLD materials to the types of hadron radiation that are prevalent at many sensor locations in LHCb, these calibrations would need to be adapted to correctly compensate the linearity deviation.

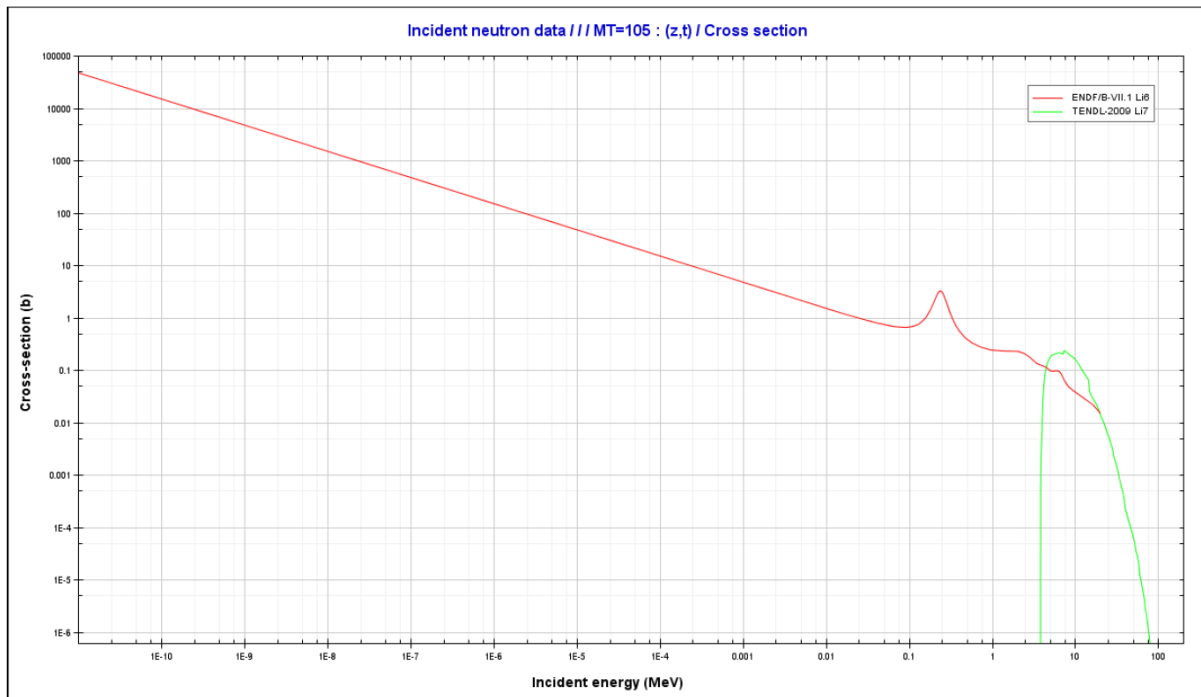


Figure 15: Cross section of neutrons of various incident energies with ${}^6\text{Li}$ (red) and ${}^7\text{Li}$ (green). The cross section of ${}^6\text{Li}$, which is used for the detection of thermal neutrons in certain types of TLDs, decreases by several orders of magnitude along with the incident neutron energy [31].

Based on a newly discovered behavior of MCP crystals, a new method of thermoluminescent measurement for this type of crystal has recently been developed at the IFJ in Krakow. It has been demonstrated that a single MCP detector can be used to measure radiation doses between 1 μGy and 1 MGy, by introducing a parameter called the “ultra-high temperature ratio” (UHTR) [32].

Additionally to these issues, some MCP sensors from 2011, specifically those at the front plane of the ECAL detector, experienced manipulation errors during the readout, which made the application of the UHTR method impossible. In the thesis, measurements of dose above 1 kGy are given only with Alanine in this case [33].

2.3 ACTIVE SENSORS

The types of passive dosimeters that are in use in LHCb had proven to be useful and reasonably accurate in various situations of applied radiation physics before their application at the experiment and were chosen for this reason. Even now being used to measure values in unprecedented and complex mixed radiation fields as they are occurring at the LHC, currently the most powerful particle accelerator in the world, they facilitate an assessment of the deposition of dose which fulfills a reasonable demand in accuracy, as will be shown during this thesis.

However, the handling of all these passive sensors involves a lot of effort concerning recuperation and readout. Dosimeter locations are sometimes difficult or even impossible to reach during normal operation of the experiment. Equipment for read out often has to be operated by hand in a very time-consuming manner, and each sensor type has specific characteristics to be aware of when converting signals into dose. Depending on the practical execution of a project where passive sensors are used for dosimetry, these circumstances might prove impractical, for example when situations might require performing consecutive measurements within a short timeframe. Passively used sensors only provide one estimation for a total integrated value over a defined period, and for practical reasons it is only possible in LHCb to conduct a passive dosimeter measurement campaign in a sufficiently long TS. It is impossible to ascertain how this value was reached when parameters are subject to change during the operation period when the irradiation takes place.

In order to mitigate those limitations it was decided in the LHCb experiment to install active dosimeters which are presently used at various locations. They were intended to provide the possibility to gain insight into the evolution of the measured dose value by connecting their readout equipment to the LHCb online control system, which offers a convenient platform to read and store the frequent measurements on any computer that can access this network. They can be readout at a relatively high frequency with only seconds in between data points, and the raw data can be processed by various means once it is saved within the network.

The sensors in use in LHCb and their readout procedure were introduced in [34]. In the experiment, active dosimeters have been placed at 28 positions, which are mostly aligned with positions of passive dosimeter boxes. To provide a better insight into what is going on inside of the experiment, 8 dosimeters are located next to passive boxes at the cross-shaped front of the M1 detector panel. Most of the other locations were chosen to cover electronic installations at the outer edges of the experiment and therefore are exposed to relatively low dose values compared to M1. While it would have been interesting to perform more measurements inside the detector itself, it was avoided because of expected and unwanted interference from the material of the dosimeters with the physics data taking campaign. Exceptions to this scheme are three special locations that are in very close proximity to the beam pipe but symmetrically upstream to where the LHCb detector develops. One of these is located a few cm from the beam pipe on the upstream wall of the experimental cavern at the position of the Beam Loss Scintillators (BLS) [35]. Two other sensors are placed in front of ECAL test modules in the LHC tunnel segment directly upstream of the experiment. The sensors next to the BLS are exposed to a very strong shower of high energy particles, originating directly from the Interaction point as well as from the interaction of those particles with the steel vacuum tank of the VELO detector, resulting in the highest dose rate that is measured at the experiment by any sensor. In the upstream tunnel, the interactions of high energy particles with the magnetic field as well as the heavy metal body of the corrector dipole are responsible for exposing the sensors in front of the ECAL test modules to at least half the dose measured at the BLS.

2.3.1 TYPES OF ACTIVE SENSORS IN LHCb

In order to adequately cover a dose range from mGy up to several kGy, each active dosimeter consists of a printed circuit board (PCB) with a chip carrier which houses 4 different types of sensors. Two of these sensors are able to measure dose from a lower limit of mGy up to several kGy, and the remaining two are able to measure 1 MeV neutron fluence equivalent with different sensitivities. In addition to these radiation monitors, each PCB features a temperature sensor on board. This NTC sensor is crucial in order to apply accurate corrections to the monitors, some of which are very susceptible to variations in temperature. A close view of the PCB is shown in figure 16.

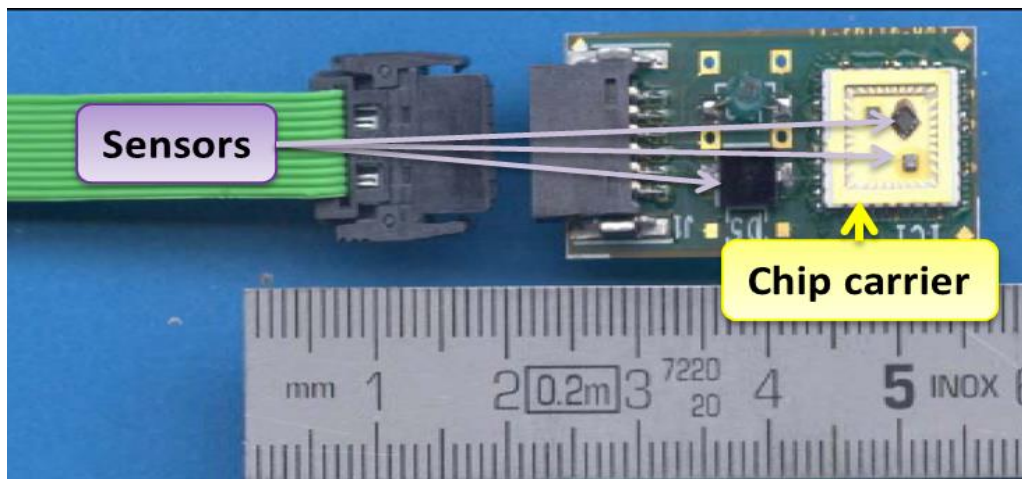


Figure 16: Close view of an active sensor PCB. 3 sensors are mounted inside the chip carrier, while 1 PiN sensor and the temperature sensor are mounted on the PCB itself. The connection to the readout equipment is designed to be detachable for easy maintenance and replacement.

2.3.1.1 RADIATION-SENSING FIELD EFFECT TRANSISTORS

Two types of radiation sensing Field Effect Transistors (RadFETs) are used in LHCb, both measuring TID for different dose ranges. The sensitive part of the device is their silicon oxide (SiO_2) layer, where incoming particles induce a build-up of charges. Specifically, electron-hole pairs are created through ionizing radiation throughout the whole layer. Subsequently, electrons that do not immediately recombine may be removed from the oxide layer via the anode gate depending on the prevalent electric field. The created holes on the other hand move comparably slowly towards the cathode, over a timespan that can extend to several years, depending on the circumstances. In a narrow region close to the interface between the silicon base and the silicon oxide, the holes may be trapped by pre-existing traps which were generated during the processing of the device. As a consequence, a positive charge develops in the gate oxide near the silicon, influencing the electric field in the device, which can be measured by a shift in its operating parameters. The measurement procedure involves measuring the shift of the voltage V_{GS} between gate and source for a constant readout current I_D . Since the charge at the Si/SiO₂ border develops over time, this provides an integrated signal which can be linked to the accumulated dose [34].

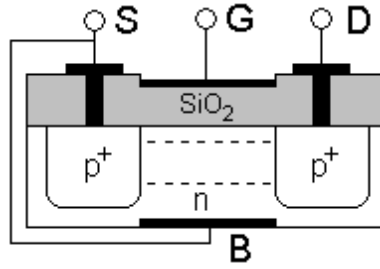


Figure 17: Scheme of a RadFET dosimeter showing Source (S), Gate (G) and Drain (D) terminals as well as the silicon Bulk (B) and the silicon oxide layer (SiO₂).

When operating in the so-called “zero bias” mode, the expected response of the voltage shift ΔV_{GS} in correspondence to the dose D is represented by the following equation:

$$\Delta V_{GS} = a \times D^b \quad (7)$$

In this equation, a and b are experimental parameters, which depend strongly on the dose range that the device is to be exposed to. It is not possible to find values for a and b which cover a dose range over several orders of magnitude [34].

The thickness of the SiO₂ layer has an influence on the radiation sensitivity of these devices. In thicker layers the electric field across the layer is reduced and may more often be too weak to keep electron-hole pairs separated. As a result, a higher recombination rate in thick layers leads to a reduced sensitivity of the device. In practice, thick silicon oxide layer RadFETs are used in applications with higher expected dose, while thin layer devices are more apt for low-dose environments.

One of the most limiting factors of the accuracy of measurements is the phenomenon of annealing of the trapped charge by recombination with electrons that are tunneling from the nearby silicon layer. This annealing is continuously in effect and its rate depends on the amount of collected charge as well as the temperature present. It leads to a reduction of ΔV_{GS} over time, reducing the measured signal and limiting the capability to measure at very low dose rates. In addition to this annealing, the devices are also temperature dependent and susceptible to low signal-to-noise ratios [34].

In LHCB, two different RadFETs are used to cover different dose ranges. The LAAS (Laboratory of Analysis and Architecture of Systems [36]) thin silicon oxide layer RadFET is used for low dose measurements ranging from mGy to 10 Gy. Two calibration curves based on different values of a and b are provided by the author of [34]: one for irradiation by high energy hadrons (HEH) and one for pure photon exposure (PPh). The REM (Radiation Experiment and Monitors [37]) thick silicon oxide layer RadFET provided with two separate calibration curves to cover the ranges from 1 Gy to 40 Gy and from 40 Gy to 10 kGy. More information on these devices can be found at [34]. The correlated parameters are listed in table 1.

Table 1: Parameters a and b used for the conversion of voltages measured with LAAS and REM RadFETs into dose values. REM measurements are sorted into calibration curves corresponding to their measured dose value, whereas LAAS measurements are calibrated by the dominant incident radiation type. PPh stands for pure photon, HEH for high energy hadron.

REM	a	b	LAAS	a	b
Dose <40Gy	0.1854	0.91072	PPh	0.432	0.9404
Dose >40Gy	0.2921	0.78778	HEH	0.239	0.6586

2.3.1.2 HIGH-RESISTIVITY FORWARD-BASED PIN DIODES

A PiN diode is defined as a p-n junction with an intrinsic layer sandwiched between a semiconductor p-layer and an n-layer, which is manufactured using tailored dopant profiles. In practice, the intrinsic layer is often approximated by either a high-resistivity p or high-resistivity n layer, as shown in figure 18 [38].

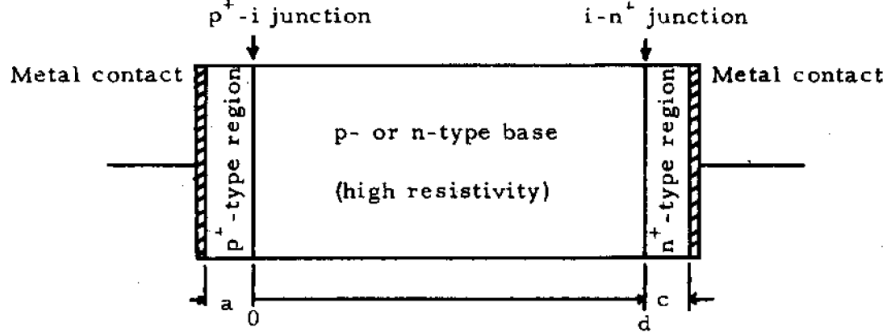


Figure 18: Scheme of a high-resistivity PiN diode. Instead of an intrinsic zone made by dopant injection, the semiconductor features a high resistivity p- or n-type high resistivity layer in between p- and n-layer.

When using a PiN diode in forward biasing, the total voltage drop V_F across the diode is the sum of the drops across the p-i junction and the i-n junction and the base. During irradiation, the silicon lattice of the diode suffers displacement damage, reducing the conductivity of the device and causing a shift in the forward voltage V_F . This effect is used to link the received damage to the encountered 1 MeV neutron fluence equivalent, as is shown in equation (8).

$$\Delta V_F = c \cdot \Phi_{eq} \quad (8)$$

In this rather simple conversion of the shift in voltage V_F to the 1 MeV neutron fluence equivalent Φ_{eq} , c stands for a calibration parameter that varies for each type of device.

On an active sensor PCB, two types of PiN diodes are used to cover different ranges of fluence: a CMRP diode measuring between 10^8 and $2 \times 10^{12} \text{ cm}^{-2}$ and a BPW diode measuring between 10^{11} and $5 \times 10^{14} \text{ cm}^{-2}$ of 1 MeV neutron fluence equivalent. The devices used in LHCb work with the following calibrations [34]:

For BPW diodes, c is defined via equation (9)

$$\frac{1}{c} = 9.1 \times 10^9 \frac{\text{cm}^2}{\text{mV}} \quad (9)$$

and for CMRP diodes, the value is given in equation (10)

$$\frac{1}{c} = 1.7 \times 10^8 \frac{\text{cm}^2}{\text{mV}} \quad (10)$$

During the measurement process, it is crucial to only use low-to-intermediate currents for very short intervals in the millisecond range, because the heating of the high resistivity device which is induced by the injected currents will otherwise anneal some of the induced effects. A too frequent read-out via online infrastructure would significantly distort the measurement signal over time [34]. The active sensors used in LHCb are therefore read out roughly every 20 minutes using an optimized current flow in order to minimize any deteriorating effects.

One main disadvantage of these devices is their high sensitivity to temperature changes. It is impossible to differentiate if the cause of an increase in impedance happened due to exposure to radiation or by a change in

temperature. The efforts to correct for temperature changes of the actively used LHCb PiN sensors profit greatly from the data recorded with the temperature sensor on board of the active sensor PCB.

On the positive side, in addition to the simple design and high availability of PiN diodes, they provide a list of advantages for measuring 1 MeV neutron fluence equivalent: the readout is simple and can be performed with commercially available programmable power sources, their small size enables high spatial resolution for various sensitivities if needed, their response is dose-independent, they might be reusable after intentional annealing and their response mechanism is actually identical to the damage in electronic devices to which the measured signal is supposed to be related to [34].

3 MONTE CARLO SIMULATION

Analytic approaches for characterizing interactions of radiation with larger structures quickly reach their limits when these structures gain in complexity. The characterization of radiation environments around high energy particle accelerators usually requires a consideration of sophisticated geometries that demand a different approach.

The Monte Carlo method uses random sampling to obtain results, circumventing many obstacles that arise when aiming for an analytical solution of a complex problem. Monte Carlo calculations are carried out by constructing a series of trajectories developing from primary particle beams, choosing each segment at random from a distribution of applicable processes, which may amount to a number of particles of varying types, energies and directions, and following the products of these interactions in turn.

Any outcome of such a simulation is a counting process focusing on certain desired events of interest. As such, it has a counting uncertainty and the variance will decrease with the square root of the number of calculations done. Of course, this means that processes occurring with high probabilities are simulated more accurately than events with rare occurrences. This effect can be mitigated using various biasing techniques.

The constant improvement and availability of computing resources make the Monte Carlo method extremely useful for evaluating radiation hazards for realistic geometries.

3.1 FLUKA: A MULTIPARTICLE TRANSPORT CODE

Designed as a general purpose tool for calculations of particle transport and interactions with matter, FLUKA [39] [40] covers a large range of applications. Since its early days as a tool for calculating hadron damage to accelerator components, it has been progressively improved by adding to its versatility, making it capable to perform a range of tasks reaching beyond calculations of radiation damage. The possibility to simulate artificial and natural radiation sources of most existing kinds allows FLUKA to be used successfully in various domains, such as accelerator shielding studies, the calculation of dose received by aircraft crews, the evaluation of organ dose due to external radiation, detector design for radiation protection as well as for high energy physics, radiotherapy, neutrino physics, maze design for medical accelerators, background studies for underground detectors, cosmic ray physics, and many more. Among all reaction steps and types, FLUKA enforces consistency between physical models with regard to conservation laws and compliancy with experimental data at single interaction level. It can simulate interaction and propagation in matter of about 60 different particles with high accuracy. This includes photons and electrons between 1 keV and thousands of TeV, muons of any energy, hadrons up to 20 TeV and even further by linking FLUKA with the DPMJET [41] code, all corresponding antiparticles, neutrinos, and very importantly neutrons down to thermal energies as well as heavy ions. Most FLUKA applications do not require programming by the user. Predefined lines of code form an input file that follows a defined pattern which is using formatted lines of text headed by predefined name-strings as so called "cards". Each number or string at a certain position of these cards specify the parameters needed to perform a simulation. In addition, a number of user interface routines are available for special requirements.

3.1.1 GEOMETRY DESCRIPTION

Geometry input is based on the Combinatorial Geometry (CG) package [42]. Several basic shapes like spheres, cylinders and planes, called bodies, can be combined into more complex shapes, called regions, by using the Boolean operations union, intersection and subtraction. In regards to the complexity of a Boolean built

geometry that is trying to convey a huge amount of detail from the actual LHCb experiment into the simulation, several tools to view and modify models for simulations as well as visualize results have been utilized:

[FLAIR](#) [43] for Linux is an advanced user friendly interface for FLUKA to facilitate the editing of FLUKA input files, running the simulation and visualization of the output files. It features an interface for easy editing and instant validation of inputs, as well as an interactive geometry editor, enabling the user to edit bodies and regions in a graphical way while instantly being shown debugging information.

[SimpleGeo](#) [44] is an interactive solid modeler available for Windows operating systems, which allows for flexible and easy creation of models. Existing geometries can be imported for viewing and modifying, or geometries can be built from scratch. Geometries can be exported into various formats besides the original FLUKA format, including other Monte Carlo applications such as MCNP(X) and PHITS as well as popular 3D formats, some of which can be used with Raytracing software. Visualization of 3-dimensional result files via display of up to 3 planes is possible using the plugin DaVis3D. This plugin allows the user to interactively move through the data set, which can be graphically superimposed on top of the displayed geometry. Also, integrated volume calculation of regions using a quasi-Monte Carlo algorithm provides an accurate tool when working with complex structures.

3.1.2 MATERIALS

For the satisfactory performance of a MC simulation, the faithful representation of materials is of equal importance as the accurate representation of geometrical objects. In FLUKA, materials can be defined based on a database of elements integrated in the code, many of which also feature different sets of cross-sections for low-energy neutron interactions. Compound materials can be defined using volume or mass proportions and can have user-defined densities. Materials are assigned to individual regions.

3.1.3 LATTICE

The FLUKA geometry input scheme features replication capabilities, which are called LATTICE. A prototype elementary cell with a detailed geometry description that is to be replicated can be defined to occupy several locations using the transformation rules of translation and rotation. In the original LHCb geometry from 2007 which this work is based on, this LATTICE routine was utilized to overcome the limit of 10000 maximum region definitions in FLUKA, which would have been exceeded by some orders of magnitude just by the very detailed description of the calorimeter module, which was replicated over the whole detector.

During the modification efforts described during the next sections, the implementation of the LATTICE routine and all related items has been undone. The affected structures were the calorimeter, which has been implemented in a simplified way, and the Inner Tracker Boxes, which have been rebuilt exactly according to the descriptions embedded in the Lattice routine. The removal of LATTICE elements was deemed beneficiary for various reasons. Mirroring structures into different places in a geometry can lead to some problems, for example when rounding errors caused by transformations create undefined spaces in the geometry. Working with an uninterrupted geometry description which does not rely on subroutines greatly facilitates future modifications of the involved structures as well as some envisioned scoring approaches. The simplified representation of the calorimeter model did not have any negative impact on the intended purpose of the simulation, as the new model includes corrections for some shortcomings of the 2007 version, as it will be explained later.

3.1.4 BEAM AND SOURCE

Proton - proton collisions and their corresponding outcome at a defined interaction point are calculated within a run of the simulation, as opposed to previous versions of the code where collision events had to be generated manually and then used as a separate SOURCE file for the simulation. For all calculations performed within the scope of this thesis, this online calculation of collisions was requested via the SPECSOUR card in the FLUKA input file. Executables for running input files using the SPECSOUR card are required to include DPMJET-III libraries and have to be compiled by hand using a script provided with every FLUKA installation. DPMJET is a code system based on the Dual Parton Model which allows the simulation of hadron-hadron, hadron-nucleus, nucleus-nucleus, photon-hadron, photon-photon and photon-nucleus interactions from 5 GeV up to the highest cosmic ray energies [45] This Monte Carlo event generator is used to calculate the collision products which are subsequently transported by FLUKA. More information can be found in [41].

3.1.5 USER ROUTINES

The FLUKA library provides template routines allowing for the use of non-standard input and output for particularly unusual or complex problems. These routines provide additional flexibility as they can be modified and extended to forward calls to private routines or external packages. All newly modified or created user routines have to be linked to the FLUKA library with an available script when producing an executable to run a simulation. The FLUKA simulation of the LHCb experiment utilizes some modified versions of standard user routines in order to be able to make use of externally supplied magnetic field maps.

3.1.6 USE OF MAGNETIC FIELD MAPS

FLUKA allows for particles to be tracked within arbitrarily complex magnetic fields. Magnetic field tracking in FLUKA is performed iteratively using sub-steps until a predefined accuracy at boundary crossings between regions is achieved, taking into account also energy losses along a given step and the corresponding decrease of the curvature radius. The step size for all simulations performed for this thesis was left at the recommended default values which is currently 10 cm within magnetic fields.

The FLUKA simulation of LHCb has to take the shape of the magnetic field of the LHCb dipole into account in order to be able to reproduce accurate results for almost all kinds of estimators. Without user routines, the user is only able to define a homogenous field in a region which does not provide sufficient accuracy. The magnetic field maps which are used for all simulations in this thesis are measured and provided by the LHCb collaboration. They consist of 4 sectors for each magnetic field direction and are called *c1_onemap_up.cdf* – *c4_onemap_up.cdf* and *c1_onemap_down.cdf* – *c4_onemap_down.cdf* and can be found in the */afs* software repository for MC physics simulation and reconstruction software of LHCb. These maps are not the most recent maps available, but after a close examination of uncertainties and fluctuations of field values close to the section borders of different map versions, these have been chosen for their consistency. While newer maps may be more accurate in other parts of a sector, the expected small differences would only play a minor role in changing the radiation field inside the detector. In order to be used by the FLUKA code, they had to be slightly reformatted by changing the format of the values.

The template user routine *magfld.f* initially supported only a single magnetic field map to be used for the simulation. As a consequence, it has been modified and extended by calling on other subroutines called *GUfld.f*, *mhcoss.f* and *usrini.f*. Now the values and coordinates of 4 preformatted sectors of a very detailed

magnetic field map are being loaded into memory via OPEN cards in the FLUKA input file. Specifically, the routine *usrini.f* is called by using a special card in the input file for this purpose. After a successful load of the maps, *magfld.f* is called every time during the simulation when a particle enters a region that is defined in the input file as being subjected to a magnetic field. The routine *GUfld.f* is subsequently called to actually calculate the field value as an interpolated value between individual map points, and *mhcos.f* is called to appropriately normalize the outcome. Additionally, a homogenous magnetic field is defined in the *magfld.f* routine for the corrector dipole in the upstream tunnel. It should always be pointing into the opposite direction of the field of the main LHCb magnet. At the moment, the direction of this homogenous field has to be changed manually by altering the sign of the field vector within the routine and compiling a new executable.

3.1.7 SCORING

Because Monte Carlo calculations are often seen as mathematical experiments, its results are called estimators. As with a real measurement, an estimator is obtained by sampling from a statistical distribution and has a statistical error. Within FLUKA Monte Carlo, these estimators are referred to as “scoring” capabilities. FLUKA offers a variety of different built-in estimators ranging from particle fluences to energy deposition and spectra, with many more options in between. Users also have the possibility to build their own scoring through user routines [39] [46].

Scoring results can be requested in either commonly accessible ASCII format, or in the form of binary files. ASCII formatted output files generally allow for more flexibility during the post-processing of results, whereas binary files can be post-processed with available FLUKA tools, which can sharply reduce the amount of time needed if a large number of files have to be processed. FLUKA inherent routines and visualization tools like FLAIR only work with binary output files.

Most of the simulation results presented in this thesis are scored by superimposing 3-dimensional Cartesian grids on the geometry. All bins of such a grid score fluence or dose in equal volumes regardless of the underlying geometrical structure. Naturally, this requires special attention during analysis in areas where heavy materials like metals and light materials like air share the same bin space, and the bin only shows an average value of the whole volume per definition.

Whenever differential fluence spectra of any particles are presented in this document, they are scored as track lengths per volume with the FLUKA USRTRACK card and shown in lethargy style. In lethargy plots, the fluence value is multiplied with its corresponding energy. As there are only energy ranges given when scoring USRTRACKs, the mean value of ranges is taken for the abscissa to form the graph. If N is the number of particles, lethargy fluence means $dN/dE \times E$ where E is the logarithmic average of a bin $\sqrt{E_{max} \times E_{min}}$. Lethargy style is generally used to gain a more detailed view at higher energy fluence structures, which are otherwise barely visible in a double logarithmic plot, because the bin sizes in a logarithmic scoring increase exponentially in size at higher energies. One has to pay attention to the fact that in this case, the area under the curve does not correspond to the integrated fluence anymore.

One specific advantage of FLUKA in regard to other available MC codes is its accuracy when simulating low energy neutron fluences. It features 260 fixed energy binning ranges for neutrons with energies below 20 MeV down to the thermal range. These special bins vary in size and therefore show discrete edges when plotted normally. Lethargy plots do not show these edges, allowing for a better view on fluence peaks within certain energy ranges of interest.

Since the start of its operation, the LHCb experiment has been exposed to an unprecedented mixed radiation field generated from the collisions of two proton beams at a collision energy of 7 TeV and 8 TeV CM. A network of dosimeters and fluence sensors covering a large measurement range was distributed around the experiment. By monitoring the prompt radiation during operation in sensitive spots, which are mostly located next to electronics reading data from and partially controlling the particle detectors of the experiment, it is possible to conclude on the behavior of said equipment under the influence of the radiation. This sensor network however has disadvantages on two important aspects:

On one hand, not every location of the experiment where sensitive equipment is placed can be covered and there are not enough sensors to effectively estimate for all intermediate positions within the experiment based on measurements alone, because of the very complex architecture of the LHCb geometry and its limitations on material placement.

On the other hand, all dosimeters are calibrated to photon radiation coming from radioactive sources, which means that in some cases, their reaction to the mixed particle field may differ in unforeseen ways from their response to γ -radiation.

Using the FLUKA Monte Carlo code in tandem with a complex and detailed geometry description of the LHCb detector, the radiation field around the experiment can be reproduced in a sufficiently accurate manner, which should allow for the estimation of dose and fluence values at locations within the experiment that are not equipped with sensors. Moreover, estimates based on the simulation facilitate the evaluation of the behavior of the various sensors at the experiment within different field compositions.

A prerequisite for this is the evaluation of the reliability of the simulation itself, which is performed by comparing results of simulations of prompt radiation obtained for different running conditions with actual measurements. Once the reliability assessment of the simulation is established, it is possible to adequately estimate various dose and fluence levels at locations where no measurements could be performed. As a consequence of an assessment of past running conditions, the simulation can also be used to project estimations for future scenarios of operation with similar conditions. Under the assumption that the experiment's geometry and materials do not change in a profound way, even scenarios considering an upgrade of the current experiment can be predicted to a certain extent.

4.1 SIMULATION GEOMETRY

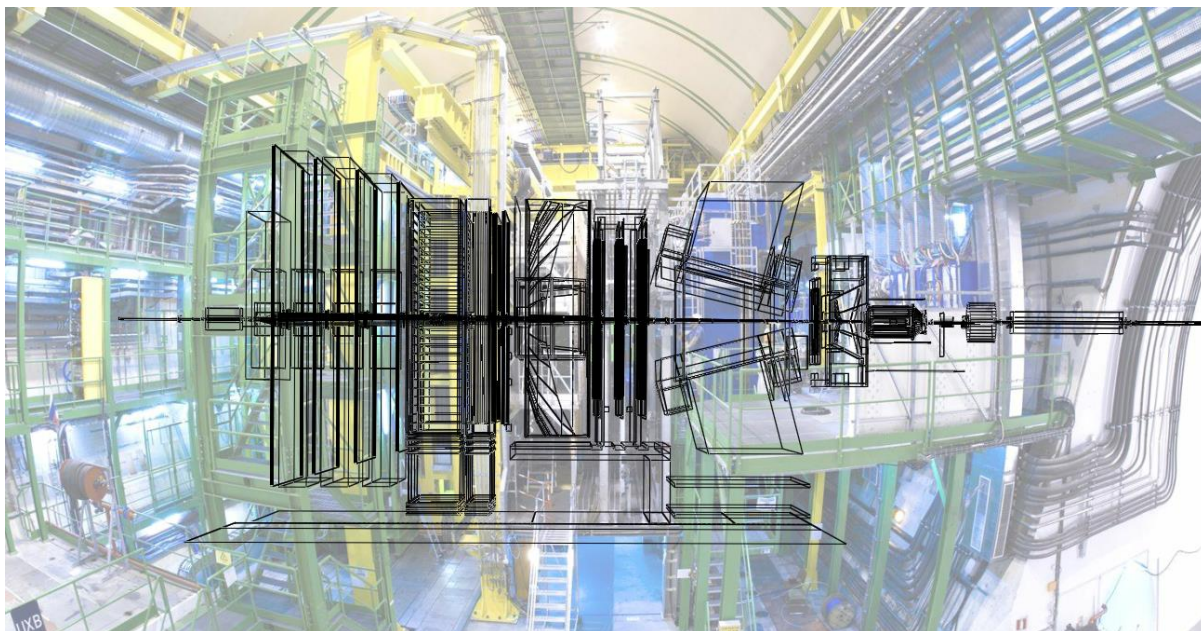


Figure 19: Sketch View of the FLUKA LHCb detector geometry layered over an actual photo of the experimental cavern using SimpleGeo. Wall structures and other elements have been rendered transparent in the geometry for clarity.

The first FLUKA simulations based on an already very detailed geometry of the experiment were performed in 2003 [47] and the geometry description was further improved until around 2007 when it was used for determining the radioactive waste zoning inside the cavern [48]. This latter model of the geometry was adopted by the author in 2010 and modified during the following years. More precisely, the adopted version was a work in progress that was slightly altered by the original author after the last official calculations were done in 2007. The attempted adjustment of the input and the user routines to the newer versions of FLUKA and compilers was not completed at that point. After an extended period of bug fixing and adapting parts of the input to conform to the latest version of FLUKA, the goal of modifying the geometry was to obtain a sufficiently realistic built without geometrical errors. A geometry free of errors is required to prevent crashes during simulation. But even overlapping region definitions, which might not induce a crash of the simulation cycle or even an error message while running, are able to distort results as FLUKA will choose the material for such regions randomly and should therefore be avoided. The geometry used for this thesis is shown in figure 19 and figure 20. The most relevant modifications to the original geometry will be described in the following sections.

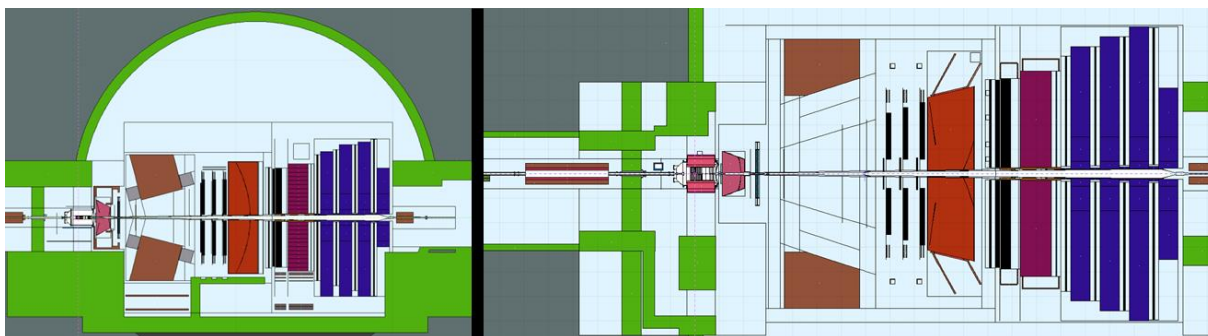


Figure 20: Cut views of the LHCb geometry displayed in FLAIR of the ZY plane (side view) on the left side and the ZX plane (top down view) on the right side. Green material indicates concrete structures. The scale is different between views in order to include the cavern ceiling in the side view.

4.1.1.1 UPSTREAM OF THE INTERACTION POINT

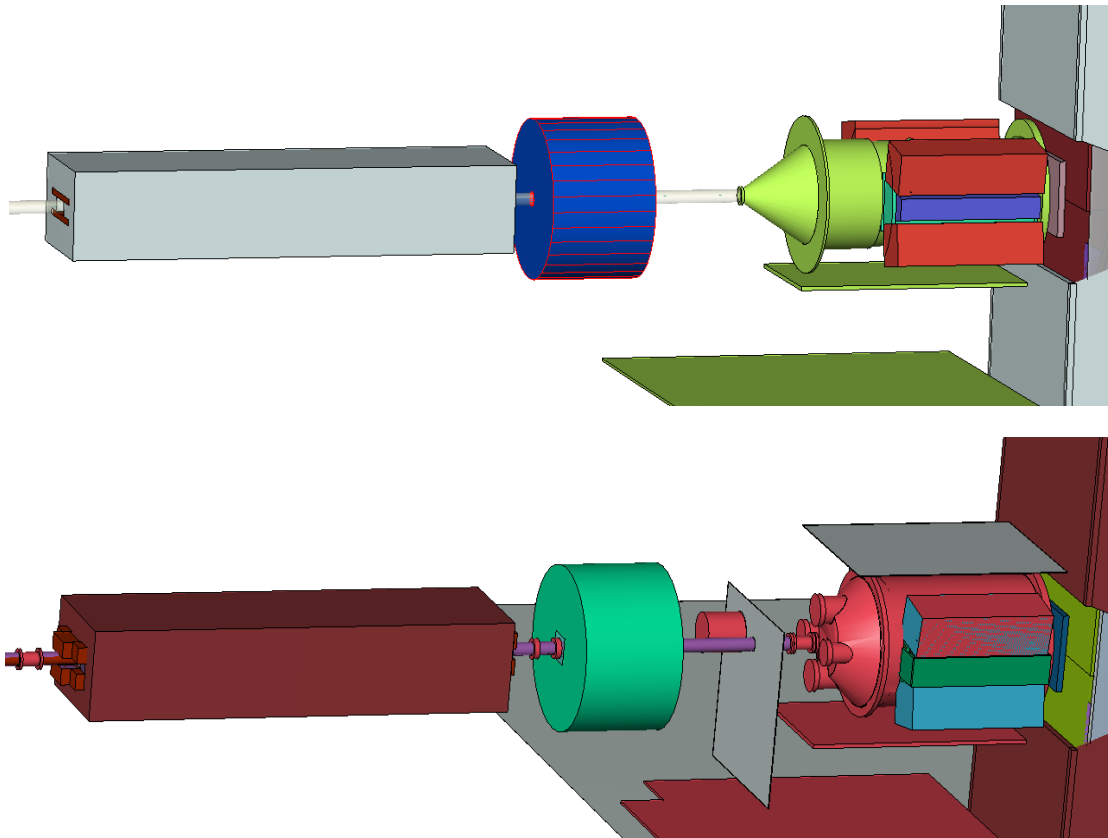


Figure 21: Comparison of 3D views of the FLUKA geometry of the VELO upstream region. Concrete walls are made transparent in these views except for a cylindrical part of the upstream wall around the beam pipe. The original geometry (top picture) has been modified and extended by adapting the shape of the VELO vacuum vessel, the distances between objects which now agree with construction drawings and by adding details such as flanges, warm modules, cover plates, a realistic opening around the beam pipe in the wall between experimental cavern and upstream tunnel and the beam pipe itself. Material colors are different in the two views due to randomized assignment, but they are largely unchanged in the geometrical descriptions.

Since the area around and upstream of the interaction point were not considered as important as the LHCb detector itself, the description was originally not given as much attention as the rest of the experiment. However since this region has been filled with additional equipment over the years, it was necessary to enhance the level of detail in its description. In addition, one set of active and passive sensors that are discussed in this thesis are located very close to the beam pipe on the upstream wall. Before modifications were finished, the estimated dose calculated by the simulation gave a value which was approximately lower by a factor of up to 10 than what all other measurements at this point suggested. This discrepancy almost vanished completely after the changes in the simulation description. A comparison between the original and the current version of the geometry showing many of the modifications is shown in figure 21.

The original description of the air volume and the simplified boxes for electronics on the VELO vacuum vessel made it very difficult to modify anything in this area. The space was partitioned into small areas using arbitrarily placed leaning planes. Region definitions were overlapping in many places in a complicated way that required many time-consuming modifications to various definitions if a newly placed object crossed region borders. Consequently, the description was changed by using simpler expressions in order to facilitate future modifications.

The beam pipe now starts already inside the VELO vacuum vessel at a newly implemented aluminum spoke cap and the attached support bars as it is shown in figure 22. In the old geometry, the vessel was empty apart

from a very detailed description of VELO detector blades. This spoke cap should connect downstream to a wakefield suppressor, which was left out of the simulation, because the influence of its 0.075 mm thin CuBe foil body on the radiation field was deemed negligible. A short piece of copper beam pipe with an inner radius of 27 mm and a thickness of 0.1 mm connects the spoke cap to the outside cover of the vessel. This beam pipe is punctured in reality, which was not taken into account for the simulation.

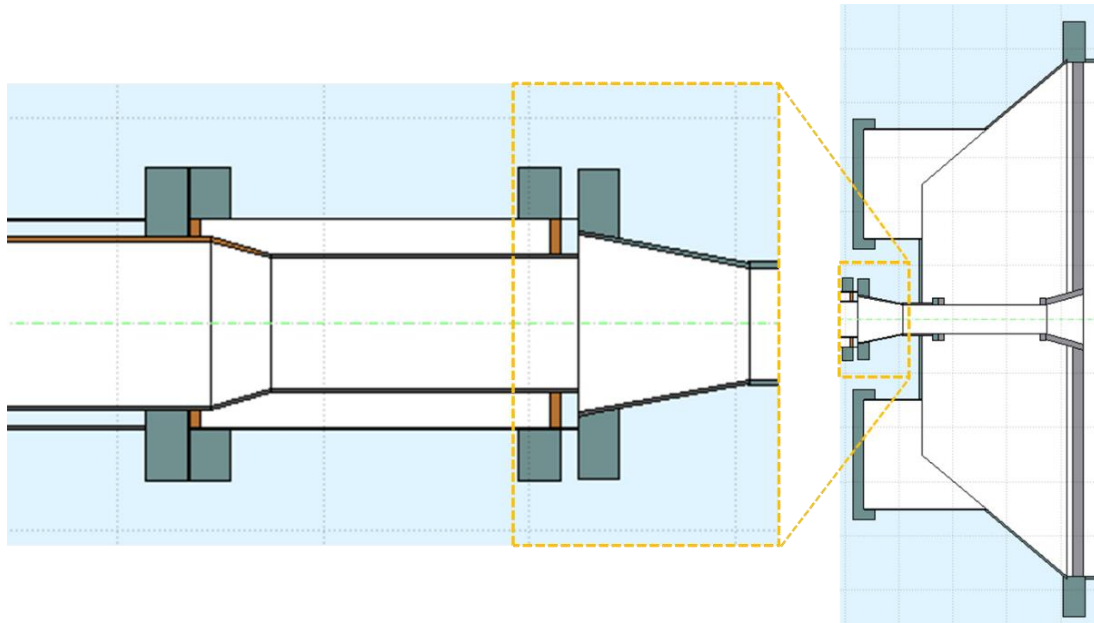


Figure 22: Close cut view from the side of the upstream part of the VELO vacuum vessel. On the left, a zoomed version of a warm module is shown, which connects the beam pipe with the vessel, shown on the right. Inside the vessel, the thin copper beam pipe and the aluminum spoke cap connecting to the top and bottom of the vessel can be seen.

A simple representation of a beam pipe warm module [49] [50] which is shown on the left in figure 22 was implemented upstream of the center flange of the vacuum vessel and before the long uncovered part of the upstream beam pipe, which can be seen in figure 23.

The beam pipe upstream was improved by implementing a 2 mm thick copper pipe with an inner radius of 40 mm according to [51]. The aluminum foil cover of the beam pipe was left in the simulation as is, but the insulating foam in between beam pipe and cover was not modeled, leaving only air in that region. Additionally, the green valve next to the beam pipe on the Accessible side has been rendered as a hollow steel cylinder, to account for secondary radiation created within its relatively large steel surface.

The metallic cover plates around the beam pipe that support it from the upstream wall are now a part of the simulation as well, together with 2 cylindrical steel shells functioning as covers for Beam Loss Monitors. These pieces are of interest, because they represent the biggest chunks of mass this close to the beam pipe and they are very close to some of the active and passive sensors that are distributed around the experiment. The sensors can be seen in as small white boxes just on top of the beam pipe on the front of the metallic cover plate on the photo in figure 23.

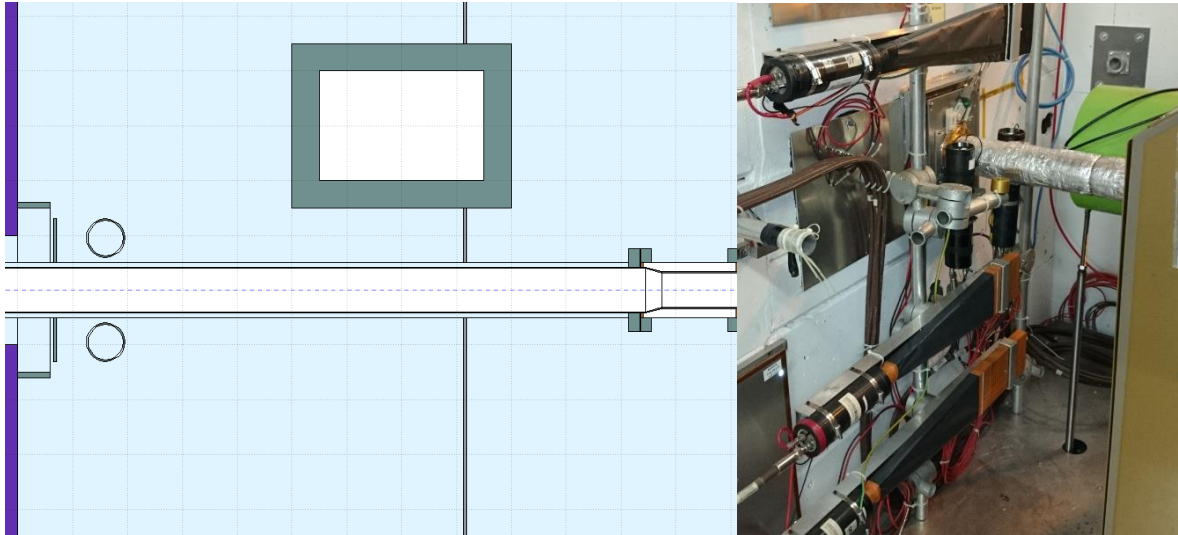


Figure 23: Schematic close cut view from above of the beam pipe section upstream of the VELO in the FLUKA geometry on the left side vs. a photo of the real counterpart in the picture on the right. On the right edge of the FLUKA schematic, the bigger part of the warm module, which in the photo is covered by the hood of the VELO described earlier, can be seen. On the left side, the purple concrete upstream wall with the rectangular opening and the metallic cover plates is shown, as well as the cylindrical bodies of two Beam Loss Monitors. On the A-side of the beam pipe, the very massive but hollow cylindrical steel shell of the “green valve” was implemented.

The wall separating the LHCb cavern from the upstream LHC tunnel now connects both areas via a rectangular hole around the beam pipe with an edge length of 100 mm, as opposed to having no significant opening in the original geometry. The hole, which was not present in the 2003 simulations, is hidden behind the base plate of the beam pipe wall attachment on the LHCb side and can only be seen from the tunnel side. However, because of a dipole corrector magnet positioned within half a meter of the upstream tunnel wall along the beam pipe, the secondary radiation coming from the tunnel along the beam pipe does have an effect on the active and passive sensors that are placed on the beam pipe wall attachment plate in the LHCb cavern.

In the RB84 tunnel segment on the other side of this upstream wall, the position of the corrector dipole represented in brown in figure 24 was moved 30 cm upstream according to [49] and the copper coils extending from the main body were added. Two more warm modules, one on each side of the corrector dipole, have been implemented as well.

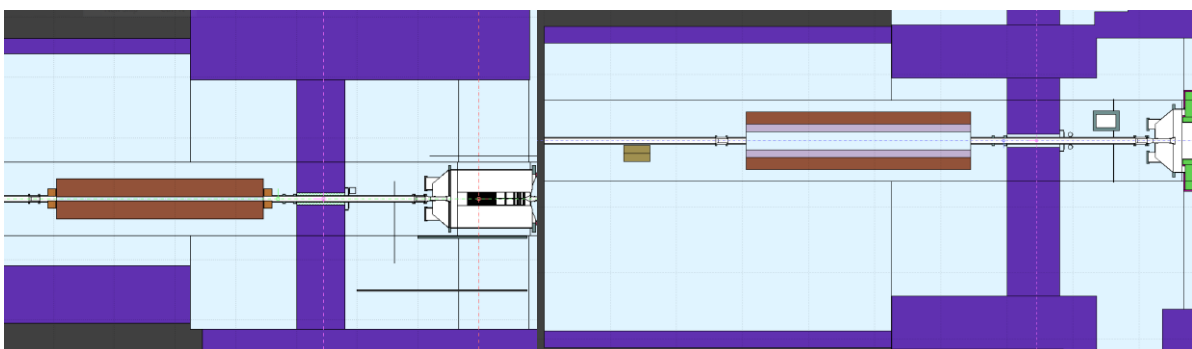


Figure 24: Side (on the left) and Top (on the right) view of the last part of the RB84 LHC tunnel segment, the region upstream of the VELO in the LHCb experimental cavern and the wall dividing those two underground areas. In the top view the representation of the two ECAL test modules (in olive green) can be seen close to the beam pipe.

Further upstream in the tunnel segment RB84, after the corrector dipole and the warm module, two rectangular shapes representing two ECAL modules in that location were put into place along the beam pipe. The reasoning for this placement will be discussed in later sections.

4.1.1.2 VELO

The geometry of the VELO steel vacuum vessel, shown in figure 25, was enlarged to match the dimensions of its real counterpart, which features a cylindrical shell with an inner radius of 475 mm and a thickness of 6 mm [52]. The spherical upstream cover of the vessel, which was described by a standard cone in the 2007 geometry, was approximated with a truncated right angle cone with an inner base radius of 475 mm, an apex radius of 25 mm and a height of 268 mm. Thick steel flanges on the upstream cover were added, as particle interactions with those influence the radiation field in the cavern upstream of the interaction point. Part of the beam pipe inside the vessel and an aluminum spoke cap have been added as described earlier.

In reality, the VELO vacuum tank and part of the attached electronics are covered on all sides by aluminum plates forming the VELO hood. Of these, only the upstream front and the top part of the aluminum VELO hood were added to the geometry, since they have the most influence in terms of particle interactions on the surrounding area.

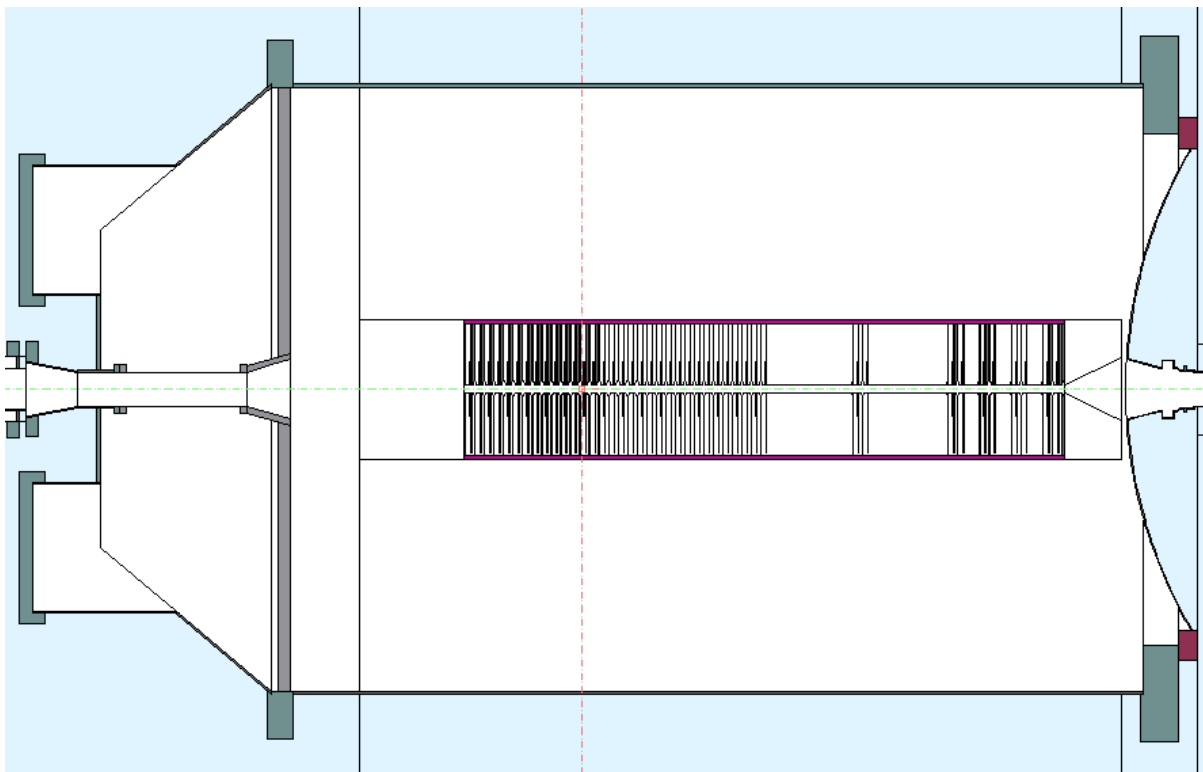


Figure 25: Side cut view of the VELO vacuum vessel and the detector inside. While the vessel was heavily modified since the original description from 2007, the very detailed model of the VELO detector itself, including all its detector blades, carbon supports and the RF foil was left untouched, apart from bug fixes in the region description.

The original geometry already featured a very detailed model of the VELO detector itself, replicating the silicon sensors, the carbon support blades, some volumes representing detector electronics and the very thin RF foil. Apart from necessary bug fixes, this part of the geometry was left untouched.

4.1.1.3 INNER AND OUTER TRACKER

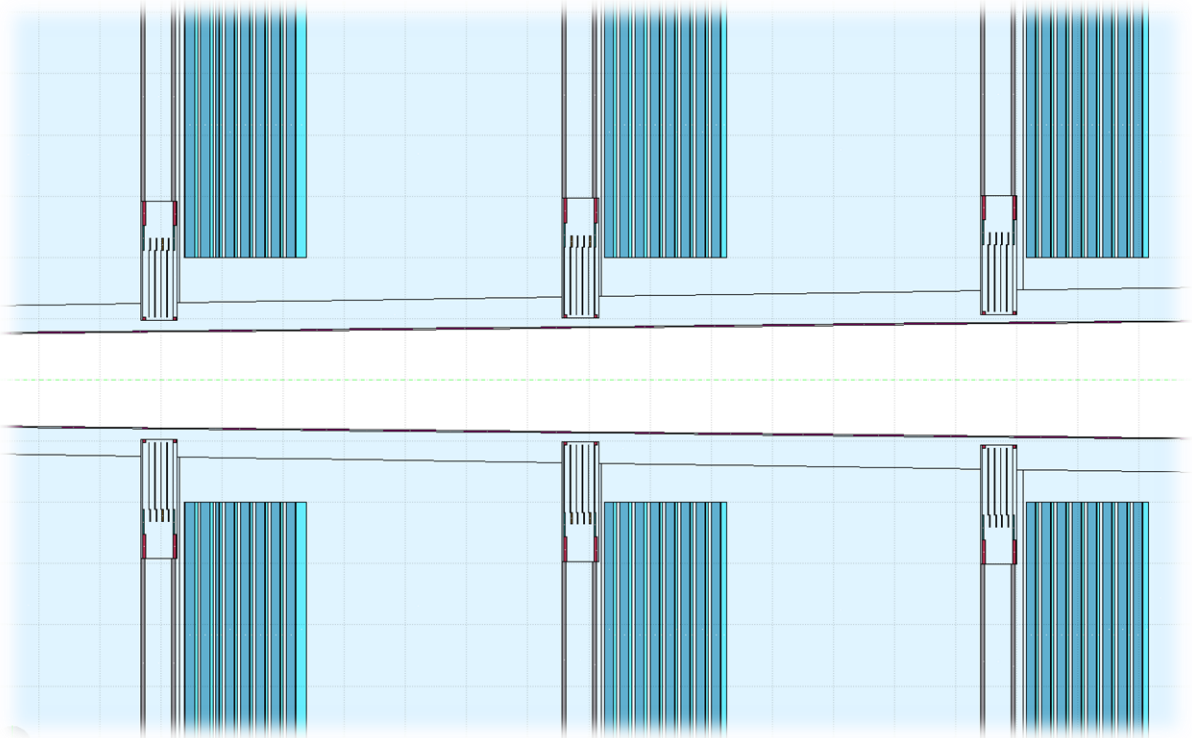


Figure 26: Close side cut view of Tracking stations 1-3. Detailed representations of the Outer Tracker panels (in blue) as well as of the Inner Tracker boxes (smaller boxes close to the conic beam pipe along the vertical center) have been modelled in the original geometry using LATTICE replicas. They have been re-implemented as standard parts of the geometry.

The representation of the tracking stations in front of RICH2 in the FLUKA geometry was already implemented in 2007 in a very realistic manner. In particular, the detector boxes of the Inner Tracker detector was built in a very detailed way, but the FLUKA replication function LATTICE was used to project one model-box to the different locations of the other detectors. While removing the LATTICE routines from the geometry to facilitate scoring and future modifications, all detector boxes were rebuilt as normal parts of the geometry in the image of the original box.

4.1.1.4 CALORIMETERS

The geometry from 2007 featured an extremely detailed model of a Hadron calorimeter module, replicating all the shifted layers of scintillator and iron as well as the holes foreseen for guiding the optical fibers out of the module. However these modules had to be replicated over the whole HCAL structure via LATTICE, since their original region count was already approaching the limits of FLUKA capability and would have clearly been impossible to implement as standard geometry. In addition to the problematic implications of LATTICE, the detailed model was missing some massive features of its real counterpart, leading to a reduced overall mass of the detector in the simulation. The high amount of detail also put a heavy strain on the available computing resources, which was seen as unnecessary, since there was no need to calculate any estimators for any small single layers of any module. As a consequence, an attempt was made to simplify the heavily detailed and therefore resource consuming prevalent model, while also adding mass to adjust for omissions of material, e.g. support structures made of iron. The HCAL geometry was restructured from scratch. It is now composed of 2x26 main modules made of a material mixture of iron and scintillator materials. A view of the original module

description vs. the simplified HCAL structure is shown in figure 27. The omission of any air pockets within this design led to a main body that is heavier than the real calorimeters by some small extent. Unfortunately it was not possible to obtain the exact weight of all different components, including unrecorded components like several tons of welding material, nor the total weight of the structure. Therefore, this rough approach to represent HCAL in the geometry was taken. Since the structure is supposed to absorb almost all of the hadronic showers developing up to that point, and the radiation field after the calorimeter detectors is mainly influenced by muons and stray radiation coming from the edge of the beam pipe, the extra mass of the HCAL is not perceived to introduce any significant bias in the results.

As another important change compared to 2007, the main body of the HCAL has been moved 90.9 cm towards the interaction point to comply with the position of its real counterpart installed in the underground cavern. In the freed space behind the main body of the calorimeter two new layers were implemented as simplified representations of the back holder support structure which is made of steel, and the adjoining layer of photomultipliers including their attached electronics' Printed Circuit Boards (PCBs).

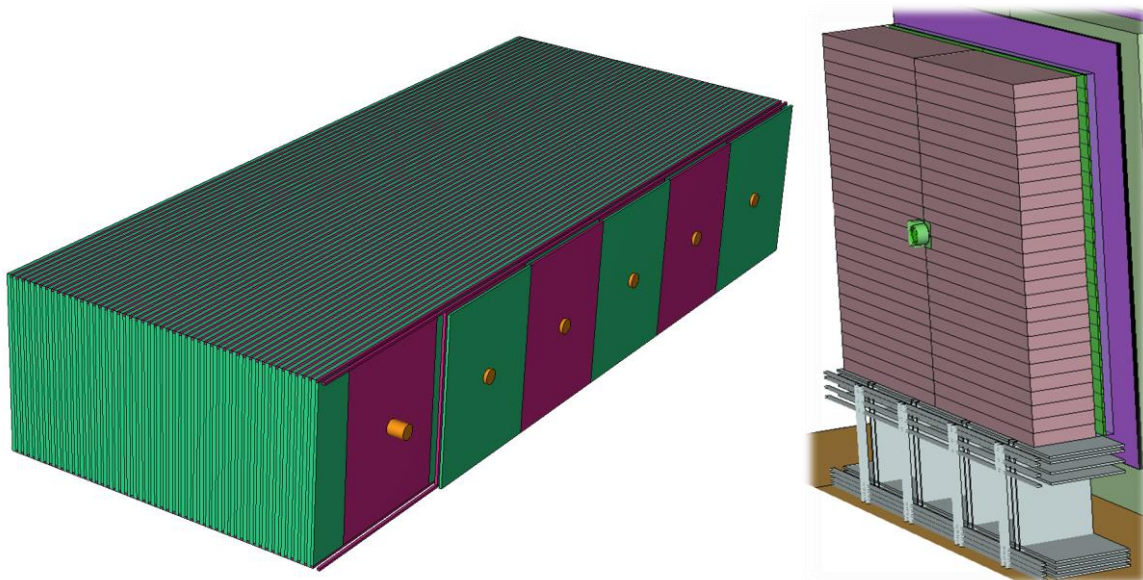


Figure 27: 3D visualizations of the 2007 version of an HCAL module (left) vs. a view of the modified HCAL with simplified modules (right). Parts of the outside of the 2007 module have been made transparent in order to provide a view on its detailed inner structure. As the large amount of detail was not beneficial for the simulation, a simplified approach with mixed materials inside a rectangular volume to substitute the original description of the modules has been implemented.

These modifications bring the additional advantage of enhancing the computing performance of the FLUKA simulation setup by simplifying and optimizing the previously overly complex description and eliminating redundant declarations.

In contrast to the HCAL, the ECAL was already modeled as a layered structure that is detailed but not composed of individual models. Since it already represented a very good compromise between detail and performance, no modifications the ECAL description were required.

4.1.1.5 CAVERN

While the cavern structure in the simulation is still not considered 100% accurate, the focus of modifications was to improve on the most obvious discrepancies that influence larger parts of the radiation environment. In this respect, the concrete wall downstream of the interaction point behind the last muon detector now starts 50 cm earlier in the z direction, as does its real counterpart. The upper edge of the floor of the RB86 tunnel connecting to the cavern in this place is now placed right below the smaller iron shielding that is behind the most downstream muon station M5, as is shown in figure 28. Before the modification, stray radiation from the LHC machine equipment around the beam pipe, represented by the short dipole with brown color in the figure, would reenter the cavern below the last iron shielding behind M5, pictured in red. In contrast to its larger upstream counterpart, this dipole does not need a magnetic field description in the FLUKA geometry since no more regions of interest are located downstream along the beam.

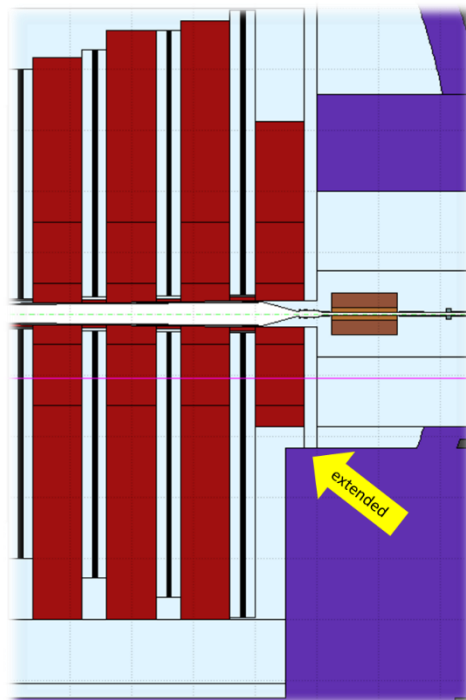


Figure 28: Side cut view of the area behind the muon detectors. The concrete (purple) lower corner of the cavern wall was extended to reach below the last iron shielding (red) of the muon detector system, which also divides the LHCb cavern from the RB86 tunnel segment. In brown, a simple representation of an LHC machine part inside RB86 can be seen to the right of the shielding.

In general, the cavern structure in this geometry is heavily simplified especially in regions at more than a few m distance from the detectors. Neither the PX84 transport shaft, nor the shielding wall including the labyrinth leading to the A-side, nor any details on the cryogenic installations on the other side of the experiment are included in the description. A new version of the geometry where the detailed detector description presented here is merged with a detailed description of the underground environment surrounding the experiment, which includes all of these and many more underground structures, has been produced by the author and is in the debugging stage at the moment. Considering the scope of this thesis, almost none of the added description of the extended cavern structure would influence simulation results around the detector in any significant way mostly because of the large distances of the objects added. Only backscattering from cryogenic installations on the C-side of the detector are suspected to possibly being able to slightly influence measurements on that side.

4.1.2 MATERIALS

In accordance with the high complexity of the FLUKA geometry of the LHCb experiment, the material definitions and assignments also feature a large amount of detail. In total, 72 materials and 55 compounds are currently defined in the input file, including definitions for specific compositions like the iron shielding between muon detectors or the lead of the beam plug at the center of the calorimeter. Most of these definitions were taken over from the 2007 geometry, as some of these are even based on spectroscopic analysis of materials.

Definitions introduced after 2010 include the material mixture for the simplified HCAL modules, a mixture representing photomultiplier tubes at the backside of the HCAL and a generic definition for electronics PCBs.

Since the material composition of PCBs is almost never known in detail because of the large variety of possible onboard components, connection types and solders, one has to refer to reference samples. Considering eventual attempts to simulate activation of critical parts of the experiment, it is necessary to ensure that components posing a higher risk due to activation are not underrepresented in the final compound. Such components include for example silver, which is often mixed within tin compounds used for soldering. The material composition for all PCB boards in the simulations in this thesis was taken from a generic example in [53], where the chemical composition of electronic circuit boards was obtained from the analysis of scrap in recycling facilities.

4.1.3 BEAM SOURCE PARAMETERS AND THRESHOLDS

In the following paragraphs, important parameters for beams, interaction parameters and particle production thresholds will be listed.

FLUKA enables the user to define a collision between two primary particles, using the Cartesian coordinates of the lab momenta of the colliding beams. In 2011 at 7 TeV CM collision energy, the proton beams were manipulated by the LHC in a way that they only crossed within the x plane of the LHCb coordinate system at the IP, while always maintaining the same height along their trajectories in the y plane. Depending on the direction of the magnetic field of the LHCb dipole, the two crossing proton beams did have a different angle with respect to the beam axis, which equals z in the coordinate system. The collision angles for 7 TeV CM are listed in μrad in table 2 for each direction of the magnetic field. In order to avoid additional tertiary collimator readjustments in the LHC when flipping magnet polarities of the LHCb dipole, a tilt of the collision planes versus the LHCb coordinate system was introduced. This tilt has to be considered as well when calculating the beam momentum vectors for the FLUKA input. For 7 TeV, the listed tilt numbers are only applied in the horizontal plane.

Table 2: Collision angles in μrad in the x plane vs. the beam axis for both magnetic field directions at 7 TeV CM collision energy.

Magnetic field DOWN	x angle [μrad]
Beam1	-590
Beam2	450
Tilt	-170

Magnetic field UP	x angle [μrad]
Beam1	-70
Beam2	-90
Tilt	-60

The rather large difference between the two magnetic field directions do have a small effect on the distribution of the various estimators in the Cartesian scoring results of the FLUKA simulation. It can be observed as a slight asymmetry in the xy plane which is most pronounced around the central region around the beam pipe. Considering that the regions of interests for the results of these studies are locations that are rather removed from the central beam line, this asymmetry becomes small against statistical uncertainties within those regions.

When the collision energy for operation was changed to 8 TeV CM in 2012, the crossing angles at the LHCb collision point were redefined as well. This time, symmetrical crossing angles were chosen for the two possible directions of the magnetic field of the LHCb dipole. In addition, a vertical incline was added to the horizontal crossing angles. The collision angles for 8 TeV CM in x and y are listed in μrad in table 3 for each direction of the magnetic field.

Table 3: Collision angles in μrad in the x and y plane vs. the beam axis for both magnetic field directions at 8 TeV CM collision energy.

Magnetic field DOWN	x angle [μrad]	y angle [μrad]
Beam1	-236	100
Beam2	236	100
Tilt	0	0

Magnetic field UP	x angle [μrad]	y angle [μrad]
Beam1	236	100
Beam2	-236	100
Tilt	0	0

The interaction point itself is defined in the BEAMPOS input card. In reference to point (0,0,0) of the actual LHCb reference system, which is identical to the origin in the geometry of the simulation, the collision point defined in the simulation is at $x = 0.04$ cm, $y = 0.001$ cm, $z = 1.0$ cm. These coordinates are used to describe both scenarios of collisions with 7 and 8 TeV CM. In reality, those coordinates differed slightly in between scenarios, but for the studies discussed in this thesis, these very small changes of the IP position are irrelevant.

Sigma values for the Gaussian sampling of the interaction around the IP have to be defined as well. The inputs were chosen as $\sigma_x = 0.005$ cm, $\sigma_y = 0.004$ cm, $\sigma_z = 4.1$ cm and $\sigma_{\text{limit}} = 10$ cm as the sampling limit in all 3 directions $x,y,z > 0$. In regard to simulating the radiation field for the whole experiment, any influences from discrepancies between these values and the real beam properties should not be significant.

The FLUKA function EMF (ElectroMagneticFLUKA) was activated by using the PRECISIO option in the DEFAULTS card in order to enable the transport of electrons, positrons and photons during simulation.

The card EMFCUT was utilized to set the energy production threshold for electron- and positron energies to 1 MeV and for photon energies to 100 keV.

The PHYSICS cards labelled COALESCE and EVAPORAT (“*new evap with heavy frag*”) activate special physics models needed for the generation and evaporation of heavy fragments, which is necessary for scoring reasonable results with simulations that handle the activation of materials. The imposed drawback on computing times was negligible, so they have been left activated during the studies concerning prompt radiation.

4.1.4 SCORING APPROACH

For a general view on the radiation environment within and around the LHCb experiment, a grid of Cartesian bins sized $20 \times 20 \times 20 \text{ cm}^3$ is placed within an encompassing box of $14 \times 12 \times 31 \text{ m}^3$. The bin size was chosen as a compromise between a need of detail on one hand and saving computing resources while still getting results with reasonable statistical errors in regions of interest on the other hand. The overall size of the binning is intended to include the whole detector as well as the upstream tunnel section of RB84, and also most of the accessible areas in direct vicinity to the detector, such as the Bunker below the Tracking Stations or the platform above the calorimeters. Almost all active and passive sensor positions are covered by this scoring volume. Only two exceptions, the sensors on the balcony and in the barracks on the accessible side behind the shielding wall, could not be included using the same bin size because the maximum number of bins per scoring is limited. The benefit of including these few sensors was limited as well, since the dose values are expected to be low and the error expected to be high due to the missing geometry at this distance.

The regions of interest are mainly areas with electronic installations, which are often sensitive to radiation, although they have been designed with the originally expected radiation levels in mind. Because of this, a large amount of the sensors described in this thesis are placed in the vicinity of these installations. Most electronics are located on the outskirts of the detectors, where the radiation field does not change very much within several tens of centimeters. Therefore the chosen grid size offers a sufficient resolution for the majority of the experiment.

A different situation presents itself in areas that are close to the beam pipe. This region is not equipped with any sensors inside the detector’s acceptance upstream of the calorimeters in order to not interfere with physics data taking. Even inside the calorimeters, all of the sensors are positioned at least a few cm away from the beam pipe. As a consequence, any predictions for this area rely on simulation. Due to the nature of the high energy collisions at the interaction point, most of the energy is released in a forward directed manner along the axis of the primary beam direction. Radiation levels are highly elevated within a few cm of the outer edge of the pipe, and the 20 cm binning does not provide a meaningful base for estimation. Especially when scoring dose, bins that include sections of the beam pipe or other vacuum filled areas might show a huge difference between their bin average and the actual maximum dose within a certain volume. There are two main reasons for this phenomenon: on one hand, energy deposition in a vacuum is zero which influences the average, and on the other hand, the gradient in a few centimeters next to the beam pipe is extremely large which is significantly distorting the average value of a bin which extend to 20 cm from the beam. In order to get better estimates for the comparison of measurements and simulation values in this thesis, smaller scoring grids with $5 \times 5 \times 5 \text{ cm}^3$ sized bins are used around the center of the calorimeters and inside the VELO alcove. Smaller bin sizes have the advantage of averaging over smaller volumes and therefore providing more accurate values, but the increase in accuracy requires computing power that quite soon becomes unreasonable.

4.2 COMPARISON OF A FIRST STABLE BUILD WITH RESULTS FROM 2003

As mentioned earlier, the first FLUKA simulations for estimations of prompt radiation around the LHCb experiment during collisions with an energy of 14 TeV CM have been conducted in 2003. For these studies, only 2-dimensional planes could be scored for estimators such as dose or 1 MeV neutron fluence equivalent because FLUKA did not have the 3D scoring capabilities it has today. These results have been documented in [47] and are still electronically available.

Before the first instance of the stabilized and improved geometry was used to produce new results, a short validation check of the new simulation setup from 2011 was required. A few rough comparisons between dose and fluence results at 14 TeV CM from the 2011 geometry versus the 2003 results have been made in order to determine any discrepancies. Many of the changes to the geometry described earlier, like the improvement of the upstream region including the VELO vacuum vessel, had not yet been implemented into this first build used for validation. The goal of these early comparison studies was to find eventual strong deviations from the 2003 results that could be linked to deficits of the new geometry or malfunctions with the adapted user routines.

Due to different Cartesian binning sizes and placements used for scoring, it was difficult to make exact statements about smaller areas or regions right next to the beam pipe, where scoring results from 2003 are sometimes missing. However in general the new simulation results showed a good agreement with the existing estimations, staying within a factor of 3 along $x=0$ at comparable locations, and within a factor of 2 along $y=0$. Taking into account the different bin sizes between scorings, the discrepancies found were considered in line with the improvements in the geometry as well as the enhanced physics models in the FLUKA code, which improved as well during the long time span between the two studies.

The biggest differences seem to be based on a much more refined treatment of electron transport within the current versions of FLUKA. This is especially noticeable in the air volume inside the LHCb dipole magnet, where electrons can be seen curling around the magnetic field lines, whereas in results from 2003 this behavior is completely missing as shown in figure 29.

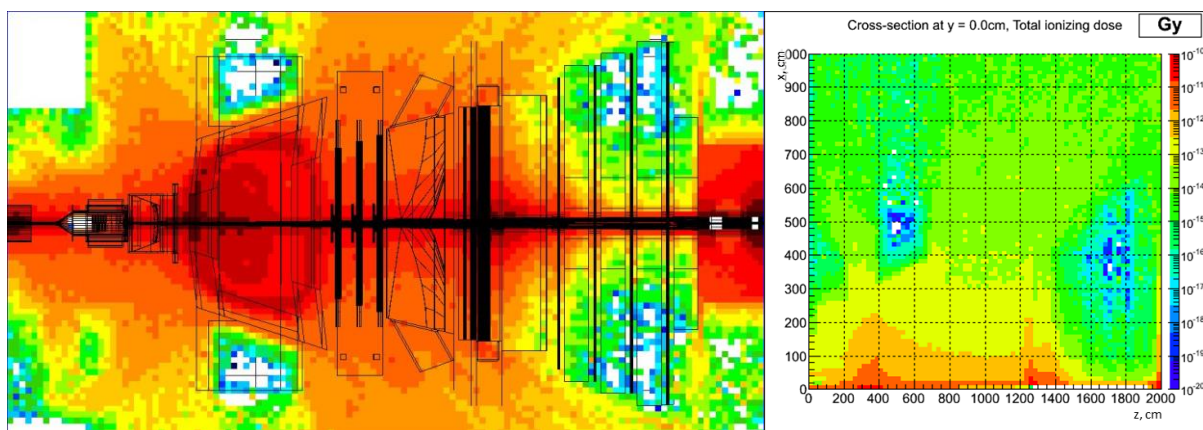


Figure 29: Comparison for 14 TeV CM collisions between total ionizing dose levels on the zx -plane between 2011 (left) and 2003 (right). The old result on the right only pictures one side of the experiment with the beam line being on the bottom of the plot. The curling dose deposition due to the magnetic field in the dipole is not visible on the right, where it should appear between 300 and 700 cm on the abscissa.

This is further substantiated by the fact that electrons are the main responsible factor for the deposition of dose in all regions before the calorimeters. The total ionizing dose per collision versus the dose deposited by electrons and positrons only is shown in figure 30 using the same color scale. The latter accounts for roughly 50% of the dose deposited around the edges of RICH2, and up to 85% inside the air volume of the magnet.

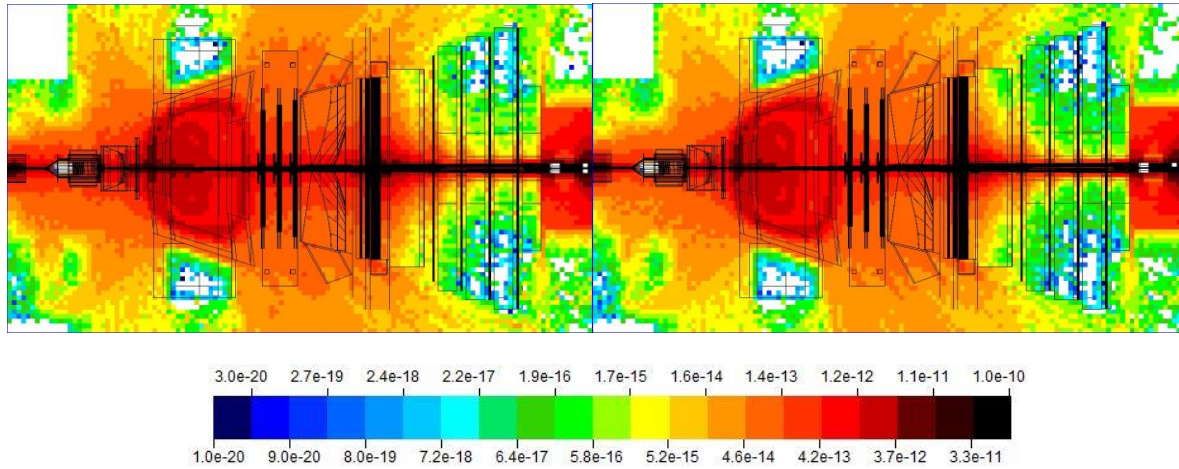


Figure 30: TID deposited by all particles (left) vs. TID deposited by electrons and positrons only (right). The same color scale is used for both plots.

Besides the evolution of the FLUKA Monte Carlo code over the last years, which includes enhanced physics and additional sophistication of particle transport and production models, additional factors play a role in constellating the differences between results from 2003 and 2011. Geometrical changes like the description of the magnet, which can be seen in figure 31, as well as the updated version of the magnetic field itself, constitute heavy differences between simulations.

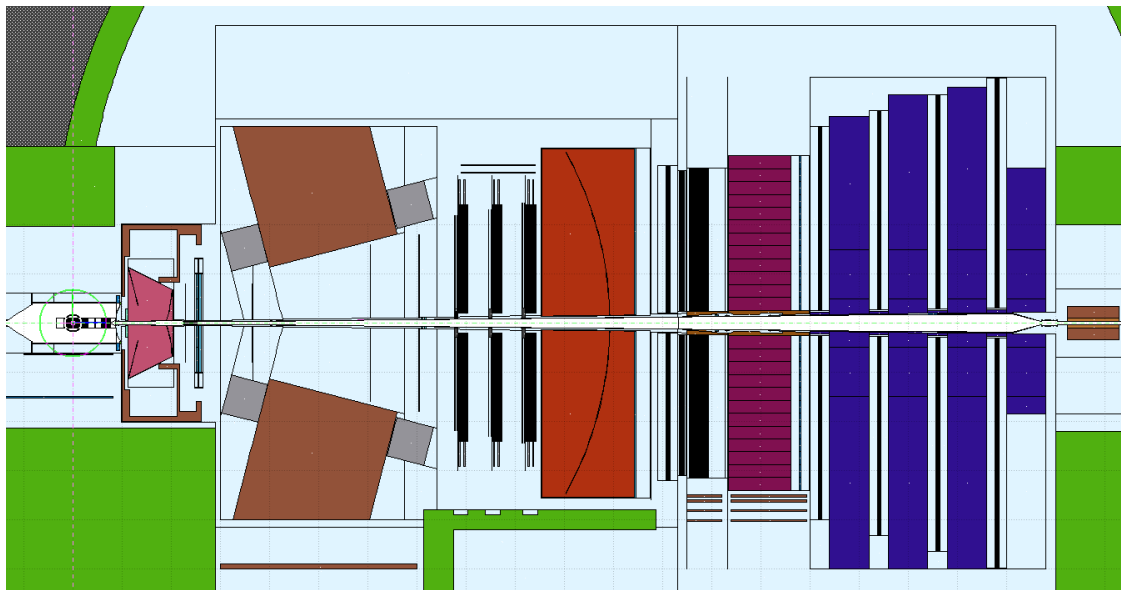
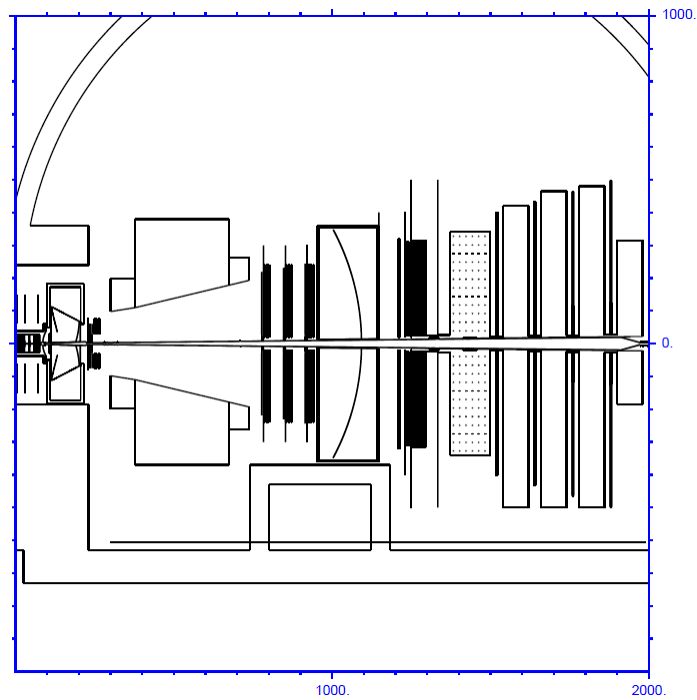


Figure 31: Cut side views of the FLUKA geometry which is the base for the studies from 2003 (above) and the geometry used for the comparison studies in 2011 (below). Some details like the shape of the dipole coils have been improved before 2010 by the original creator, but the official results from 2003 were not replaced.

Additionally, the different binning sizes which average over slightly diverging particle fields, along with statistical uncertainties because of the small initial numbers of primaries used for the first study from 2011, add to the explanation of the observed differences.

4.3 SIMULATION PREDICTIONS

4.3.1 FLUKA SIMULATIONS OF LHCb

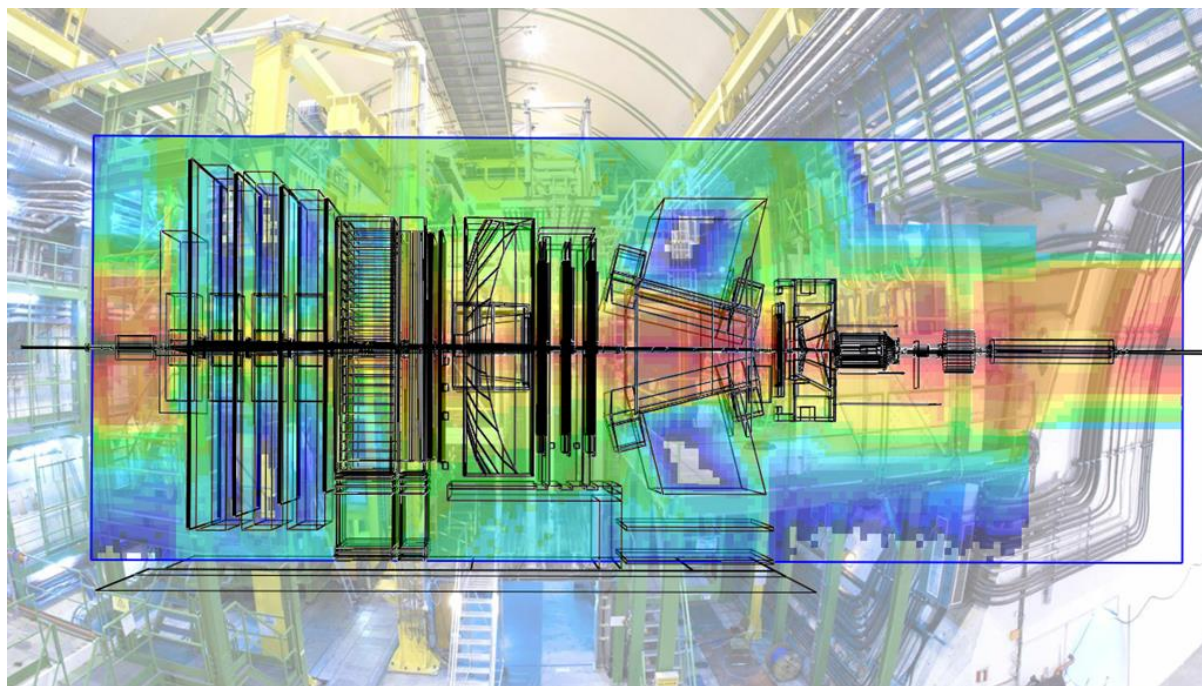


Figure 32: Result of dose scoring layered transparently over a sketch view of the FLUKA LHCb geometry using a photo of the experiment as a background to illustrate the extent of the general $20 \times 20 \times 20 \text{ cm}^3$ scoring, as well as the distribution of the deposition of dose within the detector, red colors showing the highest values.

In order to characterize the most popular properties of the LHCb radiation field originating from proton-proton collisions at these unprecedented energies, it is necessary to look at contributions from the predominantly occurring types of secondary particles as well as their impact onto integrating estimators like dose or 1 MeV neutron fluence equivalent. The current version of FLUKA provides a range of scoring options which make this possible.

However, even with the capabilities of CPU processing power developing at a steady rate, using a complex structure such as the LHCb experiment does set limits on the amount of information one can extract of a full-fledged simulation of its radiation field. Many of the dosimeters that are used for this thesis are located in areas around the edges of the various subdetectors, or even further away attached to the electronic systems of detectors. Generally, particle fluences in these areas tend to be significantly lower than on the inside of the experiment in vicinity to the beam line. In context with the FLUKA Monte Carlo method of simulation, this means that it takes a much longer computing time to obtain results with a reasonably low statistical error for estimators in these areas than it does for the central regions of the experiment. As a matter of fact, computing proton-proton collisions at these high energies and following the generated particle cascades through the geometry demands very high amounts of computing time even in today's infrastructure available at CERN. Depending on the type of CPU, the simulation of one collision at 8 TeV CM within the FLUKA LHCb geometry takes on average 1-2 minutes to fully calculate, when sometimes millions of them might be necessary to obtain a reliable result in a location at a large distance from the IP.

When using Cartesian scoring grids to obtain results like integrated fluence or prompt dose, one possibility to limit the required computing time to manageable amounts, while still keeping the statistical error within reason, is to average over larger volumes where the geometry and environment allow for it. In the case of the

LHCb experiment, this is possible at many of the locations where electronics as well as many of the active dose and fluence sensors are located, since the radiation environment does not change as radically anymore over the distance of a few tens of centimeters, as it does inside the detector close to the beam line.

In order to obtain a general overview of the radiation environment spanning the whole experiment, a grid of $20 \times 20 \times 20$ cm³ bins was used to score a variety of estimators during the simulation of prompt radiation. This 3D grid extends from -700 cm to +700 cm in x, from -600 cm to +600 cm in y, and from -900 to +2200 cm along z within the LHCb coordinate system. This volume comprises every subdetector and even includes part of the upstream and downstream LHC tunnels, as illustrated in figure 32. The size of 20 cm edge length for each bin has been decided on as a compromise. It is supposed to ensure a sufficient level of detail for most regions of interest which host one or more of the sensors used for this evaluation, while complying with the maximum bin limit of FLUKA scoring and keeping the statistical error for most bins within reasonable limits using the available computing resources. However when the region of interest lies in a central region more close to the beam pipe, this resolution of 20 cm will constitute a disadvantage, because most estimators exhibit a very high gradient of increase as you get close to the beam line. Some regions of interest, like the area around the VELO detector in direct vicinity of the interaction point, would profit from a higher level of detail when scoring. Additional Cartesian scoring with a resolution of $5 \times 5 \times 5$ cm³ has been added in the VELO alcove and the central part of the calorimeters, improving the accuracy of estimations for several locations of sensors in those areas. Many of these scored results will be shown and discussed in this thesis, however more estimators have been set for scoring during simulation which are not considered as relevant within the scope of this work. All of the Cartesian binning results have been made available to LHCb members using an internally accessible web interface. More types of estimations along with explanations and presentations will be made available on that page in the near future.

The described integrated fluence scorings are not providing any information on the energy distribution of particles, which would be of particular value in the case of neutron fluence. Therefore, differential fluence over an energy range $d\phi/dE$ was scored in places within the geometry that correspond to actual locations of active dosimeters. Besides the scoring of neutron fluence, the simulation was programmed to yield photon fluence, electron/positron fluence (both together) as well as a combined estimator for fluence of charged hadrons. These estimators have been chosen in order to attempt to gain insight into possible behavioral issues of some sensor types.

The statistical error of the simulation results which are used in this study is very low for both the 7 TeV CM and 8 TeV CM campaigns, as the available resources on the LHCb online computing farm during LS1 allowed for a very high number of primary events to be simulated. The error map for the simulation of total integrated dose during 7 TeV CM collisions in figure 33 shows the statistical relative error in % of the total value of a bin. Because FLUKA calculates dose in a different way than fluence, the relative error of fluence estimators is usually lower than the one for the dose estimator. Therefore the values in figure 33 are representative for all the simulation results with a Cartesian grid binning of $20 \times 20 \times 20$ cm³ in this document.

The relative statistical error within most of the area in and around the detector rarely exceeds 10%. This is true as well for the $5 \times 5 \times 5$ cm³ binning in the inner calorimeter area.

However this low error is relevant exclusively for the statistical accuracy of the Monte Carlo simulation itself. It is not representative of systematic errors of the simulation results, which include inaccuracies in the description of the geometry or errors in the physical models that are used to calculate individual events. While a certain feeling concerning errors can be gained from experience with measurements and knowledge about the differences to the actual detector, a quantitative error cannot be provided.

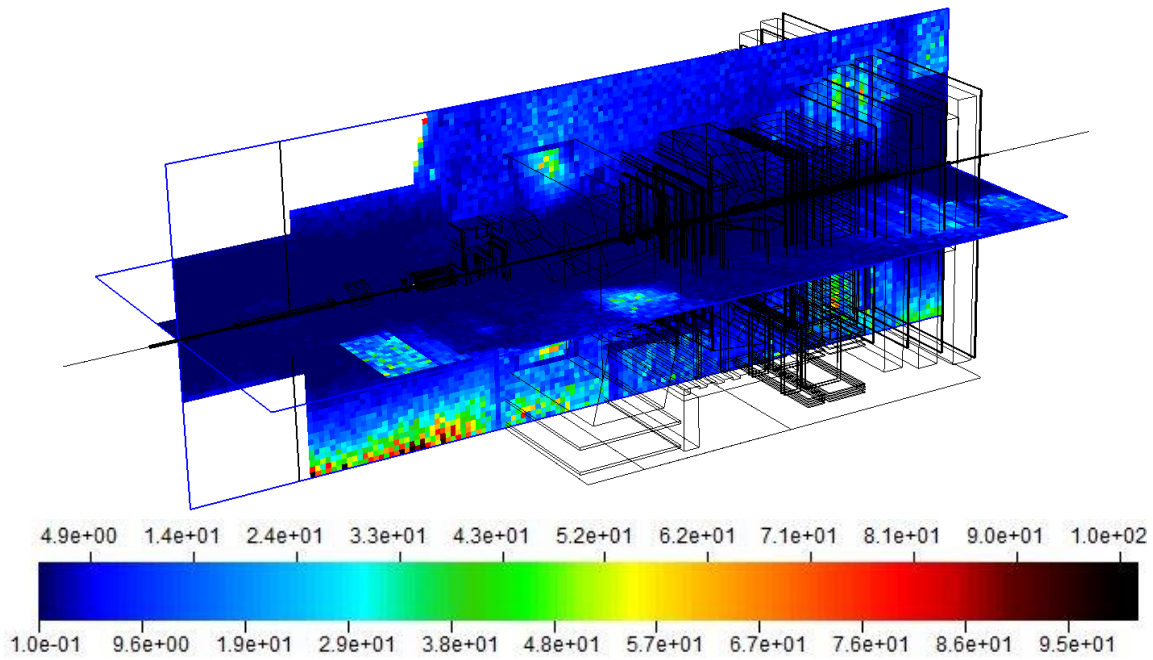


Figure 33: Map of the relative statistical error in % of the total integrated dose estimator for 7 TeV CM collisions. In most places in and around the detector, the statistical error rarely exceeds 10% and is mostly well below this value. The central areas show the smallest error because of the high number of events that are taking place around the beam. All simulation results with a Cartesian grid binning of $20 \times 20 \times 20 \text{ cm}^3$ in this document have equal or lower relative statistical error than what is shown in this figure.

4.3.2 FLUENCE MAPS

In this section, various fluence estimators are shown in order to visualize the basic evolution of the most common particle types within the LHCb detector. The following plots made with SimpleGeo display the results of fluence estimators as a grid of cubic volumes with an edge length of 20 cm as cut planes along the beam line. A side view and a top view have been chosen as they are most suited to illustrate the distribution of different types of radiation along the experiment.

These fluence plots only count tracklength fluence, which translates to a number of particles per cm^2 in the volume of a bin. They do not contain any information about the energy of the particles involved except for one estimator with an explicitly stated description. For the sake of illustration on this large scale, all the plots only show results for one direction of the magnetic field at 8 TeV CM, since the differences between magnetic field directions and between 7 TeV and 8 TeV CM collision energy are negligible. In addition, the concentration on one magnetic field direction allows for a better insight on the field effect on charged particles. Since the following plots have mostly an illustrating function, they are all presented in [unit]/collision.

4.3.2.1 NEUTRON FLUENCE

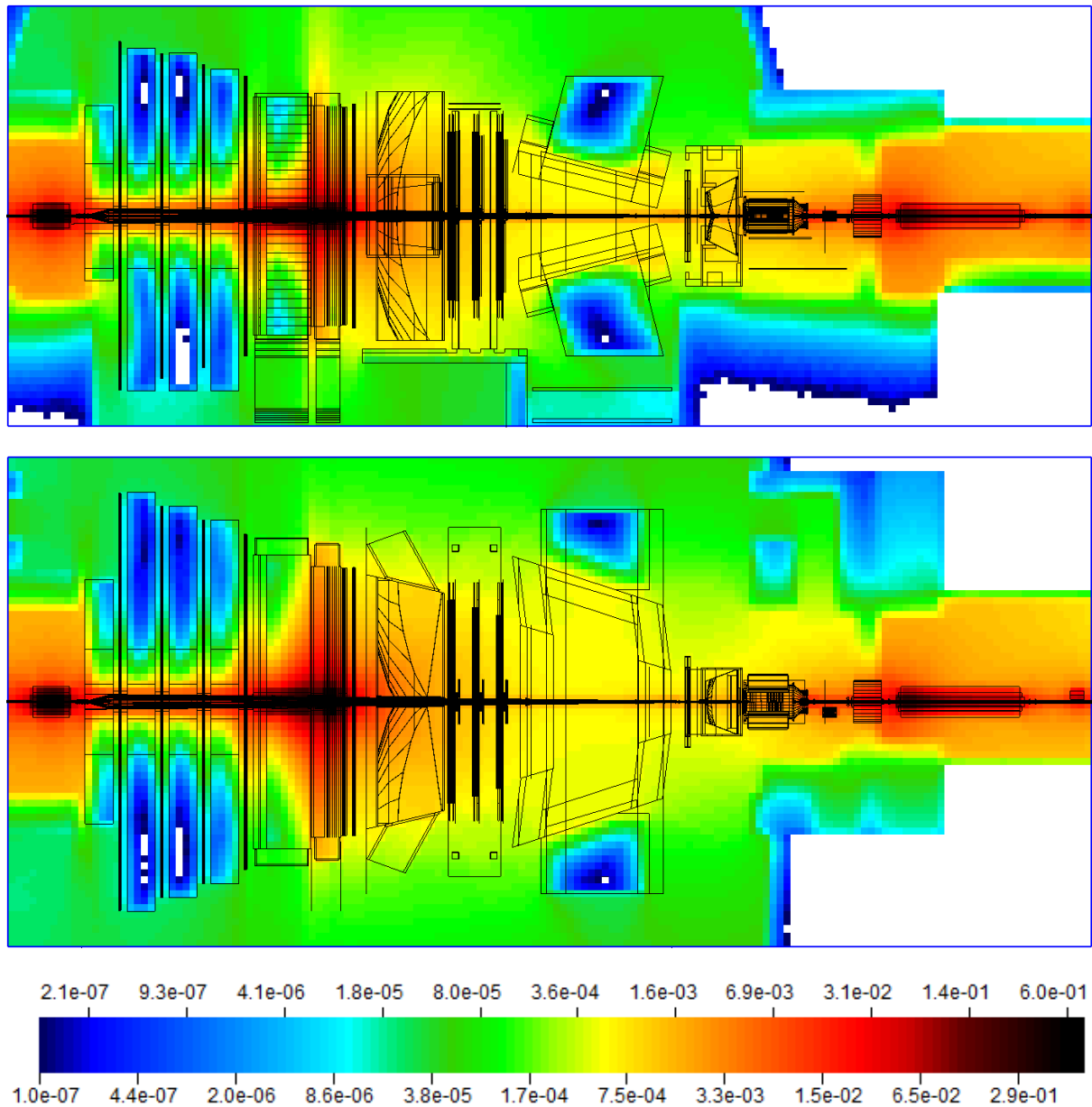


Figure 34: Neutron fluence per cm^2 per collision at 8 TeV CM with the magnetic field of the LHCb dipole pointing downwards. Side view of the yz plane (top) vs. top down view of the zx plane (bottom) using the same color scale, both at beam height. The majority of neutrons inside the experimental cavern are generated in the most massive subdetectors ECAL and HCAL. Many neutrons are backscattered from the front plane of the ECAL in the direction of the interaction point. White areas indicate values below the color scale.

Neutrons are known to have a large impact on the LHCb detector for various reasons, which differ depending on the energy of the particle. The fluence of low-energy thermal neutrons is primarily interesting for the determination of the eventual activation of detector material. It also influences the background e.g. in the chambers of the muon detectors through the generation of γ -radiation during neutron capture. Higher energy particles have a more direct influence on the performance of the detectors electronics. The neutron fluence around 1 MeV produces displacement damage effects in silicon based electronics. Neutrons with an energy above 20 MeV are able to induce a number of Single Event Effects. Both types of effects have to be thoroughly considered in the operation of the detector. The ratio between neutrons with certain energies differs greatly

between locations and has to be estimated using differential scoring in case of need. The general neutron fluence per cm^2 plotted in figure 34 is mostly useful to illustrate the shape of the overall neutron distribution without being able to provide information on energy. It shows that most neutrons are produced around the upstream wall, the downstream tunnel section and most importantly around the center of the calorimeter structure. Hadrons originating from the collision interact with the material of the calorimeter and produce cascades generating the largest portion of the neutrons that are flooding the experimental cavern. Neutrons that are backscattered from the calorimeters still reach the locations of the outer tracker electronics in relatively large numbers, where they may pose a problem to the electronics when collision numbers reach higher orders of magnitude. According to differential spectra scored in several regions around the detector, these neutrons cover an energy range from meV up to some 100 GeV.

4.3.2.2 PROTON FLUENCE

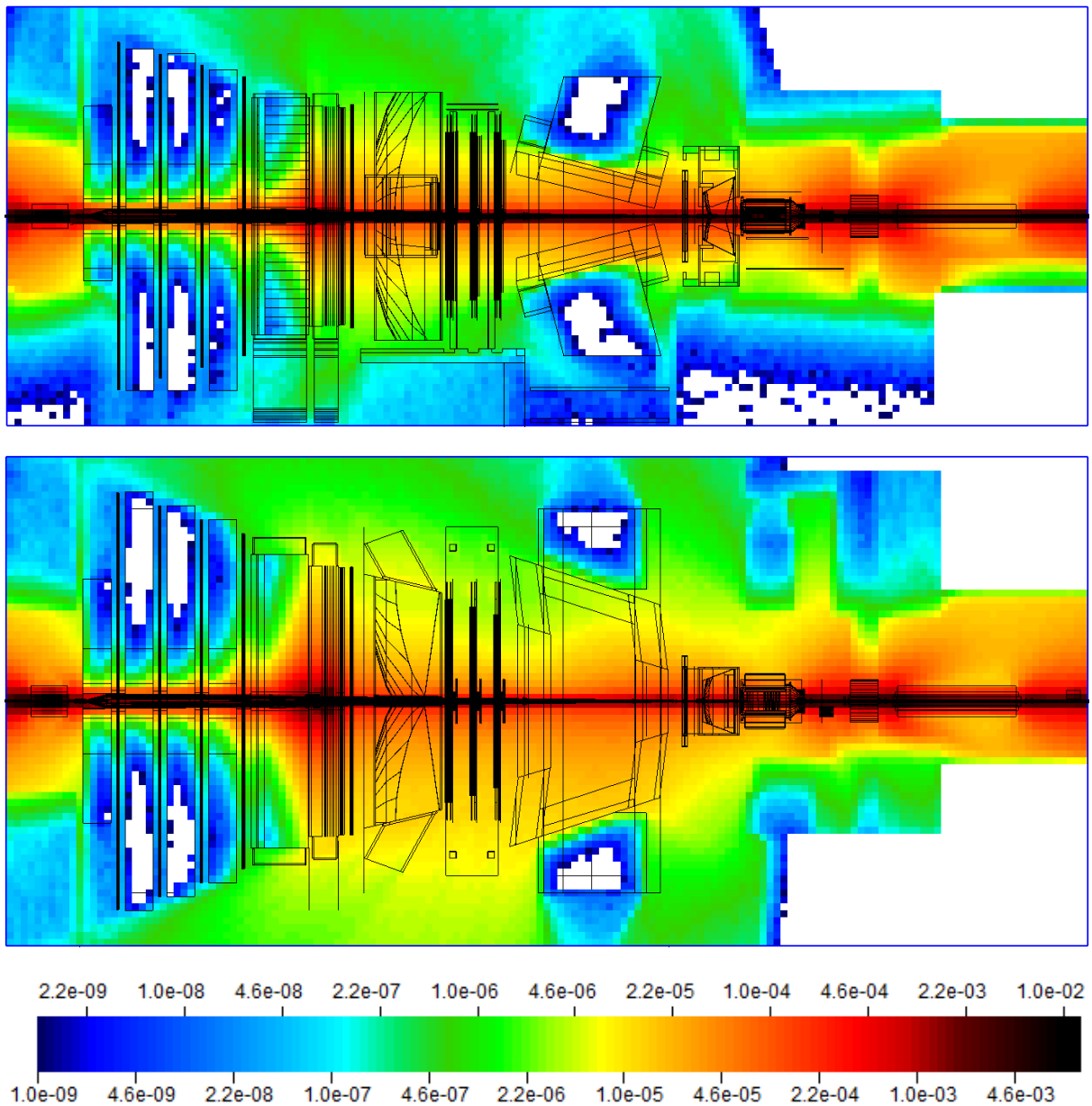


Figure 35: Proton fluence per cm² per collision at 8 TeV CM with the magnetic field of the LHCb dipole pointing downwards. Side view of the yz plane (top) vs. top down view of the zx plane (bottom) using the same color scale, both at beam height. Most protons are found close to the beam line, originating mainly from the IP, and behind ECAL and HCAL due to hadronic cascades developing inside the calorimeters. White areas indicate values below the color scale.

Since the two colliding beams in the experiment are protons with energies in the TeV range, there will likely always be a very high fluence in the bins along $x=y=0$. The main occurrence of secondary proton radiation which still carries a large amount of energy revolves around the beam line, as can be seen in figure 35. A lateral spread of protons can only be observed when large amounts of heavy materials shorten the mean free path of the highly energetic particles sufficiently and increase the number of nuclear interactions during a cascade, as it is the case inside the calorimeter structure and around the concrete wall upstream of the VELO detector. In the top down view the effect of the magnetic field is very visible. The field is responsible for not only spreading the proton fluence along the horizontal, but also for visibly shifting the positively charged fluence towards the positive x coordinates since it is pointing downwards.

4.3.2.3 PHOTON FLUENCE

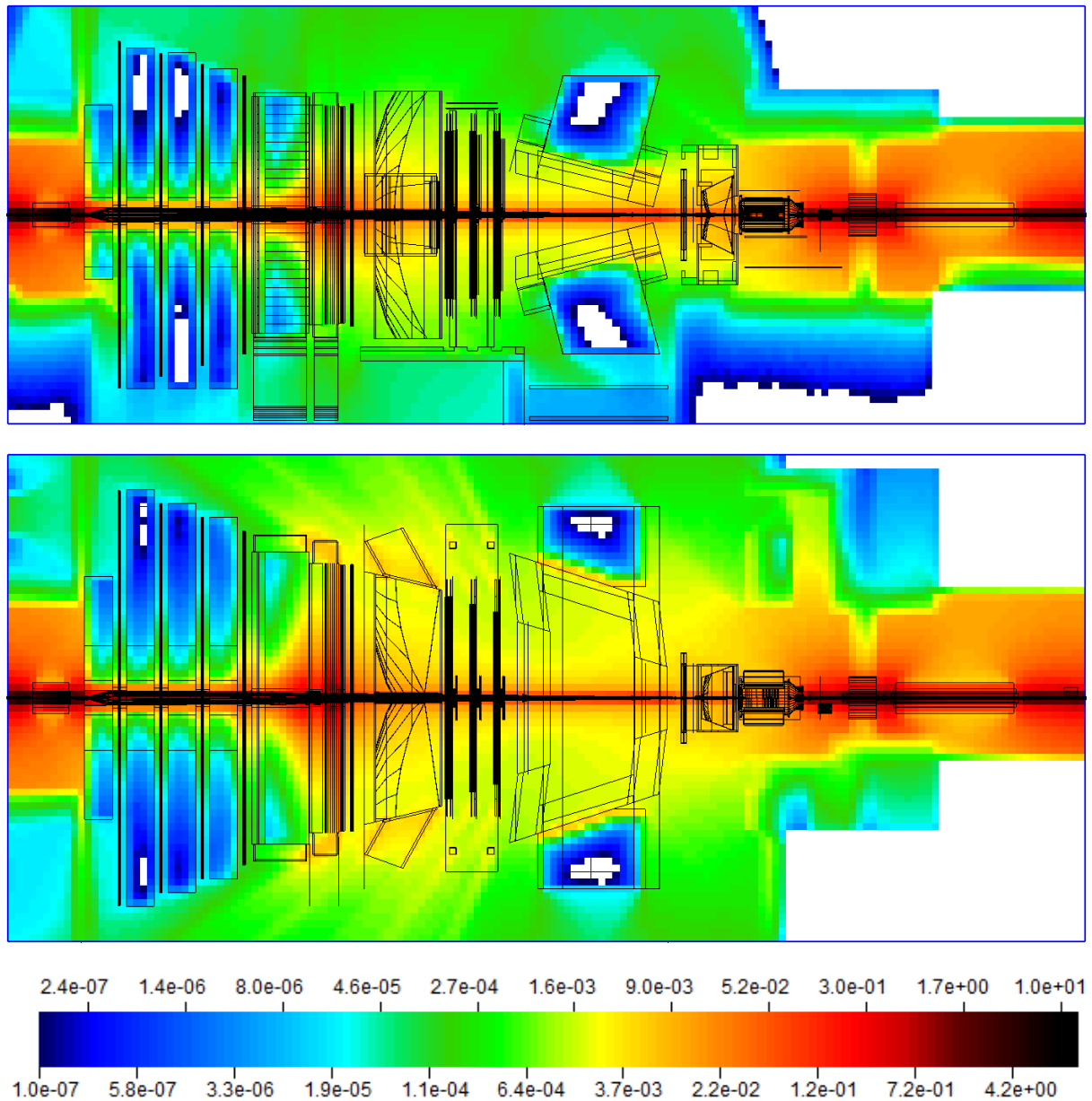


Figure 36: Photon fluence per cm^2 per collision at 8 TeV CM with the magnetic field of the LHCb dipole pointing downwards. Side view of the yz plane (top) vs. top down view of the zx plane (bottom) using the same color scale, both at beam height. White areas indicate values below the color scale.

Photons are mainly produced during electromagnetic cascades from energies of several tens of GeV down to very small energies, but their cutoff energy in the simulation is set at 100 keV. The highest photon fluence within the experiment, apart from the cascade photons developing inside the calorimeters, is concentrated inside the VELO alcove, as displayed in figure 36. Elevated levels can also be seen along the central beam line. The uncharged photons are not influenced by the magnetic field of the LHCb dipole. Nevertheless, in the top down view some cascade photons can be observed originating from support pillars at the edge of the Tracking Stations, which do exhibit different angles not pointing to the IP. This is of course caused by the charged particles, many of them electrons and positrons, which are deflected by the magnetic field, which subsequently interact with the support structures. Photons represent the largest number of particles in LHCb.

4.3.2.4 ELECTRON & POSITRON FLUENCE

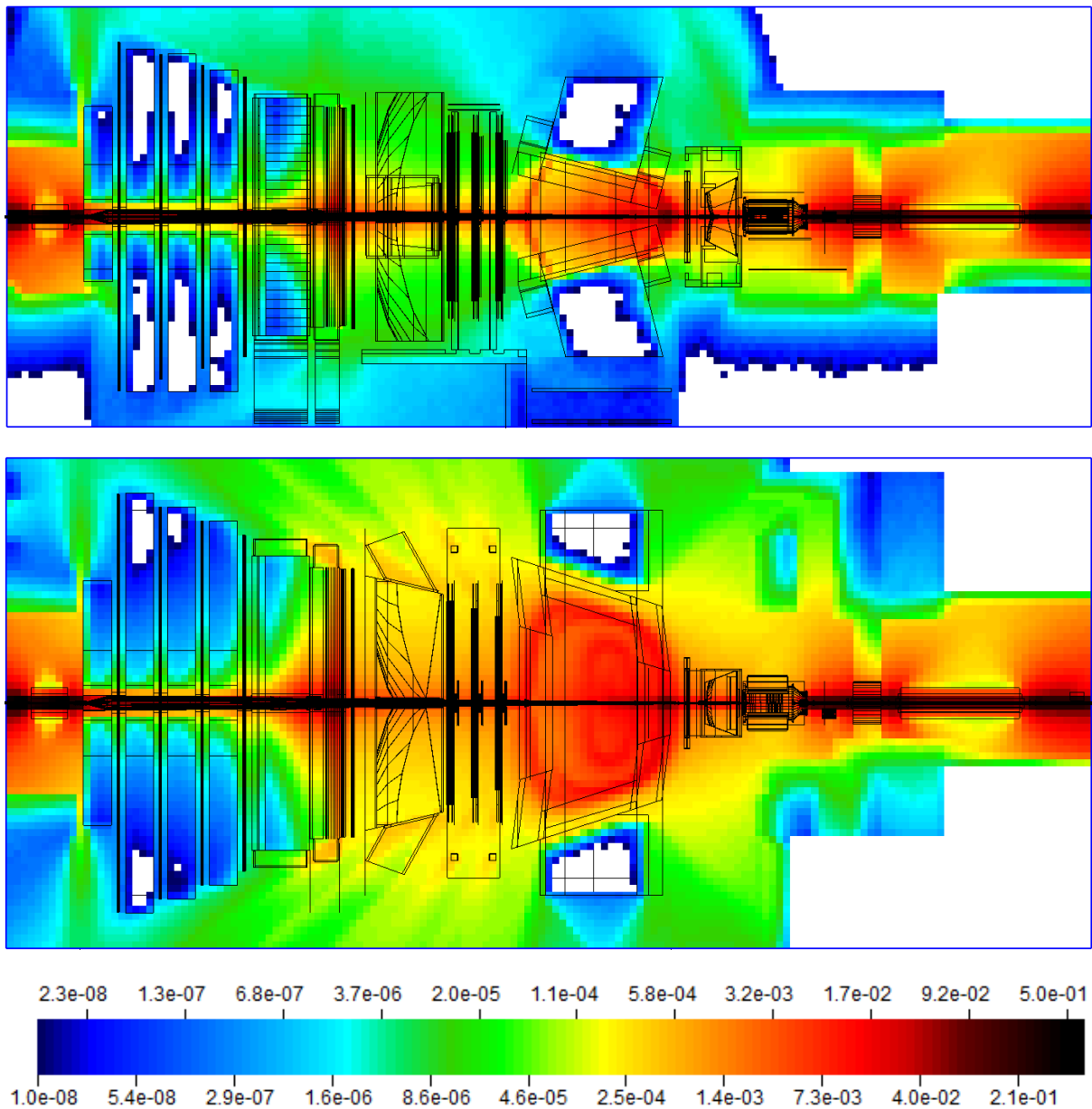


Figure 37: Fluence of electrons and positrons per cm^2 per collision at 8 TeV CM with the magnetic field of the LHCb dipole pointing downwards. Side view of the yz plane (top) vs. top down view of the zx plane (bottom) using the same color scale, both at beam height. White areas indicate values below the color scale.

The fluence of electrons and positrons at a collision energy of 8 TeV is shown in figure 37. Most of these electromagnetic particles are produced in interactions of the highly energetic products of the collisions with portions of the experiment that have higher density than their surroundings. At high energies, the impact of these highly energetic products on material produces π^0 particles, which decay with a very short half-life into highly energetic photons. These photons in turn are able to trigger electromagnetic cascades. The main part of electrons and positrons with energies above 1 MeV is produced by this mechanism. On one hand, this can be observed upstream of the electromagnetic calorimeter, where the interactions inside the lead between the SPD and PS detectors and more importantly in the electromagnetic calorimeter itself generate a lot of electrons and positrons under the bombardment of high energy particles coming from the interaction point.

On the other hand, the heavy VELO vacuum tank which is made of stainless steel with a few centimeters thickness and a few large flanges on top, is the source of the increased electromagnetic radiation upstream of the interaction point up to the cavern wall.

The most remarkable place where electrons dominate the radiation field is located within the large dipole magnet of the experiment. Particles with high energy coming from the collision, which are just barely passing through the beam pipe because of their low angle to the beam line, are hitting on the metallic flanges that hold the beam pipe in place inside the magnetic field. Although these flanges are made of aluminum, and therefore provide only little possibility for interaction, a lot of electromagnetic particles originate from them. Many of the charged electrons and positrons from these interactions are deflected by the dipole field on their way downstream. Those who do not have enough energy to escape the dipole area continue to spiral inside the magnetic field until they deposit all of their energy. This fluence distribution that is influenced by the magnetic field lines of the LHCb dipole can be very well observed in figure 37, where each flange that is placed along the beam pipe is the source of a loop-shaped area of higher particle fluence.

4.3.2.5 CHARGED HADRON FLUENCE

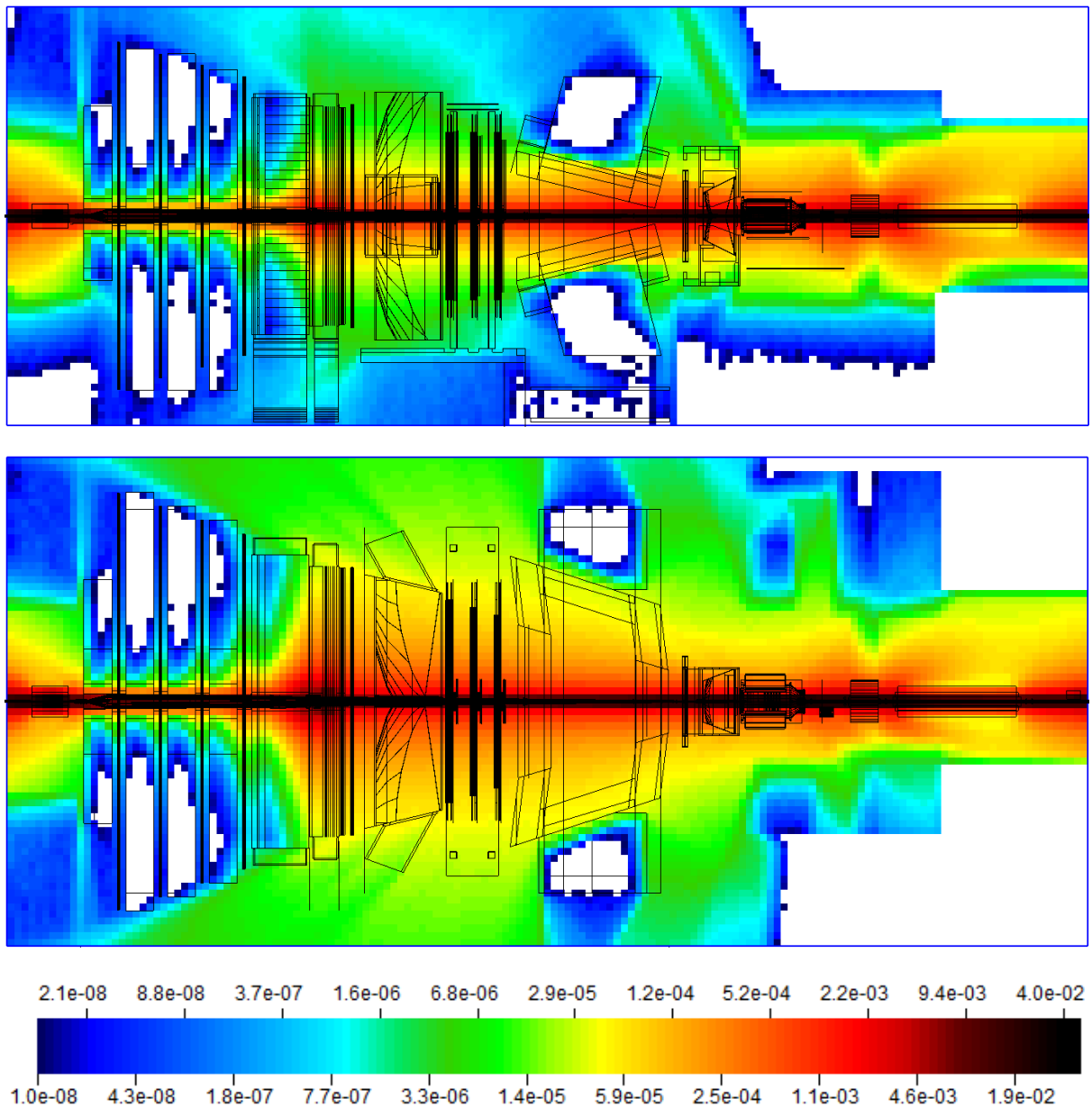


Figure 38: Fluence of all charged hadrons per cm² per collision at 8 TeV CM with the magnetic field of the LHCb dipole pointing downwards. Side view of the yz plane (top) vs. top down view of the zx plane (bottom) using the same color scale, both at beam height. White areas indicate values below the color scale.

The collision byproducts of high energy hadron colliders introduce a significant amount of particles into the radiation field mix which are not protons or neutrons. In particular, three kinds of pions are produced above a certain energy limit of a few 100 MeV. Pion energies in LHCb are generally in the higher GeV range as was shown earlier in figure 8, where they are mostly the dominant particle. During their short lifetime they behave largely like protons. Together with Kaons and other less important short-lived contributors, this selective estimator shown in figure 38 provides an overview of the fluence distribution of all charged hadrons within the experiment. In addition to the proton fluence from figure 35, this estimator also counts charged pions, which together with antiprotons are mainly responsible for the elevated values in the central regions when compared to figure 35. Due to the more equal distribution of positive and negative charges in this summarized

plot, the disparity which could be observed in the proton fluence on the zx plane in the top down view is not visible anymore. The largest fluence values can be found along the beam pipe and inside the calorimeter structure. In contrast to the general hadron distributions, the areas around the Tracking Stations and RICH2 indicate that most charged hadrons are forward directed, and much less of them are scattered back in the direction of the IP compared to the neutron distribution.

4.3.2.6 FLUENCE OF HADRONS > 20 MEV

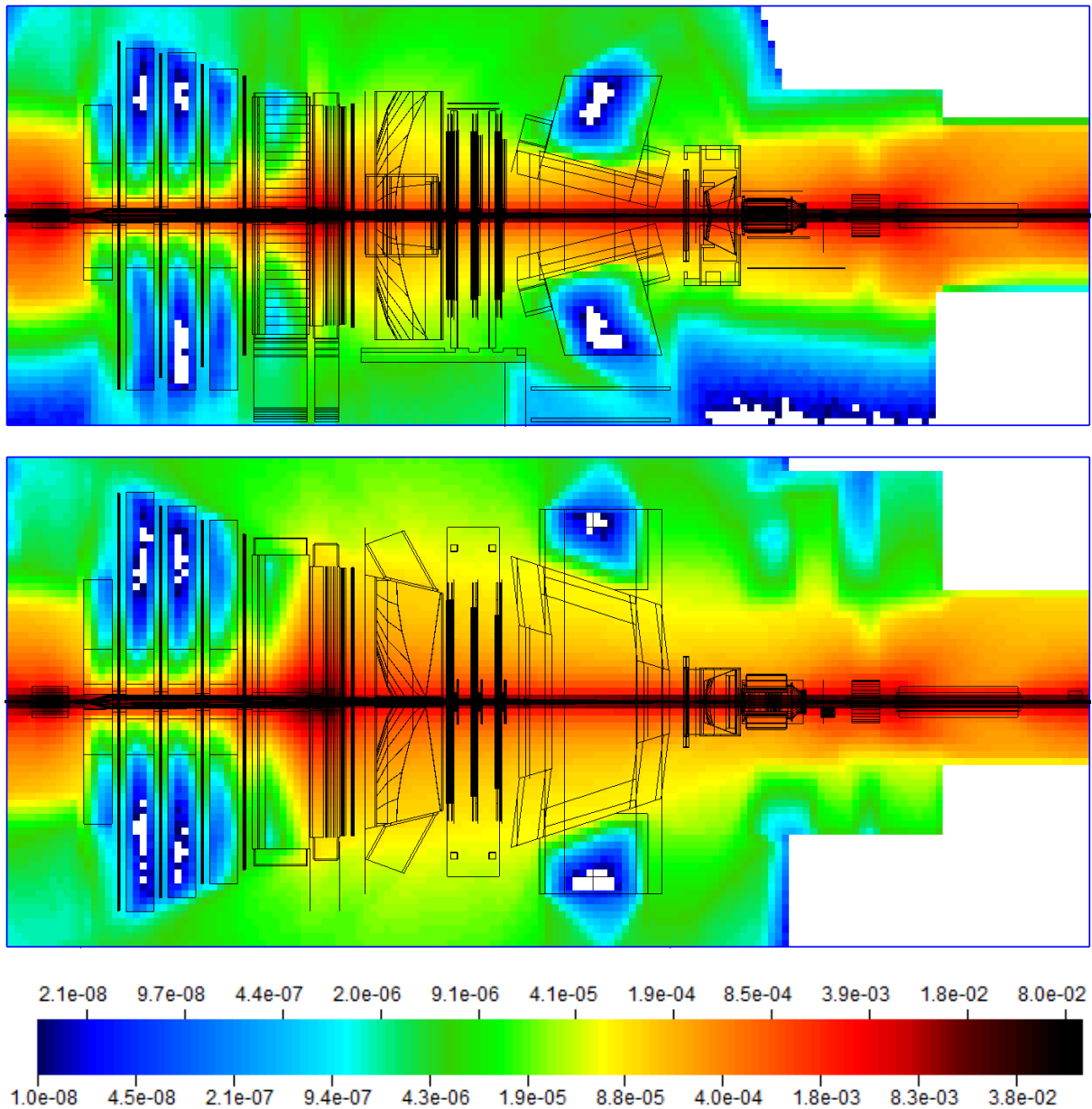


Figure 39: Fluence of Hadrons with an energy greater than 20 MeV per cm² per collision at 8 TeV CM with the magnetic field of the LHCb dipole pointing downwards. Side view of the yz plane (top) vs. top down view of the zx plane (bottom) using the same color scale, both at beam height. This value is mainly influenced by the fluence of neutrons, protons, pions and kaons. It is used to estimate the probability of SEUs in electronic devices. White areas indicate values below the color scale.

FLUKA scoring options also include a selective scoring (called HADGT20), which only counts the combined tracklength fluence of hadrons that have a kinetic energy above 20 MeV. This estimator is designed to help in assessing the possible occurrence of some Single Event Effects in electronic devices and can be used to evaluate their expected reliability during operation of the experiment. It is shown in figure 39 that the mainly affected areas are naturally located around the beam pipe and the calorimeter structure. However, the lateral distribution of the fluence shows elevated levels of high energy hadrons that reach the locations of readout electronics for several subdetectors. In addition to the integrated estimators for dose and 1 MeV neutron fluence equivalent, this estimator is often considered for prediction studies regarding the future upgrade of electronics.

4.3.3 INTEGRATED ESTIMATORS

The following plots show integrated estimators that can be directly requested using FLUKA standard options. To obtain these, internal conversion factors to calculate 1 MeV neutron fluence equivalent and dose estimators from the standard tracklength fluence and energy deposition values are being applied by the code during runtime. They are all scaled in [unit]/collision as it was the case with fluence estimators presented earlier.

4.3.3.1 1 MEV NEUTRON FLUENCE EQUIVALENT

The 1 MeV neutron fluence equivalent shown in figure 40 is an estimator that describes the damaging effect of all kinds of radiation on a material, in this case silicon, which is expressed as the equivalent to the exposure to neutron radiation with an energy of 1 MeV. This means that in addition to the regions with high neutron fluence displayed in figure 34, more areas display high fluence values because of the influence of particle showers that are not made exclusively of neutrons, because the damage caused by other particles is added to the calculation. As 1 MeV neutrons are cumulatively damaging to silicon-based electronics, this estimator is especially important as it provides useful information for the required radiation hardness of electronics in rather exposed areas.

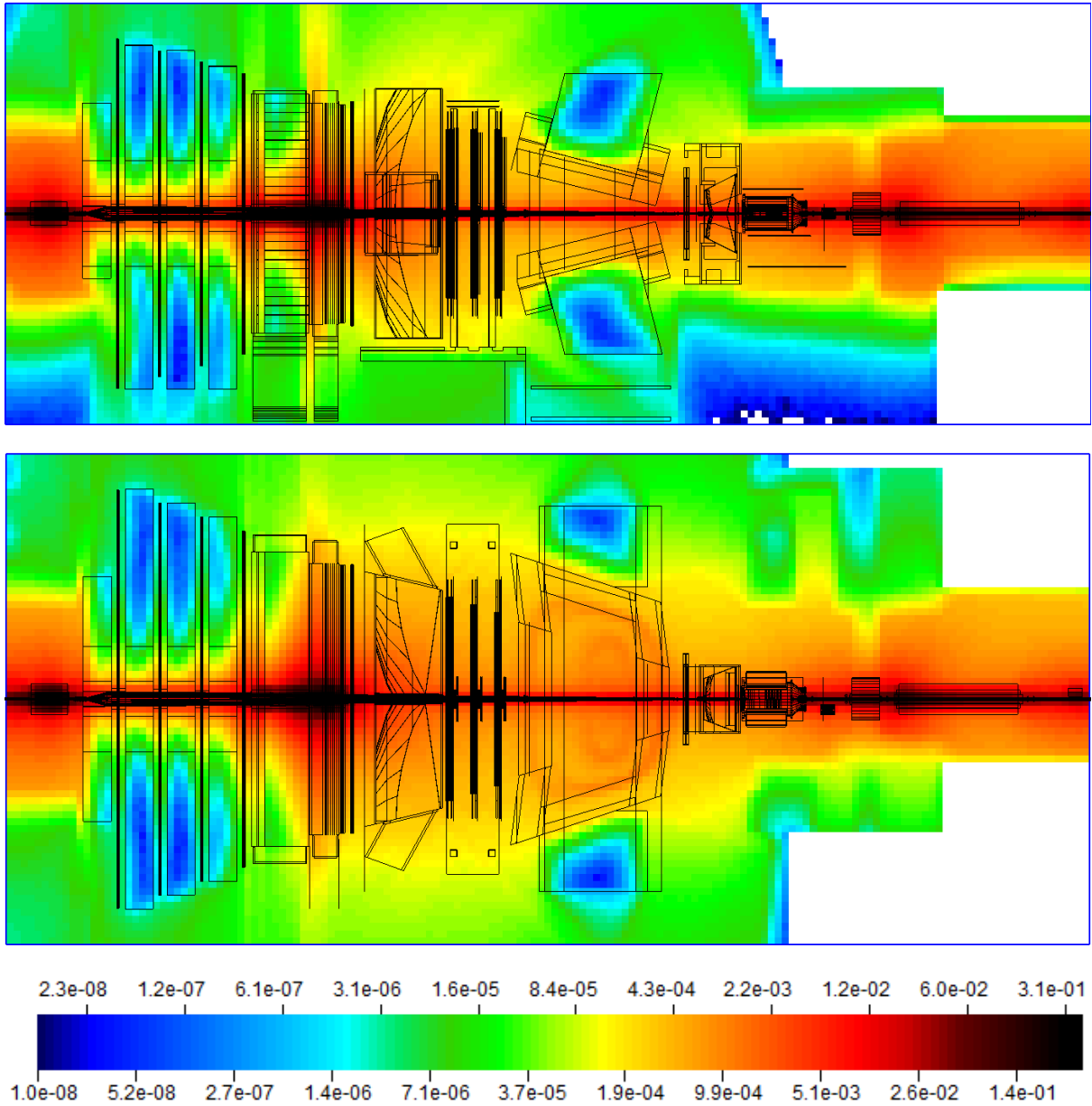


Figure 40: 1 MeV neutron fluence equivalent in silicon per cm^2 per collision at 8 TeV CM with the magnetic field of the LHCb dipole pointing downwards. Side view of the yz plane (top) vs. top down view of the zx plane (bottom) using the same color scale, both at beam height. In addition to the spots with high neutron fluence like the central calorimeter regions, other types of radiation including charged particles are increasing the count of virtual particles that are considered as damaging to silicon as 1 MeV neutrons. White areas indicate values below the color scale.

4.3.3.2 TOTAL IONIZING DOSE

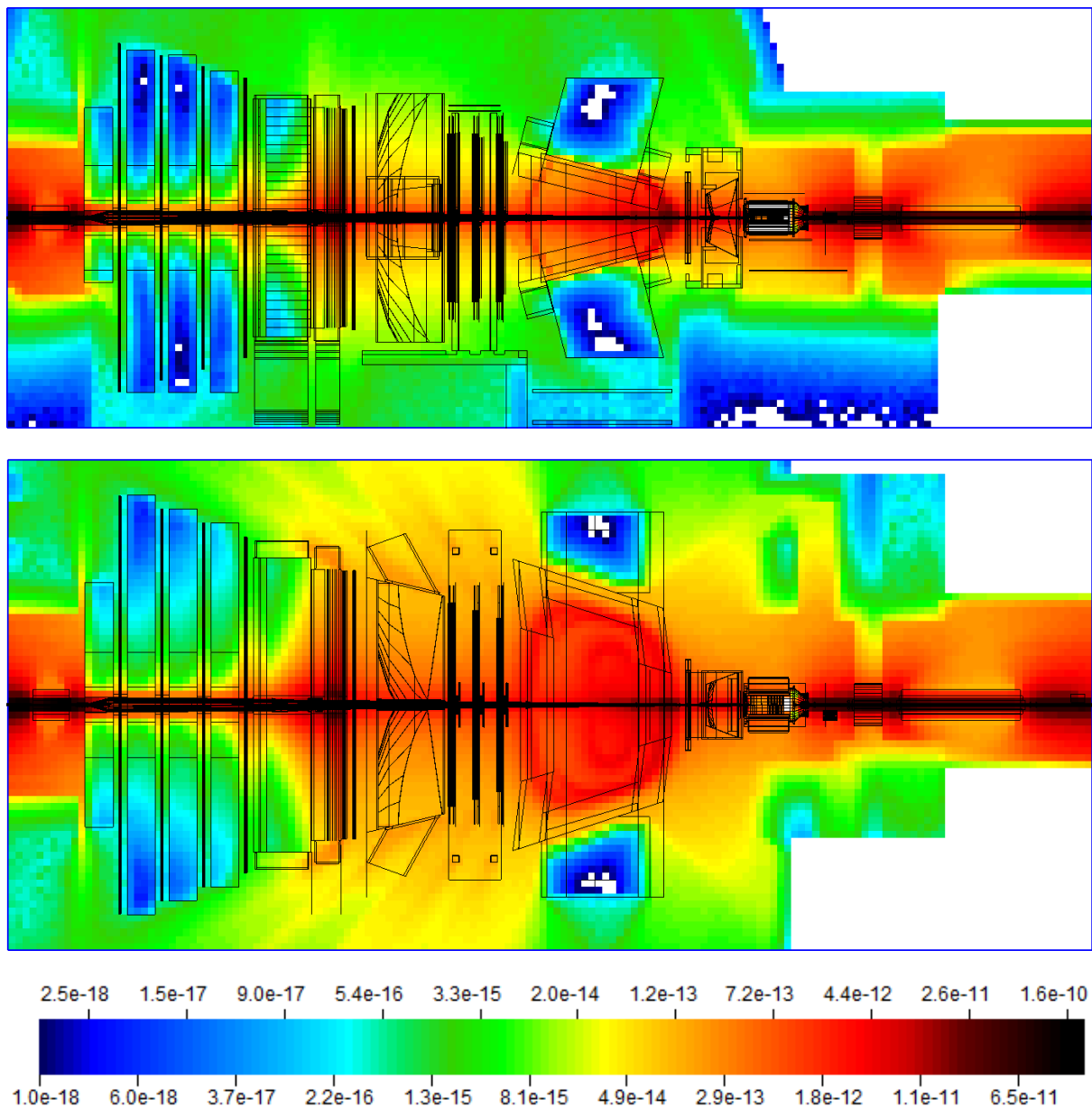


Figure 41: Total Ionizing Dose per collision in Gy at 8 TeV CM with the magnetic field of the LHCb dipole pointing downwards. Side view of the yz plane (top) vs. top down view of the zx plane (bottom) using the same color scale, both at beam height. Areas with high levels of deposited dose at the LHCb experiment include the calorimeters, the space upstream of the VELO and the center of the large LHCb dipole, where charged particles with lower energy get trapped by the magnetic field until they deposit all of their energy. White areas indicate values below the color scale.

One of the most important and valuable pieces of information on the radiation field is usually the distribution of total ionizing dose. For the experiment, its impact on the degradation of material and the performance of detector components are of interest. Therefore an evaluation of the dose estimates provided by the simulation using various measurements, which is one of the main goals of this thesis, is a necessity.

According to the simulation, there are two areas inside the experimental cavern that receive the highest values of total ionizing dose. On one hand a lot of energy is deposited inside the calorimeter structure, where most of the secondary particles that are produced in the initial collisions are being absorbed as intended. The

calorimeters are segmented into several layers of various weights and masses, with airspaces in between. Particle showers are generated and already partially absorbed in the first massive layers, which are mostly made of lead like the 1.2 cm thick lead plate between the SPD and PS detectors or most of the absorbing mass of the ECAL, and continue to deposit large amounts of dose even in the airspace between the detectors. A backscattering of radiation detectors can be observed as well in the enlarged red area upstream of the calorimeters and the shadows thrown on the outsides of the dipole yoke.

On the other hand very high values of dose can be measured at the upstream wall next to the VELO detector, where the particles created in the collisions that turn away from the experiment are interacting with the VELO vacuum vessel, which is made of steel with various grades of thickness ranging from 6 mm (vessel body) to 2 cm (flange endcaps), as well as with other support structures in the VELO alcove. The particle density around the beam pipe is very high at this small distance to the IP. The beam pipe and structures very close to it are barely obstructed outside of the VELO detector, which made it possible to attach boxes with dosimeters very close to the beam pipe, which registered dose values in the kGy range over the course of a year.

As indicated by the plot in figure 41, another area with high values of deposited dose is located within the magnetic field of the large LHCb dipole. Although there is little material to be found in this area that could interact with the incoming radiation since even the beam pipe is made of beryllium, there are some small stabilizing aluminum structures around the beam pipe that are holding it in place, which provide some opportunity for interactions with the high energy particles coming from the collisions. Charged particles with low energy which are generated by these interactions, mainly electrons and positrons, are subsequently caught in the magnetic field and start curling until they lose all of their energy. In fact, electrons and positrons account for about 85% of the dose deposited inside the airspace of the magnet, as can be seen in the result of a first study with a low amount of simulated primary collisions. This result is depicted in figure 30, where total ionizing dose is contrasted by the amount of dose contributed by electrons and positrons only.

4.3.3.3 INFLUENCE FROM THE LHC TUNNEL

The corrector dipoles in the tunnel segments upstream and downstream of the experiment are a significant source of secondary radiation. Some of that radiation is able to enter the experimental cavern and influence the radiation field around the experiment in the area close by. The rectangular hole in the upstream wall around the beam pipe, which was introduced into the FLUKA geometry during the remodeling of the VELO alcove, enables part of the radiation from the collisions as well as radiation coming from interactions at the corrector dipole in the tunnel to pass unhindered through the wall into and out of the experimental cavern. Considering the large amount of secondary radiation coming from the direction of the interaction point, which is created directly in the proton-proton collisions and within the steel hull of the VELO vacuum tank, this additional exposure of the area around the BLS from the direction of the tunnel is likely very low in comparison. Nevertheless this contribution was considered worth the effort of changing the simulation geometry.

Downstream of the experiment, the energy produced in the collisions is mostly absorbed by the various heavier structures like the calorimeters and the muon shielding. Therefore, the backscattering originating from the RB86 tunnel segment and passing into the cavern has a comparably higher influence on the less exposed surroundings than at the location of the upstream wall. The side view of the dose distribution at beam height in figure 42 shows a remainder of stray radiation that is able to pass upwards behind the last block of iron shielding from the muon detectors. In the real experimental cavern the geometry is slightly more complicated as there are additional concrete structures that prevent people from accessing this exposed area, but nonetheless this opening does exist. Some of the radiation coming from the tunnel is dispersed on mechanical

infrastructure, meaning cable trays and pipework, which is located right above the opening. As this kind of dispersion is not represented in the simulation, a dose sensor in close vicinity to this opening will likely measure more than the simulation would predict. In fact, the dosimeters placed at this position constantly measured higher dose than the simulation predicted.

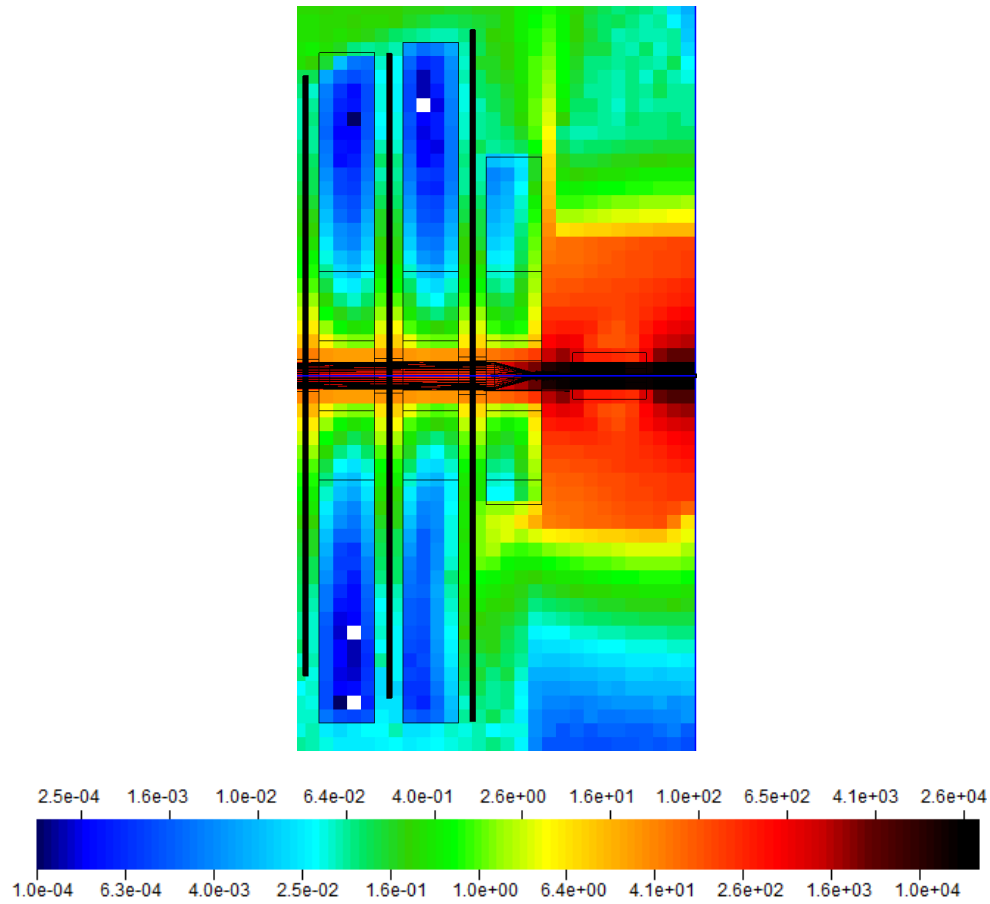


Figure 42: Side view of the total ionizing dose distribution at beam height downstream of the last muon detector in Gy. An upward pointing spike originating from the RB86 tunnel segment can be observed passing behind the last muon iron shielding. In the real cavern, infrastructure right above this opening would deflect the radiation towards a sensor placed on top of the iron shielding.

More detailed plots and zoomed-in views of regions of interest including the VELO alcove and the inside of the calorimeter detectors will be shown in later sections during the comparison and discussion of measurements.

4.3.3.4 DIFFERENTIAL FLUENCE SCORING

While certain integrated estimators such as total ionizing dose are most informative when presented as a well-defined grid of distinct values, the general fluence plots shown earlier are missing a sometimes very important piece of information, i.e. the energy distribution of particles. As explained earlier, the energy spectra for neutrons, charged hadrons, electrons/positrons and photons have been scored at several locations that correspond to the positions of active radiation monitors which are discussed later in this document.

The used scoring type (called USRTRACK) is only capable of tracking particles that pass through a region volume of the geometry which is defined by the combined geometrical CG bodies. Therefore the individual scoring volumes differ from each other as their size needs to be adjusted according to the relative fluence of particles at their location. Regions further from the beam are recording less overall fluence and therefore yield a much higher statistical error in comparable volumes. Of course the scoring volume size has to be taken in account when plotting values per collision.

As was mentioned earlier, the radiation field in LHCb is very forward-directed due to the high energy of the proton beams hitting each other head-on. This is illustrated very well by comparing spectra from different distances from the beam line. As an extreme example for the diversity of the encountered particle distributions in LHCb, two scenarios close to and far from the beam line are plotted in the following figures. In figure 43 the lethargy fluence for 7 TeV CM collisions of neutrons, charged hadrons, electrons/positrons and photons is shown for the location of the sensor boxes next to the Beam Loss Scintillators on the upstream wall of the VELO alcove. These boxes are located at only 2 m distance from the IP at 15 cm above the beam line. Because of the particle showers started in the copper beam pipe, the stainless steel vacuum vessel of the VELO and other metallic structures in this area, the measured dose values in this spot are the highest values measured with all sensors in LHCb. Due to the increase in highly energetic particles when moving closer to the beam the deposition of dose increases as well with a very strong gradient. Consequently the highest measured dose in LHCb can still be orders of magnitude below a received dose for equipment in positions at less distance from the beam or IP. The fluence values in figure 43 show values for all particles which are shifted to very high energies when compared to all other spectra scored at further distances. Photons and electrons/positrons exhibit a mostly continuous distribution up to an energy of around 100 GeV. These high energy photons originate mostly from the decay of π^0 . The only visible peak for photons is located at 511 keV, which represents the annihilation energy of positrons. Charged hadrons show a distribution with a peak in the GeV range and more particles reaching a few hundred GeV. The neutron distribution exhibits 3 characteristic peaks in this plot. The first most recognizable peak is found in every location of the experiment, representing the distribution of thermal neutrons at very low energies in the meV range. The second peak is formed around an energy of 1 MeV as a consequence of evaporation processes. Neutrons around this energy have an impact on the performance of silicon-based electronics. The third is called “quasi-elastic peak” and can be seen around an energy between 90 and 100 MeV. In a non-lethargy current density plot, the peak is displayed as a “shoulder”, i.e. a plateau which is followed by a rapid drop in current versus higher energies. This plateau is formed due to a combination of two effects. In most materials the neutron total cross section generally decreases with increasing particle energies until it reaches a minimum or a lower plateau at about 200 MeV. As a consequence, the neutron fluence around 200 MeV is minimally attenuated compared to lower energies. An additional effect can be observed in the production of lower energy neutrons, which also decreases rapidly towards higher energies in this region around 200 MeV. Both effects help to form a plateau-like shape in the current before the overall fluence drops again because of the natural fluence decrease when approaching higher energies. These effects are also combined with a more rapid decrease of the cross section in the range preceding this peak between about 50 and 100 MeV, which enhances the shape of the phenomenon, producing the quasi-elastic peak in the lethargy plot [54].

In the case plotted in figure 43 which is close to the beam, the 1 MeV peak and the quasi-elastic peak are relatively large in relation to the thermal peak. With increasing distance to the beam line, the forward-directed high-energy particles decrease in number and the thermal peak gains in relative size. An example for a situation like this can be seen in figure 44, which plots the same fluences as in figure 43 for a location below the Tracking stations. In between Tracking Station 1 and 2 (and also in between 2 and 3) a knee-high U-support made of aluminum for supporting the beam protection structure during extended LHC Shutdowns is mounted on top of the rail platform on which the Outer Trackers can be moved. On the top middle of this U-support, active and passive sensor boxes are mounted next to the OT front-end electronics, which is the reason for scoring spectra at this position. The location between station 1 and 2 is also partially shielded from a direct line of sight to the IP by the iron and aluminum body of the LHCb dipole. As a result, the whole charged hadron fluence as well as higher energy photons and electrons/positrons are heavily reduced in comparison to neutrons, which are not as susceptible to the shielding effect of the yoke and coils of the magnet. Nonetheless, the neutron spectrum is significantly changed as well in comparison to the location next to the BLS. Even though the quasi-elastic peak is reduced by roughly two orders of magnitude, the thermal neutrons have only decreased by a factor of 2-3. Another interesting observation is to be made from the error bars of the charged hadron distribution: although the error for general fluence scoring when using Cartesian binning as discussed earlier is quite small in this location, the low number of particles leads to comparably high error bars for individual energy bins, demonstrating that even with a very high number of calculated primary collisions the available amount of detail and resolution in these simulations is rather limited.

While the two examples provided here represent rather extreme varieties of the LHCb radiation field, other locations in and around the detector show all kinds of intermediate stages between those two, and possibly some light variations of shapes due to the influence of magnetic fields. The differential fluences scored for this thesis are mainly used to confirm and illustrate the expected properties of the forward-directed radiation field in LHCb. When analyzing the behavior of dosimeter in later sections, this information will be relevant. In eventual future applications, spectra similar to these can be of use for further studies such as considering the activation of materials during operation.

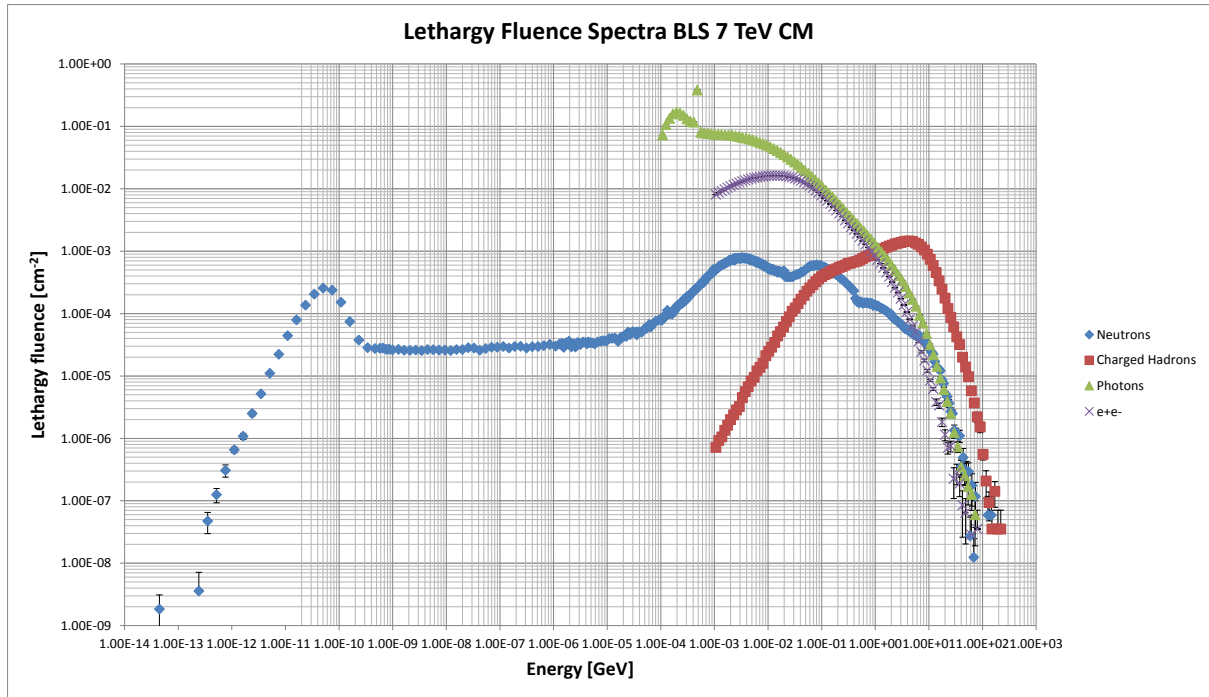


Figure 43: Lethargy fluence per collision per cm^2 for 7 TeV CM at a distance of around 15 cm above the beam line at the upstream wall of the VELO alcove. Due to the very low angle and only around 2m distance to the IP, the field is dominated by particles with very high energies.

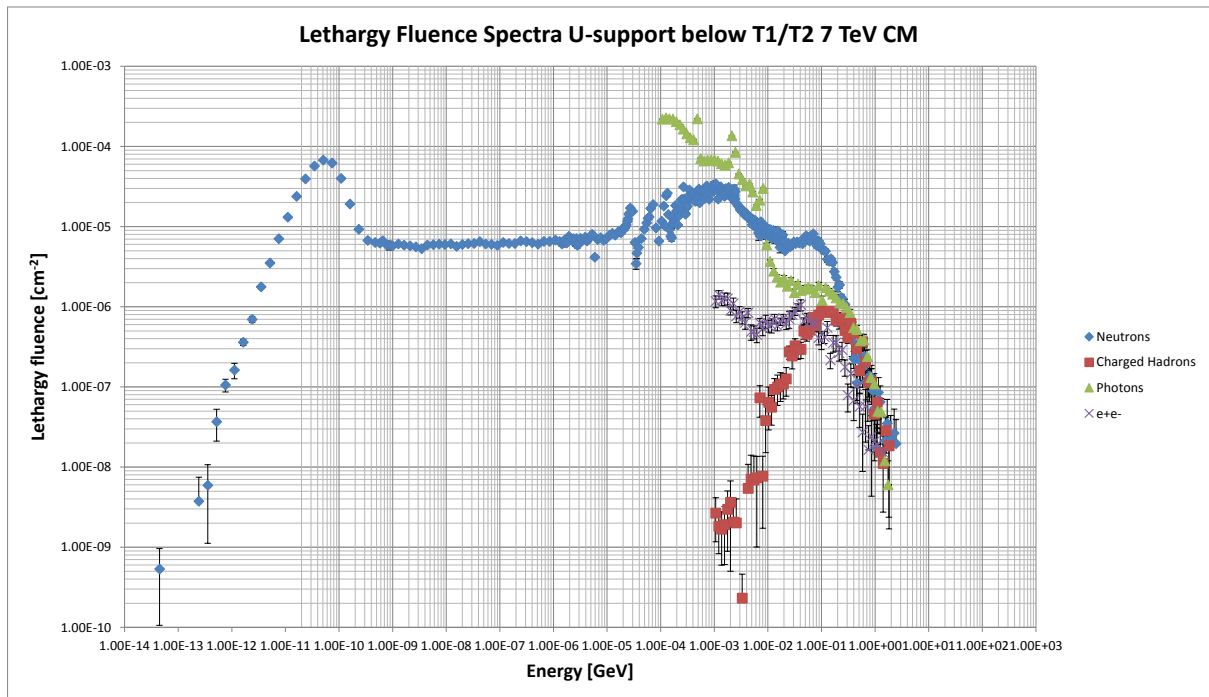


Figure 44: Lethargy fluence per collision per cm^2 for 7 TeV CM at a distance of around 2.5 m below the beam line in between Tracking Stations 1 and 2 next to some of their front-end electronics. In the real detector, a knee-high aluminum U-support is located on top of the guiding rails at this position on which active and passive sensor boxes are placed. Fluence values as well as the shape of their distribution differ greatly from areas closer to the beam. On one hand this location lies at a large angle to the IP, but on the other hand it is partially shielded by the yoke of the LHCb dipole, explaining the extraordinary low fluence of charged hadrons.

5 EVALUATION OF DOSIMETERS

In the following sections, the passive and active measurements performed with the various sensors that were introduced earlier will be analyzed. Starting with passive measurements, the analysis will concentrate on the results from the sensors placed inside and around the calorimeter detectors. Due to the high aggregation of sensors and their systematic placements, this area is very suited for the aforementioned analysis. The remaining passive sensor measurements from dosimeters that are placed mostly at the location of electronics are not mentioned in the section about calorimeter measurements. They will be discussed later in tandem with the measurements of active sensors that are placed in similar locations.

The analysis of active sensors will follow afterwards and will be partially based on the reliability assessment of passive sensors gained from the calorimeter measurements. It will be separated into three larger sections. The first section will comprise comparisons between all sensors on the front of the first muon detector M1, where sensors of all types are placed in a cross-shaped layout in order to get a detailed insight on the evolution of the radiation field inside the experiment. The second section will concentrate on the regions with the highest exposure to radiation that are not part of the calorimeters. The third and last part will entail a more detailed look into the less exposed regions at the edges of the detector, where active and passive sensors are placed in similar locations to observe the deposition of dose on many of the electronics around the experiment.

5.1 EVALUATION OF PASSIVE MONITORS BASED ON CALORIMETER MEASUREMENTS

Before the start of operation in 2009, the LHCb experiment calorimeter system was equipped with a variety of passive dosimeters in between its detector components as well as around the locations of some of its electronics. These sensors provide an independent input to measurements of cumulative radiation damage of detector components during operation. As the intended purpose of the calorimeters is to measure most particles generated from the proton-proton collisions by stopping them in their massive lead and iron structures, the resulting interactions of radiation with matter cause their surroundings to become one of a few areas in the experiment that are experiencing exceptionally high dose rates. This exposure to radiation will in turn induce damaging effects in the scintillating fibers and tiles as well as in electronic components of the detectors. Standalone measurements from passive dosimeters can help to correlate damages to the total integrated dose.

Two spare ECAL modules have been placed in an area in the tunnel upstream of the experiment (RB84) to predict the damage to the modules of the electromagnetic calorimeter (ECAL), as they are exposed to the highest radiation levels years ahead of time with respect to those in the ECAL. These modules are situated very close to the beam pipe, where the dose rate is expected to be higher by a factor of 2 to 3 than the rate in the center of the calorimeter. This allows to investigate the radiation damage to these types of modules as expected in the experiment after several years of data taking. For this purpose, the modules in the tunnel have been equipped with passive sensors of the same type used in the actual detector.

The majority of dosimetry sensors, including those on the modules in the upstream tunnel, has been collected and measured at the end of 2011 and again at the beginning of Long Shutdown 1 (LS1). The results of these measurements will be discussed in terms of applicability considering the variety of radiation scenarios encountered in the experiment. At the same time, efforts have been made to simulate the radiation field in the experiment with the FLUKA Monte Carlo code. The results of these simulations which aim to reproduce the irradiation conditions during the two measurement campaigns will be compared to the measurements.

All dosimeters discussed in this thesis were calibrated with ^{60}Co γ -radiation. However the proton-proton collisions at LHCb produce an unprecedented complex mixed field that is most heavily influenced by hadron

radiation, which necessitates a careful evaluation of the behavior of the type of dosimeter used. The results are analyzed focusing on the explanation of discrepancies between the different dosimeter types and assessed in terms of reliability. In addition, measurements and simulation results will be crosschecked against each other in order to determine their strengths and weaknesses. Furthermore, the final purpose of this analysis of the radiation environment around the calorimeter structure is to improve the understanding of the general evolution of the radiation field in the experiment by combining measurement with simulation.

It will be demonstrated, that, while not all employed dosimeters yield useful measurements, reliable dosimeters are available and in use for the whole dose range encountered in the experiment. The agreement between simulation and measurements that are considered reliable will be shown to stay within a factor of 2 inside the experiments' acceptance.

5.1.1 MEASUREMENT SETUP

Most particles generated from the proton-proton collisions in LHCb are absorbed in the massive lead and iron structures of the calorimeter detectors, leading to exceptionally high dose rates in its vicinity compared to other subdetectors. Measurements can help to correlate damages on the detector to the total integrated dose. In addition, evaluation efforts of sensors in this environment profit from exposure to a large range of different compositions of particles at various energies.

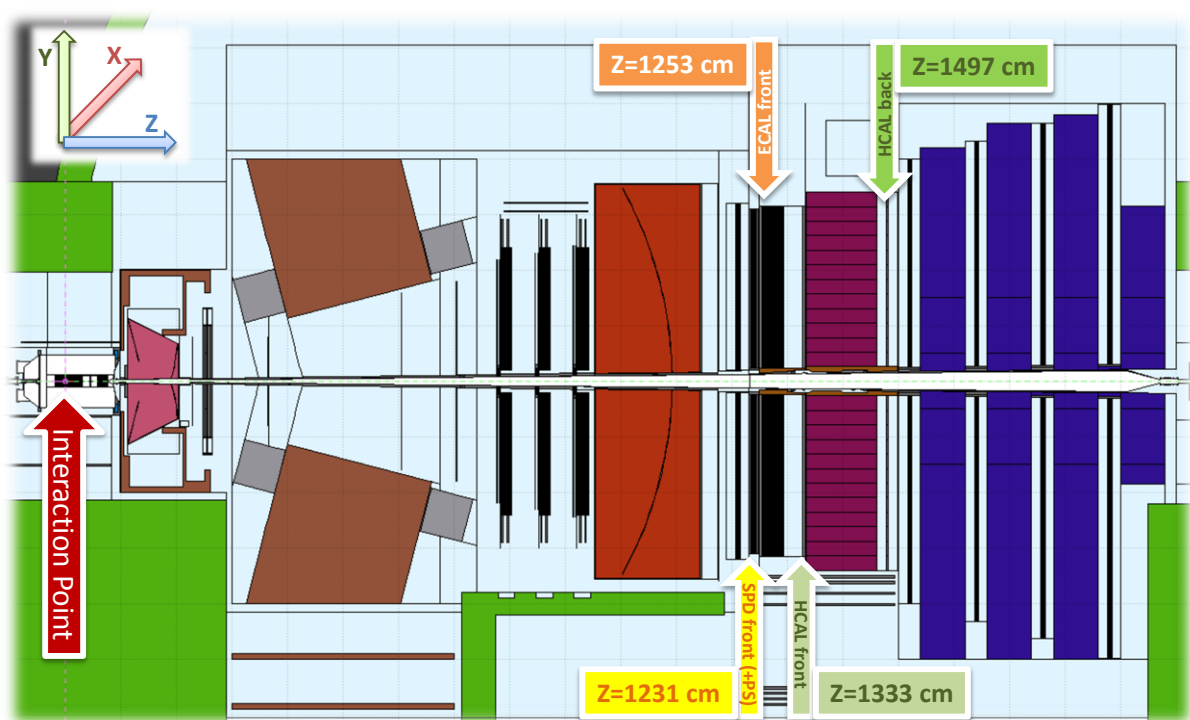


Figure 45: Schematic side view of the LHCb experiment seen from C-side showing the locations of the 4 detector planes that accommodate passive sensors. The positions of the SPD, ECAL, HCAL front and HCAL back plane are indicated by arrows. Their distance to the interaction point based on the LHCb coordinate system is given in cm.

In order to measure the development of dose in the calorimeter detectors, 17 boxes with 4 different types of sensors are placed on each of 4 planes perpendicularly to the direction of the beam. These planes are the back as well as the front of the Hadronic Calorimeter (HCAL), the front of the Electromagnetic Calorimeter (ECAL), and the front the Scintillating Pad Detector (SPD). Figure 45 shows a sketch of the side view of the experiment, with the locations of the measurement planes indicated.

The coordinates used throughout the thesis are those of the LHCb coordinate system, with its origin inside the Vertex Locator detector (VELO) [4], as mentioned in section 1.3. The cavern housing the LHCb experiment is pragmatically divided into 2 halves, separated vertically by the beam line. The part that is accessible from the PZ elevator shaft is called A(ccessible)-side, whereas the side toward the cryogenic installations, which are located on the inside of the LHC ring, is colloquially termed C(ryogenic)-side [55].

Almost all of the sensors are placed on the A-side on the lower quarter of each plane. Only one sensor per detector plane is positioned on the C-side close to the center, as shown in figure 46 and figure 47. The main reason for using mainly the lower quarter A-side planes for placement is their better accessibility compared to the other quarters, especially during shutdowns when maintenance is performed on the detectors. This accessibility combined with a lower risk of objects or persons falling from higher positions make it also a preferable location in matters of safety. Due to the expected symmetry of the radiation field in the XY plane, this layout is sufficient to estimate the exposure of symmetric positions on the whole layer.

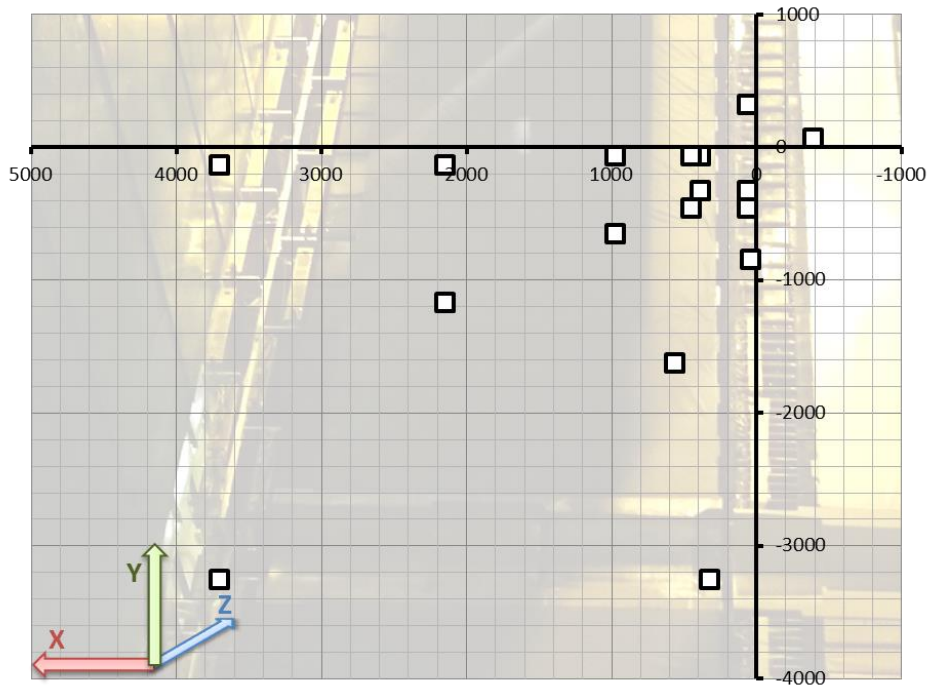
In many of the plots in this thesis, boxes or specific sensors in those boxes are referred to by the serial number S_n of that box. These numbers are based on the long-form serial number, which has the form of e.g. 4CRCERPW000023. The short form version of this example is S_n23 . The mentioned serial numbers always refer to the last 2 to 3 digits of the long form serial number of a box.

The x and y coordinates of the sensor boxes on all four planes of the calorimeters are similar to be able to compare them to a degree. The central regions around the beam are equipped with a larger number of sensors, because the dose values change within smaller distance than at the edge of the outer acceptance. However for practical reasons, these positions are not identical on the different planes. For example, the inlets for dosimeter boxes on the cover plates on the front of the ECAL had to be designed around the layout of the fibers that are exiting the modules directly behind the cover. The front of the SPD and the back of the HCAL had similar constraints that depend on the detector structures behind the cover plates, whereas the flat black paper envelope on the front of the HCAL did not pose any restrictions on the installation.

All dosimeters are positioned at least a few cm away from the central plug around the beam pipe. Simulations need to be used to estimate the dose in areas that are not covered by sensors. This is especially delicate at the edge of the beam plug, where the maximum dose will be deposited according to physics expectations and corroborated by the FLUKA simulations. Nevertheless, the chosen sensor positions on each detector plane provide a reasonable sampling of the situation.

HCAL backside

□ Sensor Positions [mm]



HCAL front

□ Sensor Positions [mm]

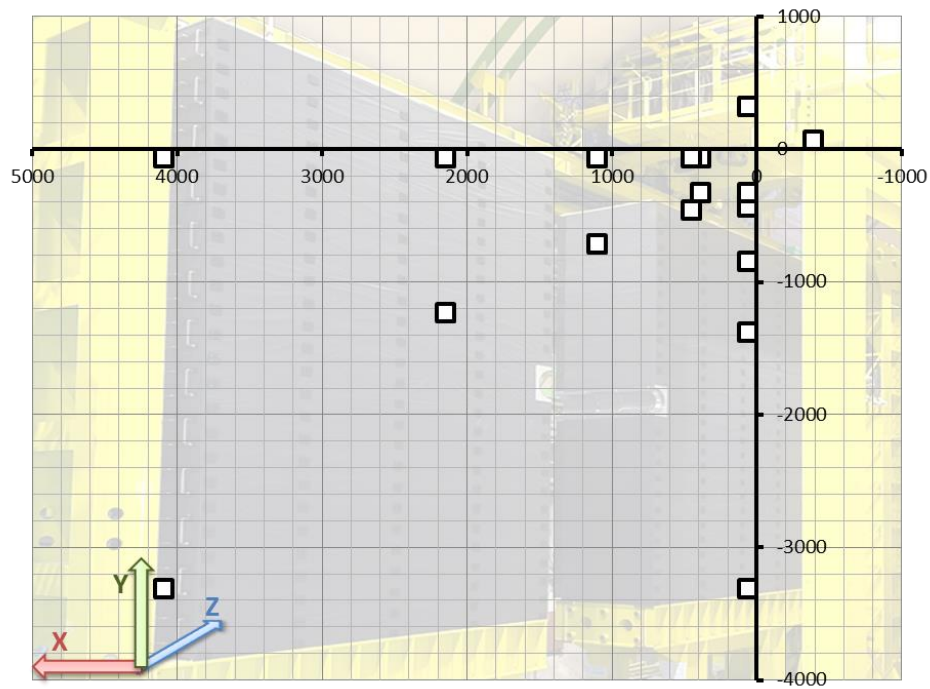
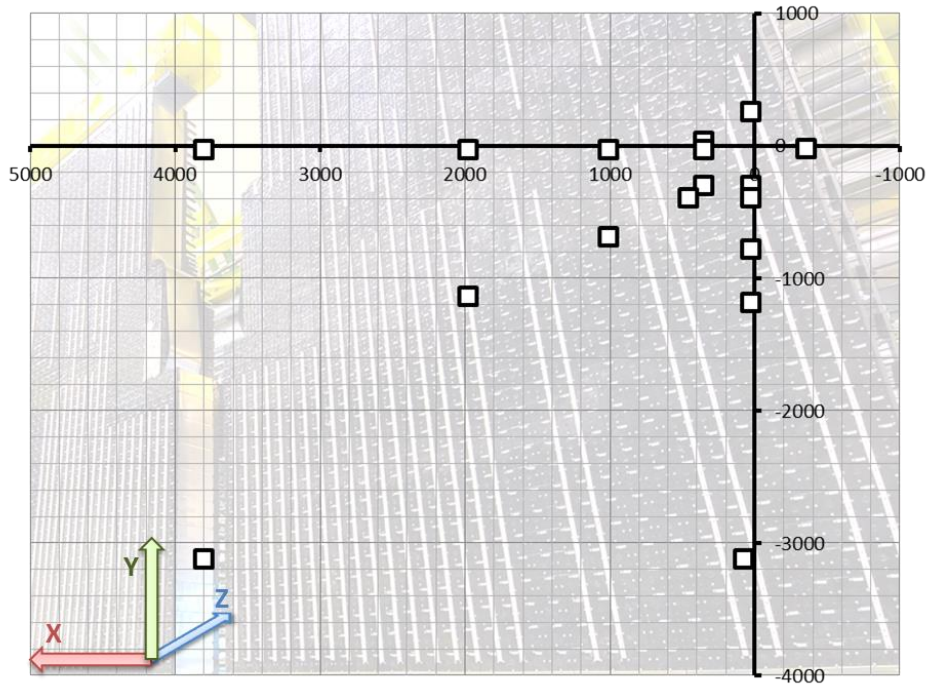


Figure 46: Positions of the sensor boxes on the back plane (top) and the front plane (bottom) of the HCAL detector based on the LHCb coordinate system.

ECAL front

□ Sensor Positions [mm]



SPD front

□ Sensor Positions [mm]

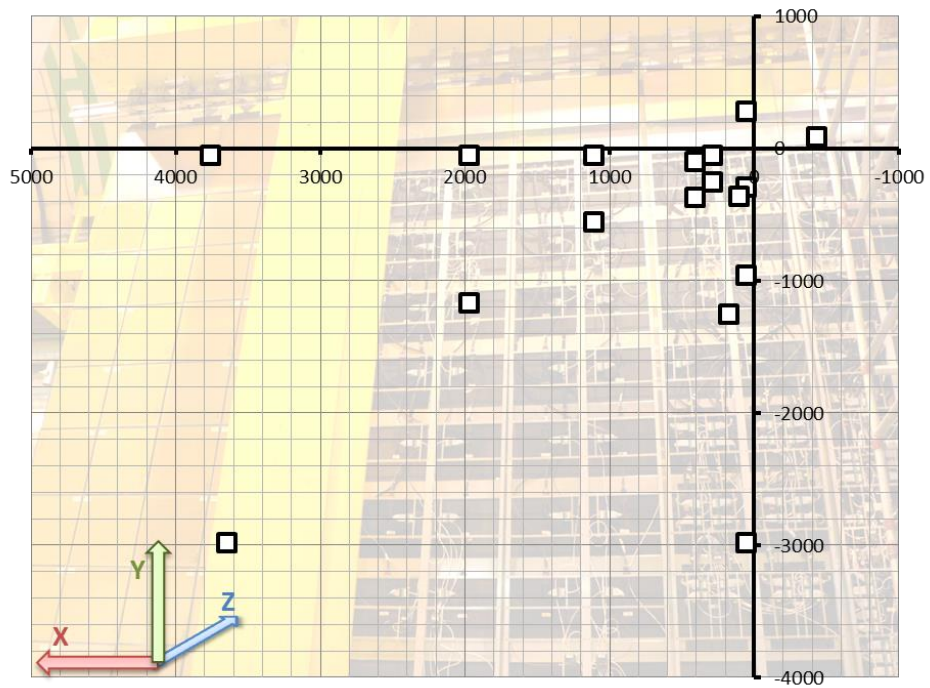


Figure 47: Positions of the sensor boxes on the front plane of the ECAL (top) and the SPD detector (bottom) based on the LHCb coordinate system.

Additional sensor boxes have been placed next to electronic racks at the top of the calorimeter support structure, and at the outer edges on the top and bottom of the PreShower (PS) and Scintillating Pad Detectors, which are positioned directly next to each other. These sensors' locations were chosen to ascertain that the present electronic installations are protected from exposure that would exceed their tolerance to radiation. None of these electronic racks are expected to receive integrated dose values above a few Gy during the combined LHCb operation in Run1 and Run2. Some of these boxes were collected during LS1 for the first time since their installation in 2009. A few others had to be left in place, because access would have necessitated a partial disassembling of some calorimeter detectors, which was not an option in LS1.

In the tunnel right behind the upstream wall of the LHCb cavern, a pair of ECAL modules was placed next to the beam pipe during Run1. The purpose of this setup is to expose these modules to a radiation field that is similar to the field surrounding the actual ECAL, but at a higher dose rate than the one which the most exposed inner modules in the experiment are subjected to. The mixed field in front of the last corrector dipole before the experimental cavern, which can be seen in figure 48 (right side) in red, was estimated via FLUKA simulations in [56] and deemed to be suitable for this endeavor. A big advantage of this location versus other irradiation facilities (including at CERN) lies in the closer similarities of the properties of the mixed field at this position with the one present in the detector. In addition, the placement of the modules in the tunnel doesn't interfere with other equipment and the location can be used for long stretches of time to achieve the desired ageing effects. The analysis of these modules allows to predict the damage due to radiation, so that future maintenance or potential replacements of calorimeter modules can be planned ahead on a reasonable timescale. Five dosimeters were attached to these modules, with two boxes on the front and back of each module and one box on a slightly elevated position between the beam pipe and the innermost module, as depicted in figure 48. The dosimeters were read out and replaced at the same times as those within the calorimeters. Further information on this irradiation can be found in [56].

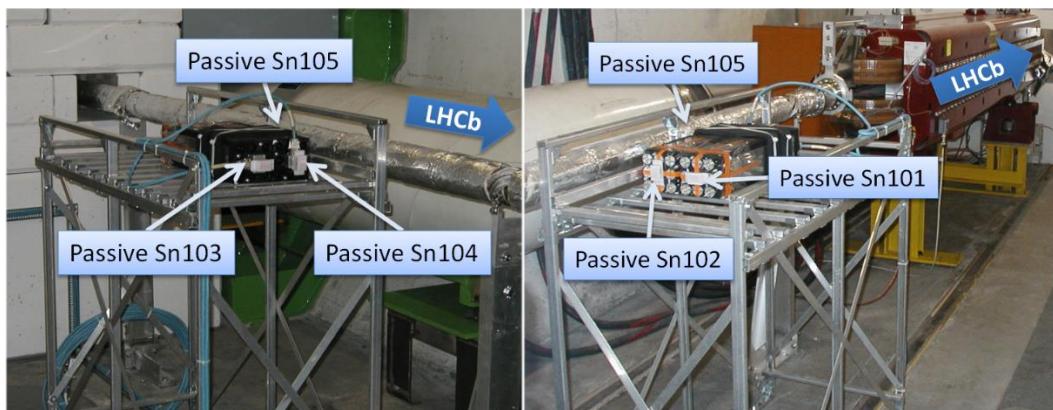


Figure 48: Layout of passive monitors on the ECAL test modules in the tunnel upstream of the LHCb experiment seen from the direction of the experimental cavern (left side) and towards the cavern (right side). The sensor with number *Sn105* is placed on the upper edge of the module, between the module itself and the beam pipe. In the back of the picture, the last corrector dipole before the LHCb experiment can be seen in red. The identification numbers in the form *Sn101* that is used in these figures are derived from their description in the LHCb equipment traceability database. *Sn* stands for Serial Number, whereas the actual number is taken from the last 3 digits of their Equipment ID.

5.1.2 SIMULATION PREDICTIONS

The LHC produces proton-proton collisions at unprecedented energies, resulting in very complex radiation fields inside large experimental structures such as LHCb. In order to get an estimate about the expected dose range and particle distribution before the start of the experiment, detailed Monte Carlo simulations of the effects of these collisions inside the experimental cavern are required. After initial studies, the simulation is used to fill in the informational gaps in between the points of measurement in the experiment. In addition, the simulation is expected to aid in understanding deviations in the dosimetry used in LHCb caused by effects of these unprecedented particle and energy distributions.

FLUKA Simulation studies from 2003 [47] based on an early but already very detailed geometry of the LHCb experiment predicted that the total integrated dose deposited at different points of the experiment will vary up to 9 orders of magnitude over the course of its operation. As a consequence, different types of passive dosimeters are used in combination in the experiment, in order to cover the indicated dosimetric range from mGy to MGy.

The FLUKA studies performed in the course of this work in 2012 and later in 2014 with an increased number of primaries use an improved updated geometry description as described in the previous sections.

Both studies indicate that even within the limits of the calorimeter structure, the expected total integrated dose over the course of a year-long operation necessitates a combined solution of low-level and high-level dosimetry to obtain useful measurements. According to the most recent simulation results of the whole experimental area, the lowest and highest expected dose values are located on the downstream side of the hadron calorimeter, and the upstream face of the electromagnetic calorimeter, respectively.

In figure 49 and figure 50 simulated dose values around the lower quarter on the A-side of the backside of the HCAL and the front of the ECAL are shown, estimated for the running conditions of 2011 with proton-proton collisions at 7 TeV in the Center of Mass (CM). As the default output of FLUKA simulations for most estimators is given per collision, these values had to be scaled accordingly.

The positions of the dosimeters are marked with white squares. The bin size used for scoring the simulations results over the whole experimental area is $20 \times 20 \times 20 \text{ cm}^3$ as previously indicated. The inner volume of the calorimeter detector (1 m from the beam) was also analyzed using a smaller grid of $5 \times 5 \times 5 \text{ cm}^3$. Each bin shows the averaged value of the estimator that was registered. By scaling the results to an integrated delivered luminosity of 1.22 fb^{-1} as the experiment received in 2011, an illustration on the range of the dose distribution within the calorimeter detectors can be obtained.

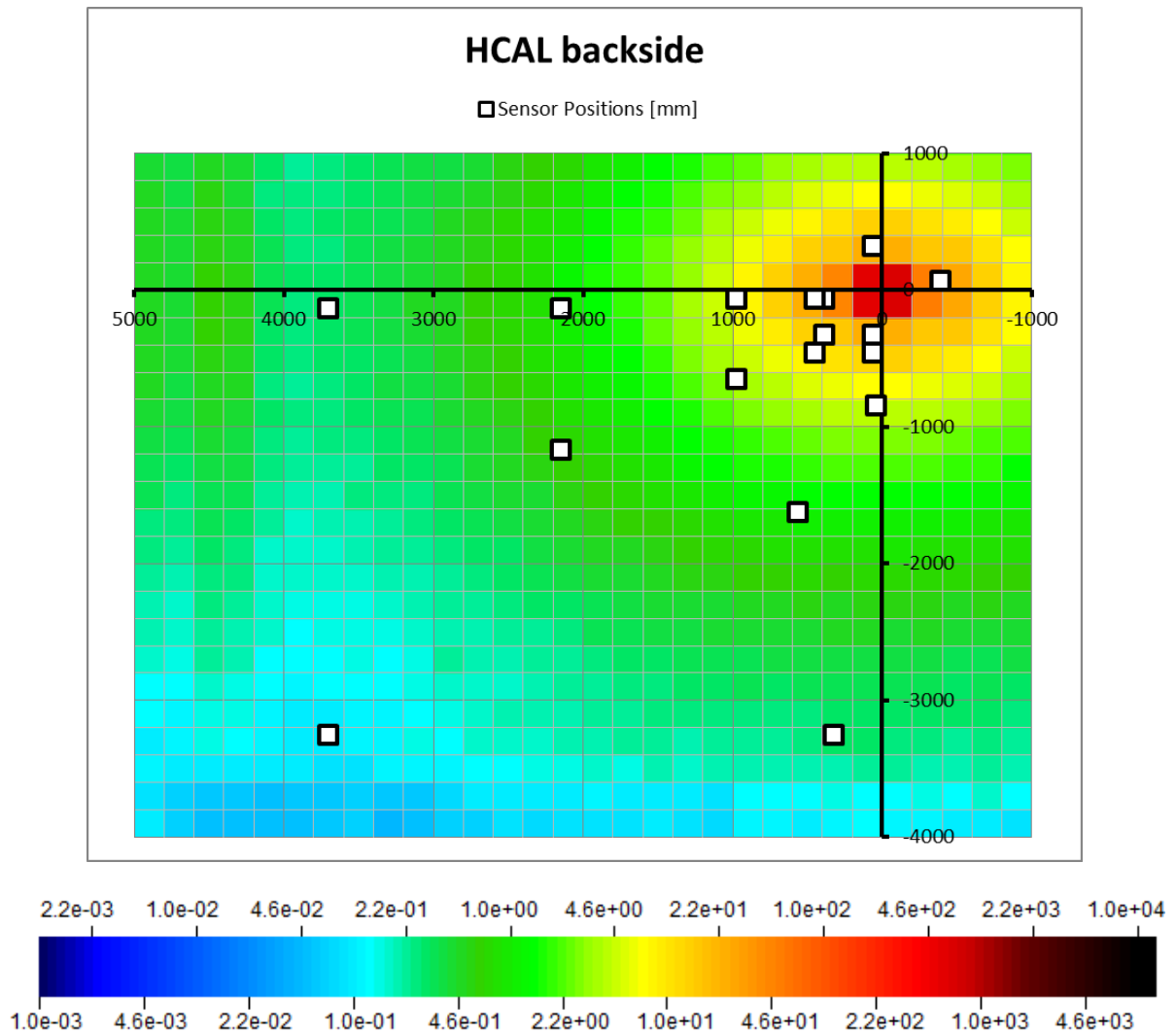


Figure 49: Illustration of the positions of dosimeters (white squares) in mm at the back plane of the HCAL. The background consists of a FLUKA simulation result of total integrated dose in Gy for 1.22 fb^{-1} at a collision energy of 7 TeV CM, with a bin size of $20 \times 20 \times 20 \text{ cm}^3$.

At the back of the HCAL, the detector itself works as a massive shielding wall against secondary radiation coming from the direction of the interaction point, keeping dose levels generally low compared to the rest of the detector. In particular at dosimeter locations along the outer edges of the detector, this means that the dose/ fb^{-1} of delivered luminosity would not exceed 1 Gy, which cannot be measured reliably with the high-level dosimeters available to us, calling for a dedicated low-level dosimetry solution.

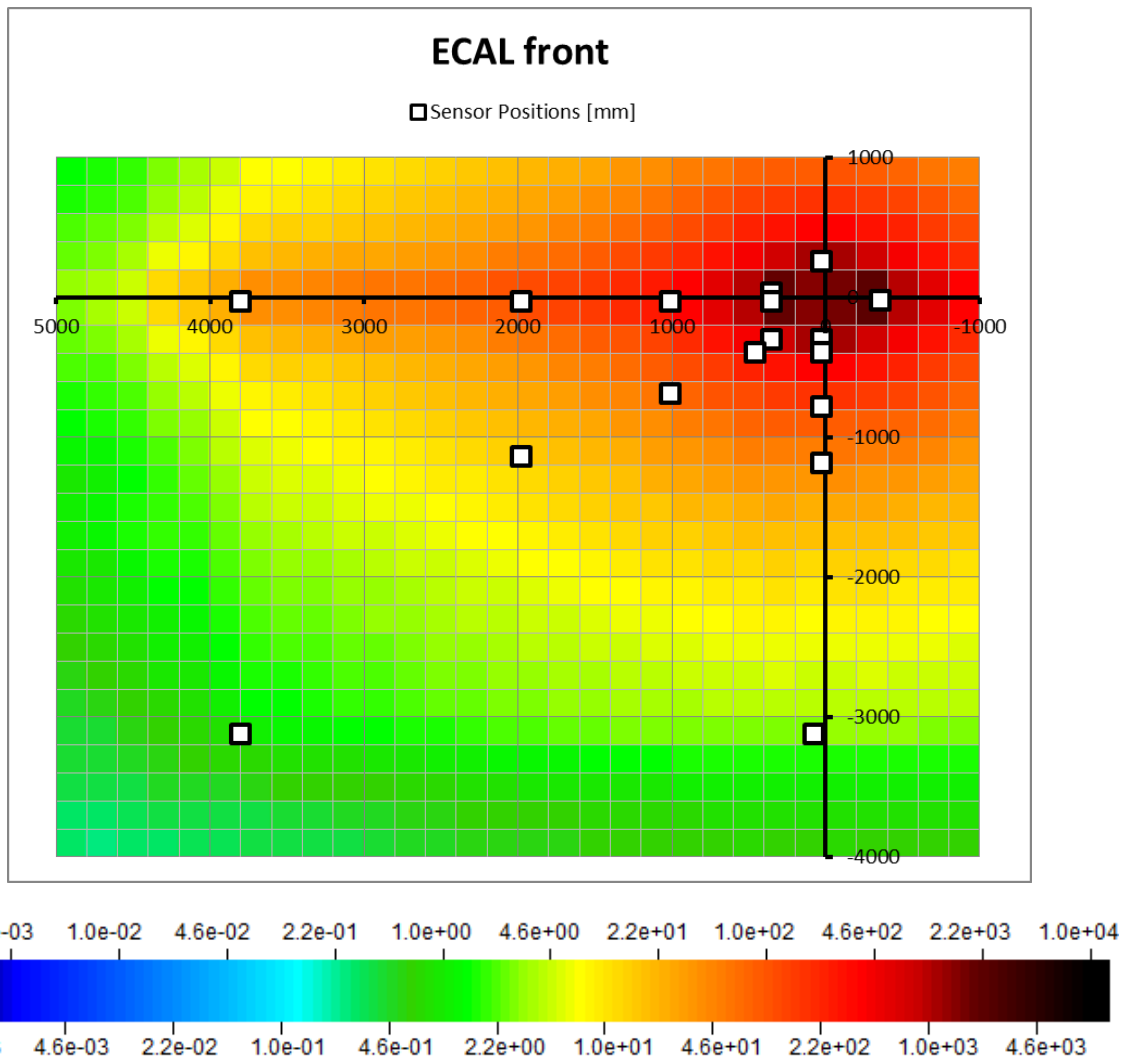


Figure 50: Illustration of the positions of dosimeters (white squares) in mm at the front plane of the ECAL. The background consists of a FLUKA simulation result of total integrated dose in Gy for 1.22 fb^{-1} at a collision energy of 7 TeV CM, with a bin size of $20 \times 20 \times 20 \text{ cm}^3$.

The front of the ECAL experiences a deliberately triggered shower of secondary particles. This shower is mainly caused by interactions of high-energy particles emerging from the collisions with the SPD/PS (ScintillatingPadDetector / PreShower) structure, composed of a lead plate with a thickness of about 1.2 cm sandwiched between the upstream SPD and downstream PS detectors. This lead is the first deliberately dense material the secondary particles from the collision encounter. Subsequently, the number of interactions of particles coming from the collision with the SPD/PS is considerably higher than those occurring within the first 10 m from the collision, where only light materials are used to keep unwanted influences on particles to a minimum. In turn, this increase of interactions leads to intense secondary cascades that generate enough electromagnetic particles to deposit the largest amount of dose within the calorimeter detectors on the front face of the ECAL. Since the particles with the highest energies are forward-directed, the highest dose on the front of the ECAL is deposited right next to the beam pipe. With its intermittent layering of lead plates and scintillating material, the ECAL itself already constitutes a kind of shielding structure in itself, which results in significantly lower dose on its backside, at the front of the HCAL.

5.1.3 SPECIFIC PROPERTIES OF RPL DOSIMETERS USED UNTIL LS1

Before measurement results of the other dosimeter types is presented in the subsequent sections, the reasoning to exclude RPL measurements from further analysis and cross-checks will be explained in this section. As mentioned in section 2.2.2, damages to the crystal surfaces have been discovered during readout in 2012, which were able to influence measurements in a negative way. They are suspected to also have influenced measurements made during 2011. Since the readout was performed by an external contractor who stopped his collaboration with CERN shortly after, this cannot be verified. However, readouts made by this contractor at the end of 2011 are also suffering from other disadvantages that are mainly connected to the equipment used. The equipment in question is a very old and outdated instrument from Toshiba, shown in figure 51.



Figure 51: RPL readout equipment used by the CERN contractor in 2011.

This equipment bases its conversion of RPL light signal into dose values on a calibration curve that was established using a ^{60}Co source. When RPL dosimeters are exposed to a mixed field including hadrons, they can emit a readout signal that is higher than the maximum value of the γ -calibration curve, which is pictured in figure 52. These readouts are subsequently downscaled to the maximum read-out result, with a provided uncertainty of this value of a factor of 2 [57]. This leaves a large gap of uncertainty where readouts within a large dose range all read the same value, even if they actually received dose values that are several hundred Gy apart. In practice, this means that all LHCb dose measurements between 700 Gy and 1400 Gy were reported as exactly 700 Gy.

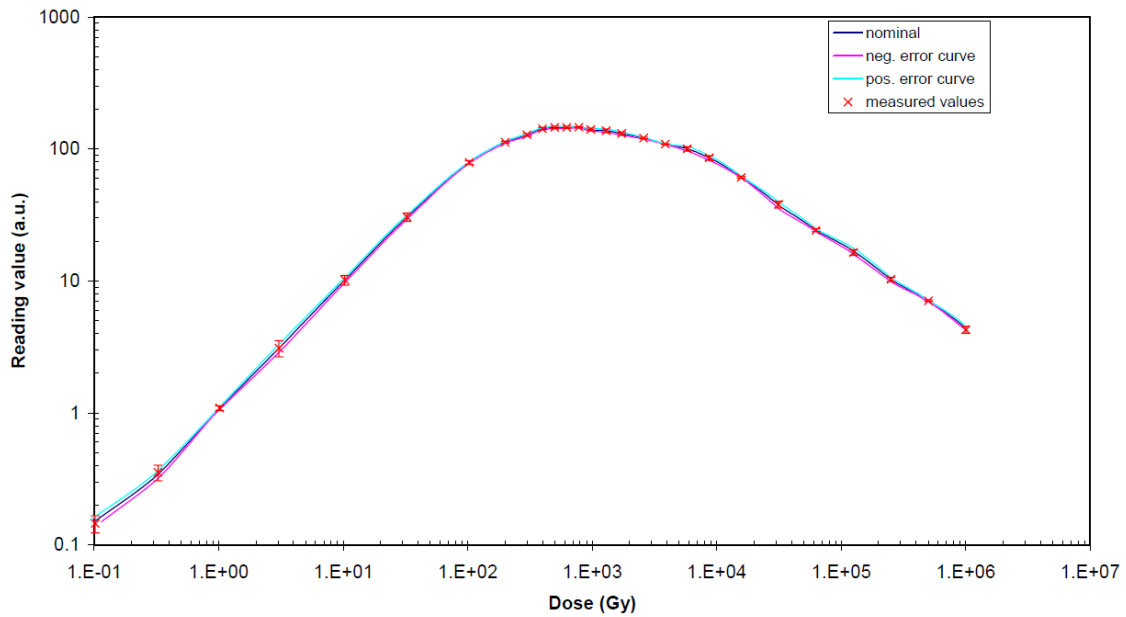


Figure 52: RPL calibration curve established with a Co-60 source

After the contractor ended his relationship with CERN in 2012, the readout machine became unusable because of a visibly degraded calibration. Technical difficulties related to the age of the equipment and the lack of replacement parts made the needed calibration impossible.

As a consequence, a new readout equipment developed by the CERN RP group [58] has been introduced in 2013. RPL dosimeters that have been collected at the beginning of LS1 were read out by the author using this equipment.

Naturally, this newly developed measurement system takes into account the calibration based on light emitted by luminescence centers of the crystal. However in addition to this traditional measurement, it also considers a calibration based on the transmission of light, as the crystals become less transparent with increased exposure to high dose. This analysis of the transmission characteristic is able to bridge the previous range gap between 700 Gy and 1400 Gy for dosimeters exposed to a mixed field. A simple γ -calibration of luminescence measurements cannot provide such a conversion of the light signal into dose otherwise. This additional calibration curve, shown in figure 53 is based on reference dosimeters irradiated by ^{60}Co as well, but it nevertheless improves the usefulness of RPL dosimetry within the aforementioned range.

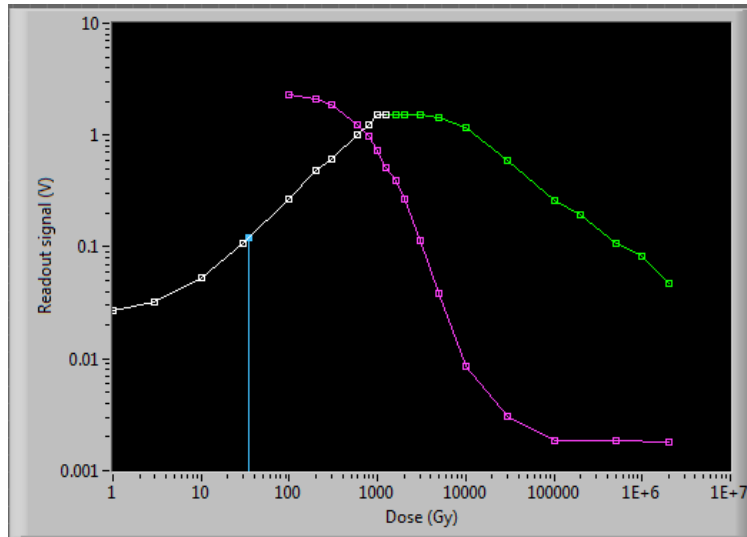


Figure 53: Calibration curves for the RPL readout equipment developed by the CERN RP group. The green/white curve represents the traditional calibration based on light emitted by luminescence centers. The purple curve represents a calibration based on the transparency of the crystal. A combination of both is necessary to convert RPL and the transmission signals reliably into dose between Gy and MGy.

The newly developed process for the readout and the equipment that is used to perform it are currently under review for patenting. Unfortunately, no additional details can be provided because of a non-disclosure agreement.

5.1.3.1 RPL SENSOR DEFICIENCIES (CRYSTAL DAMAGE)

As already mentioned, RPL dosimeters used during 2012 have already been used several times before by the CERN RP group, resulting in visible damage on some of the crystals, e.g. splintered surfaces or even large cracks along the length of the crystals. An example can be seen in figure 54.

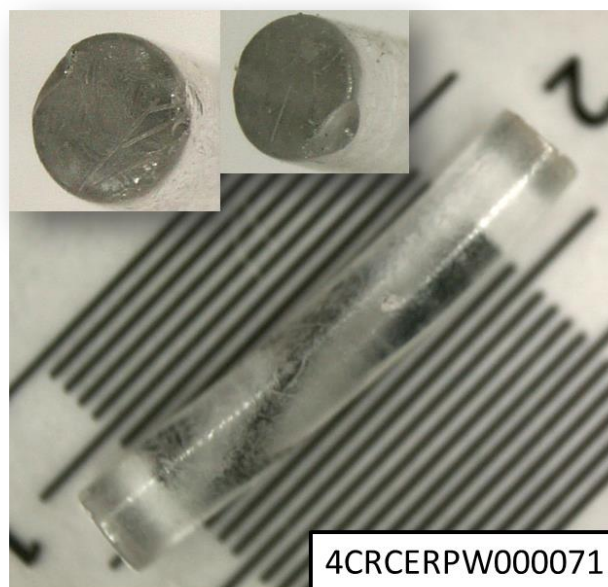


Figure 54: A photograph taken with an electronic microscope of an RPL dosimeter with severe surface damage and an overall bent shape.

These damages have an influence on the transmission and reflection of light on the crystal that directly affects the measurement of the new readout system. They can be categorized into surface damages, volume inconsistencies and deformations.

Examples of visibly damaged RPL dosimeters are shown in figure 55 and figure 54 to illustrate the generally occurring defects that can be observed with different degrees of impact on most of the RPL dosimeters used in the LHCb experiment. The difference in measurements compared to the more reliable Alanine measurements range from around 25% to a factor of 2 and above, depending on the impact of the defect on the applicable measurement method. The corresponding measurements to these pictured sensors can be found in Table 4, alongside a short description of the encountered defects.

Visible damage of the surface of a crystal leads to a diminished transmission of UV LED light into the crystal and of excited light coming from the crystal interior. RPLs that received a dose producing a signal in the transmission range of the readout procedure are therefore showing higher dose values compared to Alanine results when measured. Elongated cracks along the cylindrical shape, as well as bends along a crystal might also have an effect on its reflection of light and therefore on measurements in the lower range below 700 Gy.

When examined under the microscope, some of the cylindrical dosimeters had a slightly bigger radius, up to 0.1 mm more than the average crystal. Because of this increased volume, said crystals are emitting a higher amount of luminescence light than their standard counterparts, resulting in an increased readout signal. Sensor number 4RCERPW000060 for example shows a larger diameter between 0.1 and 0.12 mm compared to the average crystal, translating to almost a cubic millimeter or 25% more volume, which in turn yields more scintillation photons during measurements. Also dosimeters from passive boxes 4RCERPW00003 and 4RCERPW000034 are affected by a slightly larger volume, which is also indicated by their small positive deviation from Alanine readout signals.

Sensors number 4RCERPW000014, 4RCERPW000046 and 4RCERPW000071 featured strong deformations and are sometimes visibly bent, as can be seen in figure 54. These dosimeters also showed readout signals that were higher than expected. While the reason for this increase of the signal is not entirely clear, it is possible that reflections during the readout process, which would not occur on a straight standard dosimeter surface, could be responsible for directing more light into the photomultiplier tube than intended. Sensor number 4RCERPW000046 is an exception however, because its visible surface damage and a huge crack along the length of the cylinder obstructed the passage of light enough to lead the readout equipment to assume a signal within the transmission spectrum that begins around 700 Gy. Alanine measurements suggest a dose slightly below 500 Gy.

New Japanese RPL crystals of a slightly bigger size are currently being used for High Level Dosimetry by the RP group at CERN. These crystals feature very smooth surfaces, which is very beneficial to the accuracy of the newly introduced transmission measurements.

Examples of damaged crystals and the deviation of their measurement results from reliable Alanine measurements are listed in table 4, together with the measurement results of both Alanine dosimeters in the same passive box. Alanine dosimeters from those boxes have only been measured once, because the accuracy of the readout device was deemed sufficient since results did not vary more than 1% after repeated measurements of some test samples. Due to a shortage on useable RPL dosimeters at CERN at the end of 2011, only one sensor was placed in each box for 2012. Therefore, and in contrast to Alanine measurements, each crystal was measured twice, with the crystal being flipped 180 degrees in between measurements so that its end planes change in the device. In some cases of a crystal showing visible damage, this can lead to a rather large change in the second measurement compared to the behavior of an intact dosimeter. RPL measurements from intact or at least less severely damaged crystals show values that do not change as much when turned

180 degrees, and the difference to Alanine results remains within reasonable margins of around 10%. Examples for such crystals as shown in figure 56 are listed in table 5.

At the time of measurement, no estimation of error was provided by the readout equipment, because the new readout program was still missing the error curves which are normally based on a series of measurements of reference dosimeters. According to the developer, the given error did not exceed 10% in the past.

Table 4: Several examples of RPL readouts that show increased dose measurements compared to their Alanine counterparts, due to visible surface damage or other defects. Some exemplary RPL crystals from this list are displayed in figure 55. Alanine measurements are the results of single measurements from both dosimeters that were in the box, whereas the RPL result is based on measuring the same crystal twice, turning it 180 degrees in between measurements so that its end planes change place in the device. The third column displays the ratio of RPL over Alanine results for the first and second measurement, respectively. The rightmost column gives a short description of the encountered defects.

Measurements from RPL crystals with high damage				
Passive Box Nr.	Alanine [Gy]	RPL [Gy]	Ratio RPL/Alanine	Damages
4CRCERPW000001	36.7	48.1	1.31	shattered surface
4CRCERPW000001	34.7	45.9	1.32	
4CRCERPW000014	13.9	16.8	1.21	rough surface,
4CRCERPW000014	13.5	17.2	1.27	splintered, bent
4CRCERPW000015	24.5	33.6	1.37	shattered surface
4CRCERPW000015	24.2	31.6	1.31	
4CRCERPW000021	717.7	896	1.25	rough surface
4CRCERPW000021	708.7	932	1.32	
4CRCERPW000027	574.3	768	1.34	rough surface,
4CRCERPW000027	557.2	688	1.23	splintered endcaps
4CRCERPW000030	35.5	66.3	1.87	increased volume,
4CRCERPW000030	36	61	1.69	elongated crack
4CRCERPW000034	111.1	170	1.53	increased volume,
4CRCERPW000034	111.9	166	1.48	rough surface
4CRCERPW000046	495.9	993	2.00	very rough surface,
4CRCERPW000046	481.9	986	2.05	splintered, bent
4CRCERPW000060	358.6	460	1.28	increased volume,
4CRCERPW000060	369	465	1.26	splintered
4CRCERPW000071	53.5	75.8	1.42	very rough surface,
4CRCERPW000071	53.5	76.2	1.42	splintered, bent
4IRCERPW0000102	1313	1890	1.44	rough surface,
4IRCERPW0000102	1272	1860	1.46	shattered endcaps

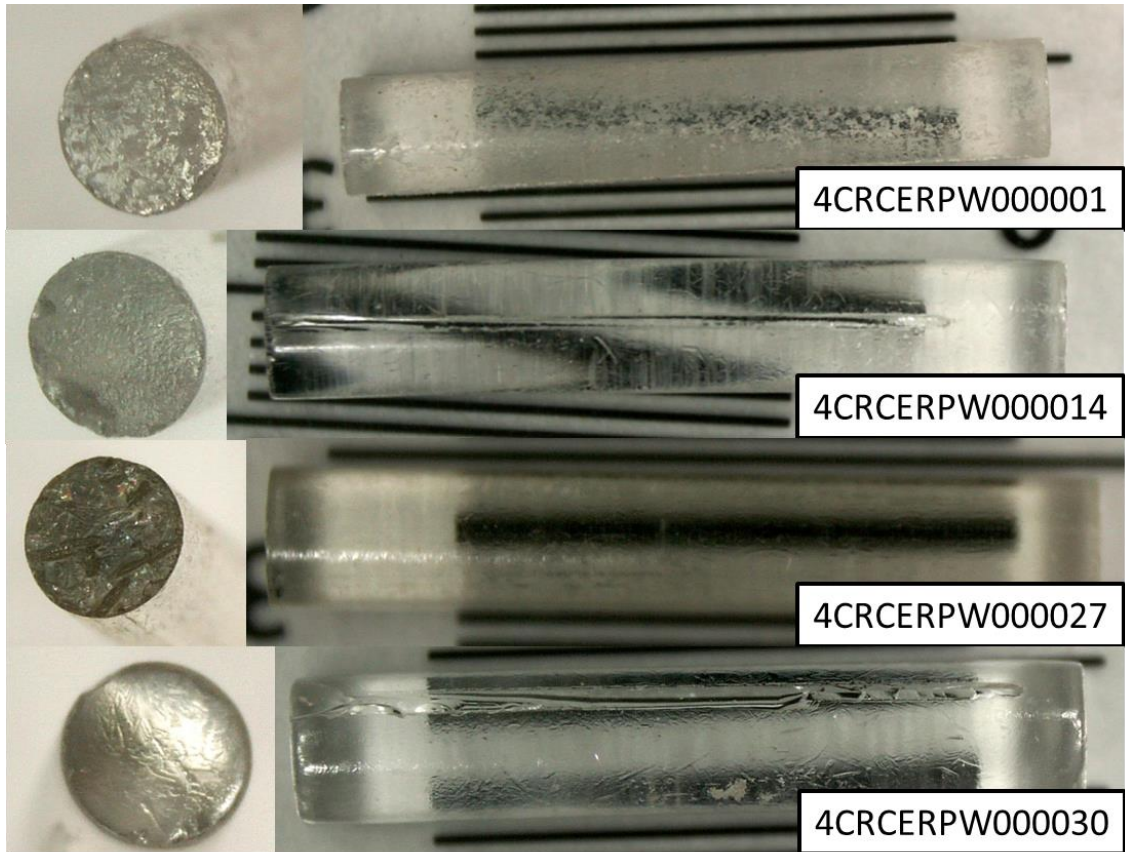


Figure 55: Four examples of RPL dosimeters with serious surface damage that is influencing the measurement. Each picture of one endcap on the left side corresponds to the dosimeter to its right. The variety of damages includes shattered or milky surfaces, as well as fissures and split edges. Some dosimeters also are slightly bent along the length of the cylinder, which might influence measurements due to a change in the reflection of UV light.



Figure 56: Two photos of the RPL sensor in passive box number 4IRCERPW0000016. Although small abrasions can be observed at the edges of the cylindrical crystal, the overall smoothness of the surface suggests a rather reliable outcome of the measurement. The difference to the Alanine sensor in the same passive box lies at around 12%.

Table 5: Three examples of measurements from Alanine sensors and RPL crystals where the crystals show less surface damage than the average dosimeter of the measured lot. The crystal measuring 28 Gy is shown in figure 56, the other two measured dosimeters are in a comparable state. Alanine measurements are the results of each of the two dosimeters that were in the same box which were measured once, whereas the RPL result is based on measuring the same crystal, turned 180 degrees between measurements. The third column displays the ratio of RPL over Alanine results for the first and second measurement, respectively.

Measurements from RPL crystals with low damage			
Passive Box Nr.	Alanine [Gy]	RPL [Gy]	Ratio RPL/Alanine
4IRCERPW0000016	25.5	28.2	1.11
4IRCERPW0000016	25.7	28.7	1.12
4CRCERPW0000048	430.3	405	0.94
4CRCERPW0000048	417.1	406	0.97
4CRCERPW0000042	2342	2210	0.94
4CRCERPW0000042	2418	2240	0.93

The total average of all RPL/Alanine ratios on each calorimeter plane, including the few severely damaged ones, is 1.01 at the back of the HCAL, 1.08 at the front of the HCAL, 1.05 at the front of the ECAL and 0.94 at the front of the SPD. These numbers would indicate a stronger sensitivity of RPL crystals to some particle types, most likely including hadrons of a given energy. According to the FLUKA simulation and to physics, hadrons accumulate in high numbers in front of the HCAL and slightly less so in front of the ECAL. However, these numbers cannot be fully trusted, since the various degrees of damage could have too much influence on the overall average. It is expected that the new Japanese RPL crystals which have been installed in the experiment during LS1 will be able to provide more reliable information on possible differences of sensitivity within the mixed radiation field of LHCb.

5.1.4 MEASUREMENT RESULTS

In the following paragraphs the analysis and possible explanation of some of the measurements taken during 2011 and 2012 is presented. The analysis covers Alanine dosimeters, as well as the TLD dosimeter types MCP-7 and MTS-7, at their relative positions within the LHCb coordinate system. It also includes estimates from FLUKA simulations that correspond to the same conditions that the sensors were exposed to. A detailed list of all measurement results can be found in the Appendix.

When the dosimeters from the calorimeter were collected for the first time since their installation, the experiment had received a delivered integrated luminosity of 1.26 fb^{-1} , of which 0.04 fb^{-1} were delivered during 2010, and 1.22 fb^{-1} during 2011 until the YETS in December. Measurements taken during 2012 until the beginning of LS1 correspond to a delivered integrated luminosity of 2.21 fb^{-1} . In total, 3.47 fb^{-1} were delivered from the start of the experiment to the start of LS1. These measurement periods coincide with the change of collision energy from 7 TeV CM until the end of 2011 to 8 TeV CM from beginning of 2012 until LS1. The experiment also took some data in 2013 from proton-ion collisions, which is ignored due to the very small delivered integrated luminosity value of around 1.6 nb^{-1} . The effect of the higher collision energy on the measured dose values will be analyzed later in this thesis. Measurements for each of the aforementioned integrated luminosity values are presented as far as they could be obtained. Sensors that are placed around electronic installations on top and below the calorimeter structure, that have been collected for the first time during LS1, measured dose values corresponding to the total value of delivered luminosity of 3.47 fb^{-1} .

According to FLUKA simulation studies, charged particles contribute significantly to the deposition of dose within the acceptance of the experiment. As a consequence of the large LHCb dipole magnet in the LHCb experiment, a horizontal spread in the dose distribution can be observed. In figure 57 the lethargy fluence per collision at a distance of about 330 cm is shown and in figure 58 at a distance of 50 cm, both along the horizontal from the beam line on the front of the M1 muon detector. Charged hadrons and electrons are prevalent at high energies, with their number increasing when getting closer to the beam, explaining the shape of the dose distribution perpendicular to the beam. The mostly homogenous vertical magnetic field of the LHCb dipole is diverting the paths of those charged particles along the horizontal axis, resulting in a dose distribution that is clearly spread along the horizontal. For illustration, figure 59 shows the dose distribution per collision at the front of the SPD, just as the lead plates of the PS detector starts to break down the incoming particles into cascades of secondary particles, for a collision energy of 7 TeV CM. This asymmetry in the dose distribution is reflected in the measurement results obtained and presented in this document.

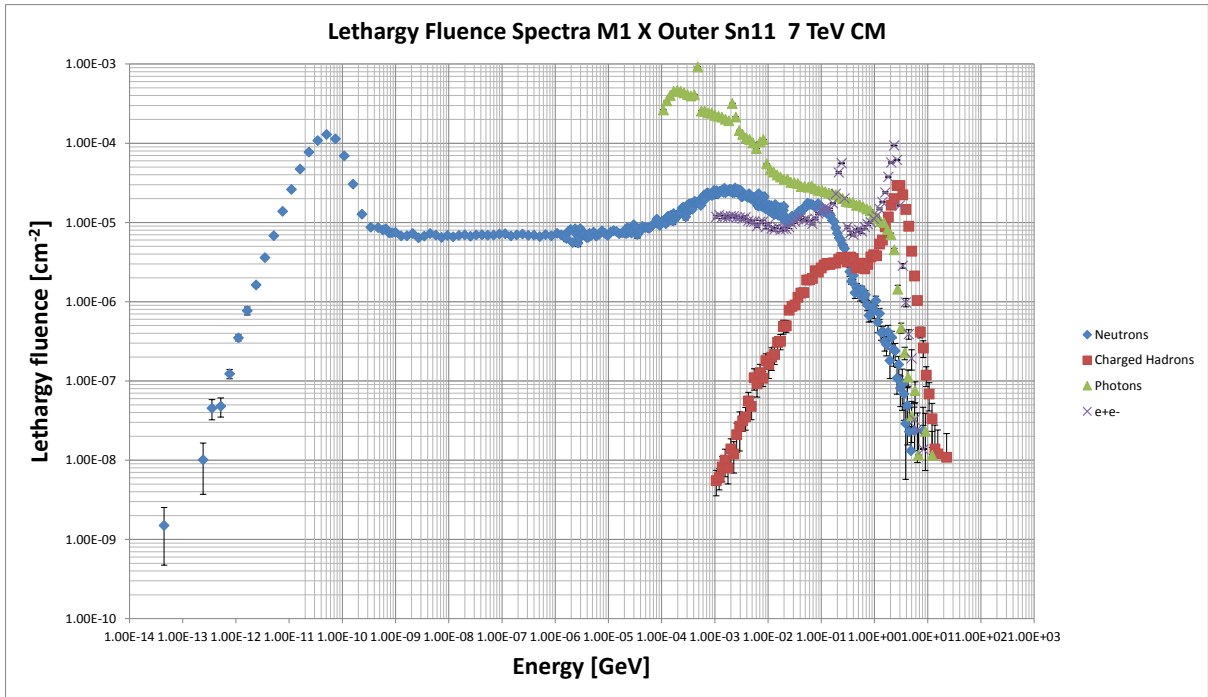


Figure 57: Lethargy fluence per collision at a distance of about 330 cm along the horizontal from the beam line at the front of the M1 muon detector at a collision energy of 7 TeV CM. Charged hadrons and electrons/positrons constitute a large part of the impinging radiation and have been deflected by the magnetic field of the LHCb dipole.

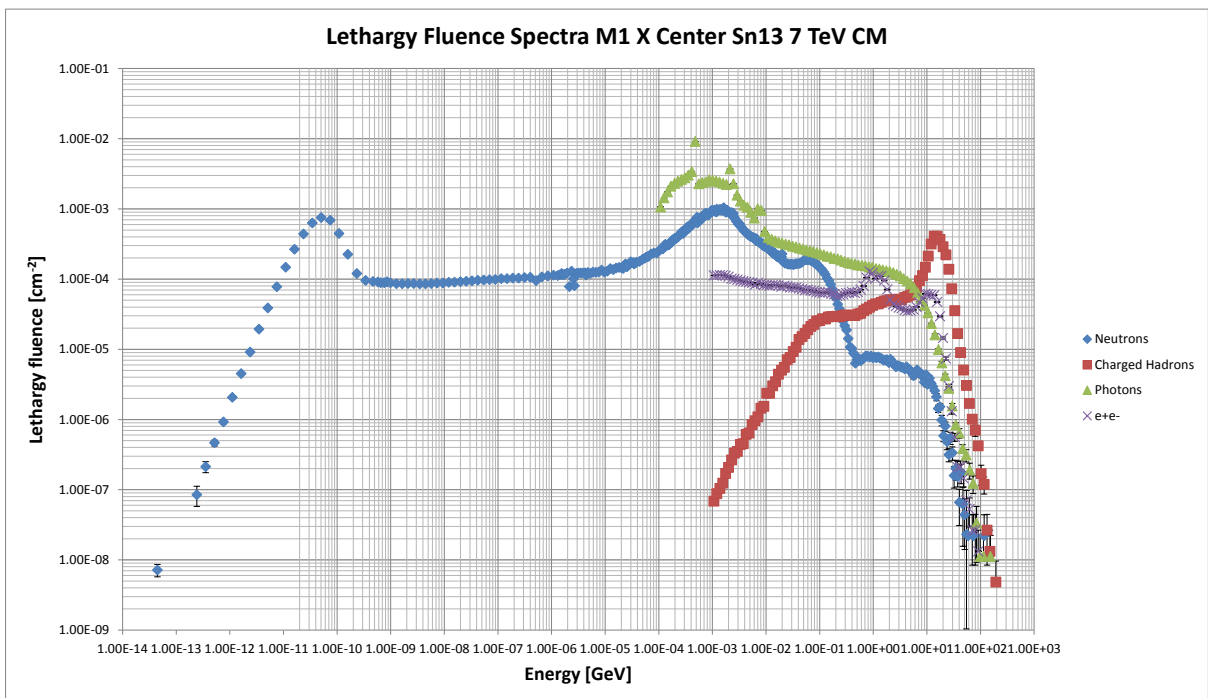


Figure 58: Lethargy fluence per collision at a distance of about 50 cm along the horizontal from the beam line at the front of the M1 muon detector at a collision energy of 7 TeV CM. Charged hadrons and electrons/positrons increase in number and energy compared to the fluence at further distance to the beam line as shown in figure 57.

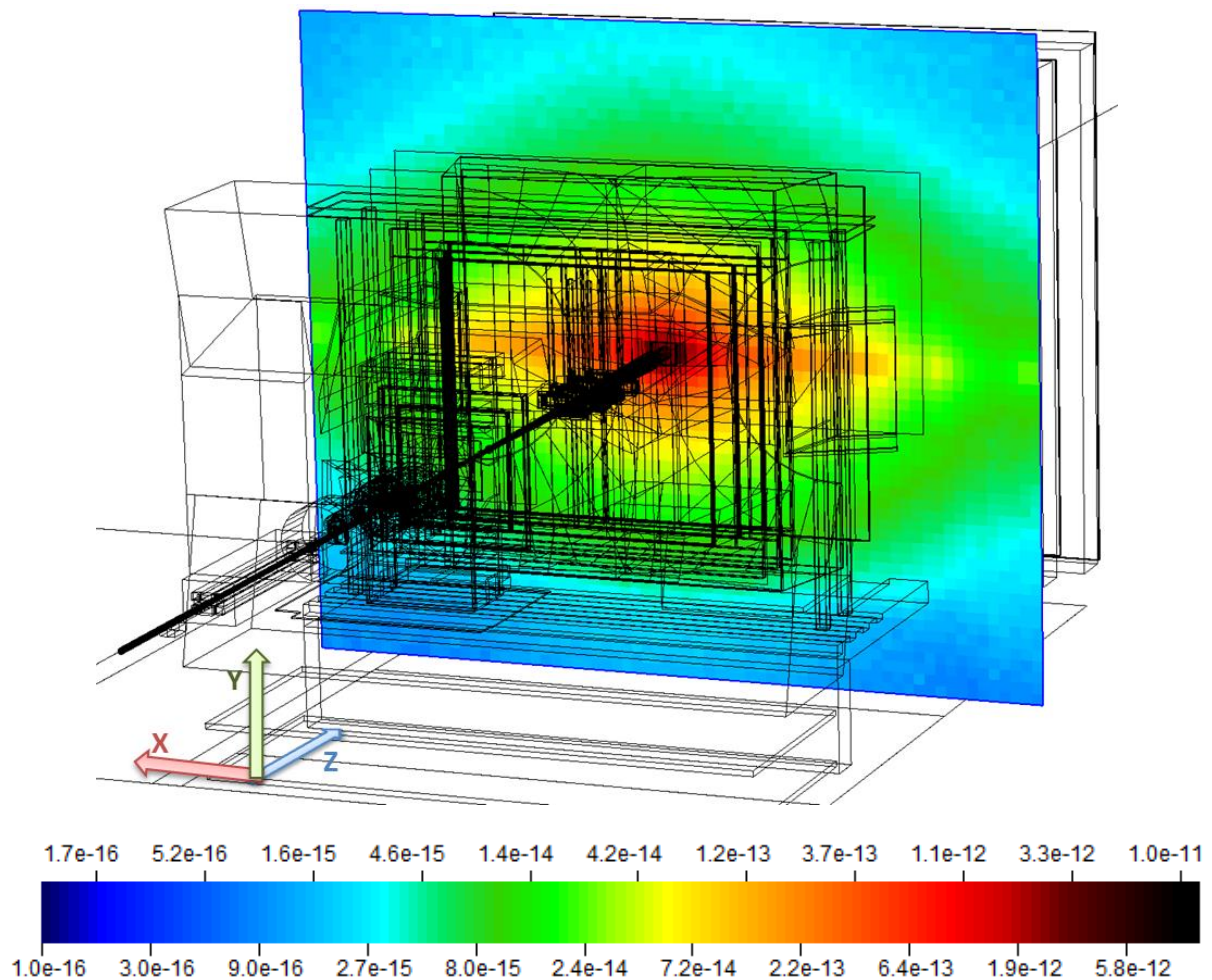


Figure 59: Illustration of the dose distribution per collision at 7 TeV CM at the front of the SPD. The LHCb dipole is responsible for the lateral expansion of the distribution by deflecting the large amount of charged particles coming from the collisions.

It should be noted that the highest measurement values obtained do not correspond to the maximum dose in the detectors. The maximum values of measurements correspond to the maximum of the available sensors on each detector plane. In figure 60 the sensors closest to the center on the HCAL front plane, corresponding to the positions in figure 46, are depicted. The laterally aligned sensor boxes are positioned at a distance of several centimeters to the edge of the central lead plug, hence the measurements of sensors in these positions will not represent the maximum dose that the modules behind them will actually receive. Detector modules of each subdetector of the calorimeter extend further than these positions and reach closer to the beam. Consequently, the actual maximum of total integrated dose on each plane has to be extrapolated and estimated via simulation.



Figure 60: Photo of the central area of the HCAL detector front plane, showing part of the layout of the positions of the passive dosimeter boxes. None of the dosimeters cover the most exposed areas touching the central beam plug (white), necessitating the use of simulations for extrapolating the actual maximum dose that these modules are exposed to.

In the dose range that sensors around the central regions of each detector were exposed to, Alanine is considered to provide the most reliable measurements. TLD MCP sensors are in principle able to measure from mGy up to one MGy, but as already mentioned some factors limit their reliability in the high dose range in the experiment. Therefore more studies are required to implement special correction factors for various mixed radiation field compositions before they can be used reliably in the special case of the LHCb complex mixed field. As a consequence, Alanine results will be used in the following sections for the results of the high dose range measurements. Results for each subdetector plane will be discussed separately, starting with the backside of HCAL and then moving upstream.

5.1.4.1 HCAL BACKSIDE

The maximum values of measured dose on each plane can be found in the sensor positions that are closest to the beam along the x-axis. This is the case with all 4 detector planes presented in this thesis. The horizontal spread of the integrated dose, which is caused by the deflection of charged particles crossing the magnetic field of the LHCb dipole magnet, is responsible for significantly higher measurement values along the horizontal axis compared to equal distances on the vertical. Other sensors are placed slightly closer to the beam pipe considering absolute distance, but are directly above or below the beam line, and are measuring 25% less dose than their horizontal counterparts at a similar distance from the beam, as can be seen in figure 61.

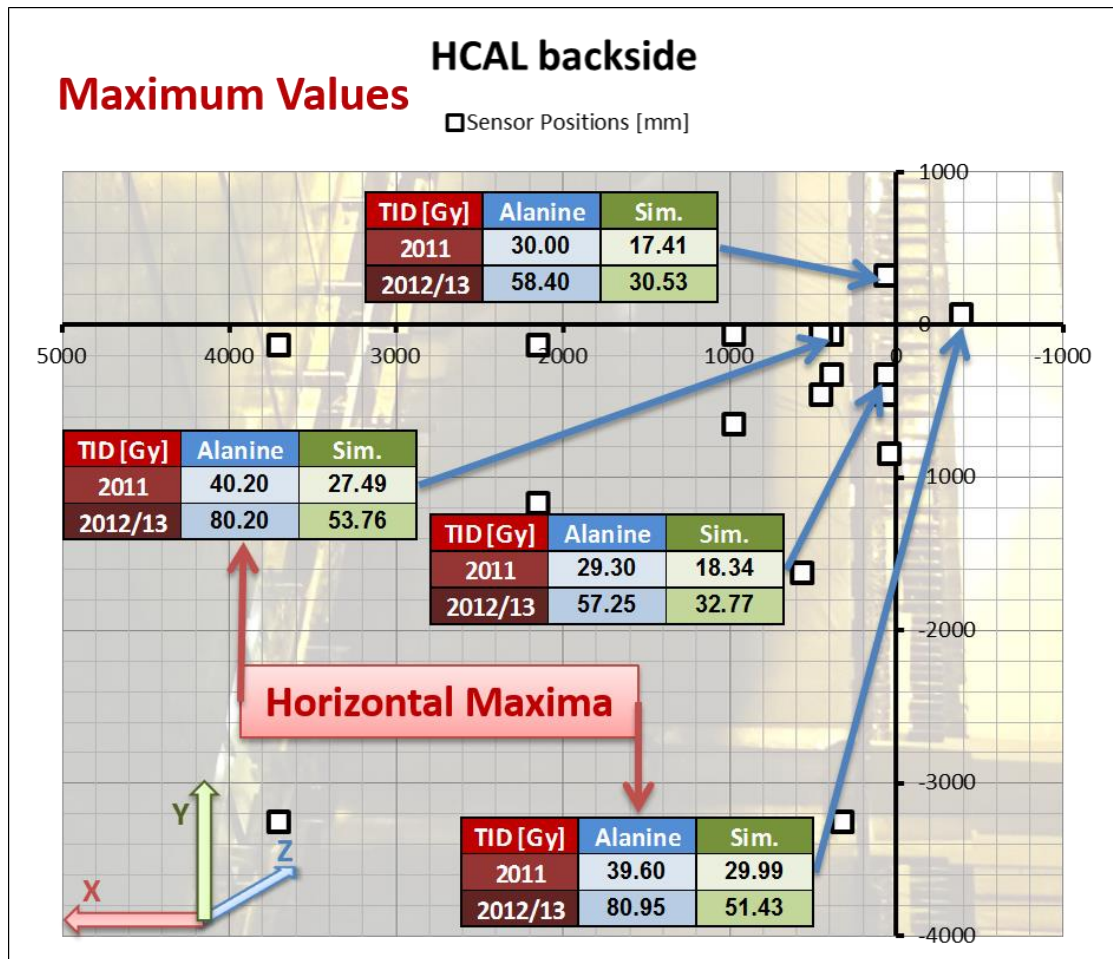


Figure 61: Maximum measured values (blue) at the backside of the HCAL for both measurement campaigns. Measurements from 2011 correspond to an integrated delivered luminosity of 1.26 fb^{-1} , and measurements from 2012/13 correspond to 2.21 fb^{-1} . Simulation estimates for the same positions and conditions are shown in green.

Of course, the calorimeters are absorbing most of those charged particles themselves, however the shape of the incoming radiation field hitting on the front of the detectors does not change radically on the way through the detector, when high energy particles are broken down into cascading secondary particle showers.

The combined mass of the calorimeter detectors causes a significant reduction of measured dose values at the backside of the Hadronic Calorimeter compared to the layers that are closer to the IP.

Estimates from the corresponding Cartesian grids in the FLUKA simulation, which are also listed in figure 61, tend to be lower than the Alanine measurements by a factor of less than 2. Part of the reason for this underestimation is connected to the layout of the Cartesian binning. The gradient of the increase in dose becomes considerably larger the closer you move towards the beam. Up to a distance of 1 m from the center in x and y, the bin size that is used for scoring is only $5 \times 5 \text{ cm}^3$ small in comparison to the usual $20 \times 20 \times 20 \text{ cm}^3$. Since each bin only represents an averaged value of the volume it encompasses, the smaller bin size enhances the accuracy of the estimation in that region. For the detector positions that are closest to the center however, even 5 cm bins cannot provide estimations that are accurate enough to exactly reproduce measurements, especially if they lie close to the edge of a bin.

Unfortunately, the sizing and placement of the bins alone can only explain some of the cases when the simulation underestimates at a small distance to the beam. These values lower than the measurements for locations close to the beam can also be observed on the other detector planes, where issues with the simulation setup, such as a lack of small detail like missing screws in the description, may play a role as well.

The smallest dose values were measured by three sensors that are the furthest away from the center. All of those values are below 1 Gy. Alanine measurements below this value are not considered reliable anymore as explained in section 2.2.1. TLD measurements on the other hand, are trustworthy for dose below 1 Gy. The three lowest values at the outer edges of the back of the HCAL are shown in table 6 and table 7 for each period of measurement along with estimates from FLUKA simulations.

Table 6: List of the three lowest values at the outer edges of the back of the HCAL measured until the end of 2011.

2011				<i>Int. Lum.: 1.26 fb⁻¹</i>		
HCAL backside	Coordinates [mm]			DOSE [Gy]		
<i>ITEM_ID</i>	<i>X</i>	<i>Y</i>	<i>Z</i>	<i>TLD: MCP-7</i>	<i>TLD: MTS-7</i>	<i>Simulation</i>
4CRCERPW000003	3705	-3250	14970	0.020410406	0.018256	0.083
4CRCERPW000007	325	-3250	14970	0.070162443	0.067415	0.23
4CRCERPW000008	3705	-130	14970	0.114045199	0.099126	0.23

Table 7: List of the three lowest values at the outer edges of the back of the HCAL measured until the start of LS1.

2012/13				<i>Int. Lum.: 2.21 fb⁻¹</i>		
HCAL backside	Coordinates [mm]			DOSE [Gy]		
<i>ITEM_ID</i>	<i>X</i>	<i>Y</i>	<i>Z</i>	<i>TLD: MCP-7</i>	<i>TLD: MTS-7</i>	<i>Simulation</i>
4CRCERPW000003	3705	-3250	14970	0.038948091	0.092641	0.17
4CRCERPW000007	325	-3250	14970	0.143318724	0.350055	0.38
4CRCERPW000008	3705	-130	14970	0.225078465	0.226201	0.45

While measurements of 2 different types of TLD sensors perfectly agree with each other during the first campaign in 2011, the measurements of MTS and MCP differ by more than a factor of two during the second measurement campaign. According to most other measurements, the changes in the radiation field due to the higher collision energy are rather small. Therefore this discrepancy is considered to be caused by an error during the readout of the 2012/13 measurements.

FLUKA simulation results in these areas suffer from two large drawbacks: on one hand, the uncertainties that stem from structural differences between the real detector and the FLUKA geometry, such as missing support structures or varying material compositions, accumulate on the way from the collision point towards the outsides of the detector in all directions. For example, the fact that the muon towers, which are housing electronic and gas racks, are not represented in the geometry might have an influence on the results at the outer edge of the HCAL backside, because scattering from the metallic tower structures is not calculated. The description of the detector is much more detailed inside the acceptance. On the other hand, the large attenuation from the heavy calorimeter structures causes a higher statistical error when compared to central regions of the experiment. Due to a very high absorption inside the HCAL, far less particles are able to pass through the HCAL than any other detector upstream, providing less data for the calculation of dose. Because of these reasons, a higher difference between measurement and simulation in the periphery is to be expected. Depending on which measurements the comparison is based on, these differences are between factors of 2 to 4 on the backside of the HCAL.

Tables with all measurements can be found in the Appendix.

5.1.4.2 HCAL FRONT

High energy hadrons, in this case pions, protons and neutrons that are able to pass through (or, to a smaller extent, are produced in hadronic cascades developing within the ECAL detector) represent a large part of the radiation field on the front plane of the Hadronic Calorimeter. The maximum measured dose close to the center plug is about an order of magnitude higher than at the back of the HCAL.

The lateral spread of charged particles that is caused by the dipole field and which is also influencing the shape of the dose distribution at the back of the HCAL as explained in the previous section, is more pronounced in this plane. As a consequence, the highest values were again measured laterally and close to the center. In figure 62 the elliptical shape in the center at the HCAL front plane is illustrated by providing a finer grained look of the dose distribution as obtained by simulation at 8 TeV CM with 5 cm resolution in x and y in the inlet.

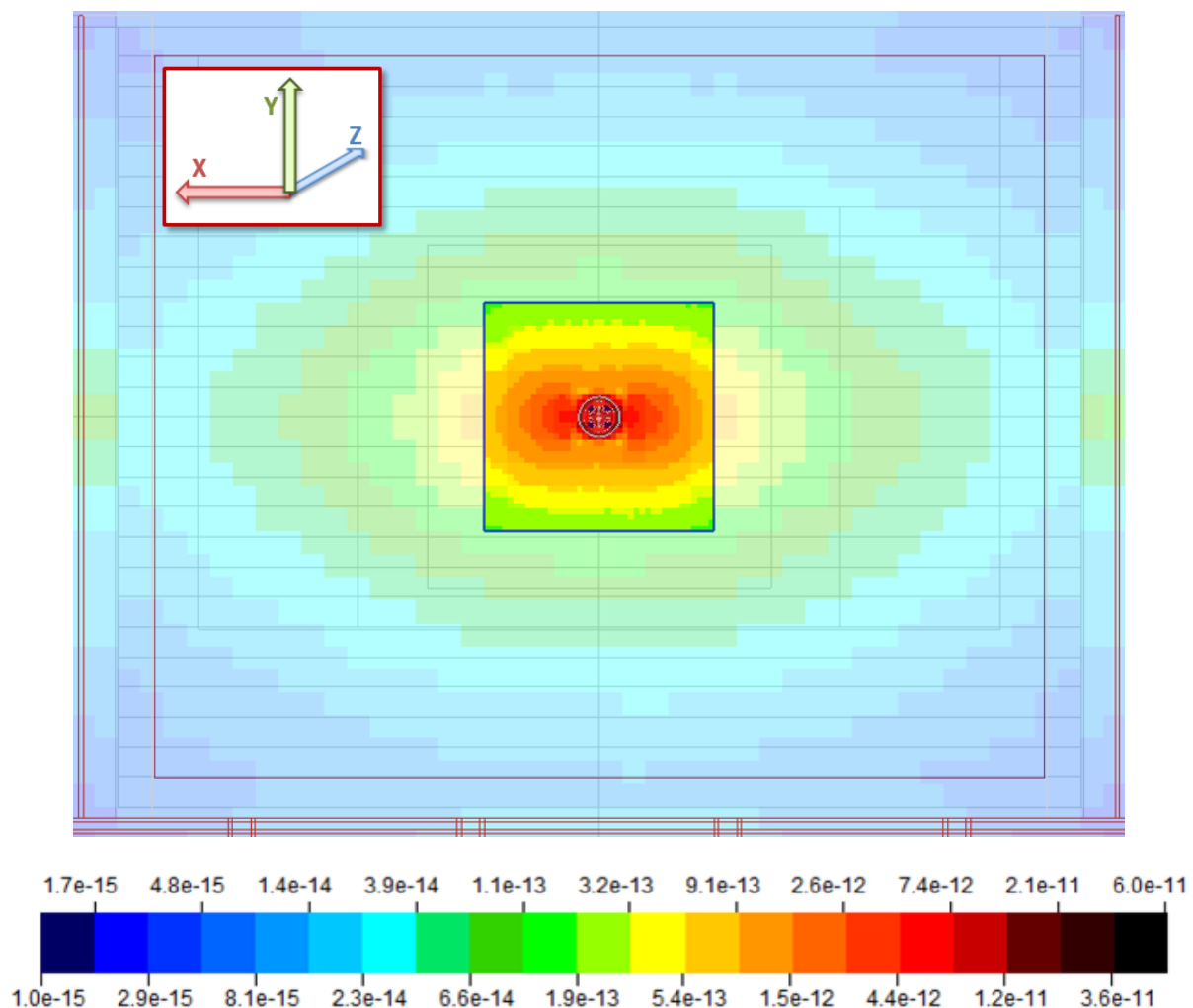


Figure 62: Dose per collision [Gy] at the center of the front plane of the Hadronic calorimeter in 5x5x5 cm³ detailed scoring extending to ± 1 m in x and y for collisions at 8 TeV CM, with the magnetic field of the LHCb dipole pointing upwards. The spread in dose distribution is clearly seen around the central region. The 20x20x20 cm³ binning of dose deposition around the center is displayed in washed out colors for illustration and orientation purposes.

Because of this shape, the sensor positioned at x=39 cm and y=6 cm in the LHCb reference plane registered the highest values of total integrated dose in this plane during all measurement periods. As a comparison, the sensors above and below the beam, at roughly the same distance, received less than half of these values during the same irradiation periods. It has to be considered, that the inner edge of the calorimeter modules

touching the beam plug at beam height is closer to the beam than the closest sensor. According to the FLUKA simulations shown in figure 62, this means an increase of dose of a factor of at least 1.5 at the inner edge of the central module compared to the position of the closest sensor. In figure 63 the highest measured values of total integrated dose during each measurement period is shown as provided by Alanine dosimeters, which as already mentioned are considered the only reliable type of sensor in this dose range. Simulation estimates for the corresponding positions and conditions are listed in green next to the measured values.

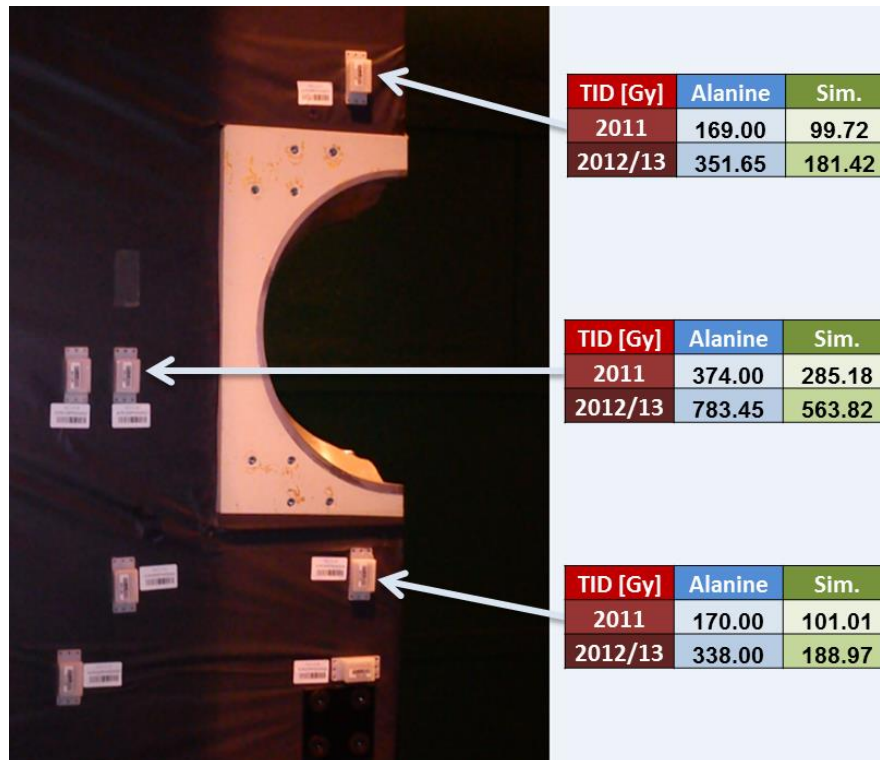


Figure 63: Alanine results in Gy from both measurement campaigns in 2001 and 2012/13. Vertical sensors are at less total distance to the beam, but register lower dose than their lateral counterparts. Measurements from 2011 correspond to an integrated delivered luminosity of 1.26 fb^{-1} , and measurements from 2012/13 correspond to 2.21 fb^{-1} . Simulation estimates for the corresponding values are shown in green.

Most of the measured dose values on the front of the HCAL lie in the reliable sensitivity range of Alanine dosimeters. Even on the lateral far side of the detector, the dose could still be measured with Alanine. Only along the lower edge of the detector, at a distance of 3 to 4 meters from the beam, the sensors were exposed to a dose $<1 \text{ Gy}$, meaning that TLD sensors provide the most accurate measurements in these few cases.

As was the case with the central region on the back side of HCAL, FLUKA simulation results underestimate the dose close to the beam even when using a bin size of 5 cm. Apart from the inaccuracy due to the bin size as explained earlier, the exact cause for this discrepancy is unknown. The most likely explanation for this could be an insufficiently detailed model of the FLUKA geometry in the area between the calorimeter detectors and the IP. Although the accuracy is still within a factor of 2, this clearly indicates that it is imperative to always apply appropriate safety factors when relying on the results of the FLUKA simulations reported in this thesis.

Tables with all measurements can be found in the Appendix.

5.1.4.3 ECAL FRONT

The highest dose values within the Calorimeter structures have been registered on the front the Electromagnetic Calorimeter. The thin lead plates sandwiched between the PS and SPD are responsible for initiating large cascades of lower energy secondary particles, which deposit high levels of dose on the front of the ECAL. As a result, the dose values that almost all sensors were exposed to rely on Alanine measurements for this plane.

Alanine measurements for the positions closest to the center in x and y, as well as for the outer lateral edge of the detector plane are shown in figure 64. As expected from the simulation, the highest values are again registered horizontally next to the beam line. The measurements stay significantly higher along the horizontal than along the vertical axis at comparable distance from the beam. For illustration purposes, the dose values from simulation at 8 TeV CM for an integrated luminosity of 2.21 fb^{-1} , corresponding to the measurements from 2012/13, have been chosen as background. The lateral spread of the dose deposition is clearly visible in the simulation as well as in the measurements. The sensor box directly above the beam pipe shown in figure 64 is only at 26 cm from the beam line, whereas the closest sensor along x is at 35 cm. Regardless, the sensor that is 10 cm further away, but placed along the horizontal axis, received roughly 30% more dose. As already explained, this is directly caused by the influence of the magnetic field on the charged particles coming from the collision. It is even more evident in this plane, because much of the electromagnetic radiation deflected by the field or generated by deflected charged particles is yet to be absorbed by the ECAL.

One has to be careful when looking at the simulation values at this plane due to issues with bin sizing and placement. Simulation values taken from $5 \times 5 \times 5 \text{ cm}^3$ binning, which is not displayed, ostensibly suggest a different result than measurements, showing a higher value on top of the beam than along the horizontal. However this is not truly the case, as the $20 \times 20 \times 20 \text{ cm}^3$ binning in figure 64 also indicates, because this disagreement is caused by the issue of bin size versus the strong gradient of dose within one bin. The value of 2418 Gy from 2012/13 for example is the average within a volume that goes from 0 to 5 cm in x and from 20 cm to 30 cm in y, spanning 2 bins. The value of a single bin between 25 cm and 30 cm in y only shows 1357 Gy for the same conditions. Since the actual measurement position is at $y=26 \text{ cm}$, a more detailed interpolation would yield a value much closer to the measurement of 1768 Gy. As this special case in the central region on the front of the ECAL shows, a few cm in distance can cause a difference in dose of a few 100 Gy. This more sophisticated method for interpolation was not applied here in order to stay consistent within the document. The 20cm binning in the central region shows values that are actually closer to measurement, but this is purely by chance which is based on the relation of bin location versus dosimeter placement. In general, the simulation still yields values that lie below Alanine measurements by a factor of less than 2.

The only dose value outside the range of the Alanine sensitivity for sensors in this plane are measurements in 2011 in the lower left corner of the detector in the figure. According to TLD measurements they should have been exposed to almost exactly 1 Gy.

Tables with all measurements can be found in the Appendix.

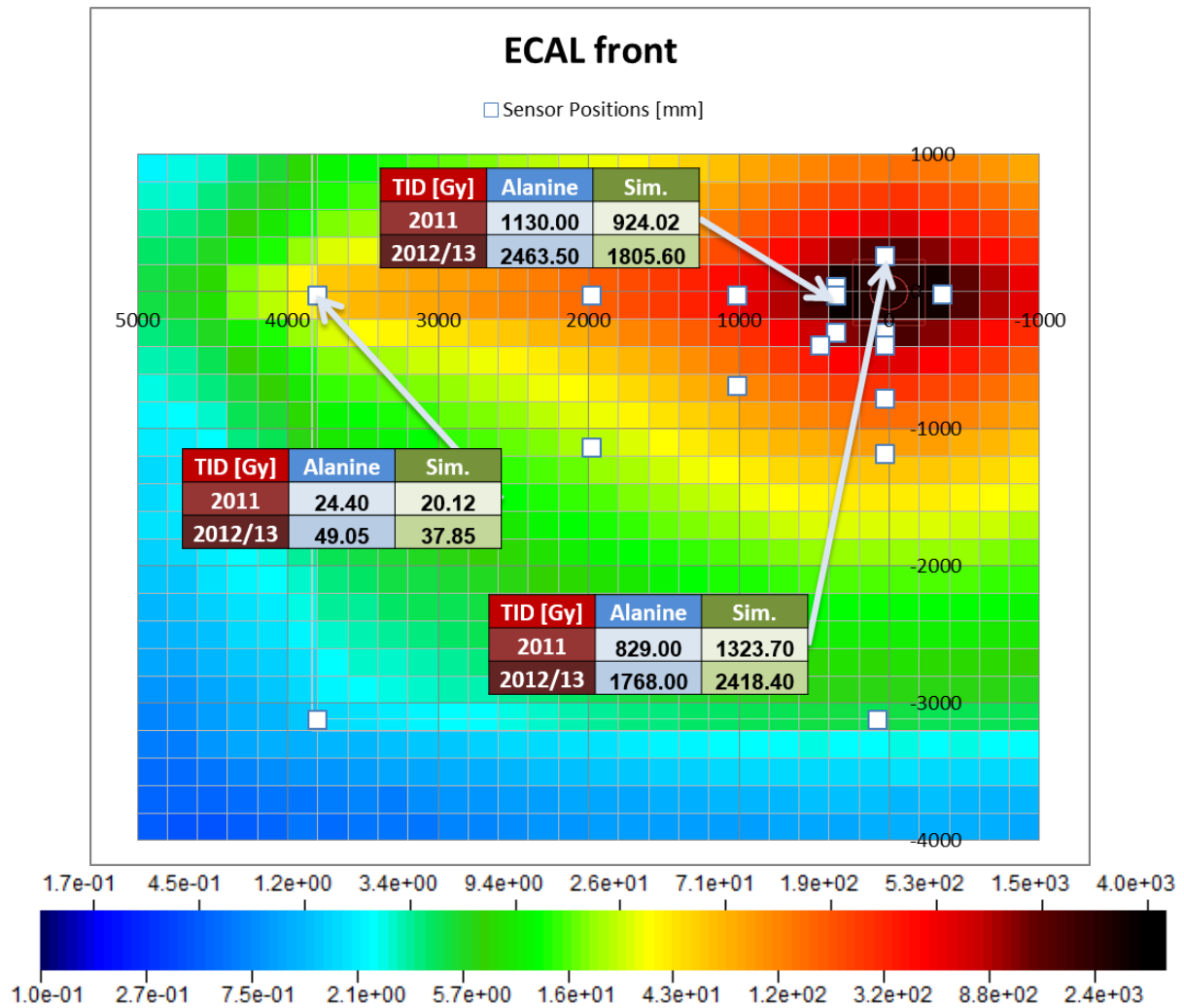


Figure 64: Results from Alanine sensors at positions close to the beam and at the edge of the ECAL detector plane are displayed in blue over a background of FLUKA simulation results for dose after being exposed to 2.21 fb^{-1} with 8 TeV CM collision energy, which corresponds to the 2012/13 measurements. Measurements from 2011 correspond to an integrated delivered luminosity of 1.26 fb^{-1} , and measurements from 2012/13 correspond to 2.21 fb^{-1} . Simulation results at the indicated positions are listed in green. The difference between measurement and simulation in the central region is mainly caused by issues with the bin size in a region where the dose values can change by a few 100 Gy within one cm.

5.1.4.4 SPD FRONT

The sensor boxes attached to the front of the SPD are exposed to a radiation field that is dominated by photons and electrons, in addition to high energy hadrons mostly concentrated around the central region. The measured dose values are of the same order of magnitude of those in front of the HCAL. However the shape of the dose distribution is similar to that on front of the ECAL and wider than at the HCAL because of the different composition of the field; areas on the front of the HCAL are shielded by the ECAL, the effect being more pronounced the farther from the beam line they are, whereas the front of the SPD is hit by the full radiation cone developing on the way from the original proton-proton collision. Alanine measurements for the positions closest to the center in x and y, as well as for the outer lateral edge of the detector plane are shown in figure 65. In the center, dose values are still significantly higher laterally than for the same vertical distance. This

lateral spread of increased dose deposition leads to measurements at beam height that are rather high even at the outer edge of the detector.

Again, Alanine sensors are reliable almost everywhere except for the lower corner of the plane that is furthest away from the beam line. TLD sensors on that position measured around 0.7 Gy.

The dosimeters are placed in a slightly different configuration with respect to the front plane of the ECAL. The different relative position of the sensors compared to the edge of the bin explains why the simulation values in the position above the beam line in this case are not higher than measurements. Simulation values are generally lower when compared to Alanine measurements, but always within a factor of 2. It is also the case here although the discrepancy is higher. Another factor based on bin placement in the z-direction plays an important role at the front of the SPD that partially explains the discrepancy in this case. It will be explained in more detail, in section 5.1.6. Tables with all measurements can be found in the Appendix.

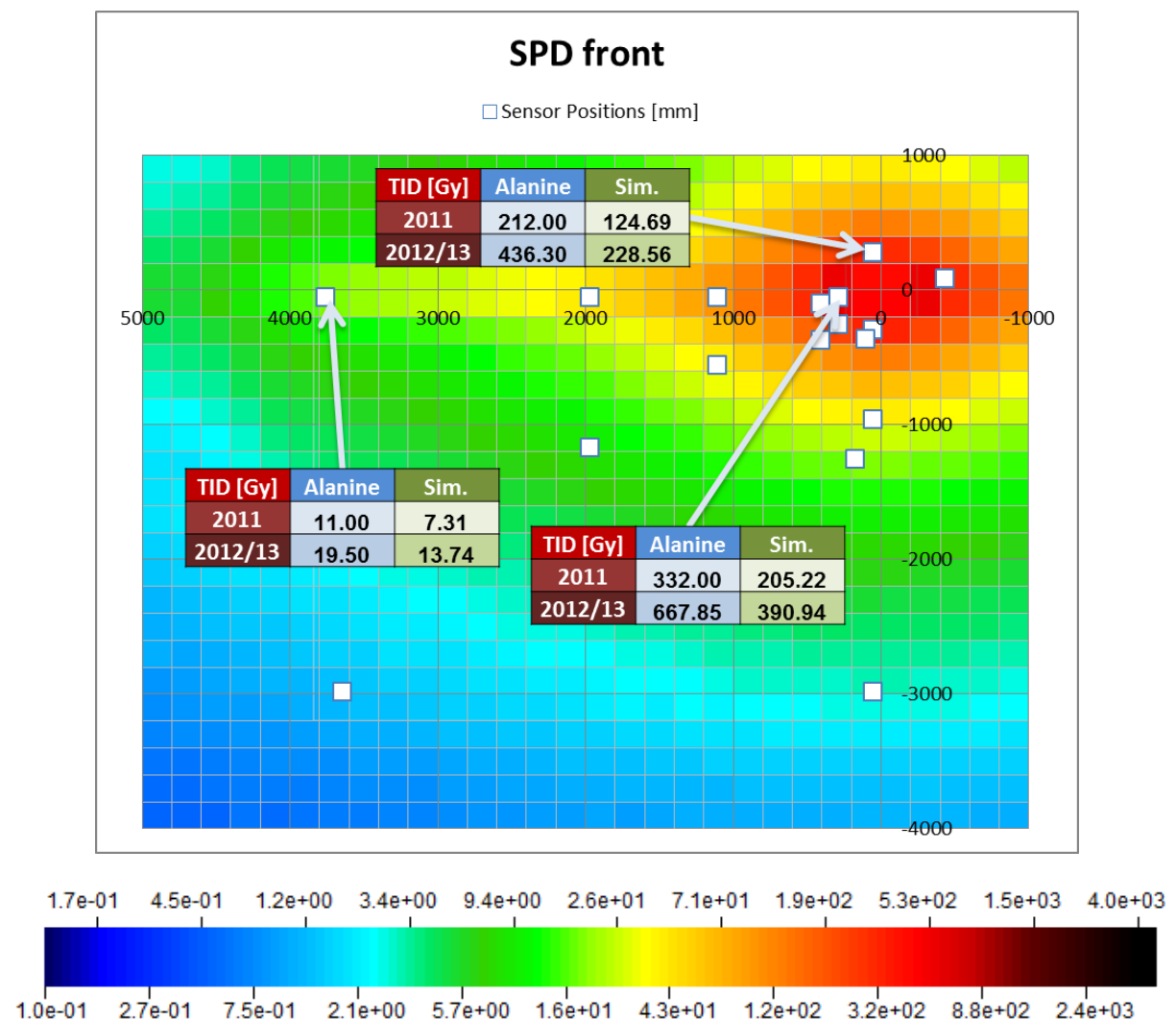


Figure 65: Results from Alanine sensors at positions close to the beam and at the edge of the SPD detector plane are displayed in blue over a background of FLUKA simulation results for dose after being exposed to 2.21 fb^{-1} with 8 TeV CM collision energy, which corresponds to the 2012/13 measurements. Measurements from 2011 correspond to an integrated delivered luminosity of 1.26 fb^{-1} , and measurements from 2012/13 correspond to 2.21 fb^{-1} . Simulation results at the indicated positions are listed in green. Simulation results are underestimating Alanine measurements within a factor of 2.

5.1.4.5 ECAL TEST MODULES

In the tunnel upstream of the experiment right next to the beam pipe, dosimeters were placed around modules of the type that is used in the ECAL. It was expected that these modules would receive higher dose per collision than the actual detector itself while being exposed to a similar mixed radiation field, and this would allow to predict cumulative damages induced by radiation years in advance. Indeed the dose values measured are higher by more than a factor of 2 than what was measured at the ECAL front plane; with large variations in measurements depending on the positions of the dosimeters.

The interaction of the secondary radiation coming from the collision point with the iron yoke and the copper coils of the corrector dipole in this area is the main source of radiation experienced by the test modules together with the particles from the IP that passed through the aperture of the magnet and are deflected by the field. An illustration of the lateral dose distribution at beam height per collision at 8 TeV CM in the upstream tunnel as obtained from the simulation is shown in figure 66. The scale has been omitted on purpose, since the estimations are not considered sufficiently precise. The corrector dipole in the simulation features a homogenous magnetic field, which is always directed the exact opposite way of the LHCb dipole, influencing the trajectory of charged particles on their way to the modules.

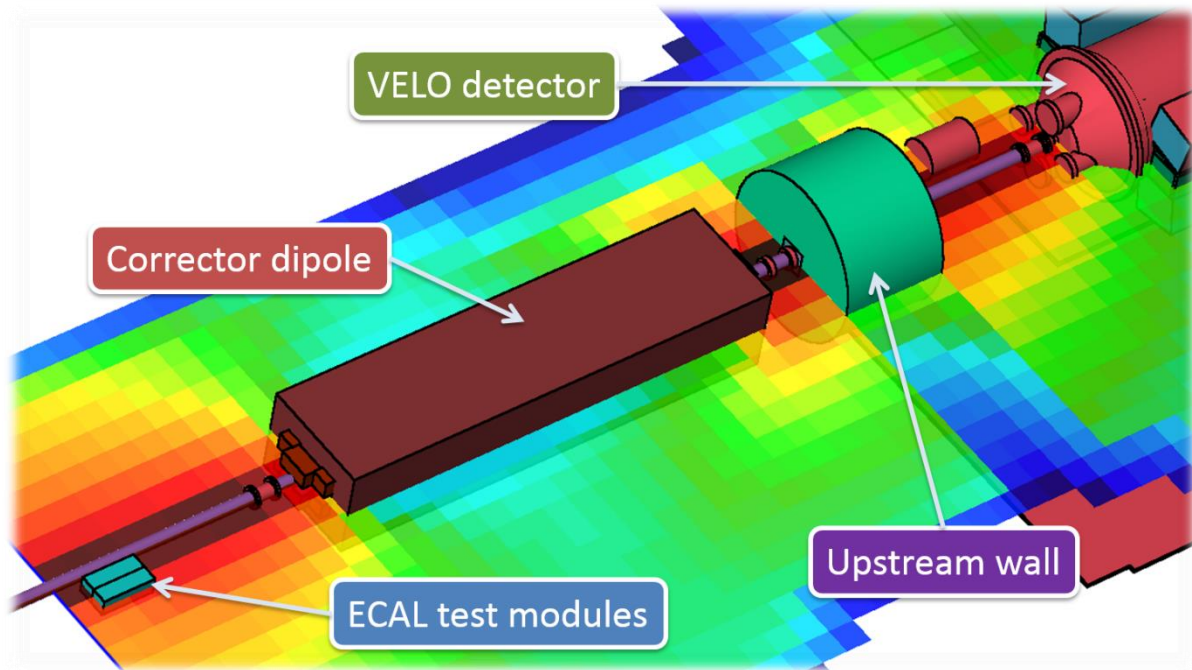


Figure 66: Illustration of simulation results of lateral dose distribution per collision at 8 TeV CM at beam height inside the tunnel upstream of the LHCb experiment. The ECAL test modules can be seen in the lower left within the main cone of radiation coming from the end of the corrector dipole. The upstream wall extends laterally beyond the cylindrical plug, represented by mostly blue values in the distribution. This part of the wall was made transparent for reasons of clarity.

The measurements of the dosimeters located next to the beam pipe in the upstream tunnel obtained for both 2011 and 2012 are illustrated in figure 67. An attempt to use the TLDs for high level dosimetry was made with the sensors in this location, but due to the large inconsistencies of TLD values in the high dose range between the two measurement periods, only Alanine measurements are considered reliable by the author also in this case.

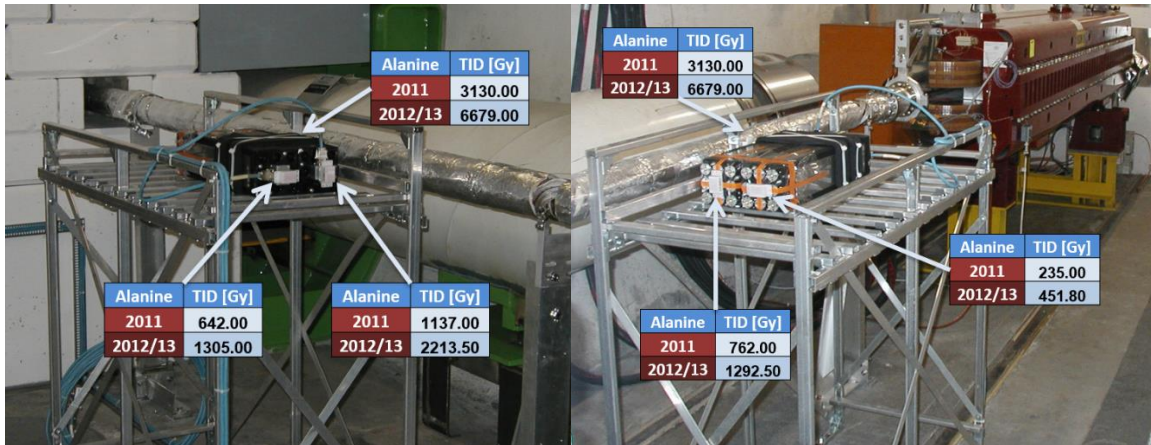


Figure 67: Results from Alanine sensors for both measurement campaigns at the ECAL test modules in the tunnel upstream of the experiment. Measurements indicate that they have been exposed to radiation levels above those that the actual ECAL detector experienced, as it was intended. As it will be shown in detail later, the measurements confirm the general shape of the dose distribution around the modules.

As can be seen in figure 67, the measured values are comparably high with respect to most measurements in the calorimeters. This is due to the ECAL test modules in the upstream Tunnel being placed very close to the beam pipe. At such a short distance, the dose deposited increases with a high gradient when moving towards the pipe. A few mm of distance can account for up to 10% difference in measurements. This is corroborated by what was observed in the measurement campaign. The highest measurement of 6679 Gy quoted for 2012 is in fact an average value of two measured Alanine sticks inside the box, with the higher one measuring 6906 Gy, accounting for an exceptional difference of 6.8%. Usually the difference between two dosimeters in the same box is less than a few percent, and repeated readouts give very consistent results. Based on earlier FLUKA simulations [56], and more recent simulations carried out by the author that include parts of the upstream tunnel where these modules are placed, the radiation field in this tunnel section is estimated to be cone-shaped and strongly forward-directed, with the cone starting from the corrector dipole magnet. The maximum dose is delivered to the side of the module closest to the beam pipe under a flat angle. The exact positions of these 5 sensors are not known and are derived from technical drawings and photos. As such, these measurements should not be used to extract the behavior of the dose distribution closer to the beam pipe. Simulation efforts to reproduce exactly the measurements in these specific 5 positions in the upstream tunnel have unfortunately failed, most likely due to an insufficient level of detail of the geometry in the upstream tunnel, as well as an inadequately accurate knowledge of the actual positions of the modules, since as already mentioned a few cm can make a huge difference in dose in this location. It is therefore recommended to only rely on the measurements for any estimate of integrated dose in the upstream tunnel area. Tables with all measurements can be found in the Appendix.

5.1.4.6 CALORIMETER ELECTRONICS

Dosimeters located around the electronics racks on top of the ECAL/HCAL and on the top and bottom edge of the PS have been collected for the first time since their installation during LS1. These sensors received an integrated dose which corresponds to a delivered integrated luminosity of 3.47 fb^{-1} , a combined 1.26 fb^{-1} at 7 TeV CM and 2.21 fb^{-1} at 8 TeV CM. The highest measurements in these locations were obtained by Alanine sensors, which were placed around the electronics racks on top of the calorimeters, showing 2.2 Gy and 2.05 Gy. Measurements from both TLD types, which are relied upon in this dose range, show results slightly below this value, therefore the Alanine measurements can be seen as an upper limit. These measurements were taken on the center top and bottom of the calorimeter supports, at 3.8 m distance from the beam line.

Considering the rather moderate amount of deposited dose in these locations, the use of electronics that are only radiation tolerant instead of radiation hard would be justified up to LS1 and beyond. All other measurements stay below the aforementioned maximum, but above 0.1 Gy. Within this dose range, measurements from TLD sensors convey a more accurate estimation of dose values, even if their calibration to γ -radiation could lead their measurements to be underestimates of the real values. In addition to the expected electromagnetic radiation in these locations, simulation estimates still suggest significant components of hadrons.

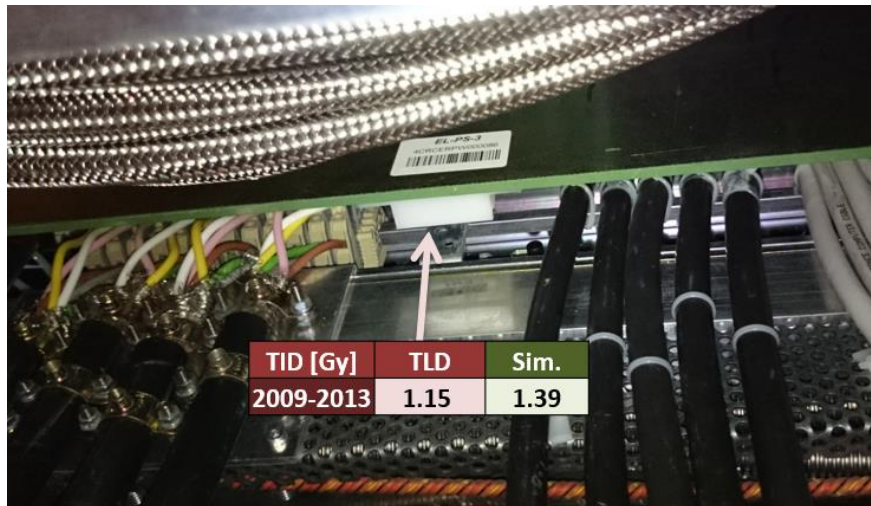


Figure 68: Photo of a dosimeter box with the corresponding TLD measurement at the bottom of the PS detector, hidden between electronic installations, at a distance of 3.8 m in y and 2.2 m in x. The dosimeters were exposed for the full length of Run1, corresponding to 3.47 fb^{-1} .

The distance to the IP combined with the large angle to the beam line already acts as an effective form of attenuation for the electronic systems. A picture of a sensor at the bottom of the PS detector, hidden in between electronic boards, at a distance of 3.8 m in y and 2.2 m in x is shown in figure 68. This location experienced an integrated dose of only 1.15 Gy over 3 years of operation according to the TLD readouts. Although this point lies even below the edge of an actual detector, and therefore at the edge of the region which is modelled in more detail in the simulation, the estimate of the dose from the simulation is still reasonably accurate. This however changes radically with increasing distance from the acceptance of the detector. In addition to total distance, massive support structures made of heavy materials like iron around the calorimeter detectors provide additional shielding to electronic racks. Most of these support structures are not implemented in the LHCb FLUKA geometry at all, which makes it difficult to obtain accurate simulation forecasts of locations that are further away from the detector. As an example, the position and the measurement after 3 years of operation of one of the sensors on top of the HCAL, close to the edge on the A-side of the detector is shown in figure 69. The simulation overestimates the dose value by a factor of almost 5, because all elements shielding some of the low energy radiation in this area are not modelled: all the massive iron bars that constitute the walkway and the roof structure housing the electronic racks, as well as the racks themselves. The simulation estimates always provide a conservative number when compared to TLD measurements for all the calorimeter electronics on top of and below the detectors. Nonetheless, it should not be assumed that the simulation is always providing a conservative estimate in the area above the calorimeters, in particular in locations closer to the edge of the detectors harboring electronics that are not covered by sensors and which might correspond to simulation estimates that are lower than the actual dose. Furthermore, some sensors are shielded from most of the incoming radiation by the electronic racks themselves, as they are sometimes placed on the downstream side of a rack. In these cases it is likely that the electronics inside these racks were exposed to larger dose than what was measured by the sensor. Hence it is recommended to introduce a safety factor of at least 2 when extracting values from the simulation. It should

be noted that regardless of the safety factor the dose level was moderately low until LS1. Tables with measurements from all sensors which could be collected during LS1 can be found in the Appendix.

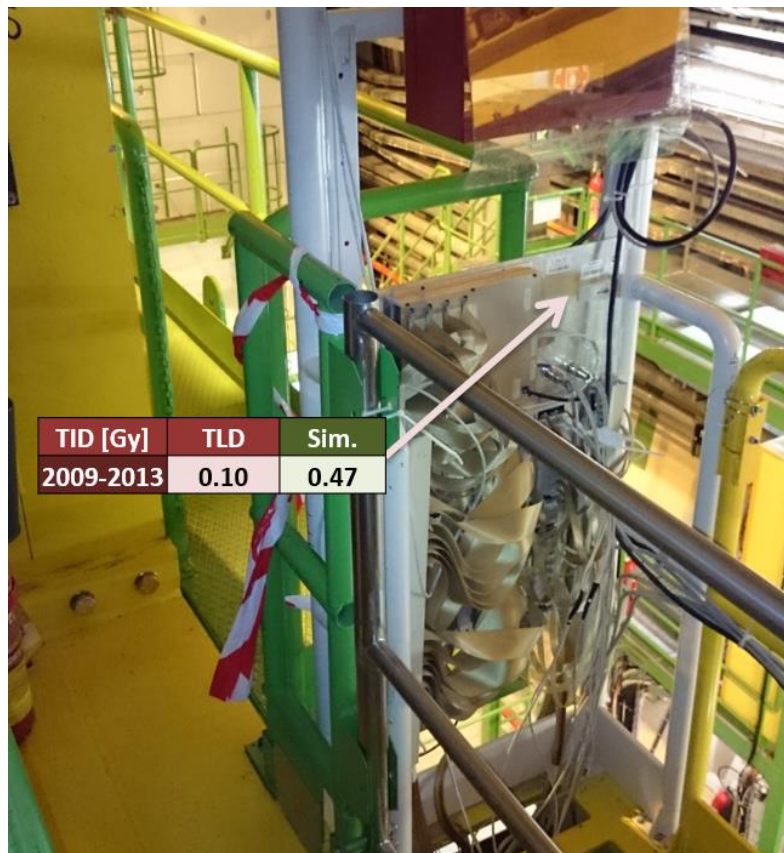


Figure 69: Photo of a dosimeter box and the corresponding measurement and simulation estimate in Gy on top of the backside of the HCAL close to the edge on the A-side of the detector, at a distance of 5.1 m in x and 5.2 m in y from the beam. The dosimeters were exposed for the full length of Run1, corresponding to 3.47 fb^{-1} .

Some dosimeter boxes could not be collected, because the small benefit of reading them out could not justify the necessary dismantling of the PS detector. Considering their placements are similar to those of the sensors collected, they should provide measurements in the same range. These boxes will be kept in place until an opportunity to extract them during the course of maintenance work, for example during the LHCb upgrade, will present itself.

5.1.5 CHARACTERIZATION OF SPECIFIC DOSIMETER PROPERTIES

The unprecedented energies of LHC collisions produce a complex mixed field of secondary particles in the experiments within the accelerator ring as explained earlier. This radiation is further modulated by the LHCb detector components themselves, adding another level of complexity to the original environment. None of the dosimeters used for the studies in this thesis are calibrated for any of the radiation fields encountered in LHCb. As discussed earlier, Alanine and TLD measurements are still considered reliable in their respective traditional dose range above or below 1 Gy, as only small deviations due to calibration issues are expected. TLDs are generally capable of measuring dose up to the kGy range by applying linearity corrections to readouts, but these corrections have only been established for γ -irradiation scenarios and the influence of a mixed particle field is not very well known [59]. Because of the layered subdetectors which comprise thin detectors as well as massive structures, the calorimeters experience a variety of different field compositions simultaneously.

Dosimeters in between layers are exposed to a large range of dose depositions from different sources. In the following sections the behavior of the TLD types used in the experiment is analyzed in these given scenarios by comparison between measurements. The goal of this analysis is the determination of the reliability of TLD dosimeter types within their extended range of applicability. The focus of this analysis is on TLDs because Alanine behavior is considered sufficiently reliable even within a mixed field environment, as discussed in section 2.2.1.

When measuring dose values between 1 Gy and 1 kGy, both MCP and MTS sensors respond with different non-linear behavior, and an appropriate correction is applied during signal-to-dose conversion. However, the correction factors for sub-linearity (MCP) and supra-linearity (MTS) are based on their response to ^{60}Co γ -radiation, and do not apply to mixed radiation fields.

5.1.5.1 MCP LINEARITY ABOVE 1 GY

In principle, TLD MCP sensors are able to cover a dose range from mGy up to one MGy. Their calibration to a γ -source, as well as some special behavior within hadron fields of high intensity which will be explained in the following paragraphs, indicate a need for more studies to implement special correction factors for various mixed radiation field compositions before they can be considered reliable when measuring dose above 1 Gy in the special case of the complex mixed field of LHCb.

A recent study conducted at the Paul Scherrer Institut (PSI) in Switzerland found that MTS and MCP detectors respond differently to proton irradiation. Four incident proton energies between 30 MeV and 230 MeV were used to irradiate the samples with several increments of dose between 0.1 and 50 Gy. Results suggest that MTS sensors measure higher dose when irradiated with protons than MCP sensors. In addition, MCP sensors show a decreasing response with an increase in the amount of incoming particles. It is unclear at this point whether this effect is simply a consequence of the linearity correction factors that are unfit to correct the sub-linear behavior of MCP detectors within a proton beam instead of a photon field, or if any other effects are involved as well. [31]

The radiation field that develops from proton-proton collisions in the LHCb experiment, combined with the layout of passive dosimeters in the calorimeters, provides an excellent opportunity to study this behavior in a more complex environment. Simulation studies have shown that in LHCb the fluence of charged hadrons with very high energies (up to several hundred GeV) is inversely proportional to the distance to the beam line. This is illustrated in figure 70, where charged hadron fluence and the fluence of hadrons with energies greater than 20 MeV per collision at 8 TeV CM as obtained by the simulation is shown in a side view of the experiment. The front planes of the SPD detector, of ECAL and HCAL are all exposed to a very high fluence of high energy hadrons close to the beam pipe. The plots only show total fluence values, whereas the energy distribution at a specific point close to the beam on the front of M1 was shown earlier in figure 58.

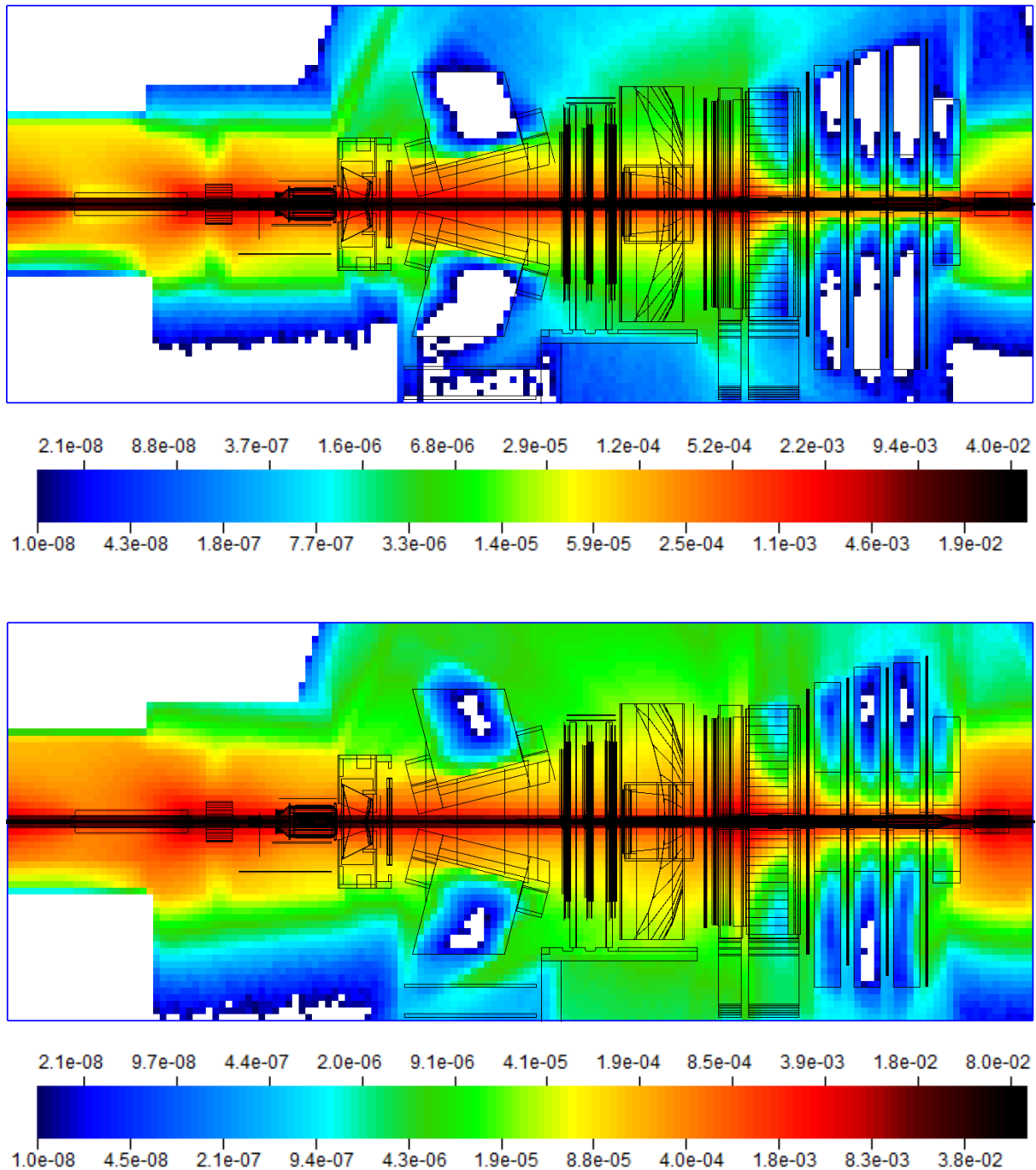


Figure 70: Illustration of the simulated charged hadron fluence (top) and the fluence of hadrons with an energy >20 MeV (bottom) of the slice between $x=0$ and $x=20$ cm per cm^2 per collision at 8 TeV CM in a side view of the experiment. The front planes of the SPD detector, as well as of ECAL and HCAL are all exposed to a very high fluence of high energy hadrons close to the beam pipe, which continue to be almost fully absorbed by the massive HCAL. White zones signify values lower than those visible in the legend.

The lower sensitivity of MCP sensors to heavy charged particles, especially when exposed to higher fluences as it was suggested in the study conducted at the PSI, can be observed when comparing measurements from the ECAL, SPD and HCAL front planes. Comparison ratios as a function of the total distance of the sensor from the central beam line are shown in figure 71 - figure 73. The response of MCP over both MTS and Alanine clearly show a decrease, at smaller distance to the center, of the ratio of MCP measurements versus MTS and Alanine, for both measurement periods. All charged hadrons are deflected horizontally by the dipole field, but sensors are distributed in an almost symmetric manner across all layers, as described previously. This of course means

that locations at the same or similar distance from the center are not experiencing the exact same hadron fluence, which explains to a certain degree the spread of values below 1 m distance to the center.

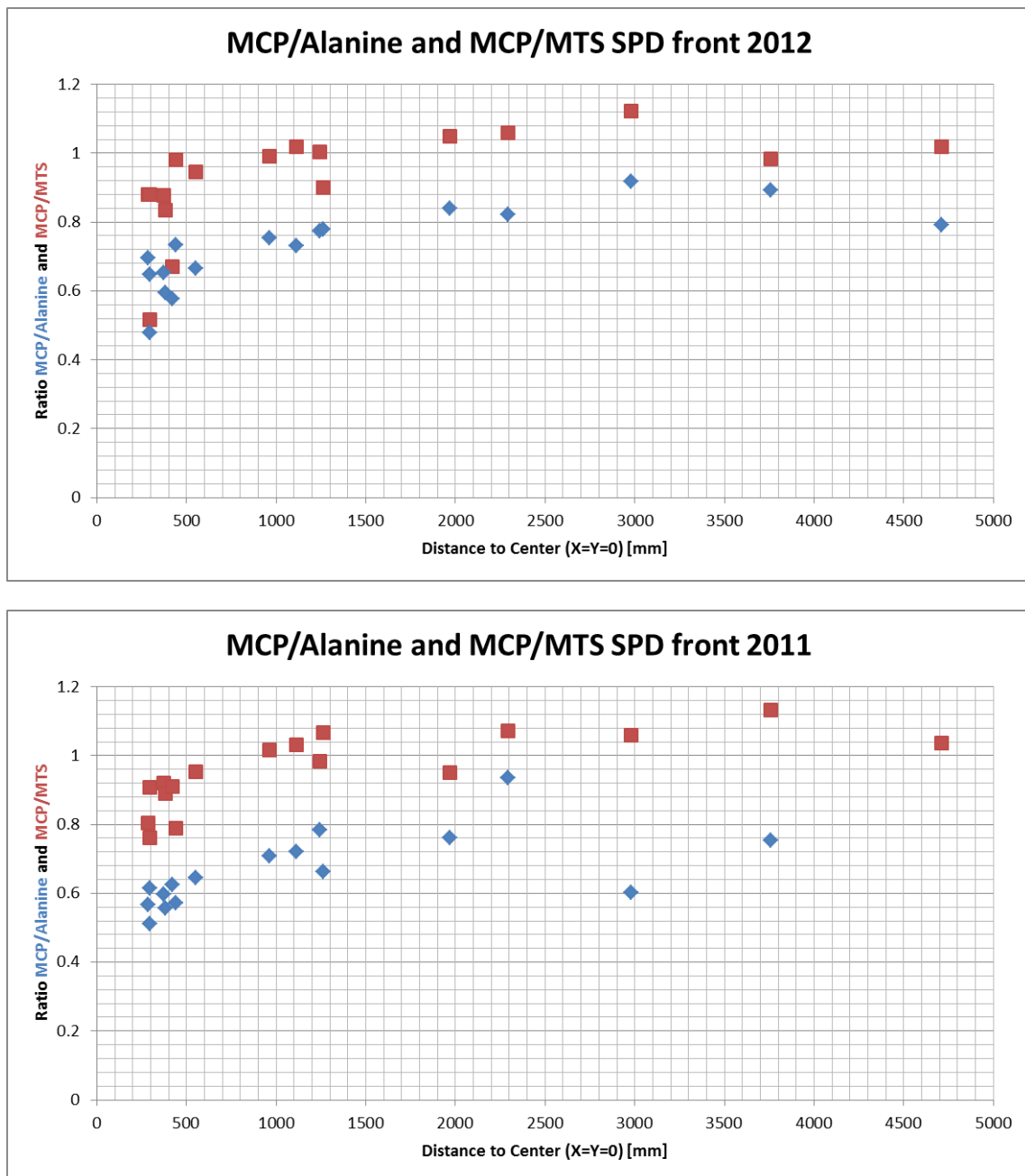


Figure 71: Comparison ratios of MCP versus Alanine and MCP versus MTS based on measurements from 2012 (top) and 2011 (bottom) over the total distance from the beam line on the front plane of the SPD. A decline in response of MCP versus both other sensor types is visible at a distance below 1 m for both measurement campaigns.

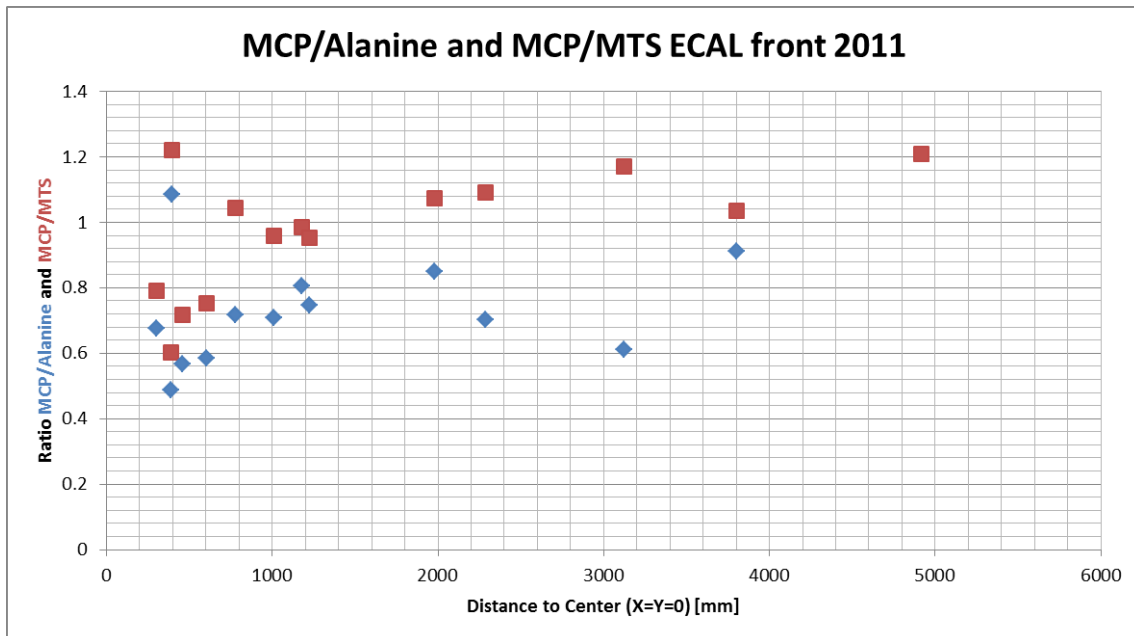
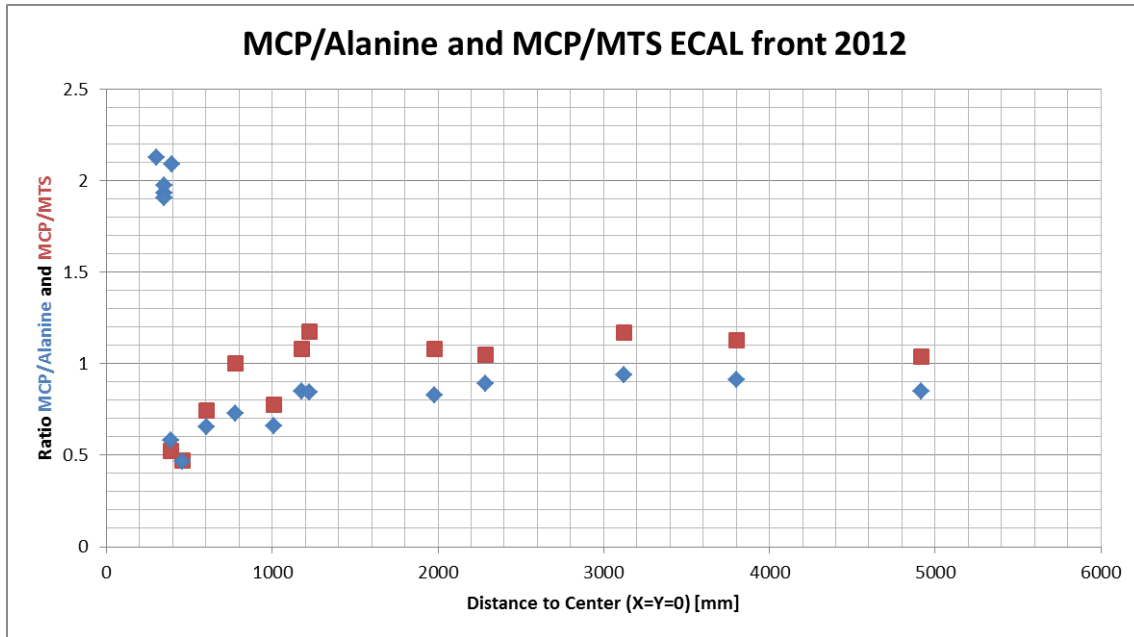


Figure 72: Comparison ratios of MCP versus Alanine and MCP versus MTS based on measurements from 2012 (top) and 2011 (bottom) over the total distance from the beam line on the front plane of the ECAL. A decline in response of MCP is visible at a distance below 1 m. The ratio of around 2 in 2012 at the very center of the ECAL front layer, in contrast to a ratio of 0.5 a few cm further from the beam, is due to the dose exceeding 1 kGy, which means that the UHTR method was employed to determine the measured dose at these points. MTS detectors at those locations were already saturated and not able to measure into the kGy range. In 2011, MTS sensors around the central area received dose above 100 Gy, which means that their linearity deviation due to calibration is countering the decrease of the MCP response in this plot.

The top plot in figure 72, in which comparison ratios of MCP versus Alanine and MTS in the ECAL front plane based on measurements from 2012 are shown, exhibits a different type of discrepancy compared to the other results. At the center of the ECAL front, Alanine and MCP measurements differ by a factor of around 2, with MCP measurements being exceptionally higher than Alanine, in contrast to all other measurements where MCP results are smaller. When the measured dose exceeds 1 kGy, as it is the case for these divergent data points, the UHTR method outlined in section 2.2.3 is applied for MCP detectors, which is also based on a calibration with ^{60}Co γ -rays. This readout method is still under evaluation for complex mixed radiation fields as

present around the LHCb experiment and fails to approach Alanine measurements in this case. MTS detectors at these locations were already saturated and not able to measure into the kGy range, which of course means there are no data points in the plot for MCP/MTS for dose above 1 kGy.

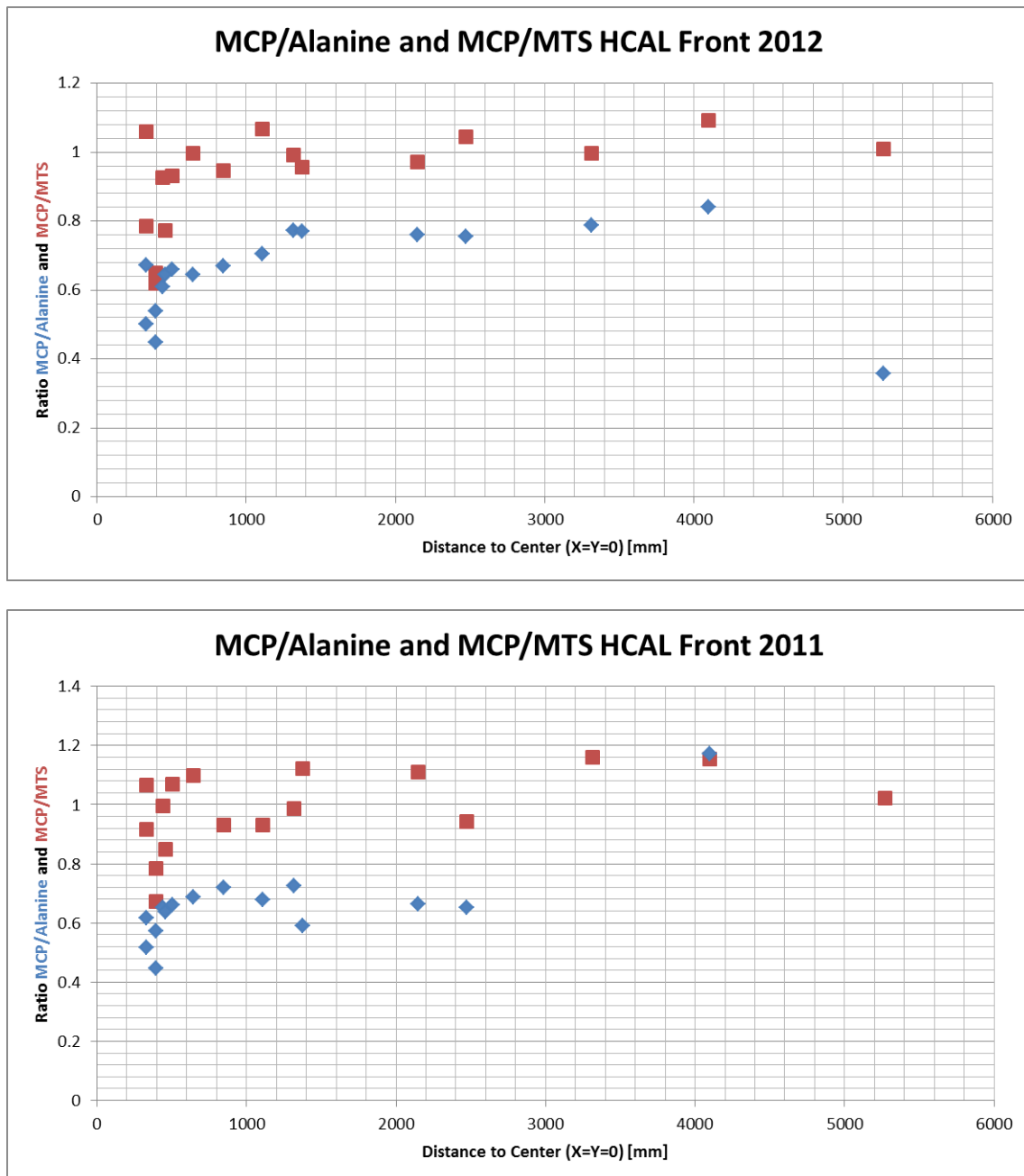


Figure 73: Comparison ratios of MCP versus Alanine and MCP versus MTS based on measurements from 2012 (top) and 2011 (bottom) over the total distance from the beam line on the front plane of the HCAL. A decline in response of MCP versus both other sensor types is visible at a distance below 1 m. At the HCAL front plane, the decline is more pronounced in close proximity to the center, where more hadrons with high energy were able to pass through the heavy detectors in front. Alanine measurements from 2011 at larger distance from the center were considered out of their measuring range and showed high deviations.

The decrease of the MCP response close to the beam line on the front of the HCAL, as shown in figure 73, is more pronounced than on the front of the other detectors. This is due to the fact that a higher fraction of high energy hadrons with respect to other particles were able to pass through the PS, SPD and ECAL in this area.

5.1.5.2 MTS LINEARITY ABOVE 100 GY

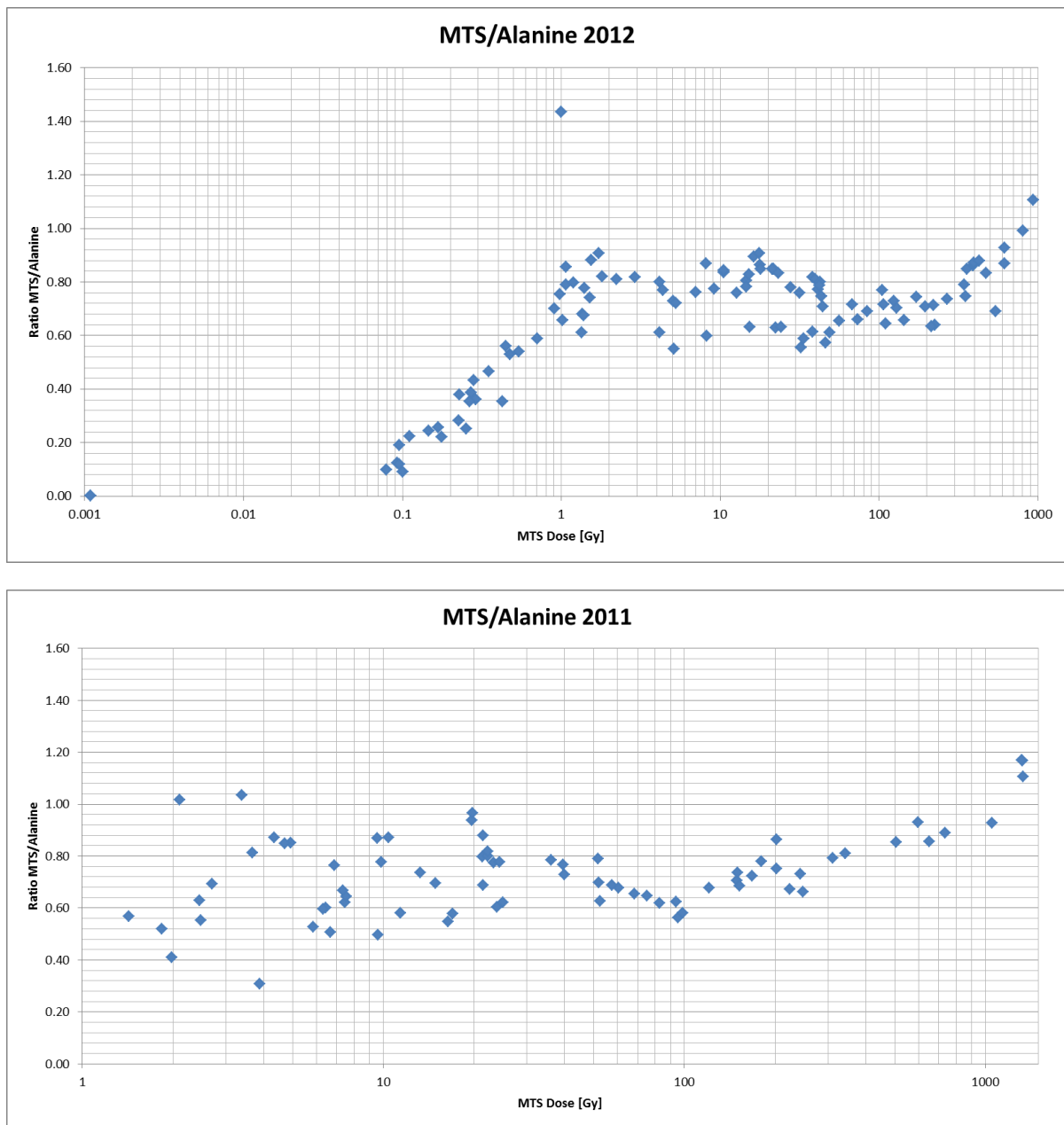


Figure 74: Comparison ratio of MTS versus Alanine measurements over the full dose range of all measurements at LHCb conducted during LS1 (top) and during the Christmas break of 2011 (bottom). Above 100 Gy, an increase of the response of MTS compared to Alanine can be observed in both plots. In the more recent measurements from LS1, the decreasing accuracy of Alanine below 1 Gy is responsible for the steady decrease of the calculated ratio. The results of 2011 do not even feature measurements below 1 Gy, as they were considered out of range. The general accuracy of Alanine measurements below 50 Gy appears to be worse in 2011 than in 2012, most likely because of the equipment used by the contractor in charge of the readout.

The behavior of Alanine above a dose of 100 Gy is more stable than that of MTS detectors, where the applied linearity correction does not take into account a different reaction to hadrons. When compared to either MCP or Alanine measurements in the range between 100 Gy and 1 kGy, MTS sensors display a response increasing with the rise of the measured dose toward the upper limit of 1 kGy. In this higher range of sensitivity (>100 Gy) of the MTS dosimeter, the deviation of the linearity correction due to a different field composition becomes even more severe than for MCP sensors. This increase can be seen in the higher dose range above 100 Gy in the plot presented in figure 74. It is showing ratios between measurements of MTS compared to Alanine and

MCP sensors for all passive dosimeters, including those of the calorimeters, which were collected in the experiment in the two measurement campaigns. Under the assumption that the measurement method and accuracy for the TLDs remained constant between the two measurement campaigns, the increased accuracy of the new Alanine readout equipment used in 2012 can also be observed in figure 74. In 2011, ratios between measurements deviate more strongly for a measured value of ≤ 3 Gy, whereas the new equipment provides a stable readout down to a lower limit of 1 Gy.

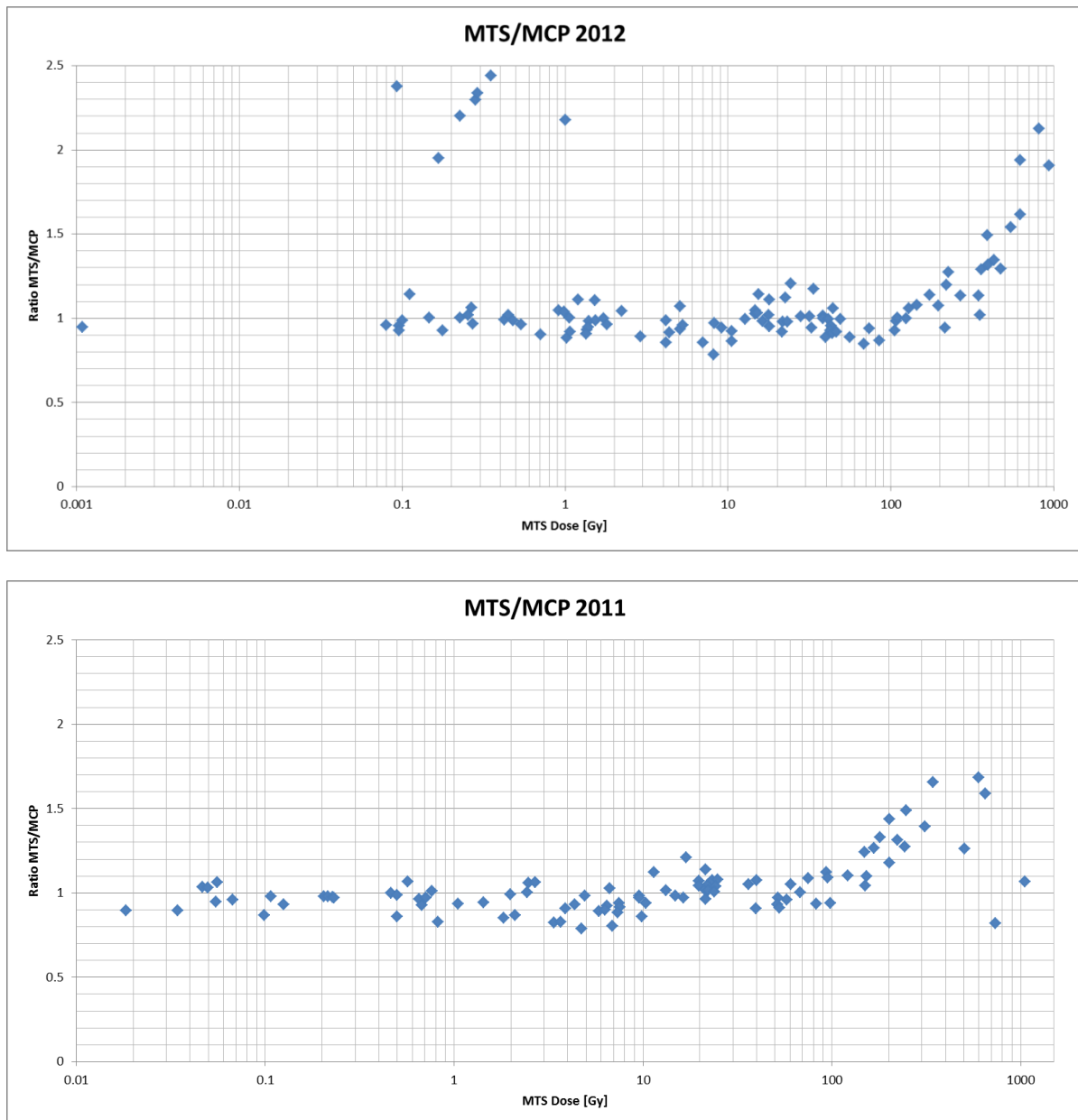


Figure 75: Comparison ratio of MTS versus MCP measurements over the full dose range of all measurements at LHCb conducted during LS1 (top) and during the Christmas break of 2011 (bottom). Above 100 Gy, an increase of the response of MTS compared to MCP can be observed. Measurements below 100 Gy from 2012 showing differences greater than a factor of 2 are assumed to be readout errors. Measurements from 2011 between 500 and 1000 Gy which do not follow the upward slope of ratio points have been readout manually because of technical problems, and do not reflect the linearity deviation that can be observed in MTS/MCP and MTS/Alanine ratio plots above a dose of 100 Gy.

In figure 75, the 7 measurements between 0.1 and 1 Gy from 2012 showing differences greater than a factor of 2 between MCP and MTS are assumed to be readout errors for at least one of the sensor types, since no such discrepancy was observed at these specific locations or at this dose range in the results from 2011 and TLD sensors in general agree very well with each other below a dose of 1 Gy.

In the 2011 comparisons of MTS/MCP in figure 75 there are three points visible between 500 Gy and 1000 Gy which seem to approach again a ratio of 1 against MCP values instead of following the upwards slope of the other measurements. However, these three values are the only ones in the plot that were estimated by hand due to technical problems with the readout process. Therefore, they do not reflect the linearity deviation of MTS above a value of 100 Gy that can be observed in the earlier plots.

5.1.6 SIMULATION AND MEASUREMENT COMPARISONS

After evaluating the behavior, and therefore the strengths and weaknesses of the various dosimeters in certain scenarios, certain measurements are considered more reliable than others depending on the situation. In order to reasonably estimate the properties of the radiation field in areas between and around those measurements, it is imperative to know where and why simulation results differ from them to be able to rely on its predictions and correct or apply safety factors when necessary. For this reason, a detailed comparison between simulation and measurements from TLD and Alanine dosimeters in all measurement locations inside the calorimeter detectors was carried out and is described in the following sections. Simulation results will be compared only against 2012 measurements, as the overall error for most readouts is considered to be less than that of readouts from 2011, due to improved readout procedures and higher dose values across the board. Hence, it will be easier to visualize trends in simulation behavior.

5.1.6.1 MCP VERSUS SIMULATION

As explained in section 2.2.3 and 5.1.5, TLD measurements are only considered reliable for dose values around and below 1 Gy, but they can theoretically measure in the entire dose range that the LHCb calorimeters have been exposed to until LS1. Of the 2 basic types that are utilized in the experiment, the analysis of MCP dosimeters has shown a decrease in response in regions close to the beam pipe when compared to MTS and Alanine measurements.

In the plots in figure 76 - figure 79 comparisons between MCP and Alanine dosimeters are shown together with the comparisons between MCP and estimates from the simulation. The comparisons between MCP and Alanine which were already provided earlier are shown again here in order to illustrate that the decrease of the MCP response close to the beam in all areas in front of the HCAL is not reproduced by the simulation either, which renders the simulation in line with Alanine and MTS measurements. In the graphs, the ratio between MCP and simulation results shows similar drops at the HCAL, ECAL and SPD front sides in regions close to the beam.

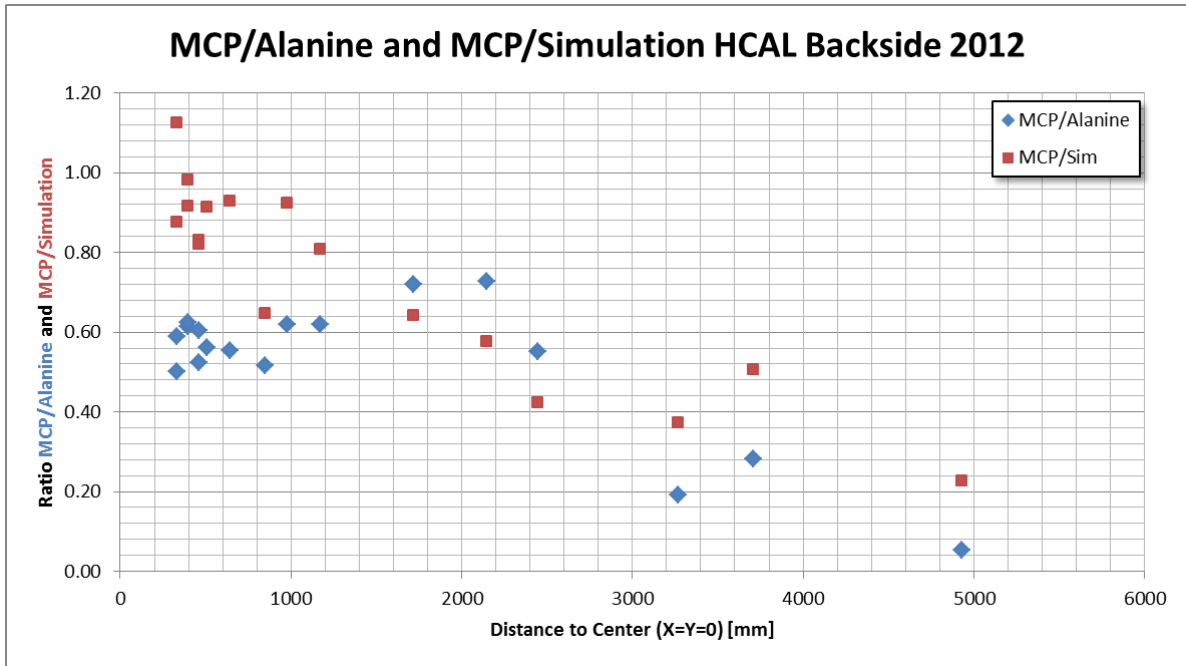


Figure 76: Comparison ratios of MCP versus Alanine and MCP versus simulation results based on measurements from 2012 over the total distance from the beam line on the back plane of the HCAL. No decrease in response of MCP is visible at a distance below 1m. The drop in ratio for positions further than 3m away is caused by overestimation of the simulation due to statistical error and insufficient detail in the description of the geometry.

Comparison ratios between MCP and simulation values as well as the comparisons between MCP and Alanine for the backside of the HCAL are shown in figure 76. In the central regions, MCP values agree better with the simulation. In contrast to the other 3 planes of measurement, no visible drop in response of MCP versus Alanine or simulation can be observed. This coincides with the fact that most high energy hadrons are absorbed within the main body of the HCAL, moving MCP results more in line with those of MTS and Alanine.

At a radial distance larger than 3 m from the beam, comparison ratios drop heavily as the simulation estimates become higher than measurements at these remote locations. The difference in dose is likely being influenced by the omission of the muon service towers and other support structures in the vicinity in the FLUKA geometry. These structures could shield positions where dosimeters are placed from radiation that is backscattered from other parts of the experiment. Alternatively, a readout error on the side of the TLDs cannot be totally excluded, since even MCP-7 and MTS-7 measurements differ by more than a factor of 2 on two of these three points.

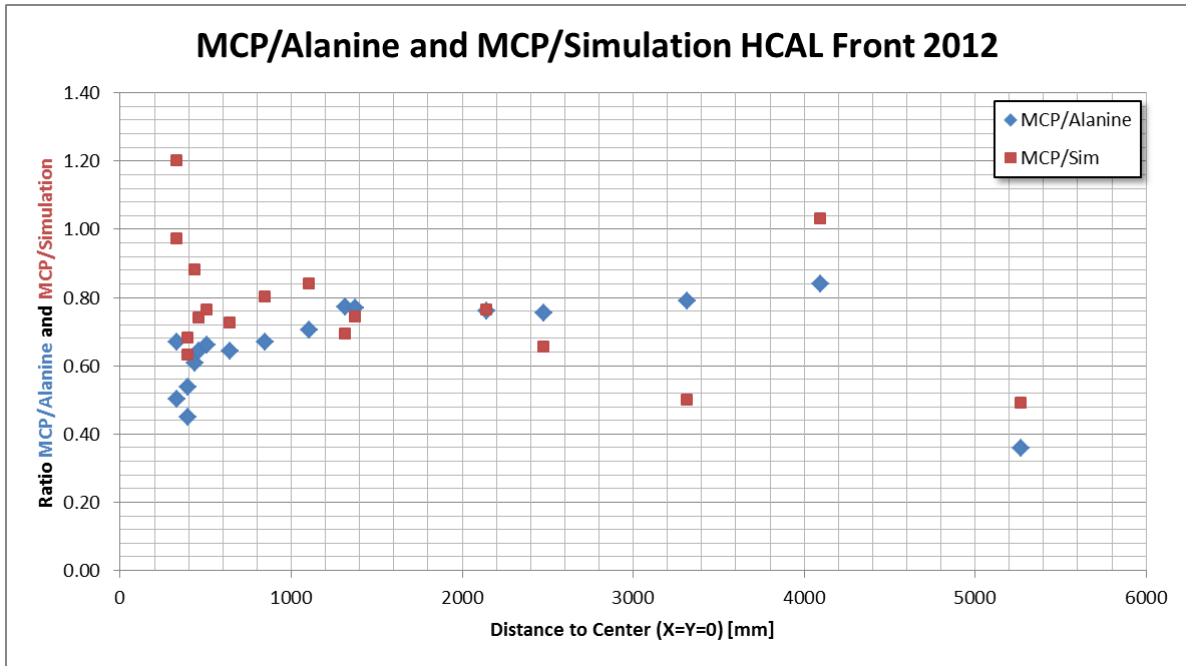


Figure 77: Comparison ratios of MCP versus Alanine and MCP versus simulation results based on measurements from 2012 over the total distance from the beam line on the front plane of the HCAL. The decrease in response of MCP is visible at a distance below 1m when compared to simulation and Alanine values.

In contrast to Alanine, and as shown earlier to MTS measurements, a decrease in response of MCP sensors is not as visible when compared to simulation values in the central region, as can be seen in figure 77. The inaccuracies relative to the three points that are closest to the beam, where the decrease should be most visible, are caused by an exceptional deviation of the simulation in the areas directly above and below of the beam (see discussion in section 5.1.4.2). As the comparison of simulation values with Alanine measurements will show in the next section, this deviation is difficult to explain and could be inherently caused by the simulation setup. Taking this underestimation into account, simulation values still agree quite well with MCP measurements on the front of the HCAL.

The situation on the front of the ECAL is illustrated in figure 78. Although the beginning of a drop of the MCP response is visible within a radius of 1 m from the beam, almost all measurements of MCP and Alanine are within a factor of 1.5 of each other as well as with the simulation. The most central values exhibit the highest deviation from the usual behavior, measuring around twice as much dose as Alanine. As explained earlier, the UHTR method was applied to the readout of MCPs, because they received dose above 1 kGy. The UHTR method is still highly experimental and has not been tested extensively enough to be reliable for mixed fields. For these points, a comparison of simulation estimates with Alanine measurements will be more informative.

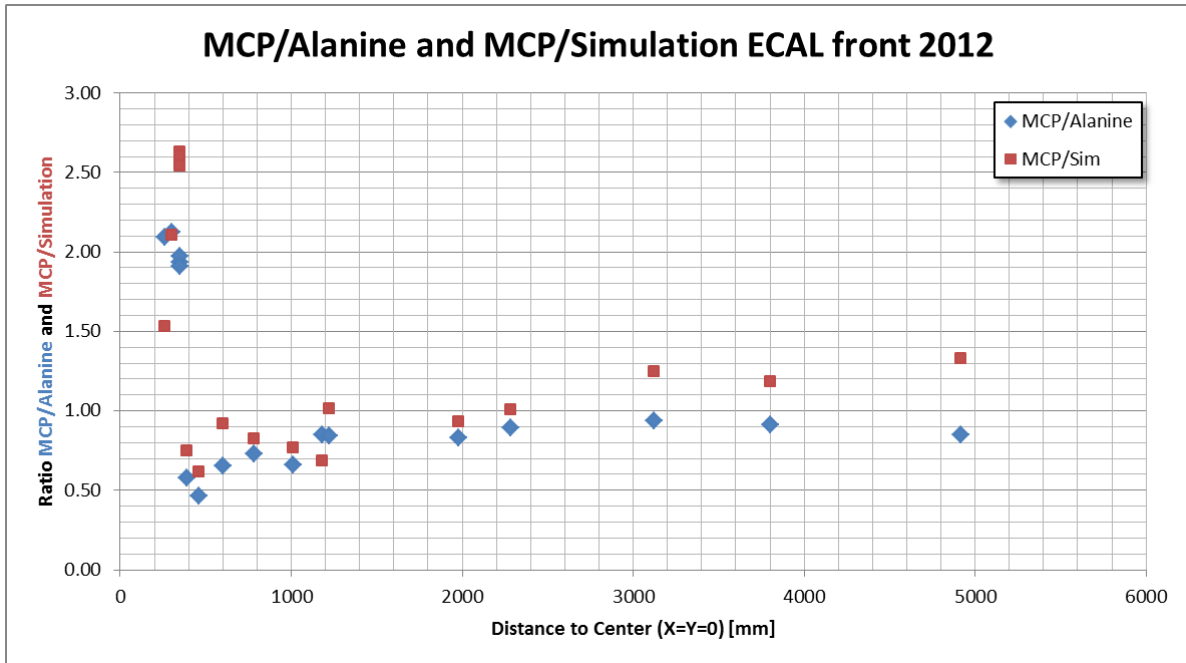


Figure 78: Comparison ratios of MCP versus Alanine and MCP versus simulation results based on measurements from 2012 over the total distance from the beam line on the front plane of the ECAL. The decrease in response of MCP is visible at a distance below 1m when compared to simulation and Alanine values. Values larger than 1.5 at the lowest distance to the beam are a consequence of the UHTR readout method for MCP dosimeters, which is applied when dose values exceed 1 kGy. The UHTR readout method has not been tested thoroughly for mixed fields and is still highly experimental.

The ratio of all values of MCP/Simulation in the plot of figure 79 is particularly higher than on any other detector plane. This discrepancy has two main reasons.

On one hand, it is an effect of the large binning region for the FLUKA scoring in comparison with the small region where the measurements apply. Dose values differ greatly between the area in front of the SPD/PS and the area inside and behind the detector, because of the lead plate in between the detector volumes. Cascades of secondary particles are started within the heavy material, and they are responsible for increasing the dose between the SPD and the front of the ECAL. Part of this radiation backscatters and hits the dosimeters that are placed inside small openings on the front side of the SPD detector structure itself, just in front of the lead. The estimation of dose with the FLUKA simulation was performed by averaging within cubic bins of 20 cm edge length on the outside and 5 cm within 1 m of the beam. The 20 cm bins encompass the region in front of the SPD, which has lower dose, as well as a very small part of the higher dose region after the lead plate in the SPD/PS. The position of the bin in relation to the dosimeters approximately represents the actual position of the measurement, but not as exactly as in the other locations within the calorimeter detector.

On the other hand, the information on the position of the dosimeters along the z axis in front of the SPD at 1231 cm from the IP, which was provided by the calorimeter group, corresponds to bins from the 5 cm grid which average dose values between 1230 cm and 1235 cm in z. This area mainly consists of a large air volume in front of the first scintillating detector volume in the geometry of the simulation, which is also missing the material of the envelope structure of the SPD, including the pockets for the passive boxes. In addition, the amount of low-energy backscattered electromagnetic radiation from the lead plate that hits the sensors decreases within a few cm of distance in upstream direction. For these reasons, the average in a bin on the front of the SPD gives a reduced value in comparison with the radiation that the actual dosimeters experience. The average in the bin is therefore expected to be lower than the measurement.

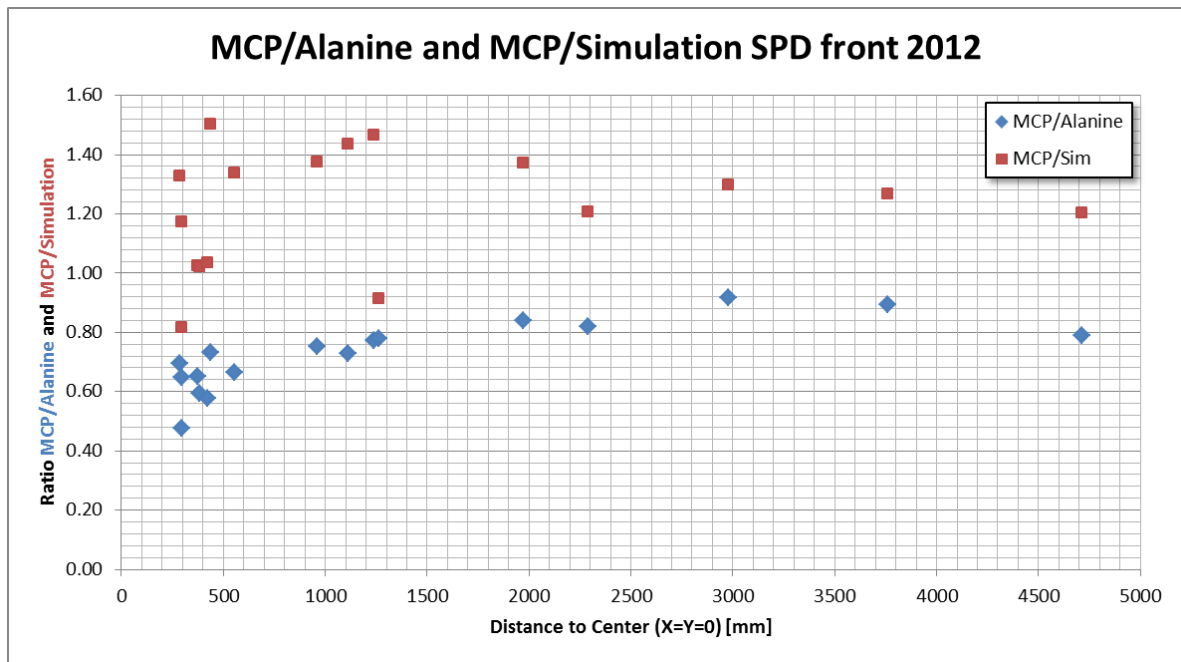


Figure 79: Comparison ratios of MCP versus Alanine and MCP versus simulation results based on measurements from 2012 over the total distance from the beam line on the front plane of the SPD. The decrease in response of MCP is visible at a distance below 1m when compared to simulation and Alanine values. MCP/Simulation values are generally higher than in other plots as a consequence of the bin placement in the FLUKA scoring, which averages over a region that is too large to be as accurate as the estimations for the other detector planes.

Nevertheless, all simulation results stay roughly within a factor of 2 of the Alanine measurements, as it will be shown in the next section. The deviation is systematic for all measurement points and the drop of MCP sensitivity that can be seen when comparing MCP to Alanine is reproduced by the simulation as well.

5.1.6.2 ALANINE VERSUS SIMULATION

Earlier plots have shown that with only a handful of exceptions, different types of measurements generally agree quite well with each other as well as with simulation results in their range of sensitivity. In order to get a better idea about the accuracy of the simulation, its results will be compared with Alanine measurements in the following plots, which are considered reliable within the range of most dose measurements inside the calorimeter detectors.

The comparison of Alanine measurements with FLUKA simulation results for the backside of the HCAL during the measurement period of 2012 at 8 TeV CM collision energy is shown in figure 80. While the ratio generally stays within a factor of 2, lower values of the simulation in regions close to the center can be observed. With increasing distance, the discrepancy becomes less pronounced. At a distance of >3 m from the beam, the simulation is giving lower values than the Alanine: this is caused by the fact that the Alanine readout is at and below its lower sensitivity limit of 1 Gy. Therefore the rightmost 3 points in the plot are not to be relied on.

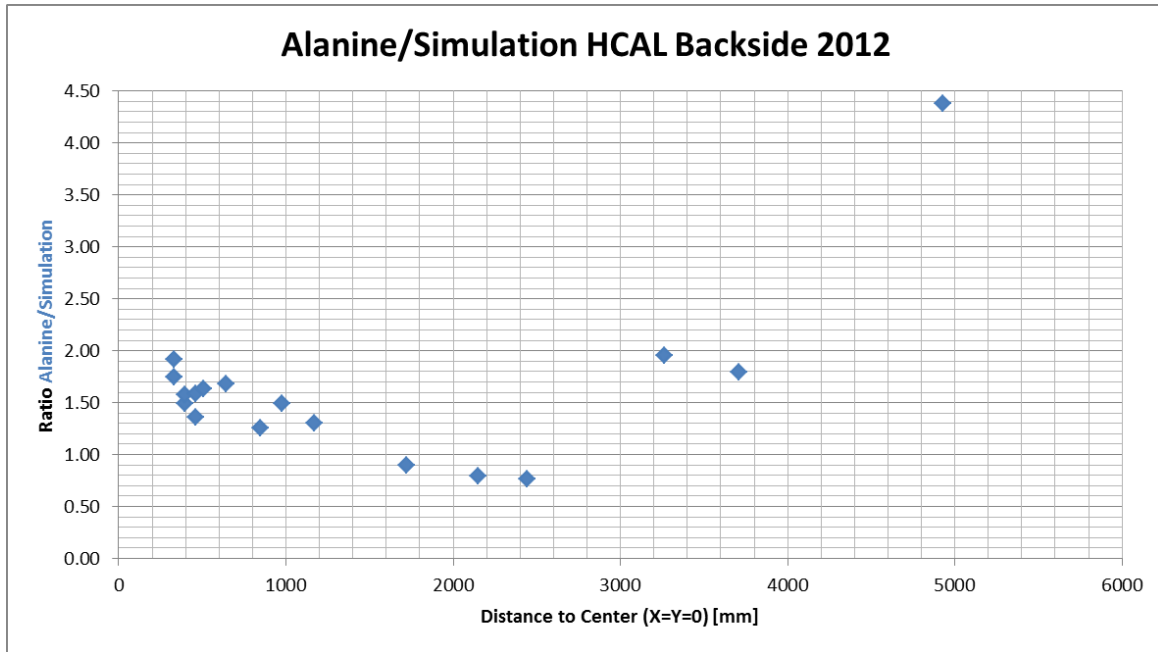


Figure 80: Comparison of Alanine measurements with FLUKA simulation results for the backside of the HCAL during the measurement period of 2012 at 8 TeV CM collision energy. Alanine measurements are higher by around 50% up to 90% close to the central region. The 3 points that are furthest from the center are not valid, as the Alanine measurements in that region were around and lower than 1 Gy, rendering them unreliable and unfit for comparison.

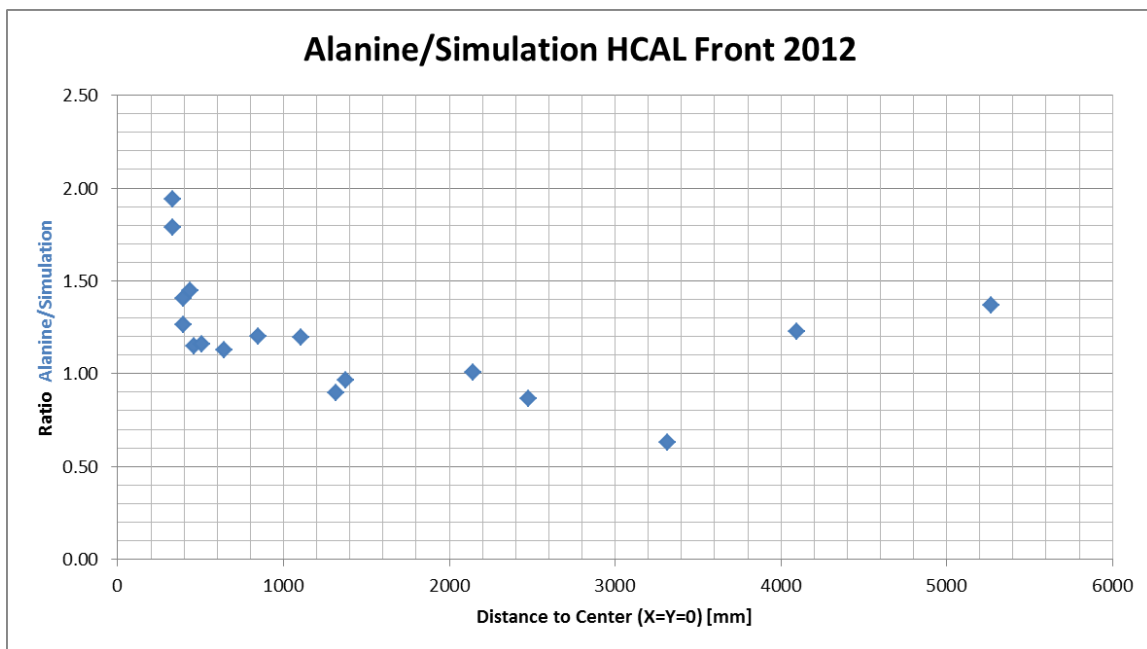


Figure 81: Comparison of Alanine measurements with FLUKA simulation results for the front of the HCAL during the measurement period of 2012 at 8 TeV CM collision energy. Alanine measurements are higher by a factor of up to 2 close to the central region.

On the front of the HCAL, the agreement between simulation and measurement is generally very good, with the exception of the most central region, where Alanine always measures higher dose values than the simulation estimates, as can be seen in figure 81. The simulation estimates are generally lower by a factor of almost 2 for the points that are closest to the beam. The shape of the simulated dose distribution, which was illustrated earlier in figure 62 suggests a highly visible decrease in dose on top and bottom of the beam line

with respect to the horizontal distribution. While this effect is expected to a certain degree because of the magnetic field of the LHCb dipole, the decrease could also be exaggerated by the simulation, although it is not yet clear for which reason this would occur. Nonetheless, even these discrepancies between simulation and measurements close to the beam do not exceed a factor of 2.

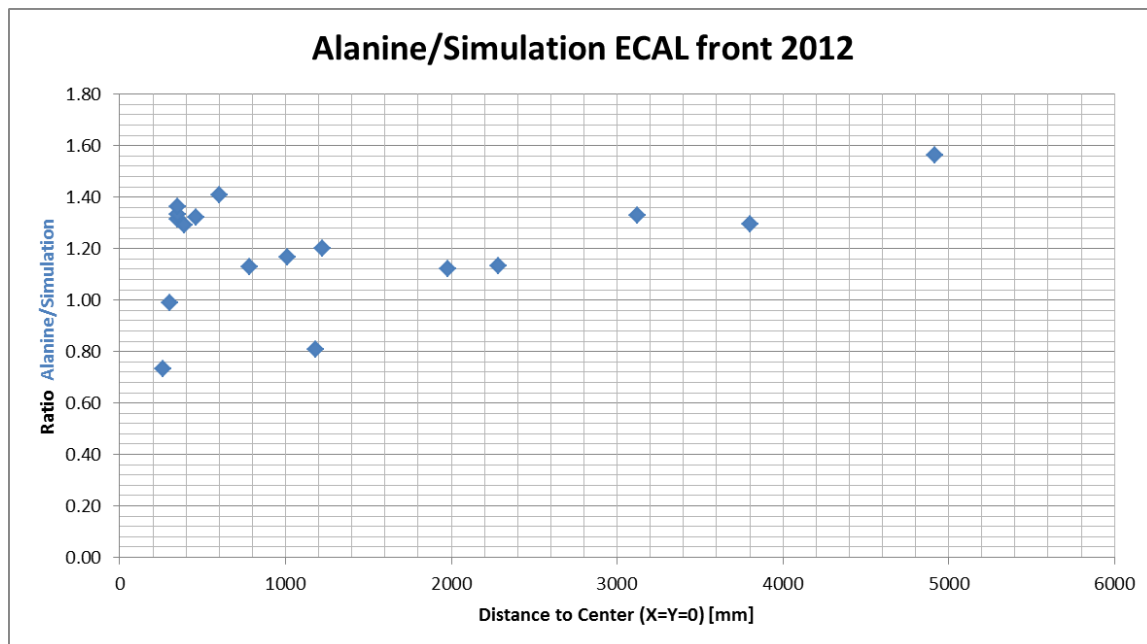


Figure 82: Comparison of Alanine measurements with FLUKA simulation results for the front of the ECAL during the measurement period of 2012 at 8 TeV CM collision energy. Alanine measurements are higher by a factor of up to 1.5 close to the central region.

The situation on the front of the ECAL, shown in figure 82, is similar to that on the front of the HCAL, as most of the values in the plot point to a ratio between 10% and 20%, with the exception of the central regions, where the simulation is lower by a factor of up to 1.5 with respect to Alanine measurements. In part, this behavior of the simulation can be explained by the size of the binning. Although simulation estimates from inner regions up to a distance of about 1 m along x and y are based on a binning of $5 \times 5 \times 5 \text{ cm}^3$ cubes, the differences in actual dose values between two opposing edges in one cube can be large enough to cause a disparity ratio of this size. The binning grid used in the simulation is not small enough to account for small variations in the positions of the dosimeters. Another part of the explanation is that the simulation estimates might be generally lower than Alanine measurements by a factor of up to 2 in the central regions of the experiments.

In one point at the center of the ECAL front the simulation goes against the trend by estimating a higher dose than Alanine at a location above the beam pipe. As explained in section 5.1.4.3 when discussing the maximum measurement results at the front of the ECAL, this is a side effect of the position of the simulation binning grid in relation to the dosimeters. A more sophisticated interpolation method for extracting the simulation result would have seen this data point much closer to a ratio of 1. This was tried and confirmed, however in order to be consistent within the thesis, the average from 2 adjacent 5 cm bins has been taken as it was done in similar cases.

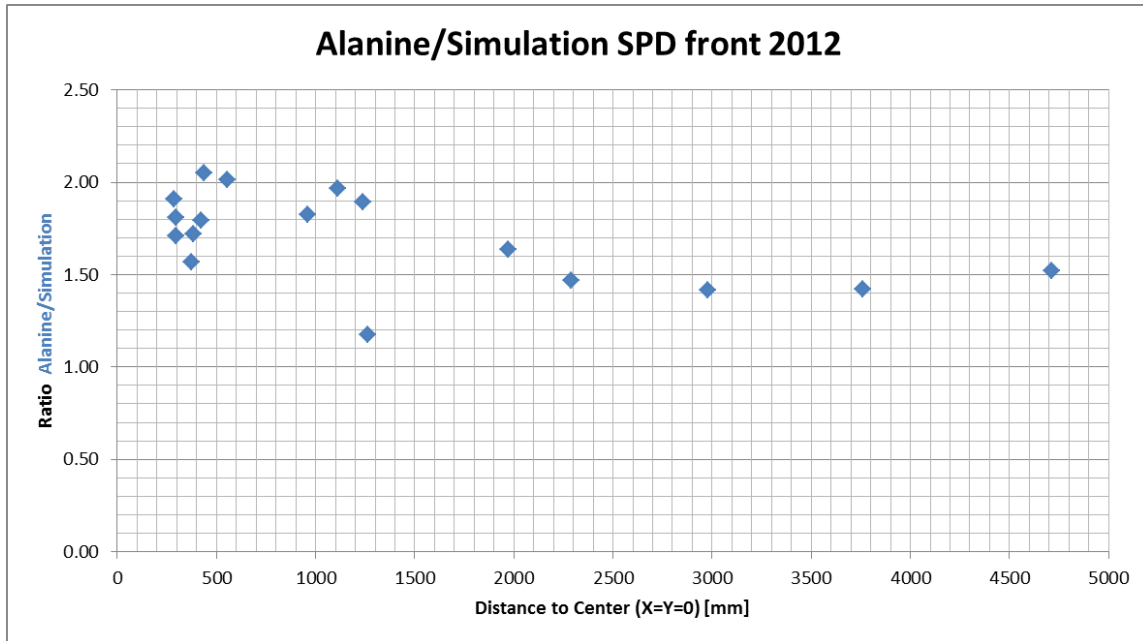


Figure 83: Comparison of Alanine measurements with FLUKA simulation results for the front of the SPD during the measurement period of 2012 at 8 TeV CM collision energy. Alanine measurements are higher by a factor of up to 2 close to the central region. Measurements on the SPD front are higher than simulation estimates at an above average rate compared to the other detector planes. This can be explained by the large bin size used for extracting simulation results compared to the thin detector volume. The radiation field inside the bin changes heavily within a few cm due to the incorporated lead plate.

The ratio in the plot of figure 83 is generally higher than those of the 3 planes discussed before, because of the large binning region in comparison with the small region where the measurements apply. Dose differs greatly between the area in front of the SPD and the area inside and behind the detector, because of the lead behind the PS detector that is placed closely in front of the SPD. The estimation of dose with the FLUKA simulation was performed by averaging within cubes of 20 cm as well as cubes with 5 cm edge length, which approximately represents the actual position of the measurement, but not as exactly as in the other locations within the calorimeter detector. Even without taking into account this systematic deviation, all results still remain roughly within a factor of 2 of the Alanine measurements.

In general, simulation and Alanine results agree within a factor of 2 or better, with a few exceptions that are caused by readout errors or high uncertainties in outlying regions where very low dose was deposited. Regions close to the beam show slightly lower values of the simulation results with respect to measurements, which becomes less obvious at a few meters distance from the center.

5.1.7 DIFFERENCES IN MEASUREMENTS BETWEEN 7 TEV CM AND 8 TEV CM

The differences in the field composition between the operational periods of 2011 and 2012 due to the increase of the collision energy from 7 TeV to 8 TeV CM are small. Nevertheless they are visible in the results of the passive dosimeter readouts. The higher energy of the primary beam particles with 8 TeV CM instead of 7 TeV CM manifests itself in a marginally more forward-directed field of secondary particles with a slightly higher penetration power. It is shown in figure 84 - figure 87 that during 2012, dosimeters consistently registered a higher dose per collision than during 2011, where the measured values have been scaled to 1 fb^{-1} for both 2011 and 2012.

To calculate the ratio in the following plots, the simple rescaling of dose measurements to 1 fb^{-1} was done with equation (11) where D_{2012} and D_{2011} are the respective dose measurements from each measurement campaign, and $\text{Int. } \mathcal{L}_{201X}$ is the integrated luminosity value, which is 2.21 fb^{-1} for 8 TeV CM proton-proton collisions (2012) and 1.26 fb^{-1} for 7 TeV CM (2011):

$$\text{Ratio} = \frac{\frac{D_{2012}}{\text{Int. } \mathcal{L}_{2012}}}{\frac{D_{2011}}{\text{Int. } \mathcal{L}_{2011}}} \quad (11)$$

Values from the simulation are calculated per collision and are scaled accordingly, using the respective (inelastic + diffractive) cross sections of 72 mb for collisions at 7 TeV CM and 74 mb for collisions at 8 TeV CM. The former number was extracted using the FLUKA DPMJET code in 2010, which uses the event generator PYTHIA for proton-proton collisions [39] [60] [61], while the latter was estimated based on the increase in collision energy in 2012.

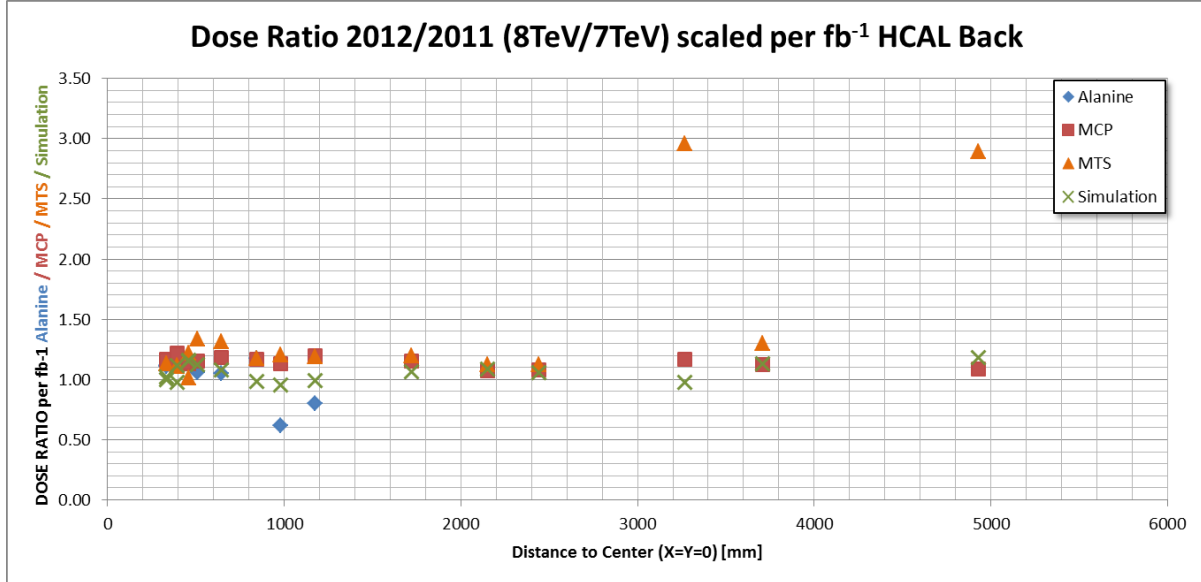


Figure 84: Ratio between measurements for each dosimeter type on the backside of the HCAL at a collision energy of 7 TeV CM during 2011 compared to 8 TeV CM during 2012, normalized to 1 fb^{-1} . An increase between 10% and 20% of measured dose for Alanine (blue), MCP (red) and MTS (orange) sensors can be observed. The two deviations for MTS with a ratio of almost 3 are considered readout errors of the dosimeters used during 2012. In green, ratios between the 2 energies for FLUKA simulation results at detector positions are given. With a few exceptions, the simulation generally predicts an average increase of 6% in dose for 8 TeV CM collision energy, which is mostly lower than what was observed by measurements.

Dose ratios from the HCAL backside are shown in figure 84. Almost all values from measurements gather around a ratio between 10% and 20% above 1, with the exception of two Alanine measurements at a distance of about 1 m from the center, and two MTS measurements further outside. Both Alanine measurements are at the lower limit for readout and therefore the measurements from 2011 have a larger readout error as described earlier. The two deviations for MTS that show a ratio of almost 3 are considered as readout errors of the dosimeters from the batch measured in 2012.

Estimates from the simulation for the backside of the HCAL point to an increase in dose between 0% and 13%, averaging around 6%. As the body of the HCAL in the simulation might be slightly more massive than the real detector because of missing airspaces in the main volume, the simulation values are expected to differ slightly from measurements.

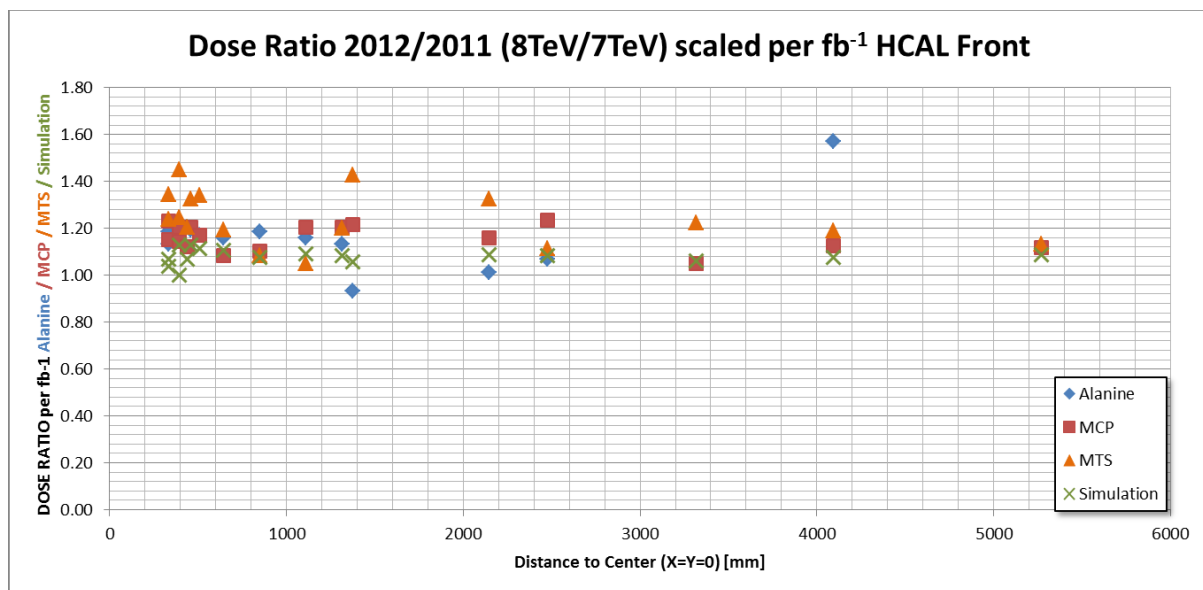


Figure 85: Ratio between measurements on the front of the HCAL at a collision energy of 7 TeV CM during 2011 compared to 8 TeV CM during 2012, normalized to 1 fb⁻¹. An increase between 10% and 20% of measured dose for Alanine (blue), MCP (red) and MTS (orange) sensors can be observed. A larger ratio for MTS sensors at low distance to the center can be explained by linearity issues of their calibration for the dose range between 100 Gy and 1 kGy. Alanine deviations at a large distance from the center are again ascribed to the low accuracy of the results from 2011 in the low dose range around 1 Gy. In green, ratios between the 2 energies for FLUKA simulation results at detector positions are given. With a few exceptions, the simulation generally predicts a 5% to 10% increase in dose for 8 TeV CM collision energy.

A larger increase of measured dose on the HCAL front with respect to its back for the collisions with higher energy is shown in figure 85. Most values lie between 10% and 20% for Alanine (blue), MCP (red) and MTS (orange) sensors. The larger ratios for MTS sensors at smaller distance from the center can be explained by linearity issues of their calibration for the dose range between 100 Gy and 1 kGy. As before, Alanine deviations at a large distance from the center can be ascribed to the low accuracy of the results from 2011 in the low dose range. The FLUKA simulation generally agrees with the trend that can be observed from measurements, although to a lesser degree, pointing to an increase in dose between 4% and 10%, when moving from 7 TeV CM to 8 TeV CM collisions. The average of the data points from simulation predicts an increase of 8%.

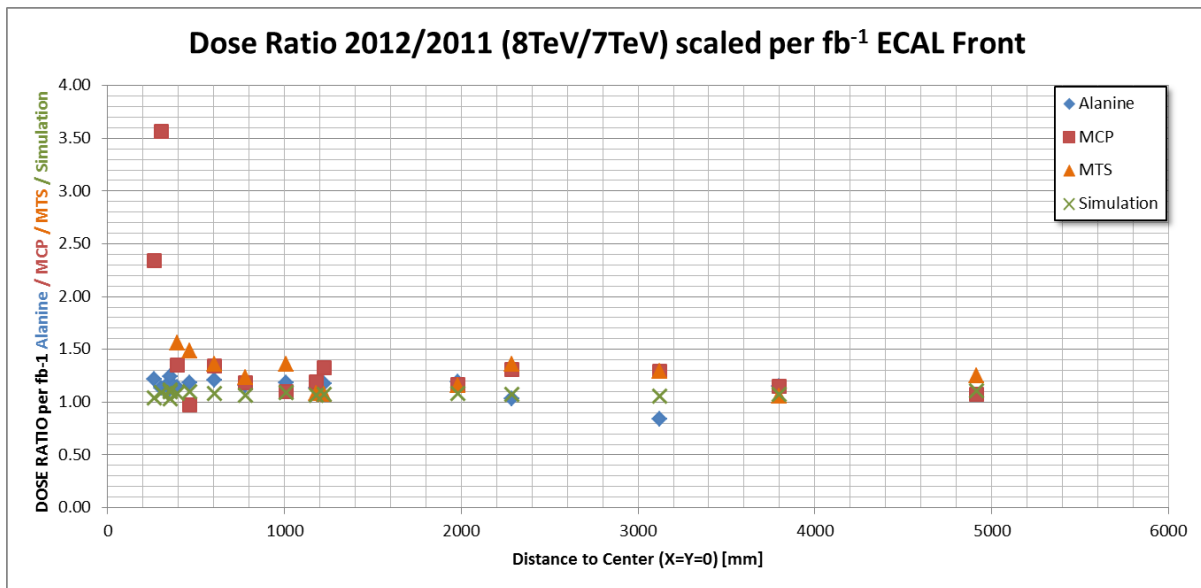


Figure 86: Ratio between measurements on the front of the ECAL at a collision energy of 7 TeV CM during 2011 compared to 8 TeV CM during 2012, normalized to 1 fb^{-1} . An increase between 10% and 20% of measured dose for Alanine (blue), MCP (red) and MTS (orange) sensors can be observed. A larger ratio for MTS sensors at low distance to the center can be explained by linearity issues of their calibration for the dose range between 100 Gy and 1 kGy. An even higher discrepancy for MCP ratios exceeding 2 near the center is caused by a larger inaccuracy of the UHTR readout method applied on sensors from 2012. Alanine deviations at a large distance from the center are again ascribed to the low accuracy of the results from 2011 in the low dose range around 1 Gy. In green, ratios between the 2 energies for FLUKA simulation results at detector positions are given. With a few exceptions, the simulation generally predicts a 5% to 10% increase in dose for 8 TeV CM collision energy.

On the front of the ECAL, the ratios, which are shown in figure 86, are comparable to the front of the HCAL. The increase in dose caused by the higher collision energy lies between 10% and 20% for most measurement positions. Deviations in the central region for MTS and on the more outlying regions for Alanine are due to the same reasons as on the front of HCAL. An even higher discrepancy for MCP ratios near the center is caused by the inaccuracy of the UHTR readout method for the measurements of 2012/13. This method was applied on sensors that received a dose of more than 1 kGy. Estimates from the simulation suggest an average increase in dose of about 8% across the plane when changing the collision energy from 7 to 8 TeV CM.

The ratio values on the front of the SPD, pictured in figure 87, are in line with the other results. An increase between 10% and 20% of measured dose for most Alanine, MCP and MTS sensors can be observed, which mirrors the values seen at the HCAL and ECAL front planes. Deviations in the central region for MTS and in the more outlying regions for Alanine are similar as well and can be explained by the same reasons. Estimates from the simulation suggest an average increase in dose of about 7% over the whole plane, where individual comparison values range from 5% to 10% change between the two collision energies.

In summary, most of the larger inconsistencies of TLD measurements in between the two measurement campaigns are in the high dose regions, where the linearity correction and the inaccuracy of the UHTR method as described earlier influence the ratio. Other strong deviations between TLD types, as for example at distances of 3 m and 5 m at the back of the HCAL, are considered to be caused by readout errors.

Discrepancies between Alanine measurements that seem to occur at greater distance to the center are explained by the rather unreliable readouts from 2011 at a dose range around 3 Gy and below, due to the properties of the readout equipment used.

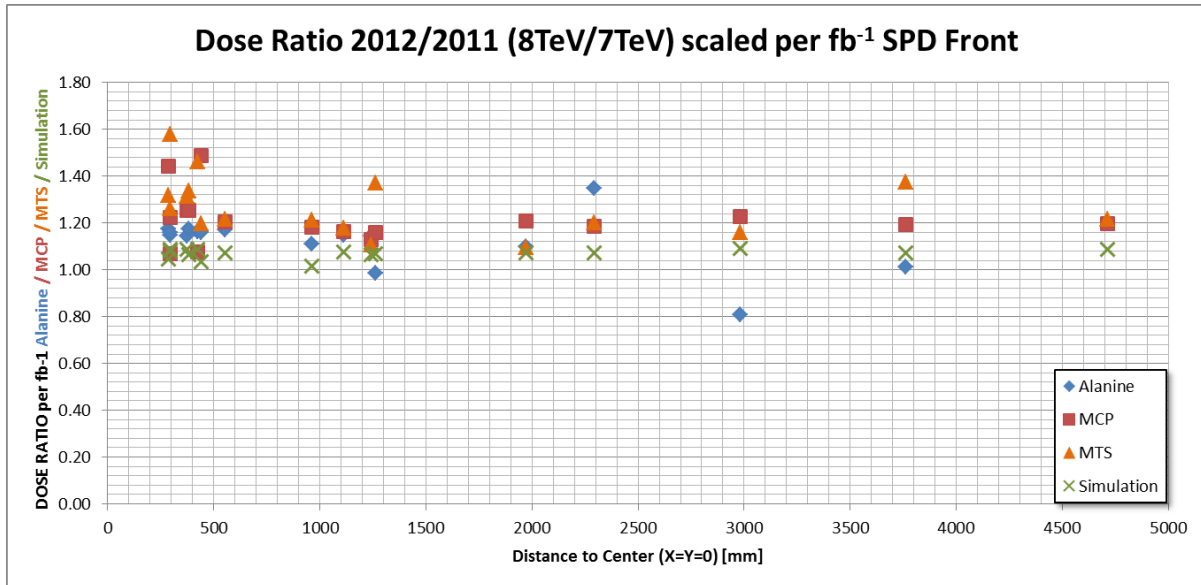


Figure 87: Ratio between measurements on the front of the SPD at a collision energy of 7 TeV CM during 2011 compared to 8 TeV CM during 2012, normalized to 1 fb^{-1} . An increase between 10% and 20% of measured dose for Alanine (blue), MCP (red) and MTS (orange) sensors can be observed. A larger ratio for MTS sensors at low distance to the center can be explained by linearity issues of their calibration for the dose range between 100 Gy and 1 kGy. Alanine deviations at a large distance from the center can be ascribed to the low accuracy of the results from 2011 in the low dose range around and slightly above 1 Gy. In green, ratios between the 2 energies for FLUKA simulation results at detector positions are given. With a few exceptions, the simulation generally predicts a 5% to 10% increase in dose for 8 TeV CM collision energy.

Most comparison values from measurements point to an increase of dose per collision between 10% and 20% within 1.5 m around the center when moving from 7 TeV to 8 TeV CM. Simulation values suggest a slightly smaller increase in dose of around 8% in most places. It is unclear whether this discrepancy between measurement and simulation is caused by issues with the simulation, or by systematic errors linked to the change in the readout procedure for dosimeters in between measurement campaigns, as discussed in section 2.2.1.

5.2 EVALUATION OF PASSIVE 1 MEV NEUTRON FLUENCE EQUIVALENT SENSORS

In addition to the low- and high-level dosimetry sensors Alanine, RPL and TLD, almost every passive dosimeter box placed at the experiment carries a PiN diode with the purpose of measuring high-level 1 MeV neutron fluence equivalent. The diodes are of the same type as the BPW diodes that are integrated into the active sensor PCBs used at LHCb. The effect used for measuring the fluence is cumulative, therefore the device is suited for both frequent online (active) as well as yearly offline (passive) read-out. The active sensor setup will be described in more detail in section 5.3.

When exposed to radiation, the diodes suffer displacement defects, reducing their conductivity in forward-bias mode. The subsequent shift of the forward voltage V_f is measurable and can be directly converted into 1 MeV neutron fluence equivalent, after performing a correction which is based on the temperature during the readout.

Due to their range for measurements, which is tailored to relatively high fluences, and the fact that they measure cumulatively, these diodes have been put back in their corresponding passive boxes after each readout during all measurement campaigns up to this point. They will continue to accumulate measurements

during Run2, as it is not expected that any of them will reach their saturation threshold at the positions they are currently deployed before the next long shutdown.

PiN diodes from passive boxes have been measured after each measurement campaign, starting with the YETS at the end of 2010, where the content of 28 passive boxes was read out, and the Alanine, RPL and TLD sensors were replaced. In the YETS of the following year, passive boxes from inside the calorimeter detectors have been added to the replacement campaign. During LS1, almost all passive boxes containing PiN diodes have been read out and their contents, again with the exception of PiN diodes, replaced in anticipation of Run2. All of the few boxes that had to be left in place and could not be read out have not been exposed to high enough levels of neutron fluence to register a signal above the PiN measurement threshold.

5.2.1 READOUT

Manual readout was performed in a laboratory of the Detector Developments group of the CERN Experimental Physics Department, using a programmable and very precise power supply from Keithley which is shown in figure 88 next to a photo of a diode during measurement. Programmability of the power supply is a requirement due to the special readout procedure, which involves a step function for the supplied current in order to receive reproducible measurement results. The readout process involves putting a step function of 3 different currents, each 50 μ s long, through the diode in forward bias, and measuring the induced voltages, which is done and then saved into memory by the Keithley instrument. The supplied current during the step function starts at 10 μ A, then rises to 1 mA, and finally goes back to 10 μ A. The first and last steps are necessary to stabilize the readout during the 1 mA stage. The actual measurement signal is the voltage difference between pre- and post-irradiation measurements of the diode at 1 mA. More detailed information on the sensor and the readout procedure can be found in [34].



Figure 88: Close-up of the PiN-diode during measurement, which is held between two conductive clamps (left side) that are connected to the readout equipment (right side). The temperature sensor was located next to the Keithley power supply, about 40 cm away from the diode.

It is important to note down the current temperature for all measurements, as small changes in the room temperature are already capable of influencing the readout. The formula to correct for temperature variations is as follows:

$$V_{corr}(t) = [V(t) - V_0] + C[20 - T(t)] \quad (12)$$

V_{corr} is the corrected voltage signal, T is the temperature in Celsius, V is the actual measurement and V_0 was the original pre-irradiation measurement. C is a calibration factor that is constant for all BPW diodes. It has the value -2.531 mV/°C.

Active dosimeter PCBs used at LHCb containing a setup of active dose and neutron fluence sensors always include a temperature measuring device, which serves as a reference thermometer used to calibrate the online measurements. In contrast to the active readout system, the manual measurement of the passively used diodes requires the use of an external temperature indicator, which is part of the measurement setup in

the laboratory. This introduces an extra source of possible error during readout due to the high temperature sensitivity of the diodes themselves, which is amplified by the expected difference in accuracy between a chip-mounted device and a commercially available sensor that is measuring at half a meter distance from the samples. Passive sensors have been left overnight in the laboratory before measurement to let them adapt to the current room temperature.

The conversion of the temperature corrected readout voltage into fluence is done with the following formula:

$$\Delta V_F = c \cdot \Phi_{eq} \quad (13)$$

ΔV_F is the difference between V_0 and the readout and c is a calibration factor. Φ_{eq} is the 1 MeV neutron fluence equivalent in cm^{-2} . The calibration factor c is described as

$$\frac{1}{c} = 9.1 \times 10^9 \frac{\text{cm}^2}{\text{mV}} \quad (14)$$

When using the above formula, signals that are converted from voltage to fluence do not start at 0, but rather at a value around $1 \cdot 10^{10}$, depending on how different the temperature during readout was compared to the reference of 20 °C. The converted value can only be considered as a valid measurement if it lies between 10^{11} and $5 \cdot 10^{14} \text{cm}^{-2}$.

The BPW diodes were originally intended to measure fluences at locations with high exposure to radiation. They are rather insensitive to almost all fluence levels present in the LHCb experiment, with a few exceptions for sensors located very close to the beam line. Most other positions where passive boxes are deployed are covering electronic installations, which are sometimes neither designed to nor expected to withstand neutron fluence levels as high as that of the lower threshold of the diode. Therefore it is expected that most of the diodes will measure almost nothing until the end of Run1 and very likely even during the whole of Run2.

5.2.2 RESULTS

After the short irradiation period during the latter half of 2010, none of the diodes were able to measure anything. Their range of measurement for 1 MeV neutron fluence equivalent begins at around 10^{11} per cm^2 . The highest expected measurements for this irradiation period would have been well below this value according to FLUKA simulations. The actual readouts of the more sensitive active CMRP sensors, which will be discussed in section 5.3, confirm this. All of the diodes that were read out gave roughly the same signal, showing no discernible measurement of fluence.

A table of pre-irradiation V_0 measurements for most of the diodes was provided by F. Ravotti (who supplied the BPW diodes installed in the experiment) in order to define a base value V_0 to be used in each subsequent measurement to determine the increase of voltage and therefore the 1 MeV neutron fluence equivalent. One diode which is placed in a box on the front of the M1 detector could not be identified and was given the arbitrary number 106 which corresponds to the serial number of the passive box 4IRCERPW000106 which contains it. The value of V_0 for this diode is defined from the first measurement in 2010, when no measurable neutron fluence was expected to be registered by this device. Apart from this unknown diode, all measurements from 2010 exhibit a negative fluence measurement using the provided V_0 , because of annealing processes that led to a decrease of the voltage measurement over time. The neutron fluence at the location of the sensors was too low to counteract this effect during the short irradiation period of 2010, when only around 0.04fb^{-1} of integrated luminosity were delivered to the experiment. For illustration, the voltage and converted fluence measurements of two of the batch of passive boxes that were read out during YETS 2010 are listed in table 8. One measurement taken from a passive box at the top of the ECAL

(4IRCERPW000077) was expected to receive almost no radiation during 2010. The other measurement was taken from a position very close to the beam pipe at only 2 m distance from the IP (4IRCERPW000037), which is the most exposed position of any passive box in the experimental cavern and should measure the highest 1 MeV neutron fluence equivalent in the cavern outside of the calorimeter detector according to FLUKA simulations. Both voltage measurements are negative, almost completely equal, and do not indicate any difference in fluence. As later measurements will show, the BPW sensors near the beam pipe will start showing increased fluence values already at the end of 2011, whereas the less exposed BPW sensor will not measure anything that is discernible from background level.

Table 8: The measurement values after the first short irradiation period in 2010 for one of the least exposed (PiN Nr. 389) and most exposed (PiN Nr. 492) sensors, when 0.04 fb^{-1} of integrated luminosity were delivered to LHCb. The pre-irradiation measurement V_0 is larger than the actual measurement at 1 mA due to annealing effects that occur over long periods of time. The resulting converted fluence value is negative for both sensors, as the measurement threshold of the sensors could not be reached even very close to the beam.

Box Serial Nr.	PiN Nr.	V_0 (Tcor.)	V [1mA] (Tcor.)	Difference	1 MeV equ. Fluence [cm^{-2}]
4IRCERPW000077	389	0.52567	0.5188	-0.00687	-6.25E+10
4IRCERPW000037	492	0.526858	0.5199	-0.0069575	-6.33E+10

All of the sensors from the calorimeter detectors and all 5 sensors in the upstream tunnel have been measured for the first time during the YETS of 2011. Additionally, another passive box at the front of the M1 detector with the serial number 4IRCERPW000201 was read out for the first time, because it was installed during the YETS at the end of 2010, after the first short irradiation period of 2010. This additional passive box at the bottom of the M1 detector plane is replacing a box which should have been in this position but was missing at the first inventory check of 2010.

In a representative function, the highest values measured at the end of 2011 and the corresponding predictions from FLUKA simulations scaled for an integrated luminosity of 1.26 fb^{-1} are listed in table 9. The ratio between measurement and simulation on the right side of the table should give an indication of the general agreement of the two, with the exception of the last 5 values measured in the upstream tunnel around the ECAL test modules. In these 5 locations, the simulation values, marked orange, are considered unreliable. In these locations, fluence as well as dose predictions from the simulation vary very much and unfortunately in an unpredictable way from actual measurements. The main reasons for this discrepancy are suspected to be the geometry definition of the dipole corrector magnet downstream of the modules, and the missing concrete labyrinth wall further upstream along the tunnel. On one hand, the deflection of charged particles by the magnetic field and their interaction with the outer edges of the magnet yoke, which is not modeled with enough detail with respect to its real counterpart, have an important influence on the measured dose on the modules. On the other hand, the upstream concrete wall would be very influential in changing the neutron fluence around the modules.

Table 9: List of PiN measurements from the end of 2011 and the corresponding predictions from FLUKA simulations as well as the ratio between the two, representing the highest values measured during that year. The delivered integrated luminosity for 7 TeV CM at this point was 1.26 fb^{-1} . The columns labeled x [mm] and y [mm] list the distance along the x and y-axis of each sensor in relation to the beam. Orange highlighted simulation estimates are considered unreliable. The ratio values are highlighted in shades of red according to their value. Only a few more sensors than the ones listed have crossed the measurement threshold of $1\text{E}+11 \text{ cm}^{-2}$. On the front face of the SPD detector, the highest measurement for 2011 was still below $1\text{E}+12 \text{ cm}^{-2}$.

Box Serial Nr.	PiN Nr.	Description	x [mm]	y [mm]	1 MeVne [cm^{-2}]	Sim. [cm^{-2}]	ratio PiN/Sim
4IRCERPW000037	492	BLS upstream wall	0	150	$5.88\text{E}+11$	$1.27\text{E}+12$	$4.63\text{E}-01$
4CRCERPW000021	337	HCAL front	390	-65	$1.59\text{E}+12$	$3.50\text{E}+12$	$4.56\text{E}-01$
4CRCERPW000027	344	HCAL Front	455	-65	$1.07\text{E}+12$	$2.20\text{E}+12$	$4.86\text{E}-01$
4CRCERPW000028	345	HCAL front	65	-325	$1.62\text{E}+12$	$3.30\text{E}+12$	$4.92\text{E}-01$
4CRCERPW000031	348	HCAL Front	65	325	$1.20\text{E}+12$	$3.30\text{E}+12$	$3.64\text{E}-01$
4CRCERPW000032	350	HCAL front	-390	65	$1.81\text{E}+12$	$3.80\text{E}+12$	$4.76\text{E}-01$
4CRCERPW000039	439	ECAL front	-350	-20	$1.80\text{E}+12$	$5.00\text{E}+12$	$3.61\text{E}-01$
4CRCERPW000040	340	ECAL front	30	-300	$1.12\text{E}+12$	$2.70\text{E}+12$	$4.14\text{E}-01$
4CRCERPW000042	356	ECAL front	350	30	$1.84\text{E}+12$	$4.60\text{E}+12$	$3.99\text{E}-01$
4CRCERPW000043	357	ECAL front	350	-30	$1.79\text{E}+12$	$4.60\text{E}+12$	$3.89\text{E}-01$
4CRCERPW000045	360	ECAL front	30	260	$1.82\text{E}+12$	$6.30\text{E}+12$	$2.88\text{E}-01$
4IRCERPW000101	101	Tunnel modules	-264	0	$2.17\text{E}+11$	$4.90\text{E}+11$	$4.42\text{E}-01$
4IRCERPW000102	102	Tunnel modules	-132	0	$4.17\text{E}+11$	$1.60\text{E}+12$	$2.61\text{E}-01$
4IRCERPW000103	103	Tunnel modules	-264	0	$3.21\text{E}+11$	$9.00\text{E}+11$	$3.57\text{E}-01$
4IRCERPW000104	104	Tunnel modules	-132	0	$3.93\text{E}+11$	$3.00\text{E}+12$	$1.31\text{E}-01$
4IRCERPW000105	105	Tunnel modules	-70	60	$1.48\text{E}+12$	$4.00\text{E}+12$	$3.69\text{E}-01$

The highest fluence values in the experimental cavern were measured on the front of the ECAL detector. When comparing values to the positions of these measurements, the shape of the fluence distribution is stretched along the horizontal, as it is the case with dose levels. FLUKA simulation also predicts this shape for 1 MeV neutron fluence equivalent values at the front of the ECAL, which is pictured in figure 89. Most of the neutrons in this energy range are created inside the lead plate in front of, and the heavy material inside the calorimeter detectors by interactions of heavy charged particles, which have been deflected on their way from the IP by the magnetic field of the LHCb dipole, resulting in this oval shape of the distribution.

On HCAL front, 4 out of 5 measurements support the prediction of a horizontally stretched shape, while the measurement of 4CRCERPW000028, considering its position below the beam, measures an exceptionally high value rather in the range of its horizontally positioned counterparts. Although the measurement value itself still falls reasonably into the expected range, it could also be influenced by a readout problem, caused by either applying the wrong temperature correction or a wrong value of V_0 . The small sample size of measurements unfortunately does not allow for a more accurate evaluation of single deviations.

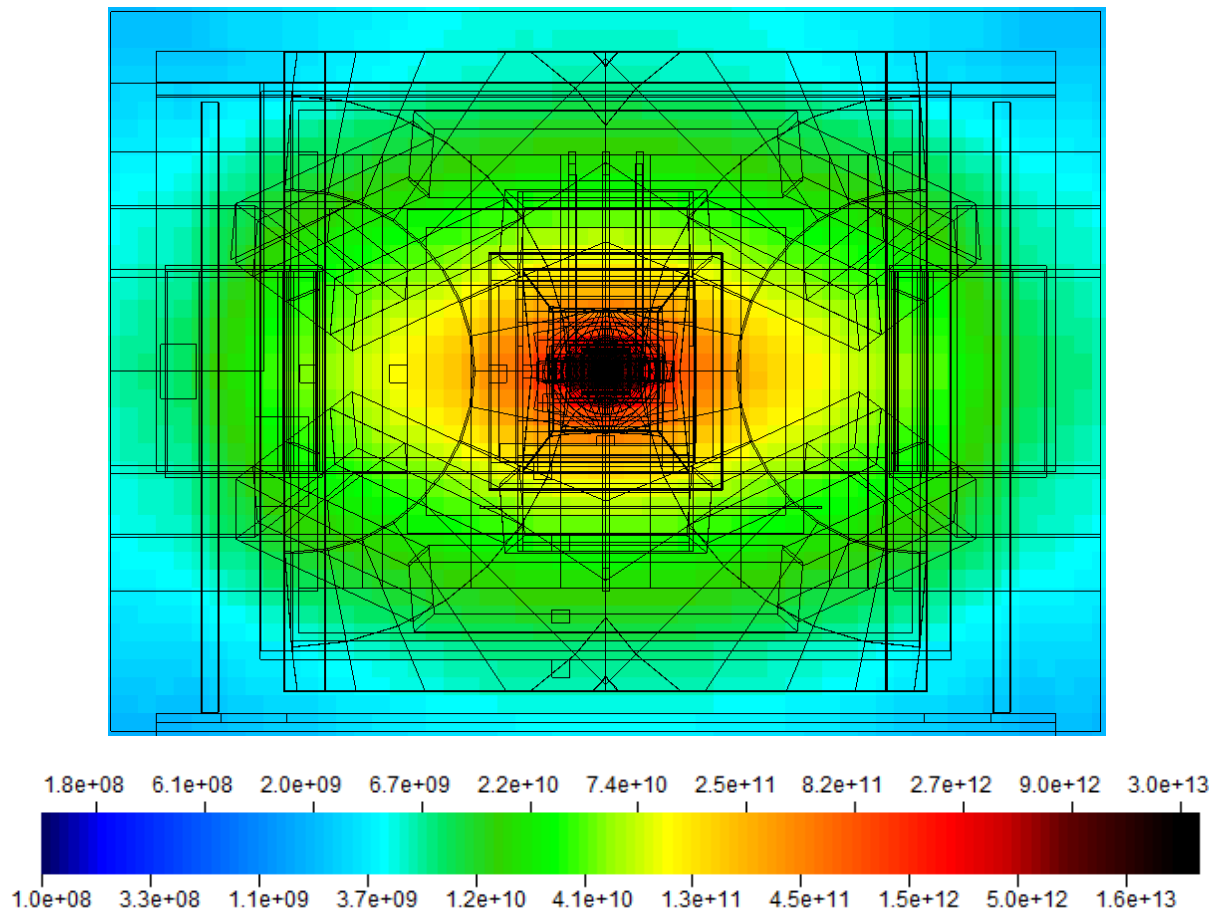


Figure 89: Distribution of 1 MeV neutron equivalent fluence at the front of the ECAL detector in between z [1240, 1260] cm. The shape is clearly stretched along the horizontal, due to the influence of the magnetic field of the LHCb dipole which deflected highly energetic charged particles on their way from the IP. In addition to the effect of charged particles being folded into the 1 MeV neutron fluence equivalent, the incident particles produce neutrons during interactions with the heavy material of the calorimeter detector.

It is also indicated in table 9 that values of the BPW measurements, while being in the same order of magnitude, are lower than simulation estimates by a factor of more than 2 both on ECAL and HCAL front. The simulation estimates themselves are taken from a binning with 20 cm edge length. This bin size is far from optimal for retrieving values in the area close to the beam line, where they change significantly within a few cm of distance. Although a bit of interpolation was done by averaging over adjacent bins when applicable based on the location of the measurement, these estimations should be treated as ballpark figures to evaluate the general applicability of BPW sensors in these cases. The agreement between measurement and simulation before YETS 2011 is not as good as with dose sensors, but it still lies within the same order of magnitude without a lot of variation between individual comparison values.

The passively used diodes attached to the ECAL test modules in the upstream tunnel did not register fluences as high as those at the central modules of the ECAL, although they were exposed to higher amounts of TID. In contrast to the sensors in between the calorimeter subdetectors, these tunnel sensors are not surrounded nearly as much by heavy metallic bodies. Most neutrons in this area are produced either by interactions with the metallic body of the dipole downstream of the modules, or with the concrete wall a few meters upstream, leaving a lot of space for the particles to disperse. Unfortunately, no initial measurement of V_0 has been performed for the PiNs with the ID ending with 101-105 before they have been installed in the tunnel. As a consequence, an average value of 0.5227, calculated using all provided initial BPW V_0 values, has been used to

convert all five measurements. Despite this small source of error for the V_0 , the measured fluence follows the expected pattern and visibly increases in positions that are closer to the beam line.

In table 11 the corresponding values for the same positions for the end of 2012 are listed in the same manner as in table 9. Since the signal stored in the PiN diodes is cumulative, these measurements correspond to an integrated luminosity of 3.47 fb^{-1} , with the most recent 2.21 fb^{-1} being delivered at a collision energy of 8 TeV CM. During the YETS of 2011, three passive dosimeter boxes from the C-side of the calorimeter detectors had to be fully replaced because they were only accessible for a very short time and could not be measured and refilled like most of the other boxes. This means that the serial number of the box changed for this location, as well as the PiN diode itself. The serial numbers of the boxes removed along with the numbers of their replacements are listed in table 10.

Table 10: Serial numbers of the originally placed and the replacement boxes from the C-side of the calorimeter detectors, along with their positions in the LHCb coordinate system. They are located on the front and backside of HCAL and the front of ECAL.

Box Serial Numbers		Position [mm]		
original	replacement	x	y	z
4CRCERPW000032	4CRCERPW000100	-390	65	13330
4CRCERPW000039	4CRCERPW000099	-350	-20	12530
4CRCERPW000059	4CRCERPW000093	-430	90	12310

Two of the measurements from these locations are listed in table 11. They had the initial numbers 4CRCERPW000032 and 4CRCERPW000039 and are highlighted in purple to discern them from continuously used sensors, since their final value in the table is made from the sum of two individual measurements from 2 different PiN diodes. This could be an issue because of the nonlinearity of the conversion of measured voltage into fluence. However in these cases the summed up values lie reasonably within the expected range of their similarly placed counterparts.

Although the slightly different collision energy of 8 TeV CM should not have any meaningful impact on the registered signal, it can be seen by comparing table 9 and table 11 that the measured fluence does not seem to increase linearly with luminosity. The increase of measured fluence in 2012 vs. 2011 per fb^{-1} is larger by a factor of up to 2. This is very likely a consequence of the way the signal is converted into the measurement. While the direct conversion of voltage to fluence explained in (13) is linear, the temperature correction (12) can introduce a large offset to the measurement. Given that the temperature during these manual readouts is taken with a device at some distance in a laboratory which does not allow control over temperature or airflow, this might explain part of the non-linearity between the two measurement campaigns.

The default V_0 of PiN sensors is usually situated between 0.5 V and 0.55 V, but unless a measurement was done before irradiation, it is difficult to precisely determine the amount of fluence that has been experienced by a sensor. A difference in the voltage measurement at 1 mA of slightly above 20 mV is converted into an increase in fluence of around $3\text{E}+11 \text{ cm}^{-2}$, which is roughly 10% of what was measured at the BLS at the upstream wall during Run1. Even if a pre-irradiation measurement exists, annealing effects and inaccuracies produced by the manually performed temperature correction reduce the accuracy significantly when only low fluence is measured by a sensor over a prolonged period of time.

Table 11: List of PiN measurements from the end of 2012 and the corresponding predictions from FLUKA simulations as well as the ratio between the two, representing the highest values measured during that year. The delivered integrated luminosity for 8 TeV CM at this point was 2.21 fb⁻¹ adding up to a total of 3.47 fb⁻¹ at the end of 2012. Two cells that are highlighted in purple represent the sum of 2 diodes measuring in the same location which were swapped during the YETS of 2011. Orange highlighted simulation estimates are considered unreliable. The ratio values are highlighted in shades of red according to their value. The columns labeled x [mm] and y [mm] list the distance along the x and y-axis of each sensor in relation to the beam. A few more sensors than the ones listed have crossed the measurement threshold of 1E+11 cm⁻².

Box Serial Nr.	PiN Nr.	Description	x [mm]	y [mm]	1 MeVne [cm-2]	Sim. [cm-2]	ratio PiN/Sim
4IRCERPW000037	492	BLS upstream wall	0	150	2.40E+12	3.61E+12	6.64E-01
4CRCERPW000021	337	HCAL front	390	-65	6.17E+12	1.03E+13	6.01E-01
4CRCERPW000027	344	HCAL Front	455	-65	4.42E+12	6.44E+12	6.87E-01
4CRCERPW000028	345	HCAL front	65	-325	6.41E+12	9.55E+12	6.72E-01
4CRCERPW000031	348	HCAL Front	65	325	4.91E+12	9.45E+12	5.19E-01
4CRCERPW000032	350	HCAL front	-390	65	5.90E+12	1.05E+13	5.63E-01
4CRCERPW000039	439	ECAL front	-350	-20	7.72E+12	1.40E+13	5.51E-01
4CRCERPW000040	340	ECAL front	30	-300	4.14E+12	7.70E+12	5.38E-01
4CRCERPW000042	356	ECAL front	350	30	8.04E+12	1.34E+13	6.00E-01
4CRCERPW000043	357	ECAL front	350	-30	8.15E+12	1.36E+13	5.99E-01
4CRCERPW000045	360	ECAL front	30	260	7.15E+12	1.12E+13	6.38E-01
4IRCERPW000101	101	Tunnel modules	-264	0	5.34E+11	1.43E+12	3.74E-01
4IRCERPW000102	102	Tunnel modules	-132	0	1.28E+12	4.60E+12	2.78E-01
4IRCERPW000103	103	Tunnel modules	-264	0	7.81E+11	2.08E+12	3.75E-01
4IRCERPW000104	104	Tunnel modules	-132	0	1.17E+12	6.90E+12	1.70E-01
4IRCERPW000105	105	Tunnel modules	-70	60	5.18E+12	1.14E+13	4.55E-01

Many passive boxes with BPW sensors inside the cavern are located at the outer edges of detectors and at other more remote locations of electronic equipment. These were not able to measure any discernible fluence during the entire Run1. Due to their low sensitivity and high threshold for measurements, the BPW sensors are in general not very well suited to measure 1 MeV neutron fluence equivalent around the electronics on the outliers of the LHCb experiment. Even in the areas at half distance between beam line and outer edge of the calorimeter detectors, BPWs only measure around or below their threshold.

The accuracy of BPWs compared to simulation values was demonstrated to be within a factor of slightly above 2 inside the central areas of the calorimeter when measurement values lie well above their lower threshold. Although not very precise, they manage to provide a good indication of the level of potential radiation damage at the respective placement of the sensor. Since this was stated to be the initial objective by the person that suggested their use for these types of measurements, this should nonetheless be considered a success for these devices.

In order to obtain more meaningful measurements of 1 MeV neutron fluence equivalent during Run2, a handful of passive boxes inside the calorimeter detectors and at the front face of the M1 detector have been equipped with a batch of more sensitive diodes in LS1. These so-called Si-2 diodes are supposedly similar in behavior and measurement range to the CMRP diodes, which are measuring successfully on board of the active sensor PCBs used at LHCb. The accuracy and applicability of the CMRP diode in the LHCb environment will be explained in the following section. A more detailed characterization of the Si-2 sensor can be found in [34].

It will be shown in the following evaluation of active sensors that the few passive measurements from PiNs agree with active sensors in similar positions where they are available. It has to be noted that the signal drift due to annealing, which could already be seen after the first measurement campaign at the end of 2010, is only being accounted for during active sensor measurements. Therefore the passive sensor is expected to measure a smaller value after a certain amount of time, in this case at the end of each year-long measurement campaign.

5.3 EVALUATION OF ACTIVE DOSIMETERS

In contrast to passive sensors that are only measured once a year, the active sensors at LHCb are able to provide a more detailed insight into the evolution of the radiation field during operation. Each of the active sensor boxes holds a PCB incorporating 2 RADFET sensors measuring dose and 2 PiN diodes measuring 1 MeV neutron fluence equivalent, each covering a different range. Their measurements are read out in constant intervals and the signals are stored in a database from where they can be accessed via a WinCC [62] interface in the LHCb online network. WinCC is a Supervisory Control And Data Acquisition (SCADA) interface, which is used at all LHC experiments to drive a large range of devices by the Experiment Control System (ECS). At the moment, signals are stored and displayed only as voltage signals. Signal conversion to dose or fluence values has to be performed offline because of the required complexity of the process. The active sensor PCBs have been conceived for use at the LHC's high-energy radiation environment [34] and are also deployed in other experiments at CERN. While they have been exposed to a mixed field for tests at a CERN irradiation facility, the effect of the vastly more energetic radiation field in LHCb as well as eventual problems due to long-term deployment were still unknown. Considering the relatively high reliability of some of the passive sensors discussed earlier, the measurements of active sensors will be evaluated in reference to the most reliable passive sensors that are placed in close vicinity. The behavior of the active sensors will be analyzed based on three scenarios that emphasize different aspects of the radiation environment of the experiment.

The first scenario focusses on the M1 muon detector plane that is located in between RICH2 and the calorimeter detectors. It houses 8 groups of passive and active sensor boxes. These are placed in a half-cross-shaped form on the lower quarter A-side facing the IP as pictured in the WinCC interface screenshot in figure 90, with 4 placements along the positive x-axis on beam height and the other 4 along the negative y-axis almost below the beam pipe. This layout allows for a detailed comparison between estimations from the simulation with measurements from active and passive dosimeters in varying radiation field compositions. The compact layout on this single plane provides a rather reliable way to collect information on the behavior of the active sensors when exposed to different dose-rates and a mix of particle types. All other locations for active sensors are positioned at much further distance from each other and have different boundary conditions, e.g. due to significantly different levels of reliability of the simulation, making comparisons between those more difficult.

Effects that mainly occur due to high dose and fluence levels will be discussed in section 5.3.4. The active sensors next to the BLS detectors at the upstream wall of the experimental cavern, as well as the two PCBs at the position of the ECAL test modules in the upstream tunnel, are exposed to the highest dose rates during operation of the experiment. In these three positions, sensors with high sensitivity were saturated and no longer providing useful signals after a short amount of time. High dose and fluence rates and the resulting high integrated measurement values in the kGy range also cause high rates of annealing in the sensors, leading to a problem of accuracy in the long term. The correction of the continuous decrease of the signal, which is referred to as drift correction in this document, plays an important role when handling the measurement signals.

The remaining active sensors are discussed in section 5.3.5. These are distributed around the edges of the experiment, mostly next to passive sensor boxes covering areas that house electronic installations for the various subdetectors. In general, these electronic installations can have components that are radiation tolerant only up to a small amount of integrated dose. They were designed and placed to operate in areas with low exposure. As a consequence, the sensors that are attached to these installations only measured low to very low dose values within the whole measurement period.

In the following sections, it will be shown that one type of dose and one type of fluence sensor generally agree very well with reliable passive measurements and the simulation. The usefulness of the remaining two sensors suffers from calibration issues that are difficult to solve and from their limited applicability within their respective placements in the LHCb radiation field.

5.3.1 MEASUREMENT SETUP

Compared to the number of passive sensor boxes, the active sensor boxes are far less in number with only 28 of them installed in the cavern. While there are no active sensors installed inside the calorimeter detectors where most of the passive boxes are located, they are usually placed next to the remaining passive boxes which are mostly located on the outside of the experiment next to electronics. Those remaining passive boxes have not been mentioned in the analysis of the calorimeter measurements, with the exception of figure 74 and figure 75, where they have been included. In an attempt to gain more insight into the development of the radiation field inside the detector itself, 8 positions for both active and passive sensor boxes have been established in the form of a half-cross shape on the front of the M1 muon detector plane in between its gas chambers. The alignment of these sensors is shown in figure 90, with 4 boxes placed along the x- and y-axis, respectively. This very compact layout on a single plane placed orthogonally to the beam line facilitates comparisons between different sensor types, as well as between different field configurations. In addition, simulation estimates on a xy plane inside the experiment's acceptance are expected to be much more accurate and reliable than in the locations at the edge of the detector, where shortcomings like missing support structures in the geometry can reduce accuracy. The remaining active sensor positions are shown in the screenshots of the WinCC online readout interface in figure 91. Most of them are placed around the edges of the detector, in locations where electronics for the various subdetectors are found. Due to the issue of projection, the yellow lines in the left part of figure 91 which are pointing to the approximate locations within the sketched top-down view of the detector sometimes point to its center. However, these lines actually refer to positions either on top of the detector, such as the calorimeter platform where many racks housing electronics are located, or below the experiment, such as in the middle of the Bunker which is below the Tracking Stations. In addition to the positions mentioned above, the active sensor network also controls two active boxes inside the tunnel upstream of the VELO, on the front of the ECAL test modules. These are placed directly on top of the passive boxes with the serial numbers ending with 103 and 104, which are displayed in figure 92 and were discussed in section 5.1.4.5. One last sensor box is placed in the permanently accessible area of the underground complex, behind the large shielding wall dividing the underground area. It is located on the third floor of the container barracks that are housing the LHCb data acquisition and computing farm, in between electronics racks. Because of the efficient shielding wall separating this accessible area from the experimental cavern, this sensor should never measure any dose or fluence values above background. Since the background in the LHCb underground complex is actually quite low compared to values measured on the surface, this sensor can be regarded as a sort of non-irradiated reference.

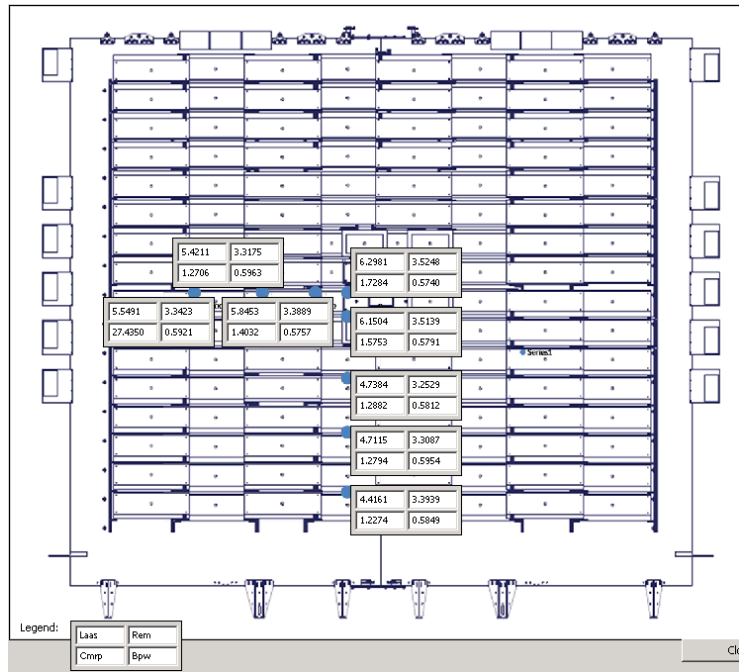


Figure 90: Screenshot of the WinCC interface display for the active monitor readout of sensors on the front of the M1 detector. The positions of sensors in a half-cross-shaped layout are displayed as blue dots on the background of a sketch of M1. The readout numbers for the 4 different sensors on each PCB are placed adjacently to the dots. The numbers themselves only represent temperature corrected voltage signals, because the software necessary for signal conversions could not be implemented into the online system yet.

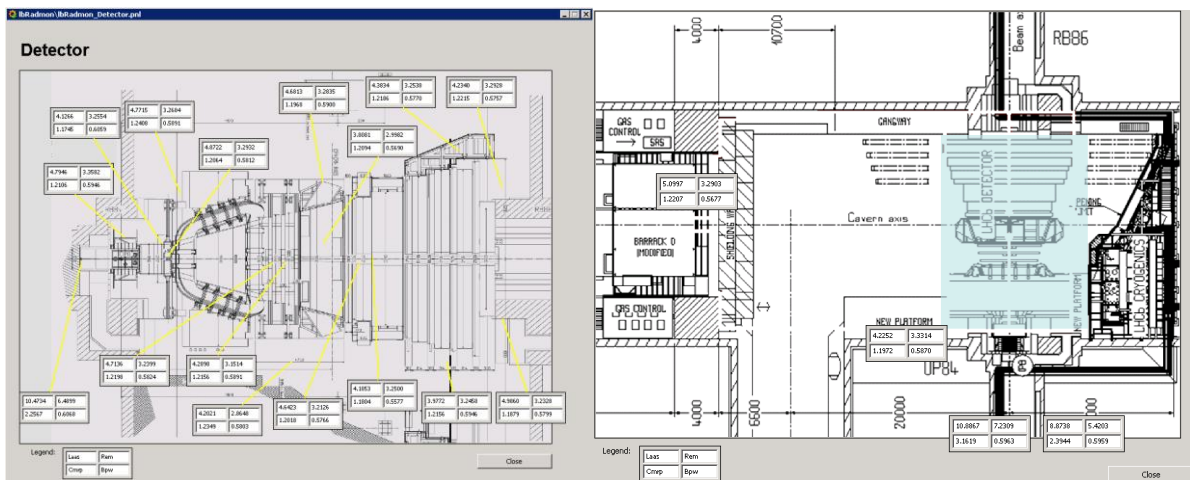


Figure 91: Screenshots of the WinCC interface displays for the active monitor readout of sensors around the LHCb detector (left) and in the upstream tunnel (bottom right), on the balcony next to the detector and as a reference in the barracks housing the computing farm behind the shielding wall. Both show sketches of top-down views of the experiment in the background. In order to indicate the actual sensor positions, the interface on the left has yellow pointers, while in the interface on the right the signal display boxes themselves are placed accordingly.

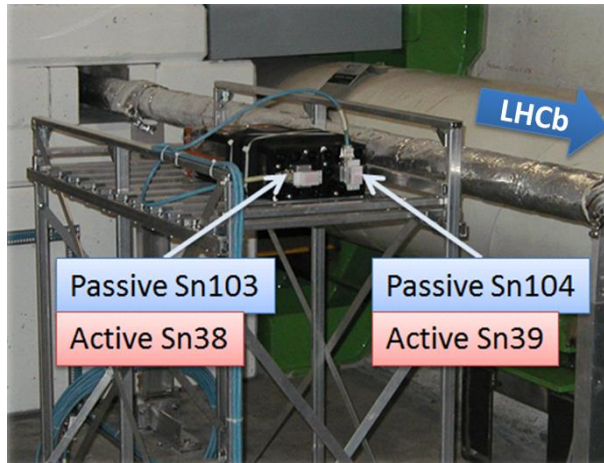


Figure 92: Photo of the front of the ECAL test modules in the tunnel segment upstream of the VELO. The active sensor boxes, which are connected via the visible blue cables, are placed directly on the front of the passive boxes.

The active sensors at LHCb are measured every 23 minutes by a WinCC controlled system. The readout interval was set to be a compromise between a sufficiently detailed readout curve and the limitation of signal loss caused by the measuring process. Each measurement step leads to a very small neutralization of charge in the SiO₂ layer in addition to the temperature driven annealing processes. With the interval currently chosen between measurements, this loss mechanism should be negligible. The WinCC interface provides the possibility to plot the time evolution of measurement values of a single sensor next to temperature and luminosity values. An example of such a display is shown in figure 93. The voltage signal of the sensor is displayed in the red curve, the integrated delivered luminosity over time in light blue and the temperature in dark blue. In the example, the voltage signal is following the luminosity value exceptionally well, as it would be expected since the number of collisions and the received dose are proportional as long as the collision energy does not change. At a different energy, only the proportionality factor changes accordingly. On a side note, the spike of the dark blue curve is exemplary of one of many readout errors stored in the database, caused by either power cuts, faulty connections or other electronic disturbances. Most of these kinds of errors are corrected for during offline conversion by using the methods described in the following sections.

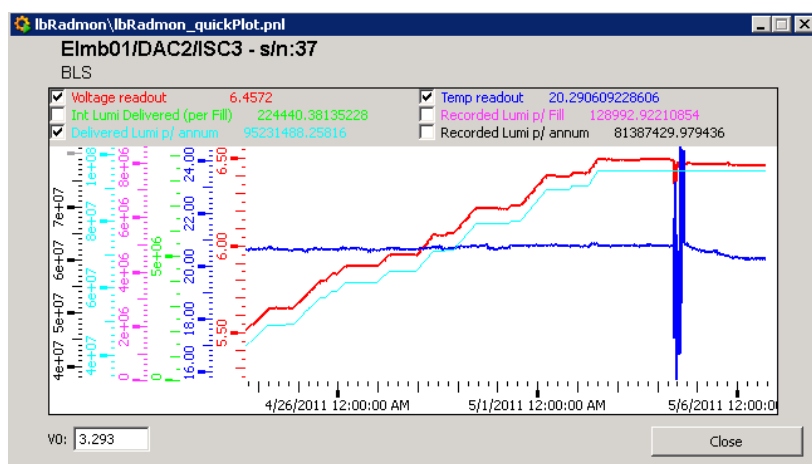


Figure 93: Exemplary display of the evolution of the sensor signal of the REM sensor with the serial number Sn37, which is located close to the beam line on the upstream wall of the cavern. The measured voltage is shown in red, the corresponding level of integrated luminosity in light blue and the temperature in dark blue. The large spike in temperature is exemplary for one of many different electronic problems that can occur during readout.

5.3.2 SIGNAL CORRECTIONS

The active sensors and their online readout capability carry advantages in terms of availability of measurements and usability. However being electronic devices, they also share some common disadvantages like signal noise, connection problems or sensitivities for changes in temperature. In addition to these, the sensors accumulate damages as a form of measurement signal, which means they are also susceptible to annealing processes happening on a constant basis. All of the issues mentioned above lead to various problems to be dealt with and corrected for when trying to convert the signal into an informative and useful measurement of the evolution of dose or fluence. In order to mitigate these influences during conversion, a set of functions has been conceived which are to be applied on the dataset. Besides rather simple corrections such as for temperature which is just applied once on all data points of every sensor, some more sophisticated methods are necessary to at least partially counter signal drops, high noise or loss of signal during annealing. These methods require many instances of functions and loops that go over the dataset of a sensor. The methods described in this thesis take several minutes to execute on a current PC, which is the main reason why these corrections are only applied offline at the time of writing. Modifications to the code are underway in order to implement an online correction of sensor data into the WinCC framework, allowing for an almost real-time observation of the evolution of dose and fluence levels in the cavern. The various correction functions will be explained in more detail in the following sections.

5.3.2.1 TEMPERATURE AND OFFSET CORRECTIONS

Voltage signals given by the semiconductor devices are all influenced to a certain degree by the ambient temperature $T(t)$. All active sensors have been calibrated to a reference temperature of 20 degrees Celsius. Although the temperature in the experimental cavern is rather stable during operation compared to the situation on the surface, small changes due to ventilation necessitate a correction based on the changing temperature environment. As a consequence, each PCB features an additional sensor dedicated to measuring the temperature every time the dose and fluence sensors are read out.

As an example for a strong dependence on temperature, the raw vs. the temperature corrected curves of both 1 MeV neutron fluence equivalent sensors of *Sn14* which is placed almost at the center of the M1 detector are shown in figure 94. All of them have been converted from voltage to fluence using equations (9) and (10) before plotting them. The actual correction for temperature is modeled after (15). The single green curve in the bottom plot shows the temperature measurement over the course of more than 2 years, varying between 19 and 25 degrees Celsius. The drops in temperature mostly happen during long technical stops during winter where maintenance on cooling and ventilation is performed and the cover of the PX shaft might be opened for transporting equipment into and out of the cavern, letting in cold air from outside. The raw readout of the BPW sensor on *Sn14* is displayed in blue, exhibiting extreme fluctuations that correspond to the changes in temperature in addition to the high noise of the signal. When applying the temperature correction, the high noise of the signal remains, but the overall trend of the signal curve is significantly more stable. Also, due to the generally high influence of the temperature on BPW sensors, the offset of the fluence value changes from 0 to 10^{11} cm^{-2} , which is the lower threshold of its measuring range. The idea of the calibration curves of BPW and CMRP is that BPW signal starts high but will only begin visibly increasing when the accumulated fluence rises above 10^{11} cm^{-2} , taking over for the CMRP signals which will slowly start to deteriorate above that level. In figure 94, as is the case with most sensor positions in the experiment, 1 MeV neutron fluence equivalent levels are too low to clearly exceed the lower measuring threshold of BPW sensors, resulting in a BPW curve showing a measured fluence around 10^{11} cm^{-2} over the course of almost 2 years while the actual fluence was much lower as is shown by the CMRP sensor. The CMRP sensor, which is displayed by the black and green curves that overlap each other almost completely, is not as sensitive to temperature changes. It succeeds in

measuring the fluence reasonably well within its measuring range, while clearly following the integrated luminosity.

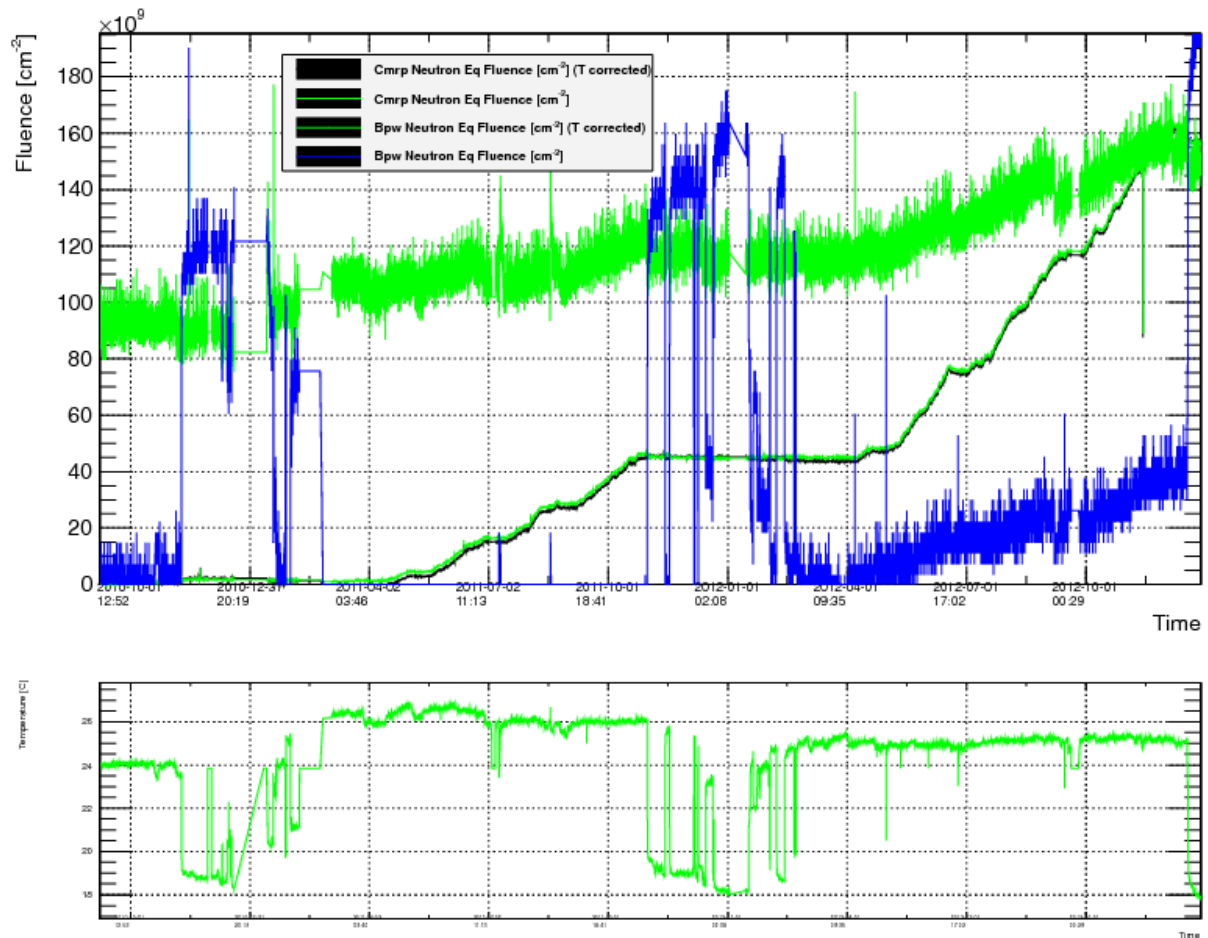


Figure 94: Example of temperature correction for the 1 MeV equivalent neutron sensors of *Sn14*. The BPW sensor (blue and green curve in the top plot) shows heavy noise because it has barely reached its sensitivity threshold. Its uncorrected signal (blue) is also visibly correlated to the temperature changes, which are plotted as a green curve below the fluence on a separate canvas. The temperature in the lower plot occasionally drops from around 25 degrees to 19 degrees Celsius during technical stops. The CMRP sensor (black and green curve) on the other hand is generally not as sensitive to T , and its signal to noise ratio is much lower than for the BPW because it operated well within its measuring range during the plotted timeframe. All corrected and uncorrected curves have been converted into fluence before plotting.

The same formula that was already applied to passive BPW sensors is used for the temperature correction of all sensors:

$$V_{corr}(t) = [V(t) - V_0] + C[20 - T(t)] \quad (15)$$

However each sensor requires a specific value of C . Whereas both low sensitivity sensors use the same number for all devices of each type (REM: 1.045; BPW: -2.531), both high sensitivity sensors need specifically adjusted correction parameters. For the LAAS type, these vary between -4.959 and -1, and for the CMRP type between 1.2 and 1.27. The parameters for LAAS and CMRP had to be found by hand using quick drops in temperature as seen in figure 94 to adjust the corrected curve.

For actively used sensors, the signal offset V_0 in formula (15) is obtained by calculating the average of $V(t)$ over the first available days of data taking, where no increase of the signal is expected. This method is considered more accurate than taking values from the available calibration sheets of the sensors, because during the time between calibration and first deployment, some of these have shifted over time due to

annealing effects. This decrease of the signal before the first irradiation took place could also be observed with passively used BPWs, as described in section 5.2. This shift towards lower voltages would have resulted in a negative ΔV and consequently a negative measurement until they are sufficiently irradiated to overcome this added threshold. Besides annealing effects, the shift might also have been influenced by high signal noise or an unregistered shift in temperature during the initial measurement of V_0 . A precise definition of V_0 is crucial for the subsequent conversion of voltage signals into dose and fluence levels.

For the two LAAS sensors *Sn15* and *Sn30* the average of $V(t)$ could not be calculated because they started to drift to lower values during the first few weeks of operation, even during short periods of low irradiation where only 0.04 fb^{-1} of integrated luminosity were delivered to LHCb. Besides the measured difference in total value compared to the calibration reference, the drift itself was observed after recording started in autumn 2010. For these sensors, V_0 would show a relatively large offset when using the standard method, which would in turn delay the beginning of measurements crossing this artificial threshold. Therefore, the lowest value recorded during autumn 2010 was taken as V_0 .

While most sensors would not be able to measure any dose or fluence during the delivery of 0.04 fb^{-1} in 2010, five sensors were exposed to non-negligible radiation in that timespan. The sensors which are located at the center of the M1 detector (*Sn12*, *Sn13*), next to the beam line on the upstream wall (*Sn37*) and on the ECAL test modules in the upstream tunnel (*Sn38*, *Sn39*) already accumulated some signal before their measurements started to be saved in the database. In these cases, the offset accumulated during the unrecorded time had to be calculated to arrive at a correct V_0 . Under the assumption that the growth of the voltage signal is proportionate to the growth of delivered luminosity as long as the sensor is far from reaching saturation, the offset was computed going backwards in time and correlating the luminosity to the expected increase in voltage. The difference between V_0 calculated as described and the standard averaging process of first measurements is in the order of a few %.

5.3.2.2 READOUT CURRENT (“JUMPS”) CORRECTION

Over the first months of operation, some sensors were read out with a wrong readout current. A WinCC property table for the active monitor application comprises the values necessary for the correct operation of the sensors and is consulted by the controlling electronics and power sources. A default parameter in this property table was listed with a wrong value from the beginning of the operation for unknown reasons. This resulted in a weaker than required readout current, which in turn produced measurements that were strongly below their nominal values. The affected sensors had the numbers *Sn40*, *Sn16*, *Sn28* and *Sn22*.

After these sensors and their corresponding parameters were identified to be at fault, the parameters in the table were manually changed by the author and the measurements continued to be registered in the database with their nominal values. The name *jump* has been used in the plots to identify this behavior between the periods of faulty and normal operation. Because past faulty measurements taken at too low currents could not be retroactively changed in the database, measures have been taken to correct for these deficiencies during application of the correction algorithms. These *jumps* have to be corrected first, before handling annealing countermeasures (drift corrections), which will be explained in the next section. This is due to the fact that drift corrections would be heavily detracted if these signal *jumps* were still present during the application of those corrections' algorithm.

The *jump* correction itself is performed in a rather simple way: all values before the *jump* are multiplied by a factor that corresponds to the difference between the two values before and after the discontinuity. No other significant deviations of these sensors could be seen apart from the one just described, and the values after the *jump* were not altered by this measure. The correction resulted in an overall smooth curve that closely

follows luminosity values from the start. Before each individual correction it has been verified that none of the 2 values of the discontinuity are part of an unexpected signal spike, which would distort this first period of taking signals and therefore also subsequent efforts of drift correction of later measurements.

5.3.2.3 DRIFT CORRECTION AND LUMINOSITY

Using the V_{corr} calculated with (15), it would already be possible to directly convert measured voltage into dose or fluence values. However, a mixture of short-term and long-term annealing effects distorts the signal measurements over time, which becomes apparent as a decrease of the measurement value. This will be referred to as “drift” during this thesis. The effect is more noticeable at higher measurement ranges in dose sensors and it produces readout results that are clearly below expected values. Drift correction is crucial in order to obtain any meaningful measurements for the most exposed sensor positions at LHCb.

Based on discussion of the drift effect with the engineer who devised the active monitor PCB [34], the following assumption has been made: when the beam is on, and therefore collisions are happening at the experiment, it is assumed that the active sensors do not experience drift when taking data. As the analysis will show later on, this assumption is very likely not true, because annealing effects will continue even during collisions. Characterizing those annealing effects and calculating correction functions to counter their impact however is far from trivial. The combination of strong short-term and weaker long-term effects would require a delicately adapted function which would have to be applied to each measurement point and which would itself be a function of the dose already measured in the sensor. No such function has been considered up to now. The assumption mentioned earlier as outcome of the discussion was therefore intended to search for a solution addressing the biggest component, which is drift during periods without irradiation. Such a solution could also be implemented in a much simpler way.

After the beam is stopped, signals from sensors that already measure clearly above their lower measurement threshold start dropping over time. The integrated delivered luminosity, which can also be accessed by the WinCC interface, acts as a trigger for the drift correction process. Increasing integrated luminosity is considered “beam on”, while a stable luminosity value in the database indicates a “beam off” period. As soon as the beam is off, the last value during a beam on phase is stored. When the delivered luminosity starts increasing again, the new value is used to calculate the difference Δ caused by the drift of the signal, and Δ is added to the signal from that point onwards. There is an added benefit to this solution: if the recorded signal during a beam off period happens to drop to the default value (0 or 27) for short intervals, which sometimes occurs because of connection errors during maintenance operations or power outages, these sharp drops would be ignored by applying the described drift correction, as long as the signal is read correctly again at the start of the next period with collisions.

A time-stamped and regularly updated file containing values of luminosity delivered to the LHCb experiment is necessary to perform the drift corrections for the measured voltage signals from the active sensors. Its primary use in this context is to indicate when collisions are happening at the experiment to correlate the start and end times of measurements of the active sensors. The integrated delivered luminosity data is extracted from available database values provided by the collaboration, which are also used for displaying history plots as in figure 93:

LHC:LHCCOM/LHC.LHCb.Internal.Luminosity.LumIntDel_annual_3500 for the years 2010 and 2011, and *LHC:LHCCOM/LHC.LHCb.Internal.Luminosity.LumIntDel_annual_4000* from June 2012 until the beginning of LS1 are the names of the database entries where the delivered luminosity values are stored. The nomenclature of 3500 and 4000 stands for the energy in GeV per proton during collisions within that time.

Due to technical difficulties at the beginning of the data taking period in 2012, the integrated delivered luminosity could not be stored in the database point *LHC.LHCb.Internal.Luminosity.LumiIntDel_annual_4000* between the beginning of April and the beginning of June 2012. Even a different entry called *LHC:LHCCOM/LHC.LHCb.Internal.Luminosity.LumiIntDel_GP*, which contains data of integrated luminosity per fill, only provides faulty values for April and May 2012, adding up to a 15% larger total sum than what was actually delivered. The luminosity data for these two months in 2012 was subsequently provided by a member of the collaboration, who managed to clean the original values from a different source from most errors, so that the resulting values are within 0.5% of the real amount [63].

In order to be used with the correction algorithms, all of the available luminosity data was merged and integrated by the author into a formatted file with 6 columns structured

Day Month Year hour minute second luminosity

showing the total delivered integrated luminosity from 0 fb⁻¹ in 2010 up to 3.47 fb⁻¹ at the beginning of LS1. All values in the list are only separated by spaces. Any commas, colons and hyphens have to be eliminated before that file can be used together with the correction routines. A few lines in the original format of the integrated luminosity files showed values of luminosity smaller than 1 with a negative exponential. Those lines had to be manually removed for the file to conform to the procedure.

In contrast to the readout schema of the LHCb sensors, which foresees a measurement every 23 minutes, the luminosity values are updated every few seconds during collisions. For periods of no activity, only the last time the luminosity values increased and the first time they increase again are usually recorded by the logging process.

An additional benefit of producing a file showing the evolution of the integrated luminosity over time is gained by connecting this information with the actual measurements. The shape of the integrated luminosity curve allows for an easy comparison to the similarly shaped signal of the sensors, providing for example information on the change of sensitivity of a sensor until it reaches saturation.

5.3.2.4 SPIKES AND NOISE CORRECTION

The drift correction explained in the previous section is very susceptible to noise amplitudes and especially to spikes in the voltage signal, which are sometimes registered because of electronic faults or power cuts. Any positive deviation from the average signal will be added permanently to the integrated value if it happens at the right point in time. Therefore, it is vital to clean the raw data from noises and spikes before applying drift correction, to prevent adding an unpredictable and significant source of error.

A customized smoothing algorithm was designed to yield a curve that is closest to the actual measurement. A loop over all data points P that are linked to individual timestamps t_i is performed. The computed mean value μ and the standard deviation σ of a given number of points $P(t_i)$ before and after the currently processed data point are used to fine tune the parameters necessary to smoothen the curve. The parameters are a number N , which is a factor that determines how much of a deviation from σ will be accepted from any data point, and a step size S that defines the number of data points before and after the current point that are being considered for calculating μ and σ . If

$$|P(t_i) - \mu| < N\sigma$$

then the point is considered “good” and will be kept as is. If

$$|P(t_i) - \mu| > N\sigma$$

the point is considered to have too much of an error, so it will be replaced by a linear interpolation between the last and the next “good” point. The parameters N and S have to be defined by hand for each sensor in order to obtain the best results. Step sizes S range between 40 and 5000 points, depending on the level of noise of the signal. Factors for N range between 0.0001 and 1. The more extreme values are used for sensors that are exposed to very low dose or fluence. For these sensors, it is generally very difficult to attribute measurements considering the high basic noise. The effect of this correction algorithm is illustrated in figure 95, which shows a zoomed excerpt of a noisy LAAS voltage signal. The green curve represents raw voltage data, and the thin blue overlaid curve consists of the points remaining after the corrections are applied. Although the signal of this particular sensor is extremely noisy, the algorithm manages to transform it into a significantly more useful curve that stays true to the original measurement.

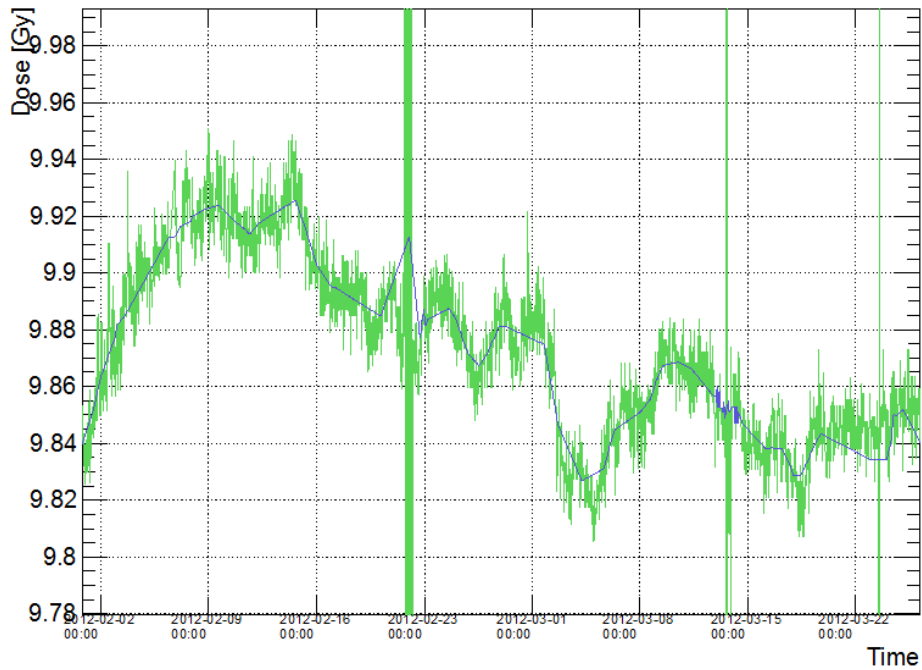


Figure 95: The effect of the spike and noise correction algorithm by the example of a zoomed in LAAS measurement curve. The green curve was only corrected for temperature and exhibits strong noise and large spikes. The blue line represents the curve after noise and spike correction, following the average values in a very faithful manner.

5.3.3 INSIDE THE EXPERIMENT: MUON STATION M1

As discussed earlier in section 5.1, passive sensors positioned inside the calorimeter detector provide valuable information about the behavior of the passive sensors within different compositions of the radiation field, as well as insights on the evolution of the field itself. Active sensors in LHCb provide fewer opportunities to analyze their behavior within a mixed field due to their lower number and more restrictions concerning their placement. However a very interesting set of placements covering a larger range of dose and fluence is located on the front of the first muon detector M1. This detector is located in between RICH2 upstream and the SPD/PS calorimeter detectors downstream. On its front plane facing the IP, the radiation field is measured along the horizontal and the vertical perpendicular to the beam in 4 sensor positions on each axis. All positions are equipped with active as well as passive sensor boxes.

The secondary particles reaching M1 did not interact with a lot of material on their way from the IP, since the first comparably heavy structure is placed downstream in the form of the lead plate in between SPD and PS. Particles are passing through the vacuum-filled VELO tracker, then the first Aerogel- and gas-filled RICH1, are subsequently deflected by the magnetic field of the LHCb dipole if applicable, pass through another 3 Tracking Stations and the gas-filled RICH2 and finally impinge on the surface of M1. Consequently, the measurements made on M1 are very helpful in verifying the reliability of the simulation for the whole area in between M1 and the IP, because there are few structures on the way that could influence the field in a strong and complex way as it is the case with the calorimeters. The most defining feature in this area is the influence of the magnetic field on charged particle tracks, which in turn affects the measured distribution of total ionizing dose on the front of M1.

5.3.3.1 LOCATIONS

Placed in the direct vicinity of each other, the active sensors at the front of M1 share the same layout as the passive sensors and are placed in their close vicinity. Due to constraints during placements in order to minimize the risk to the muon detector electronics, the boxes are usually placed a few cm apart from each other, as it is pictured in figure 96.

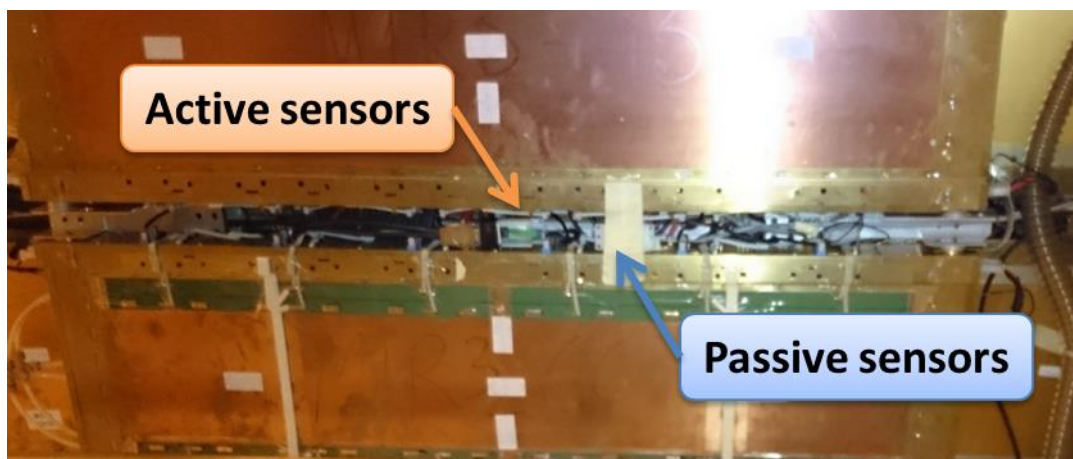


Figure 96: Placement of active and passive sensor boxes between muon detector chambers at the front of M1. To minimize the danger to the chamber electronics, sensor boxes that correspond to the same measuring position are placed a few cm apart from each other. This applies to all 8 positions on the front of M1.

For the majority of positions on M1, these few cm do not impose a large difference between measurement signals from each sensor group, since the radiation field changes less dramatically the further you move away from the beam. For the most central positions however, these gaps do very likely play a role regarding discrepancies between active and passive measurements.

The sensors that are placed along the horizontal on the A-side of the experiment are almost exactly at beam height, with active sensors usually being a few cm further away from the beam than their passive counterparts. The closest sensor along the horizontal is at 78 cm and the furthest is at 337 cm distance from the beam. All sensors are placed on the A-side for accessibility reasons. Vertically, the sensor positions are always shifted about 60 cm along the positive x-axis of the LHCb coordinate system, with one exception (M1 Y C+1) at x=78 cm. The reason for not positioning these sensors along the vertical y axis of the LHCb reference system and for them being offset with respect to the beam is partially accessibility and partially technicality and safety. Even when the two halves of the M1 detector are fully opened, there is little space available to manipulate small parts and cables exactly at the inner edge of the detector with the immovable body of the RICH2 detector in the way. In addition, the two detector halves have to match precisely when closed, and the active monitors' small movable boxes and connection cables would pose a non-negligible risk during the closing procedure by potentially moving and possibly damaging other equipment on the way. Therefore the 4 vertical positions are all located at a horizontal distance of 60-78 cm from the beam line along x. The positions of all sensors on the front of M1 are given in table 12. A sketch of the layout on the basis of the graphical interface layout of the WinCC readout system is shown in figure 97. Sensor positions are labeled based on their position along their axis, going from *M1X Center* for the position closest to the beam along the horizontal over *M1X C(enter)+1*, *M1 M1X C(enter)+2* to *M1X Outer* at the edge of the detector. Vertically, labelling is done in an analogue fashion using the prefix *M1Y*.

Table 12: Positions of sensors on the front of M1 given in cm distance from the IP. The Labels are indicating their positions as pictured in figure 97.

Position	x [cm]	y [cm]	z [cm]
M1 Y Outer	60	-325	1210
M1 Y C+2	60	-200	1210
M1 Y C+1	63	-115	1210
M1 Y Center	78	-40	1210
M1 X Center	78	0	1210
M1 X C+1	140	0	1210
M1 X C+2	237	0	1210
M1 X Outer	337	0	1210

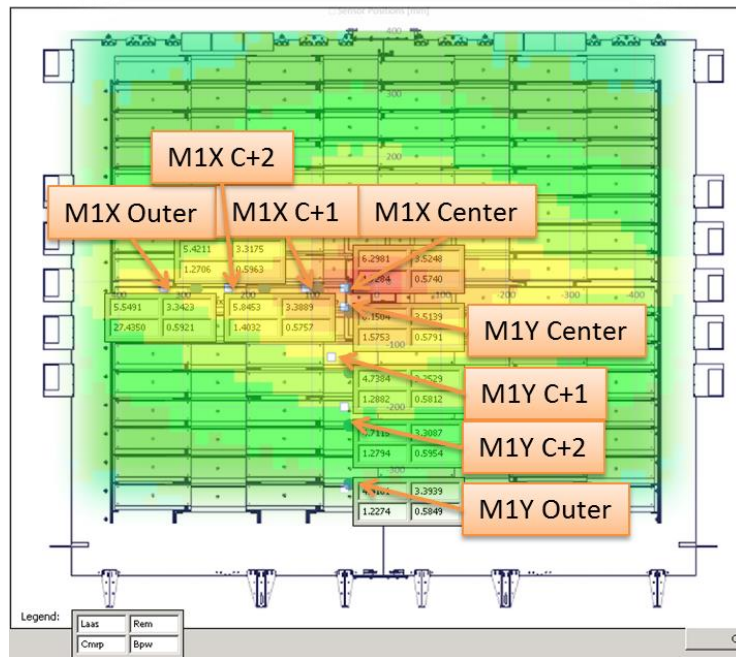


Figure 97: Layout of the sensor positions on the front of M1, based on the WinCC graphical interface panel for sensor readouts. The positions of sensors are given as a sketch and indicated by orange arrows extending from the corresponding labels. A sketch of the distribution of total ionizing dose on the position of M1 is provided as an overlay to illustrate the shape of the radiation field covered by the sensor layout.

The overlay of a plot of dose distribution to the sketch in figure 97 illustrates an interesting aspect of the radiation field perpendicular to the beam at this position. These sensor positions experience a difference in dose deposition of almost 2 orders of magnitude as well as an exposure to varying field compositions. The latter was already mentioned in section 5.1.4.

5.3.3.2 MEASUREMENTS AND COMPARISON WITH SIMULATION

In this section, the measurements from active sensors will be compared to most of the available passive sensors as well as the simulation. For dosimeters, measurements from both REM and LAAS RadFETs are compared to measurements from TLDs and Alanine. REM values are obtained applying the appropriate calibration, i.e. for dose smaller or greater than 40 Gy. According to the measured response plots taken from [34] and shown in figure 98, REM sensors should perform equally when exposed to either the most prevalent types of hadrons or photons or electrons. LAAS sensors were provided with 2 different calibrations based on the dominant impinging particle type, either high energy hadrons (HEH) or photons (PPh). Since the radiation field in LHCb is a mixed field composed of large amounts of both types, an averaged calibration curve has been added for LAAS, which is defined as the exact average between HEH and PPh curves at any point. An example of the difference between the LAAS calibrations is given in figure 99. Since the properties of the radiation field change depending on the position of the sensor, this average curve is of course only a temporary placeholder for a proper calibration using field parameters. Attempts to perform this more complex calibration will be discussed in a later section.

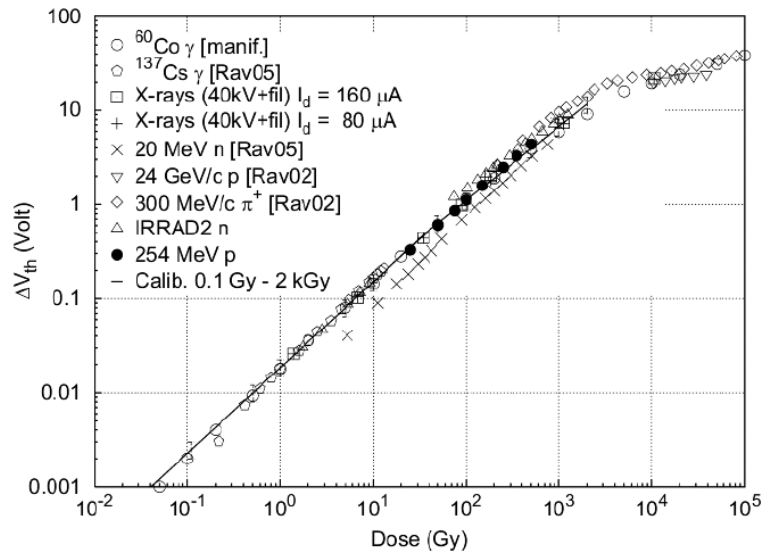


Figure 98: Radiation response of REM RadFETs as presented in [34]. The RadFET threshold voltage shift at 160 μA is plotted versus the TID. With the exception of 20 MeV neutrons, the response to γ -radiation and high energy protons (24 GeV/c) is almost identical, presumably allowing for precise measurements within the mixed field in LHCb.

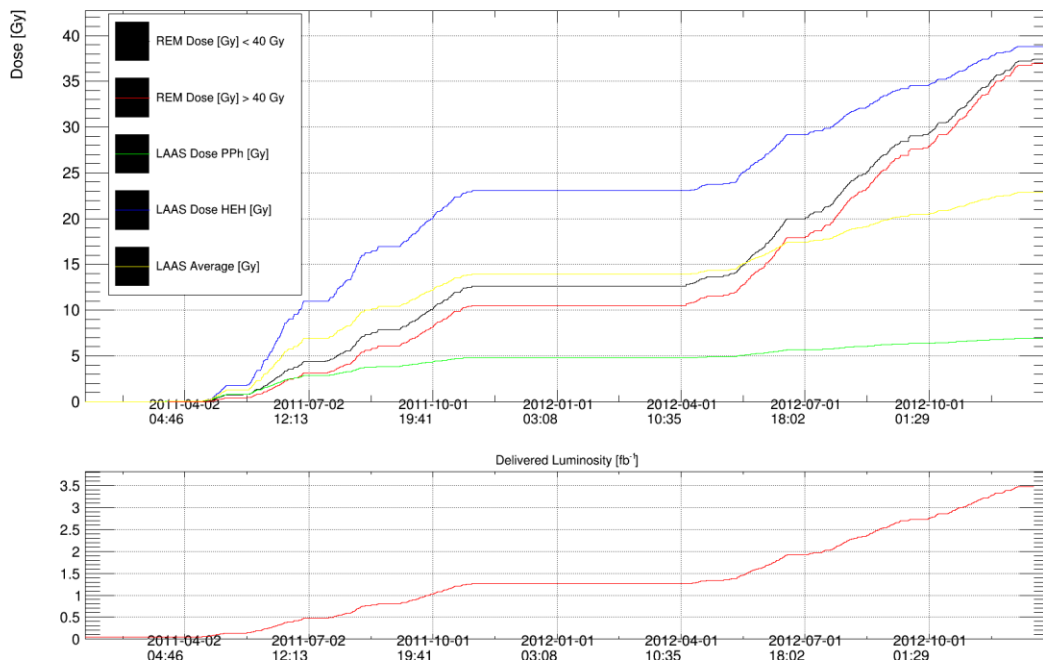


Figure 99: All available calibration curves for LAAS (blue for HEH, green for PPh and yellow for the average between both) and REM (black for <40 Gy and red for >40 Gy) RadFETs. While REM sensors only provide one possible calibration for every given point depending on the value being below or above 40 Gy, the converted signal from LAAS sensors differs strongly between the available calibrations. When the HEH curve in blue touches the upper measurement limit of 10 Gy, the green PPh curve barely reached 3 Gy.

In order to analyze the performance of active dosimeters on the front of M1, Alanine measurements are taken as reference in most cases, since they have been proven most useful in the prevalent dose range. If Alanine measured above 10 Gy, LAAS sensors are expected to be saturated, resulting in a lower value. This limit is a rather soft one that depends on one hand on the sensor itself, as some saturate significantly earlier than others, which may be able to read well up to 15 Gy. On the other hand, calibration values between HEH and PPh curves are very different and therefore the average calibration mentioned earlier will not fit well on all points of M1.

The M1 TID simulation estimates that are used as background for figures are gathered from the 20x20x20 cm³ binning of the general scoring. An additional tailored scoring in a volume between exactly $z = 1200$ to 1205 cm on the lower quarter A-side plane in 5x5x5 cm³ binning has been set up, encompassing an air volume right in front of the detector plane in the simulation geometry. Dose values that are scored within this volume are in general about 15% lower than the 20x20x20 cm³ binning, and much lower than actual measurements. The cause of this disparity is very likely at least partially based on the circumstance that the dosimeters themselves are physically placed in between the metallic muon detector chambers. In this position, they are exposed to small secondary particle showers that originate from the edges of the muon chambers that they are sitting on. This form of embedding of the sensors entails that the simulation estimate should be taken from a plane that is already slightly inside the material of the geometrical representation of the M1 detector. The 20x20x20 cm³ scoring spans from $z = 1200$ cm to 1220 cm and averages over the whole geometrical representation of the M1 detector as well as over the air volume in front of it. While the larger binning is considered to be more accurate in many cases, the values that are used for comparisons in the next section are taken from the higher resolution scoring with 5x5x5 cm³ binning. As discussed earlier, the 20 cm resolution is not sufficiently precise in the central area around the beam line, since the gradient of deposited dose is increasing too steeply. The higher resolution enables to make more precise comparisons on sensor locations while taking a systematic reduction of the estimation because of the aforementioned reasons into account.

5.3.3.3 COMPARISONS OF TID BETWEEN ACTIVE AND PASSIVE SENSORS AND SIMULATION

The location of M1 and the fact that it has been equipped with an assembly of all types of active and passive sensors available in LHCb provide an excellent opportunity for gaining a detailed view of the radiation field of LHCb upstream of the calorimeters, before particles are attenuated and absorbed on a large scale. Due to the grouped placement of active and passive sensors, the measurements can be compared to each other for each of the 8 spots of the cross-like placement scheme. It is only in the central areas that a few cm of distance between boxes might already result in a noticeable discrepancy between measurements due to the high gradient of dose distribution alone. The simulation estimates are also expected to be rather consistent in relation to each other for these 8 spots, since all are located on the same xy plane inside the experiment's acceptance, where the geometry is most detailed and true to reality.

Summaries of all dosimetric measurements for the campaign of 2011 and the campaign of 2012 are shown in figure 100 and figure 101, respectively. Regardless of the actual discrepancies between dose values, the first noticeable characteristic in both plots is the horizontally widened distribution that is caused by the LHCb dipole as already discussed in earlier sections. The simulation results, which also serve as background image, mirror the majority of measurements, most importantly those of Alanine values. Dosimeters at roughly equal distance from the beam line but on different axes gave largely different values, while dosimeters in the same spots usually agree with each other. The highest dose was measured as expected for the most central location *M1X Center* at 122.85 Gy with Alanine and 126.24 Gy with the active REM sensor in 2012, corresponding to 2.21 fb⁻¹ at 8 TeV CM collisions. It is important to note that, since the distance to the beam line is already 60 cm for this location, the actual maximum dose value at the central edge of the M1 detector is considerably higher. The lowest values are always registered at the bottom of the detector at *M1Y Outer*, at the highest distance along y from the beam line. The values lie around 1 Gy for 2011 and around 2-3 Gy for 2012.

There are only two points in figure 100 for which TLD measurements are taken as a reference. Both are on the bottom of the plot along y at the farthest distance from the beam line. On the outermost spot, the Alanine measurement was below threshold for the old readout equipment at the end of 2011, which is confirmed by a TLD measurement of 1.13 Gy. In the location above, Alanine shows 3.9 Gy, which is higher within a factor of 2 than all other values. However, the analysis shown in figure 74 has shown that very likely Alanine values from

2011 measuring between 1 and 10 Gy have a very large statistical error. Therefore the TLD measurement is considered more reliable in this case. For 2012, all Alanine measurements shown in figure 101 are considered reliable.

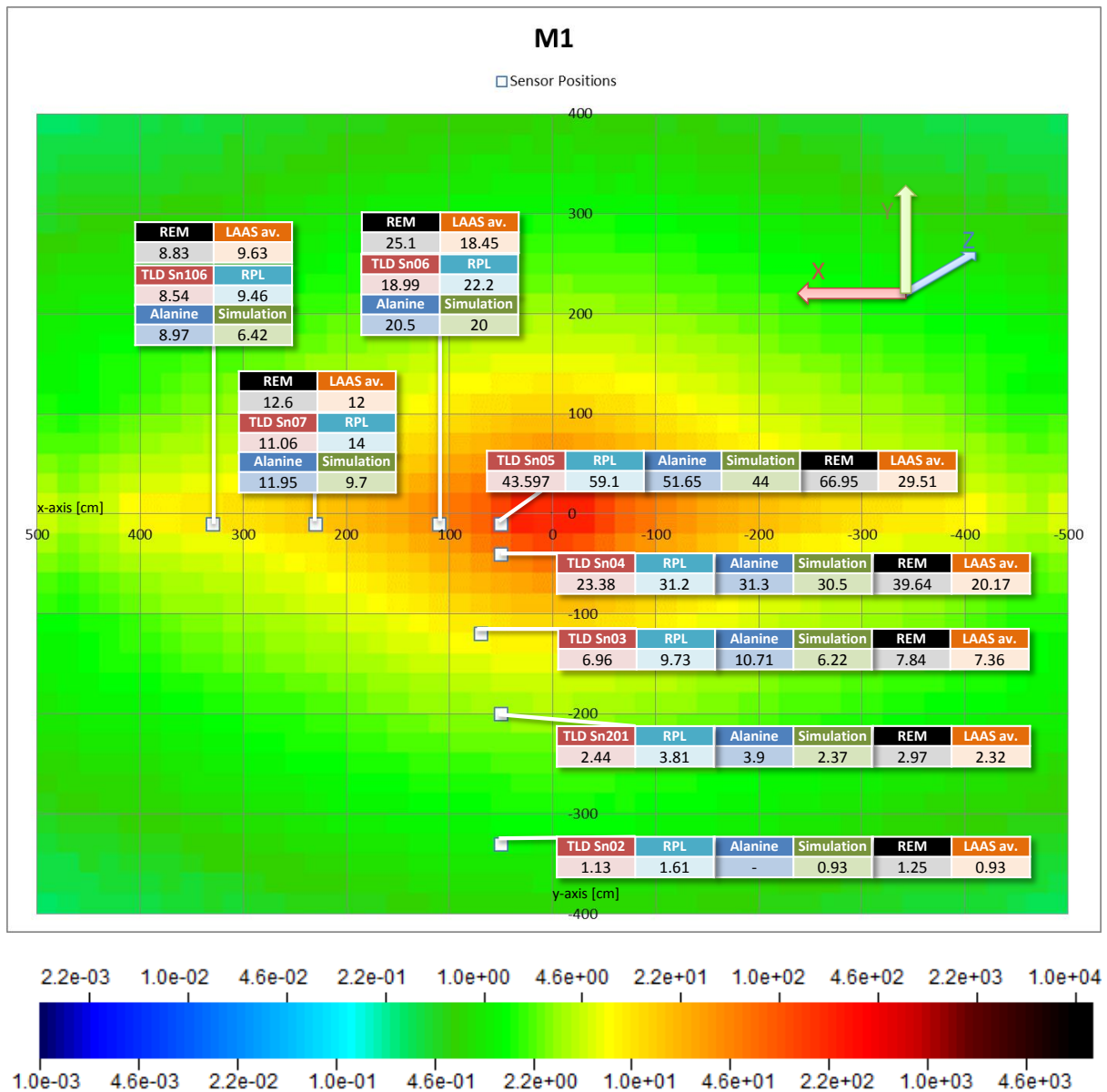


Figure 100: Compilation of measurement and simulation results for 7 TeV CM and 1.26 fb⁻¹ on the front of the M1 detector. White squares indicate the positions of sensor boxes. For each point, the dose values of each type of measurement is displayed in [Gy]. The distribution of the dose according to the simulation for 7 TeV CM is visible in the background of the plot. TLD measurements are taken from MCP-7 only, their serial number refers to the passive box, not the active one. RPL measurements are provided for illustrative reasons only, since they are not considered reliable for this campaign. For LAAS measurements, the average between the HEH and PPH calibration is displayed. Some of the LAAS sensors that are only capable of measuring up to max. 10 Gy were already saturated at this point, explaining the larger discrepancies in the central area in regard to the other values.

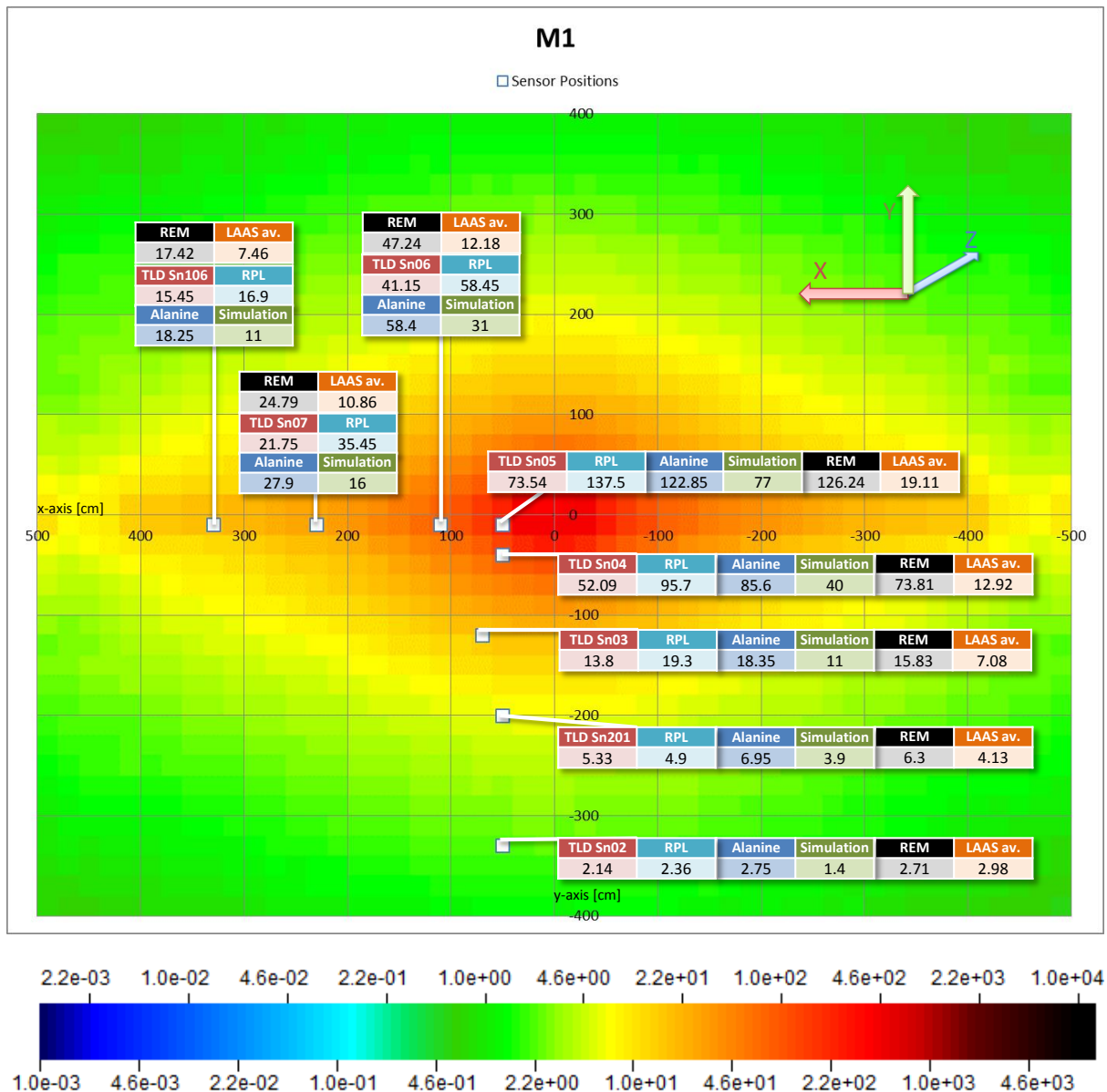


Figure 101: Compilation of measurement and simulation results for 8 TeV CM and 2.21 fb^{-1} on the front of the M1 detector. White squares indicate the positions of sensor boxes. For each point, the dose values of each type of measurement is displayed in [Gy]. The distribution of the dose according to the simulation for 8 TeV CM is visible in the background of the plot. TLD measurements are taken from MCP-7 only. RPL measurements are provided for illustrative reasons only, since they are not considered reliable for this campaign. For LAAS measurements, the average between the HEH and PPh calibration is displayed. Many of the LAAS sensors that are only capable of measuring up to max. 10 Gy were already saturated at this point, explaining the large discrepancies in regard to the other values.

REM measurements in general are very reliably within the range of trusted measurements for both measurement campaigns. The largest discrepancies are seen in 2011 in the positions of *M1X Center*, *M1X C+1* and *M1Y Center* where they differ from Alanine by up to 30%. In the measurement campaign of 2012, these discrepancies decrease to less than 20% for *M1Y Center* and almost vanish for *M1X Center*. At *M1X C+1*, the relative difference remains but Alanine now measures more than REM instead of less. This behavior could be caused by at least two reasons: on one hand, calibration curves for REM are based on power functions, which inherently have varying levels of accuracy depending on how close the measurement is to the fit of the calibration. On the other hand, these three sensors already started measuring dose values before they were connected to the current database. As described earlier, an offset correction has been performed for the

sensors *M1X Center (Sn13)* and *M1Y Center (Sn12)*. If the shift of V_0 was not corrected with sufficient precision, this could have influenced the fit of the calibration in a negative way. For sensor *M1X C+1 (Sn40)*, this correction was not performed at all since it was not deemed meaningful at the time, although the current results suggest that it should have been tried. For all other points, REM and Alanine results are in very good agreement with each other at less than 20% difference. The only exception to this is *M1Y C+1* which differs by around 37% in 2011. However in this case the absolute value of the difference remains in 2012, but due to the increased dose measurement the relative error decreased. This might point to a small systematic error that could be confirmed in future measurement campaigns.

In comparison to REM values, measurements from the more sensitive LAAS sensors tend to be accompanied by more complications in this location. Firstly, 3-4 sensors around the center already reached saturation before the end of 2011, when the passive measurements were collected. These cannot be easily benchmarked anymore without resorting to interpolation. The 4th sensor of these would be *M1X C+2* measuring 12 Gy in 2011, which is in perfect agreement with Alanine and REM. As explained earlier, the saturation limit of 10 Gy is not a hard one and may vary between different sensors. Other measurements from 2011 are equal or below REM and Alanine values, with sensors on the y-axis measuring significantly lower than on the outer two positions on the x-axis. Since all plot values are based on the averaged calibration, this could suggest a different sensitivity to charged hadrons, which are impinging in greater number along the horizontal axis due to the magnetic field. LAAS measurements below 10 Gy generally agree quite well with TLD MCP values from that year. Even in that comparison, positions along x and one location still close to the center (*M1Y C+1*) are showing slightly higher values than TLDs, while *M1Y C+2* and *M1Y Outer*, where the dominant particle type starts to change from high energy hadrons to photons and electrons, measure less. At least for *M1Y Outer*, this behavior might actually be influenced by a severe sensor deficiency, as will be explained after this paragraph using figure 102. More importantly, while a different sensitivity to high energy protons was indeed measured in [34], LAAS sensors are actually supposed to show less sensitivity to hadron radiation. Therefore, the seemingly sensible behavior described above could be dismissed as a coincidence due to measurement errors and limited precision of sensor readout. In 2012, LAAS values seem to be off by a very large margin for all points except *M1Y C+2* and *M1Y Outer*. This is caused by the fact that the active measurements shown in the 2012 plot are in fact subtracted from the integrated measurement of the whole Run1. Active sensors provide continuously updated accumulated values. Consequently, since most sensors saturated at one point during 2012, their signal increase, meaning the difference to the measurement point of the end of 2011, was not proportional to the dose anymore. The only sensor that should have provided a reliable measurement is *M1Y C+2*. Its measurement of 4.13 Gy is at least close to the expected value of almost 7 Gy, if not very accurate, being even lower than the TLD measurement.

A special case of a LAAS failure resulting in a discrepancy with successive passive measurements can be observed for sensor *M1Y Outer*, which is the outermost placed location in y direction in front of the M1 detector. In figure 102, fully corrected dose measurements compared to only temperature corrected measurements for all calibrations of both active dosimeters of *M1Y Outer (Sn28)* are shown. Not only are the readout curves for the LAAS sensor rather noisy before the smoothing algorithms are applied, they also display a very irregular behavior starting around May 2012. A huge spike in the signal leads into an unexplainable drop, after which the signal starts to increase in an exaggerated manner over the course of the following weeks, until another drop seems to bring the signal back into its regular behavior at the beginning of July. The smoothing and drift correction algorithms that are successfully applied to most other sensor readouts, are not able to recognize this gravely prolonged irregularity as such and therefore handle the increase as normal, while ignoring the large drops at the beginning and the end of this month-long bump. The measurements from the LAAS sensor on this M1 position cannot be considered truthful for 2012 although the signal lies well within the sensors measuring range. The overall noisiness including two less large but still significant bumps of the signal during 2011 suggests that this kind of irregularity might have happened before, distorting the measurement. The exact cause of this type of malfunction, which only affected this sensor with such magnitude, could not be

determined. Luckily, the REM sensor seems unaffected and is able to take over for the upcoming operation campaigns.

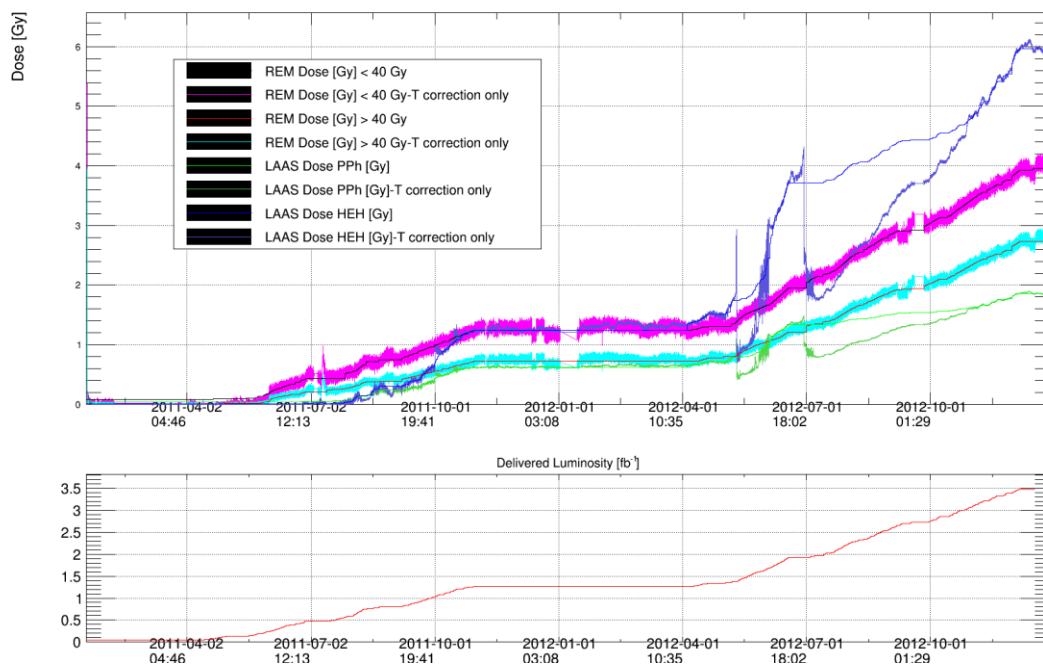


Figure 102: Dose measurements for Sensor *Sn28* on the lower edge of M1 (outermost sensors along the y-axis). Starting around May 2012, the LAAS sensor readout suddenly drops and then continues to increase in an exaggerated manner over the course of the following weeks. The curve smoothing and drift correction algorithms are not able to recognize this as faulty behavior, so the final corrected signal is overestimated. This can be best observed in both dark blue HEH calibration curves. For comparison, the integrated delivered luminosity curve is plotted in red over the same timespan on the lower canvas.

Regarding only passive measurements, in particular Alanine and TLD MCP which are shown in the figures, their behavior is as expected from the analysis of calorimeter measurements. TLD measurements are generally lower than the Alanine reference. Considering all measurements made during both campaigns, the discrepancy between MCP and Alanine in the dose range of M1 sensors of 1 to 150 Gy can be slightly higher than a factor of 2, the average being around a factor of 1.4, as it is shown in figure 103. The main cause for this discrepancy is the γ -calibrated sub-linear response of MCP above 1 Gy as described earlier.

Numbers for simulation estimates in the plots are all taken from the tailored scoring placed in the air volume in front of a flat M1 geometry representation. It does not take into account that the dosimeters are actually placed in between the metallic chambers of the M1 detector, which are not individually modelled in the simulation. As explained before, this already accounts for a large part of the difference based on significantly lower simulation values that can be seen in the figures. However even when accounting for these systematic errors, the simulation still exhibits a characteristic underestimation, which is most pronounced in 2012. For the most central points, another cause for the discrepancy could be a misalignment of the assumed positions of the boxes and their actual location in the detector. These positions were re-measured by hand during a long technical stop, but the modular nature of the M1 detector itself and the limited access even when fully opened made it difficult to correctly reference the position of the beam line during the measurement. Therefore, a positioning error of some cm at a distance between 50 and 100 cm from the beam can play an important role. Nonetheless, the comparisons in the calorimeter detectors have already shown that the simulation estimates tend to provide lower values than Alanine in all cases inside the experiment's acceptance. The front of M1 is no exception to this rule. As it was the case in the calorimeter detector, the estimations are within a factor of 2 of measurements also on the front of M1 and agree even better when considering the systematic difference due to the position of the scoring grid.

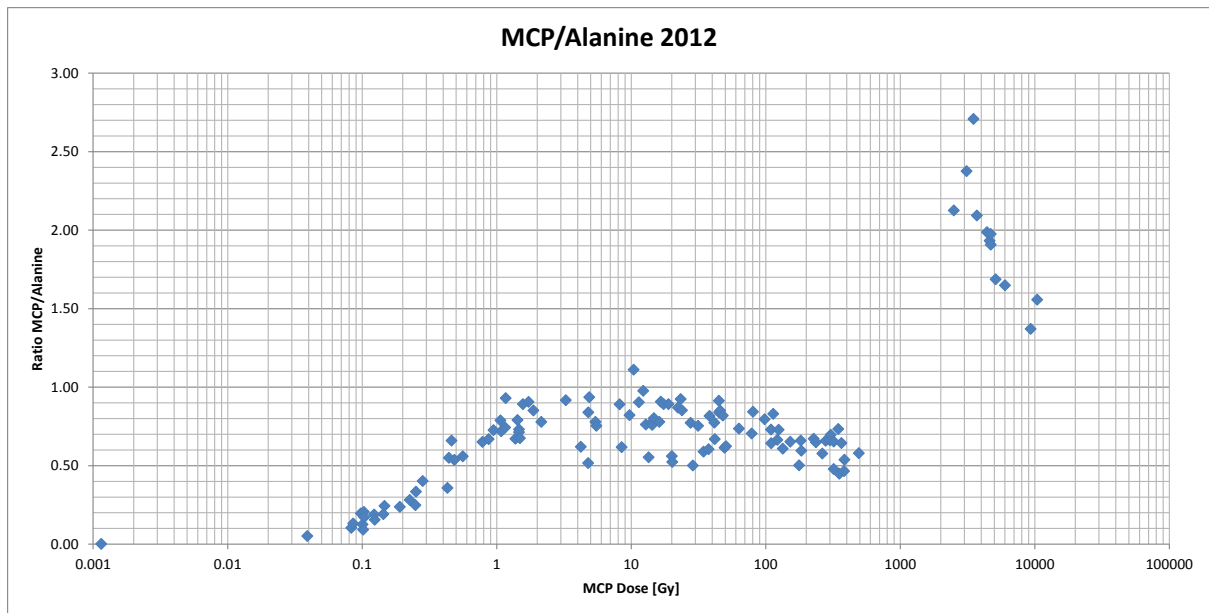


Figure 103: Comparison ratio of MCP versus Alanine measurements over the full dose range of all measurements at LHCb conducted during LS1. TLD measurements are generally lower than Alanine measurements due to the sub-linear response of MCP above 1 Gy. Above 1000 Gy, the MCP measurements are made based on the UHTR method and are significantly higher than Alanine measurements, in contrast to all points below. The decreasing accuracy of Alanine below 1 Gy compared to a reliable measurement from MCP is responsible for the steady decrease of the calculated ratio.

In contrast to results from the calorimeter detector given earlier, also RPL measurements are provided in figure 100 and figure 101. As it was explained in section 5.1.3.1, these are not to be trusted and are no confirmation of other results. However even considering some small discrepancy between RPL and Alanine, they are in line with all other measurements during both campaigns. In this case, RPL dosimeters on the front of M1 seem to have suffered less from crystal damage than in other locations. However there has not been confirmation through visual observation of the damage in the case of RPL dosimeters on M1.

On the front of M1, the REM sensor was able to provide useful measurements for all measurement positions within a few months of the start of operation of the experiment. At the end of 2012, REM and Alanine values are generally in very good agreement, as is shown in figure 104. In this plot, Alanine measurements have been summarized for the whole Run1, while the REM values are taken from the fully corrected measurement data in December 2012. The only location with a slightly larger disagreement is *M1Y Outer*, where the measurement campaign of 2011 didn't yield any result for Alanine. Therefore the ratio is calculated by using the corrected REM value from the calibration for dose >40 Gy representing 3.47 fb^{-1} , compared only against the Alanine measurement from 2012 which corresponds to 2.21 fb^{-1} . The latter should account for two thirds of the 2011 dose, which again would bring the ratio very close to 1 in this point. These results suggest that REM sensors could prove to be a very reliable and very valuable type of sensor for an online dosimetry system in the range of 1 Gy to several kGy, once all necessary signal corrections, in particular the drift correction, are implemented into the online system in a sound and efficient way.

As already mentioned, the simulation estimations are lower than all measurements on the front of M1, as expected from results inside the calorimeter detector. The discrepancy between simulation and Alanine for summarized values from the start of operation until the start of LS1 always remains quite stable within a factor of 2.

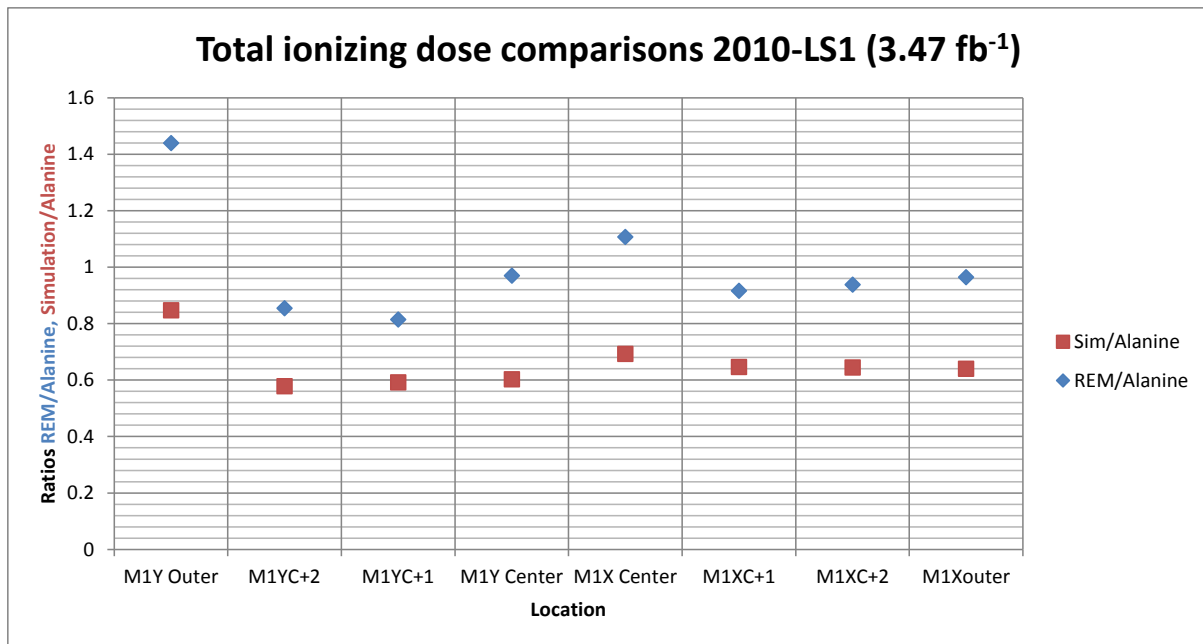


Figure 104: Comparisons of total ionizing dose measurements from REM sensors on the front of M1 with Alanine measurements and simulation estimates summarized for the whole Run1 until LS1. Measurements and simulation estimates have been added accordingly from both 7 TeV CM and 8 TeV CM campaigns. The ratio between REM and Alanine values is given in blue for all 8 positions and ratios between simulation and Alanine values are given in red for comparison. With the exception of M1Y Outer, where the REM signal is still barely above threshold, all REM values measure within 20% of Alanine.

5.3.3.4 COMPARISONS OF 1 MEV NEUTRON FLUENCE EQUIVALENT BETWEEN ACTIVE AND PASSIVE SENSORS AND SIMULATION

In contrast to the dosimetry efforts discussed in this thesis, the evaluation of 1 MeV neutron fluence equivalent measurements rely mostly on comparisons with simulation estimates. The only passive sensor that measures this quantity is a passively used BPW diode of the same type that is present on the active sensor PCBs. As mentioned earlier, this sensor is not sensitive enough to measure the rather low fluences in most areas of LHCb. This is emphasized by the individual active measurements and simulation estimates from each campaign listed in table 13, where only the most central locations close to the beam show a significantly higher fluence than the BPW threshold of 10^{11} cm^{-2} .

CMRP sensors on the other hand were able to measure well within their range of 10^8 to 10^{12} cm^{-2} for the whole length of Run1. The sensor at *M1X Center* in particular reached its upper limit and is likely already showing signs of signal deviation. A comparison of summarized simulation estimates for both campaigns and the final fully corrected values of CMRP and BPW sensors is shown in figure 105. The ratios between CMRP and simulation are in exceptionally good agreement for 5 out of 7 values. The small discrepancy in the two most central locations can also be easily explained by looking at the actual measurements in table 13, which show that the signals are nearing or exceeding their maximum range of 10^{12} cm^{-2} . In contrast to REM or LAAS dosimeters, this fluence sensor actually becomes increasingly responsive above this value. This phenomenon can be seen in the fluence plots of the most exposed sensors of LHCb, which will be discussed in the next section.

The simulation of 1 MeV neutron fluence equivalent is expected to estimate more precisely than that for dose, since it is based on track length fluence of various particles instead of energy deposition events. Consequently, less statistical error is expected, and systematic errors due to geometry and material inconsistencies have a

smaller impact because of the low interaction potential of high energy neutrons with most of the detector material inside the acceptance. In this regard, the excellent agreement with CMRP measurements indicates a reliable estimation of 1 MeV neutron fluence equivalent via simulation on one hand, and a reliable fluence measurement device which can even be used online to document the evolution of the signal on the other. For Run2 and upgrade campaigns, the passive sensor boxes at M1 have additionally been equipped with passively used Si-2 diodes, which should be very similar in performance to CMRP diodes. Unfortunately, CMRP diodes could not be used since they are not produced any more.

Table 13: Values of 1 MeV neutron fluence equivalent taken from CMRP and BPW sensors on the front of M1 after 1.26 fb⁻¹ at the end of 2011 and after 3.47 fb⁻¹ at the end of 2012, which remained stable until the beginning of LS1, compared to the corresponding simulation estimates. The correlations between the numbers are visualized in figure 105.

1.26fb-1 (Dec. 2011) [cm ⁻²]				3.47fb-1 (Dec. 2012) [cm ⁻²]		
Simulation	CMRP	BPW	Position	Simulation	CMRP	BPW
5.55E+09	6.57E+09	1.25E+09	M1Y Outer	1.54E+10	1.96E+10	1.67E+09
1.72E+10	1.83E+10	6.61E+10	M1Y C+2	4.74E+10	5.80E+10	7.83E+10
5.39E+10	4.49E+10	1.21E+11	M1Y C+1	1.49E+11	1.62E+11	1.56E+11
1.95E+11	1.95E+11	2.32E+11	M1Y Center	5.39E+11	7.83E+11	3.70E+11
2.70E+11	2.99E+11	2.50E+11	M1X Center	7.47E+11	1.40E+12	4.75E+11
9.52E+10	7.10E+10	1.28E+11	M1X C+1	2.63E+11	2.67E+11	1.80E+11
3.50E+10	2.89E+10	6.81E+10	M1X C+2	9.67E+10	9.60E+10	8.93E+10
1.88E+10	1.75E+08	1.24E+10	M1X Outer	5.20E+10	1.75E+08	1.82E+10

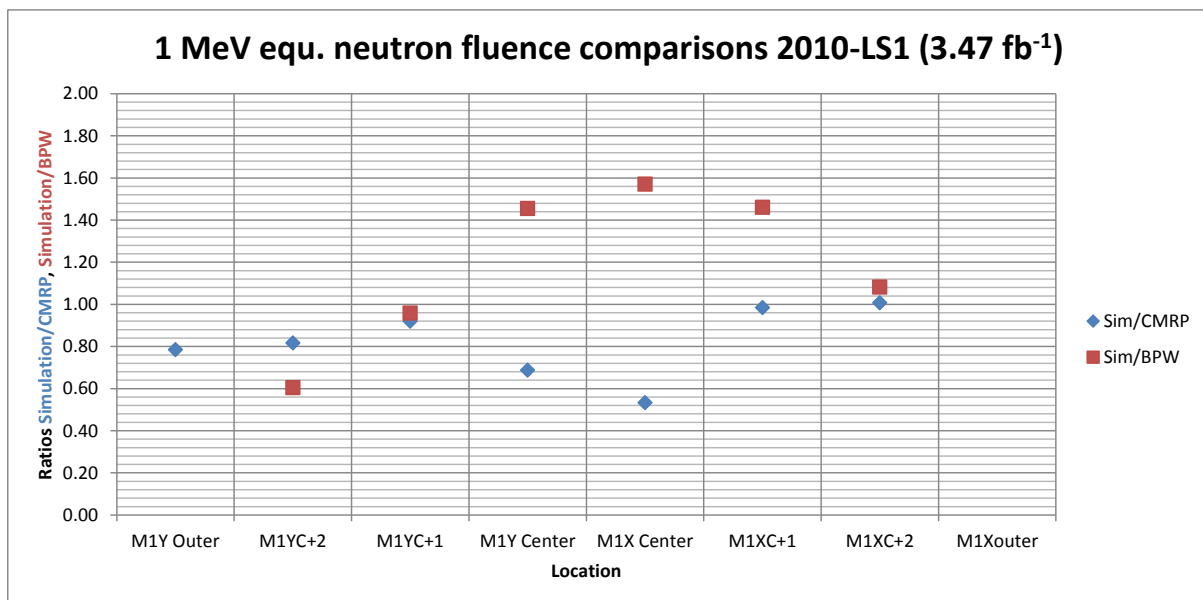


Figure 105: Comparisons of 1 MeV equivalent neutron measurements from CMRP (blue) and BPW (red) sensors on the front of M1 with simulation estimates summarized for the whole Run1 until LS1. Simulation estimates have been added accordingly from both 7 TeV CM and 8 TeV CM campaigns. Assuming a reliable prediction from the simulation, CMRP measurements seem to underestimate slightly at the central positions, but are generally well within a factor of 2 of expectation. BPW values seem to exhibit a sensible pattern of sensitivity compared to the simulation. This shape might be produced by pure coincidence. The fluence sensors at the position M1X Outer unfortunately ceased to work before the start of 2012.

At the end of 2012, the BPW measurements on the front of M1 have mostly exceeded the threshold of 10^{11} cm^{-2} . Results of passive PiN sensors at that time have shown only 2 sensors from the very center that measured above 10^{11} cm^{-2} during Run1. The passive PiN in the *M1Y Center* position accumulated $1.87\text{E}+11$ cm^{-2} in LS1 after 3.47 fb^{-1} , while *M1X Center* measured $2.40\text{E}+11$ cm^{-2} . For these two positions, both active and passive versions of the PiN sensor are measuring within an almost exact factor of 2 of each other, with the active sensors giving the higher value. This discrepancy can be explained by the generally high temperature sensitivity of BPWs influenced by the less accurate passive temperature measurement. In addition, as was shown in figure 94, some BPW diodes exhibit very high noise within successive measurements. Since passively used diodes are only read out once, a potential error is very high, although the risk of electrical connection errors which occur during readout of active sensors is minimized by careful handling and using short direct connections to the power supply. In contrast to that, the active sensors are connected over dozens of meters of cables to the next crate. In future measurement campaigns, passive BPW should be read out at least 3 times in direct succession in order to determine if the sensor suffers from high noise and to subsequently mitigate it by averaging measurements.

At the beginning of LS1, the active BPW measurements all seem to lie within a factor of 2 of the simulation predictions, displaying a shape which seems to indicate a varying sensitivity to the radiation field. However the shape might as well be pure coincidence since many sensors only recently passed their sensitivity threshold. Individual plots for 2011 and 2012 do not show any reasonable data since the initial BPW offset is not 0. Considering the relatively low dose and fluence rates on the front of M1 compared to the calorimeter detector, the BPW sensors are only just starting to be of use and will hopefully be providing more precise measurements during the upcoming campaigns of LHC Run2 and the following LHCb upgrade, when the collision rate and consequently the fluence and dose rates during operation are going to be significantly increased.

No values are given for the position of *M1X Outer* in figure 105, because the fluence sensors ceased to function correctly at some point before the start of 2012. Although there are replacement sensor PCBs available, it has been decided to leave the PCB untouched because the more interesting REM sensor on this position is still measuring very well, which could not be guaranteed for the replacement. Besides, the passive box at this position has been equipped with an additional passively used PiN diode for Run2 which shares most of the properties of a working CMRP diode and should provide reliable yearly measurements in the following campaigns.

5.3.4 HIGHLY EXPOSED RADIATION AREAS

Although there are many accessible locations in the experiment close to the beam pipe where the accumulated dose deposition reached far into the kGy range before LS1, only 3 of all 28 active sensor boxes were placed where such high irradiation levels occur. Of those 3 sensor boxes, only 1 is actually inside the experimental cavern on the upstream wall next to the beam pipe, whereas the other 2 are located in the upstream tunnel, attached to the ECAL test modules. As explained earlier, these test modules are supposed to receive more dose than the central modules of the ECAL detector in the same timeframe. As a consequence, only the less sensitive REM dose monitors provide actually useful information on measured dose, since LAAS sensors were driven into saturation very shortly after the start of operation. Furthermore, the measured signal of REM and CMRP sensors became high enough to experience a visible and impactful drift over time. It will be shown that efficient drift correction measures are an absolute requirement to continue to collect useful information from these sensors over time.

The active and passive sensor boxes next to the Beam Loss Scintillators (BLS) in the experimental cavern are pictured in figure 106. They are located on top of a metal plate in front of the upstream concrete wall, right above where the beam pipe passes through the wall. At only 15 cm vertical distance from the beam line and slightly over 2 m distance from the interaction point, these sensors are exposed to a high energy radiation field depositing very high levels of dose.

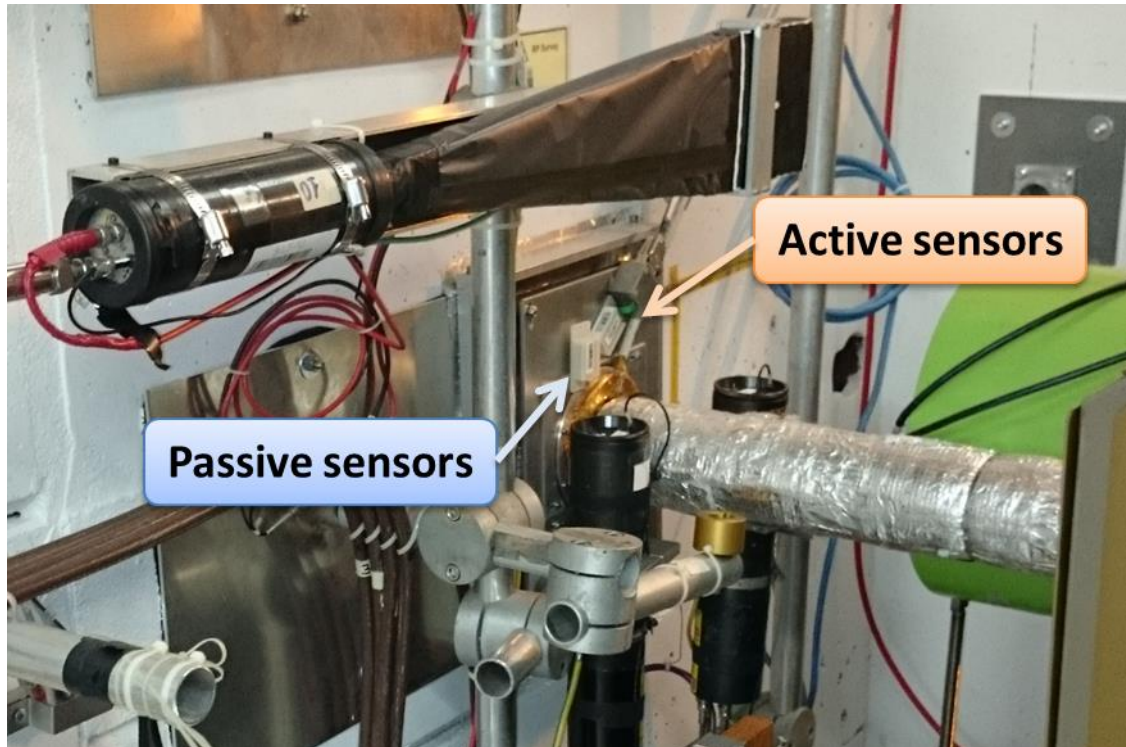


Figure 106: Active and passive sensor boxes located right above the beam pipe on the upstream wall. The sensors are placed about 15 cm from the beam line.

The ECAL modules in the upstream tunnel are placed at a slightly greater distance from the beam line. A photo of the position of those two sensors which are placed directly on top of passive boxes was shown earlier in figure 92. However the radiation fields in these cases are not directly comparable. In the tunnel section, the magnetic field of the corrector dipole close to the modules is responsible for widening the cone of radiation that is hitting them. In contrast, the sensors at the BLS are exposed to the direct byproducts of the collisions inside the VELO, and the showers started by them inside the VELO vacuum vessel. Nevertheless, the resulting measured dose values on the ECAL modules are within the same order of magnitude that is experienced by the sensors next to the BLS in the cavern.

5.3.4.1 TOTAL IONIZING DOSE VALUES

The distribution of dose at the position of the BLS sensor is mainly influenced by the radiation coming directly from the direction of the IP, which can be seen in figure 107. The high energy products from the collision either reach the sensors directly or interact mostly with the steel tank of the VELO vacuum vessel. The resulting secondary particle showers are still very forward-directed and the particles impinging on the upstream wall where the BLS sensor is placed are highly energetic, containing a comparably large quantity of hadrons in the GeV energy range in addition to the electromagnetic showers. The lethargy distribution of the most relevant fluences is shown in figure 108.

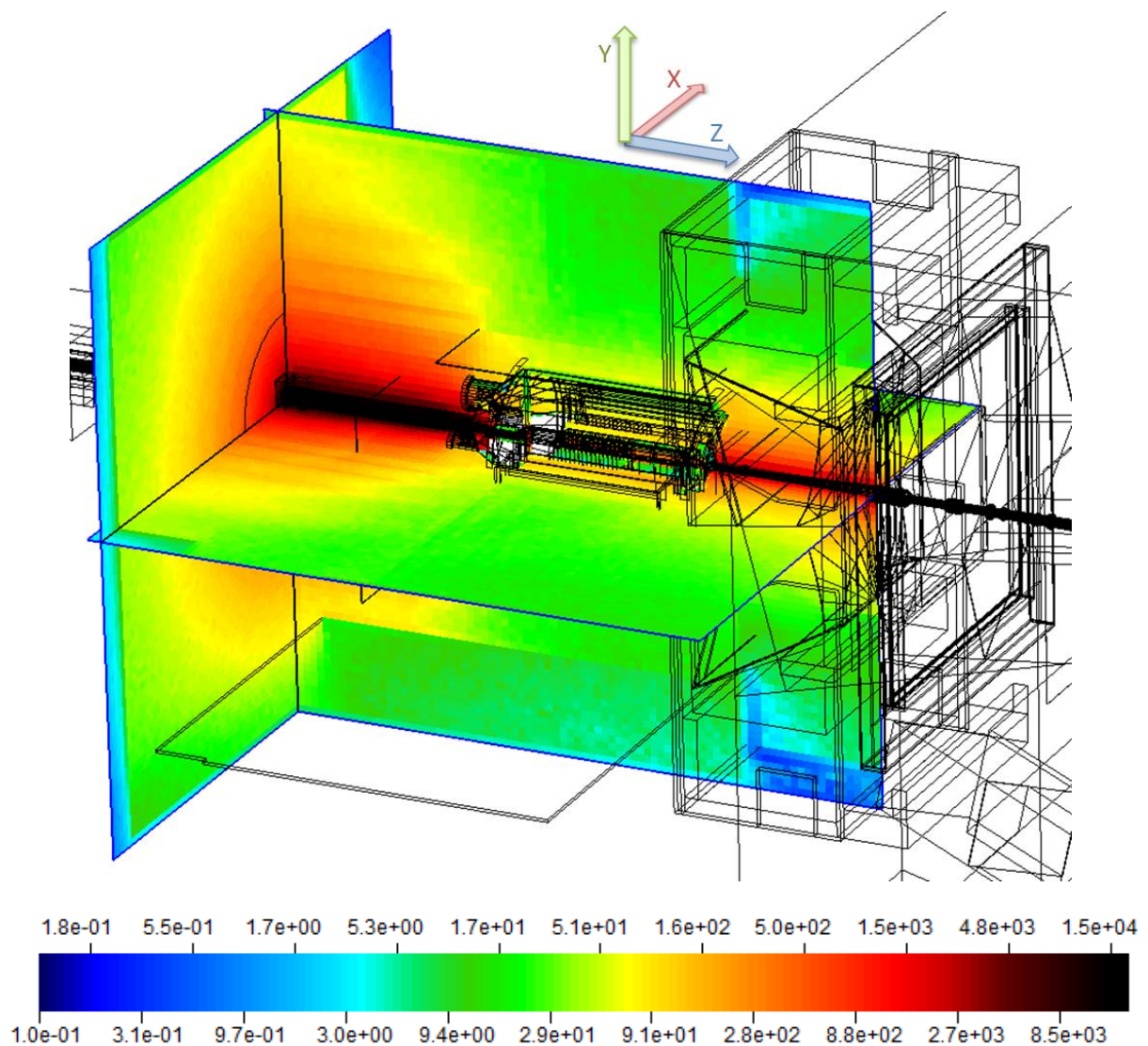


Figure 107: 3D plot of the dose distribution in the VELO alcove in 2012 estimated for 8 TeV CM collisions and corresponding to 2.21 fb^{-1} . The xy plane on the left side is placed exactly on the surface of the upstream wall, displaying values averaged over 5 cm in front of it. The other two planes cross exactly along the beam line. The radiation cone originating from the collisions and the interactions of the collision products with the VELO vacuum vessel can be clearly seen.

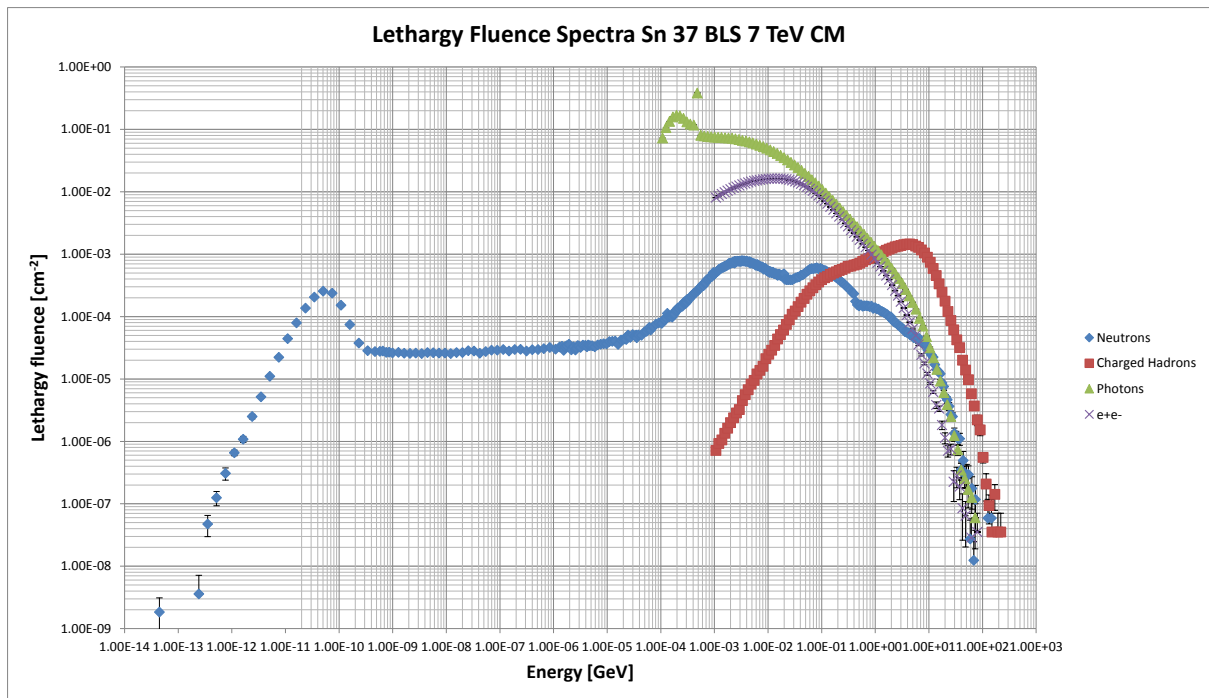


Figure 108: Lethargy distribution of the fluences of neutrons, charged hadrons, photons and electrons/positrons at the location of the passive and active sensors *Sn37* close to the BLS on the upstream wall in the VELO alcove. The sensors are exposed to a high energy field containing a particularly large quantity of hadrons in the GeV range.

With the dose value transcending 1 kGy, REM signals start to experience an increasingly impacting influence from annealing effects, leading to a strongly visible drift of the signal towards lower levels. This effect is displayed for the sensors of *Sn37* in figure 109, where the drift can also be observed in the LAAS curve that is operating orders of magnitude above its defined measurement range. The effect of the annealing is only corrected for during periods with no collisions happening. However, it is safe to assume that annealing happens as well during collisions when the measurement signal is continuously rising. As a consequence, even though the REM measurement is largely following the shape of the luminosity curve, it is expected to deviate from Alanine measurements more strongly with increasing dose levels. This expectation is confirmed by the measurement comparisons listed in table 14. While the lowest of the 3 measurements around 2 kGy shows less than 3% deviation from the Alanine measurement, the difference increases to around 10 % at 3 kGy and it differs by more than a factor of 2 for the sensor at the BLS. Another important observation can be made in figure 109 regarding the annealing behavior. During the long technical stop between December 2011 and April 2012, the drift of the signal exhibits a changing slope over the course of time. Short-term annealing effects are responsible for a sharper decrease right after beam stop, while long-term effects lead to a rather straight flatter curve towards the end of the stop. The currently applied correction functions are oblivious to the difference between the various forms of annealing since it is of no importance for their implementation. A correction function which also counteracts annealing during collisions would need to also take additional factors into consideration. The algorithm would have to be itself a function of the already measured dose and likely of the dose-rate and also of the time of operation to consider the effects of the long-term annealing. Designing such a function would be far from trivial and has not yet been tried. As a consequence of the expected increase of the discrepancy in the measurement of dose, the 3 active sensor PCBs described in this section have been exchanged against fresh ones during LS1. The reason was to again receive accurate measurements for the Run2 operation that do not have to rely on even more sophisticated correction algorithms not yet conceived.

Table 14: Dose values for the three most exposed dosimeter positions in LHCb, summarized for the whole Run1 until LS1. Alanine values are used as reliable reference. REM values are within the same order of magnitude, but the highest value shows a very clear discrepancy caused by heavy annealing. Simulation estimates are only given for one position, because estimates in the upstream tunnel area are not considered reliable.

<i>Dose accumulated until LS1 [Gy]</i>			
<i>Location</i>	<i>Alanine</i>	<i>REM > 40 Gy</i>	<i>Simulation</i>
Sn37 (Passive Sn37): BLS	9871.00	4115.70	7880
Sn39 (Passive Sn104): ECAL TM beamside	3350.00	3019.90	NA
Sn38 (Passive Sn103): ECAL TM wallside	1947.00	1893.61	NA

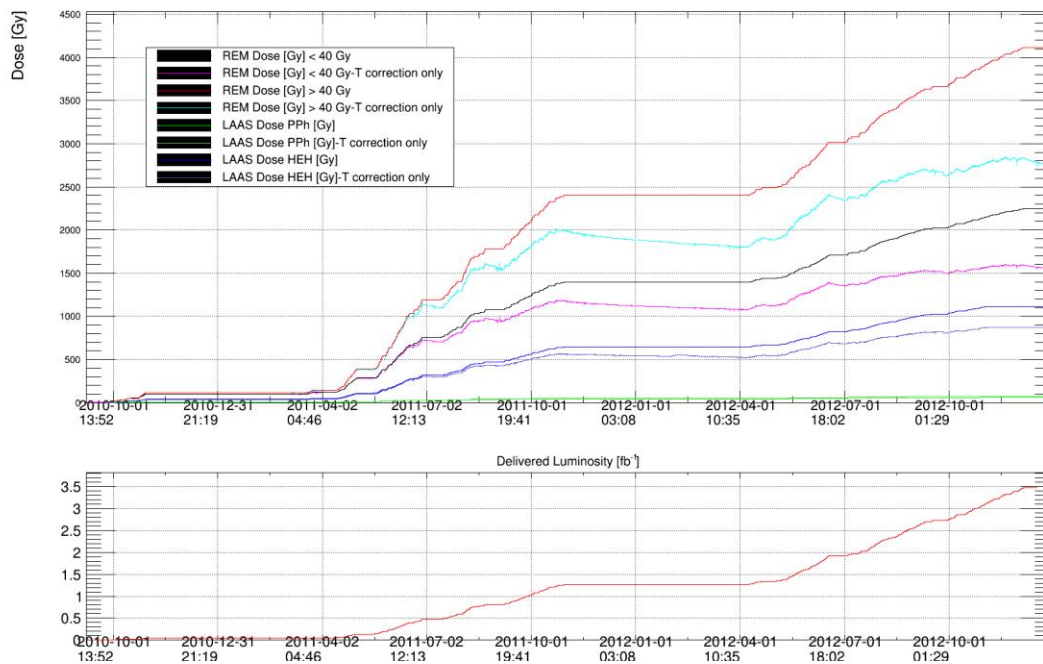


Figure 109: Dose measurements from REM and LAAS sensors of Sn37 at the BLS until LS1. The final fully corrected signals are plotted together with raw measurements where the voltage has only been temperature corrected and then directly converted into dose. Both sensors exhibit a visible drift of the signal over time due to annealing which becomes worse with increasing dose levels. The REM signal based on a calibration for dose >40 Gy (top curves in red and light blue) gains around 1400 Gy from drift correction during beam off periods. LAAS sensors are considered saturated in this case and their signals are not used. However they are still following the luminosity shape to an extent. For comparison, the integrated delivered luminosity curve is plotted in red over the same timespan on the lower canvas.

The simulation estimate in table 14 for the BLS location is taken from the 5x5x5 cm³ scoring in the VELO alcove, summarized from both irradiation scenarios. The value in the bin containing the position of the box is around 25% lower than the Alanine measurement. Due to the very small distance to the beam line, the dose gradient is very steep. A smaller 1x1x1 cm³ scoring performed in this region has shown that between 10 cm and 15 cm distance from the beam, the dose can change by about a factor of 2. Since the actual position of the Alanine dosimeter inside the box in relation to the beam line is only known to a precision of a few cm, this estimate is already considered useful. A more accurate information of the dosimeter position and a corresponding scoring with a higher resolution will likely yield an estimation which is closer to the Alanine measurement. In fact, the 1x1x1 cm³ scoring has suggested this, but its statistical error is too large to fully trust it. In any case, apart from the evaluation of the simulation's accuracy, information on the dose in this area in a cm³ resolution is not needed as of now. The 5x5x5 cm³ scoring is able to provide useful values for most applications. As explained earlier, no estimations can be provided for the ECAL test modules in the upstream tunnel, because attempts to reproduce results in this region have failed for various reasons.

In the case of these 3 highly irradiated positions, LAAS sensors are effectively without use at the moment. Once their practical maximum measuring limit of about 10 Gy is reached, which happened quite early for these sensors, every LAAS sensor signal starts to deteriorate visibly and quite quickly. As the sensors are getting saturated, their voltage readout ceases to be useful in combination with their provided calibration. However, in the figures depicting the final corrected measurement curves of sensors number *Sn37*, *Sn38* and *Sn39*, the drift-corrected LAAS curves apparently still continue to follow the luminosity curve. Since this is the case with every LAAS sensor in the experiment which did not exhibit any other problems besides showing symptoms of saturation after being exposed to more than 10 Gy, it might be possible to find a fine-tuned calibration for saturated and drift-corrected LAAS signals which makes them applicable to measure dose well into the kGy range.

As it was already attempted in the central regions of the ECAL, the TLD MCP sensor at these three locations have also been evaluated using the UHTR method, which allows to measure into the kGy range. It was already mention in section 5.1.4 that large inconsistencies have been found in between measurements from the two measurement campaigns in 2011 and 2012. While the single TLD UHTR result from the ECAL test modules in the tunnel is reasonably close to Alanine values in 2011, the values differ by a factor of 2 to 3 from Alanine in 2012. The values from Alanine and MCP from both campaigns at the BLS and at the ECAL test modules are listed in table 15. The sensors placed close to the BLS are no exception to this behavior, although the discrepancy is lower. TLD MCPs measured within 10% of Alanine in 2011, but are off by around 37% in 2012. This inconsistency between campaigns could not be explained up to now. Future measurement campaigns from Run2 and the LHCb upgrade will yield more candidates for UHTR evaluation due to higher expected luminosities and also a higher collision energy. These might prove to be more helpful in determining the cause of this phenomenon, and maybe even a possible calibration to enable the use of TLDs on a significantly enlarged dose range.

Table 15: Passive TLD results compared to Alanine from both measurement campaigns where the UHTR method was applied. While results are reasonably accurate in 2011, the TLD measurements in 2012 show large deviations due to unknown reasons.

2011 <i>Location</i>	<i>Position [cm]</i>			<i>Dose [Gy]</i>	
	<i>x</i>	<i>y</i>	<i>z</i>	<i>Alanine</i>	<i>TLD MCP</i>
Sn105 ECAL TM	-70	60	-8660	3130	3360
Sn37 (BLS)	0	15	-215	3090	2915

2012 <i>Location</i>	<i>Position [cm]</i>			<i>Dose [Gy]</i>	
	<i>x</i>	<i>y</i>	<i>z</i>	<i>Alanine</i>	<i>TLD MCP</i>
Sn102 ECAL TM	-132	0	-8820	1292.5	3500
Sn103 ECAL TM (Sn38 active)	-264	0	-8380	1305	3100
Sn104 ECAL TM (Sn39 active)	-132	0	-8380	2213.5	4400
Sn105 ECAL TM	-70	60	-8660	6679	10400
Sn37 (BLS)	0	15	-215	6781	9300

5.3.4.2 1 MEV NEUTRON FLUENCE EQUIVALENT VALUES

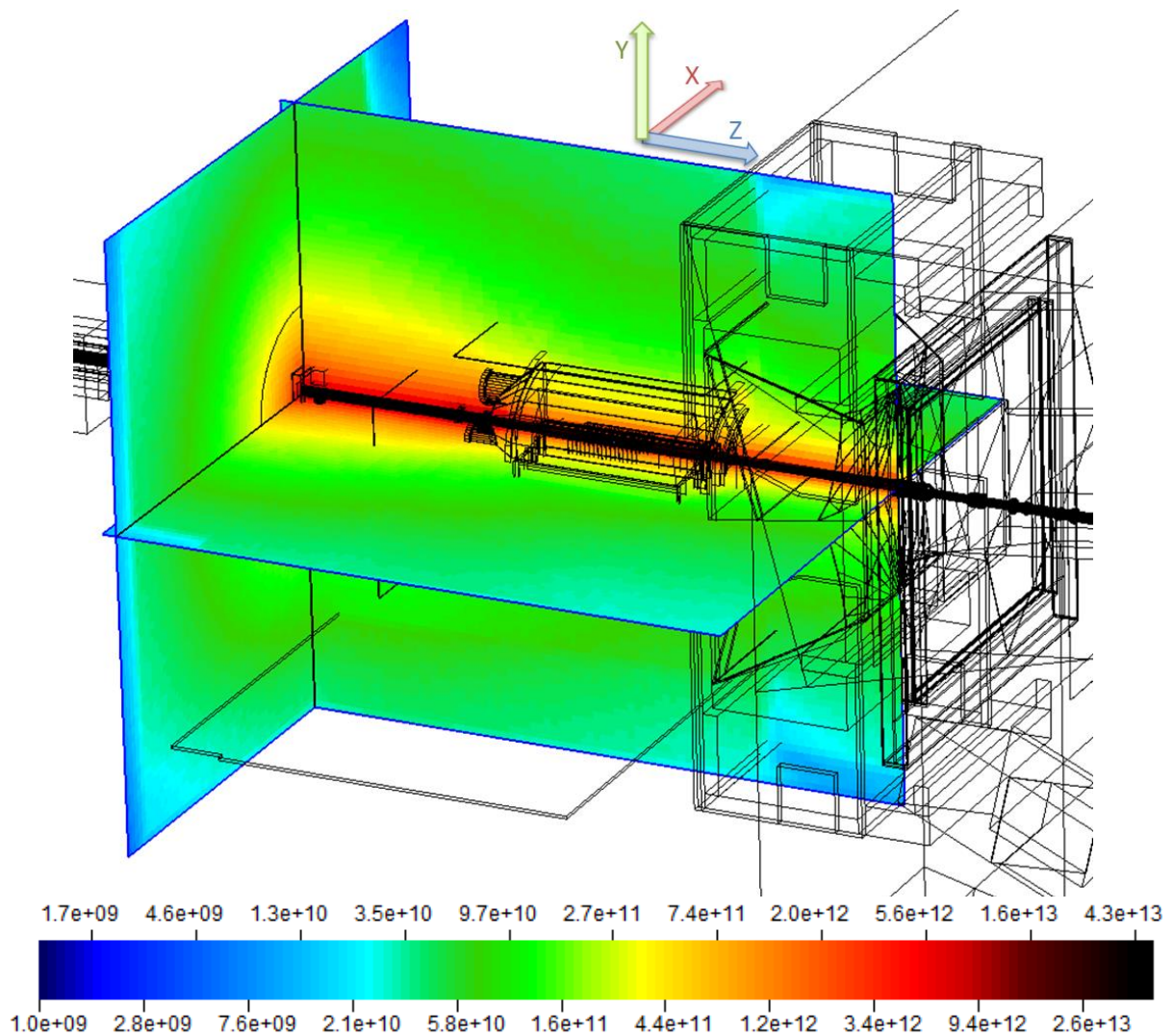


Figure 110: 3D plot of the 1 MeV neutron fluence equivalent distribution in the VELO alcove in 2012 estimated for 8 TeV CM collisions and corresponding to 2.21 fb^{-1} . The xy plane is placed exactly on the surface of the upstream wall, displaying values averaged in front of it. The other two planes cross exactly along the beam line.

The 1 MeV neutron fluence equivalent distribution in the VELO alcove is similar in shape to the dose distribution, but it is much more forward-directed with a non-negligible backscattering of neutrons from the upstream concrete wall. A three-dimensional simulation plot of the distribution is shown in figure 110.

Unlike the convenient layout of active and passive sensors in M1, the three locations discussed in this section do not provide as many opportunities for cross-checking fluence measurements, since the simulation cannot be used for two of them, and the expected fluence levels are above the upper measurement limit of CMRP diodes, leaving only BPW sensors to provide values. Nonetheless, CMRP measurements are listed besides BPW and one simulation estimate in table 16, although they are considered out of their valid range.

Table 16: 1 MeV equivalent neutron values for the three most exposed dosimeter positions in LHCb, summarized for the whole Run1 until LS1. BPW measurements are within their quoted measurement range, but seem to be lower than simulation values in the case of Sn37. Active and passive BPW measurements agree quite well in all cases. CMRP values are always higher because of the specific sensor behavior of increased response above its measuring limit. By chance, the CMRP value for Sn37 is nearing the simulation estimate in LS1 due to the signal ceasing to increase after the first half of 2012. The sensor measured much higher than simulation values during the time before. Simulation estimates are only given for one position, because estimates in the upstream tunnel area are not considered reliable.

1 MeV neutron fluence equivalent accumulated until LS1 [cm⁻²]				
Location	BPW	CMRP	BPW (pass.)	Simulation
Sn37 (Passive Sn37): BLS	2.78E+12	4.58E+12	2.40E+12	4.05E+12
Sn39 (Passive Sn104): ECAL TM beamside	1.28E+12	4.98E+12	1.17E+12	NA
Sn38 (Passive Sn103): ECAL TM wallside	7.69E+11	3.63E+12	7.81E+11	NA

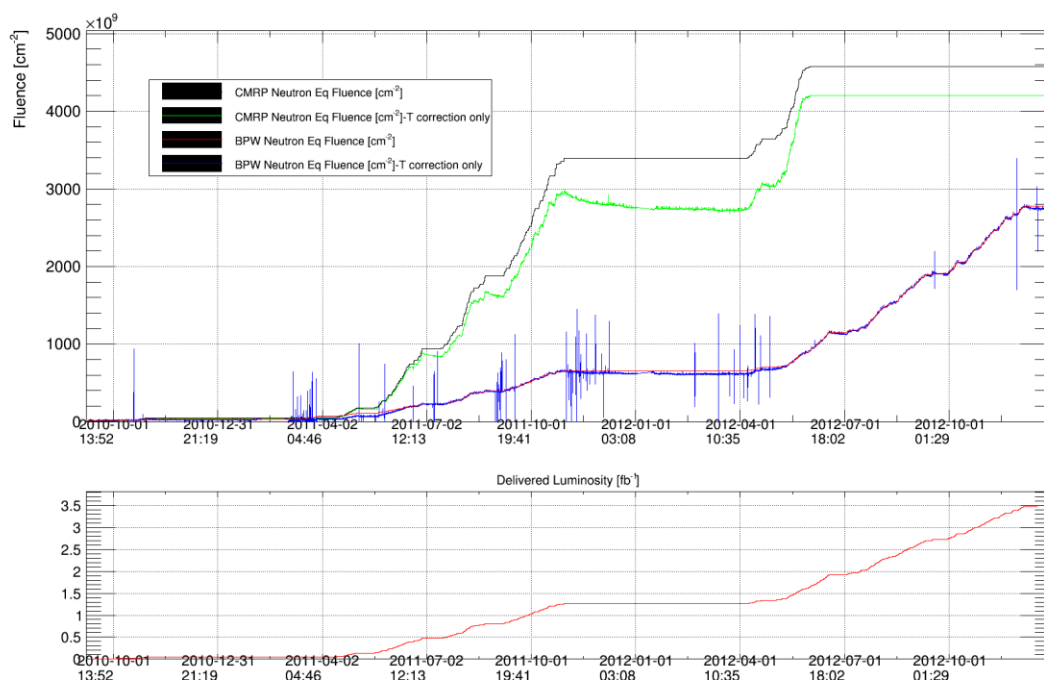


Figure 111: 1 MeV neutron fluence equivalent measurements from CMRP (black and green) and BPW (red and blue) sensors of Sn37 at the BLS until LS1. Fully corrected curves are plotted next to values which are only temperature corrected and then converted. The BPW sensor is showing high instances of noise, but is otherwise following the luminosity. CMRP values also seem to follow luminosity, but its upper measurement limit of 10^{12} cm⁻² has been already exceeded in 2011, at the crossing point with the BPW curve. Instead of a flat saturation curve, this sensor type actually shows an increased response with heavy signs of annealing. After the first half of 2012, the CMRP signal ceased to move. For comparison, the integrated delivered luminosity curve is plotted in red over the same timespan on the lower canvas.

In LS1, the measured fluence from BPW on the active sensor PCB Sn37 at the BLS, which is plotted in figure 111, is only about 16% higher than the passive measurement which yielded $2.40E+12$ cm⁻². Both of the other two passive BPW measurements from the passive boxes attached to the active sensors on the ECAL test modules agree even better with their counterparts. Considering that the visible annealing in comparison to the curve without drift correction seems very low, this points to a very good agreement between passive and active BPW sensors in these high radiation areas. However the plots also show that the provided calibration curve for BPW does not scale well with the luminosity. The amount of measured fluence up to the winter shutdown at the end of 2011, corresponding to 1.26 fb⁻¹, is around $6.5E+11$ cm⁻², and with an additional 2.21 fb⁻¹ of delivered luminosity it suddenly increases to $2.8E+12$ cm⁻². This means that with the change in collision

energy from 7 TeV CM in 2011 to 8 TeV CM in 2012, the measured fluence per collision on average almost doubled between the two measurement campaigns. According to simulations this is highly unlikely. The explanation for this phenomenon can be glimpsed in the measured response of the BPW sensor presented in [34], which is shown in figure 112. The calibration of the sensor defined in (8) and (9) is assumed to be linear, while the response of the sensor up to a fluence equivalent of around 10^{13} cm^{-2} is clearly not. Since the BPW measurements only arrive just below $3 \cdot 10^{13} \text{ cm}^{-2}$, it is expected that the response of these sensors will increase further during Run2. In comparison with the simulation estimate taken from a $5 \times 5 \times 5 \text{ cm}^3$ scoring, the BPW signal is lower in the BLS position, but still lies within a factor of 2. Unfortunately no reliable simulation estimates are available for the positions on the ECAL test modules, therefore it can only be assumed that the simulation would estimate in a similar way. A direct comparison with CMRP values listed in table 16 also suggests that the BPW measurement might be too low in its lower measurement range. All CMRP sensors have passed their upper measurement limit of 10^{12} cm^{-2} . Judging from the CMRP curve in figure 111 as well as from the comparisons in the previous section at the center of M1, it is likely that CMRP measurements start deteriorating already halfway between 10^{11} cm^{-2} and 10^{12} cm^{-2} . Up to that point, they have shown very good performance in their range of measurement. They also continue to follow luminosity values, although in an exaggerated way. In June 2011, CMRP and BPW measurements differ almost by a factor of 5, although they are both within their established ranges between 10^{11} cm^{-2} and 10^{12} cm^{-2} . Considering that the increase per collision for BPW was only half as large during 2011 compared to 2012, and that the values at the end of 2012 were still lower within a factor of 2 than simulation estimates, the true value of June 2011 is expected to lie in between BPW and CMRP measurements. Based on the nonlinear response of BPW to increasing integrated fluence, its measurements are expected to approach simulation estimates during Run2. On a side note concerning CMRP values, the most exposed sensor at BLS showed heavy signs of actual saturation if not malfunction in the middle of 2012 after an exaggerated increase of the signal during 2011, as it can be seen in figure 111. Nonetheless, maybe a multi-faceted calibration covering a higher fluence range for CMRP as well as increasing precision towards its current upper measurement limit could be found in the future so that more of them can continue to be of use during upgrade scenarios.

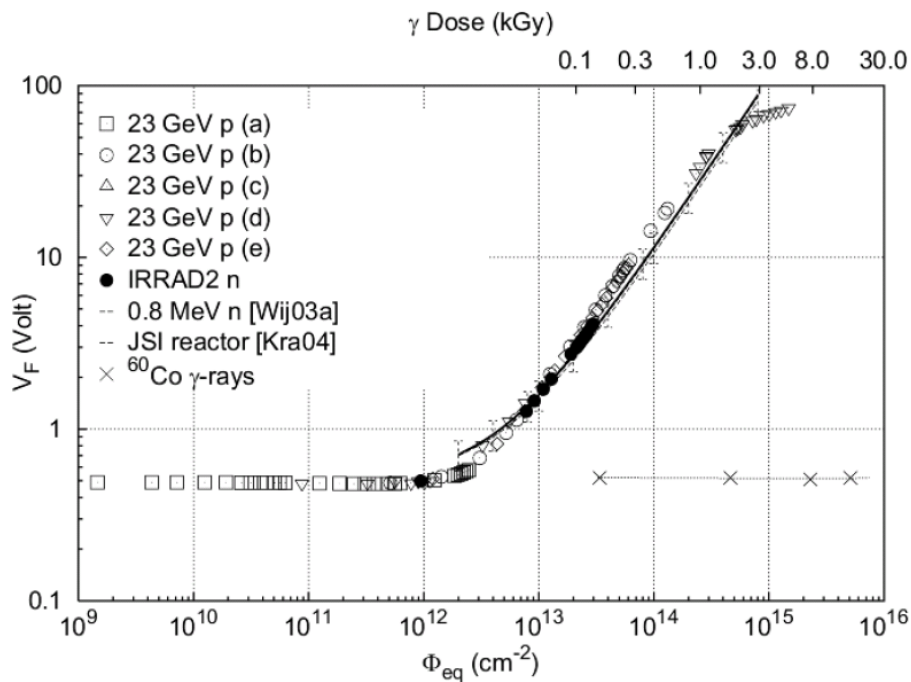


Figure 112: Radiation response of BPW PiN sensors according to [34]. The forward voltage of the diode is plotted versus the fluence equivalent for several different intensities of a 23 GeV proton beam, as well as irradiation from neutron sources. While the assumed fit for the calibration of the sensor is linear, a clearly non-linear behavior in the region below 10^{13} cm^{-2} can be observed.

5.3.5 AROUND THE EXPERIMENT'S ELECTRONICS

While some active dosimeters are used in moderately to highly exposed areas of the experiment as shown before, the bigger part of them is distributed at a larger distance to the beam line and exposed to only small amounts of dose and fluence. The main reason for those placements was to observe the radiation field in the vicinity of many electronic racks and other installations close to the experiment. The monitored electronics are responsible for controlling the individual subdetectors as well as reading out and pre-processing the data. Therefore they are vital for the experiment's successful operation. Eventual malfunctions or failures due to unexpected exposure to radiation should be recognized and possibly avoided using information from these sensors.

In the following sections, 17 sensor groups containing active and passive sensors which are distributed all over the experimental cavern plus one which is even further away are described. All but two of these 17 positions which are closer to the detector are pictured in figure 113. The remaining two which are placed at a greater distance to the detector, one on the balcony and one in the barracks on the accessible side of the shielding wall in the underground cavern are pictured in figure 114. Both figures only depict projections of locations on a top-down view taken from the WinCC interface for the active sensors. In reality, many of the sensor locations are at up to 6 m distance in height from the beam line. Apart from the "RICH1 exit" location which is located at less than 1 m distance from the beam line, all other places where arrows point to the center of the experiment are outside the experiment's acceptance. Almost all of the locations are exposed to different radiation field compositions, making it difficult to compare individual values of any of those, bearing some exceptions. In the following section, locations will be grouped according to their suitability for comparison. Due to the large number of groups, any detailed descriptions of locations will be given alongside the measurement results.

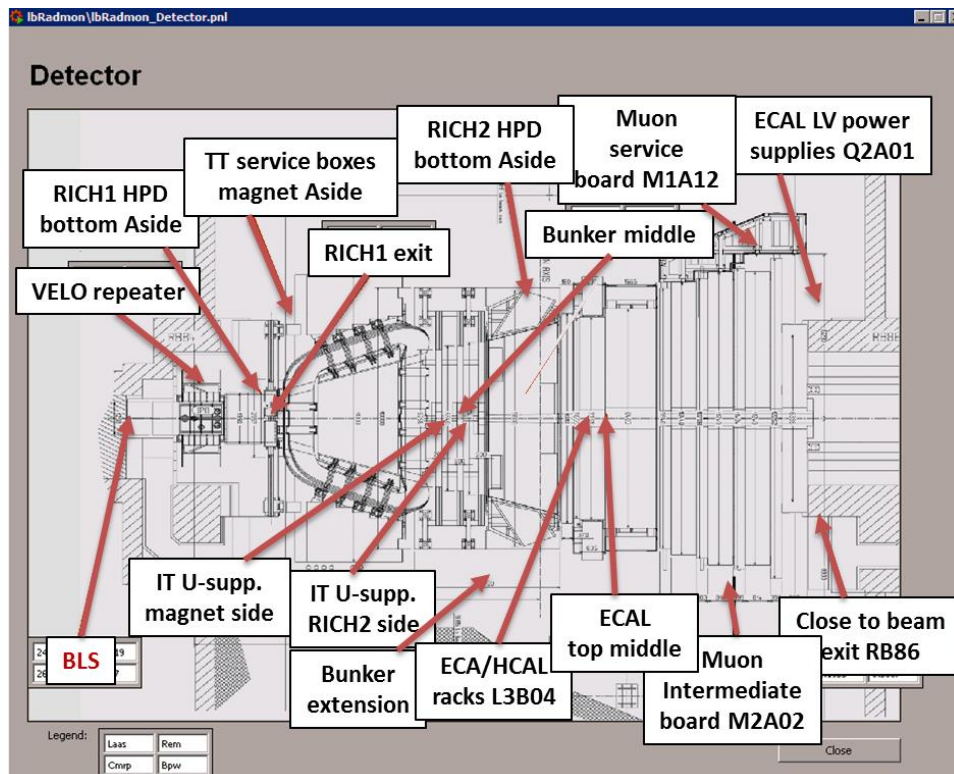


Figure 113: WinCC interface showing most of the positions of active sensors around the LHCb detector in a top down view. Red lines leading from the readout panels are pointing to the areas of placement. Since this is a 2D projection, many of them are actually placed at different heights, up to 4.5 m below and 6 m above the beam line. The leftmost position on the upstream wall near the BLS has been discussed in a previous section.

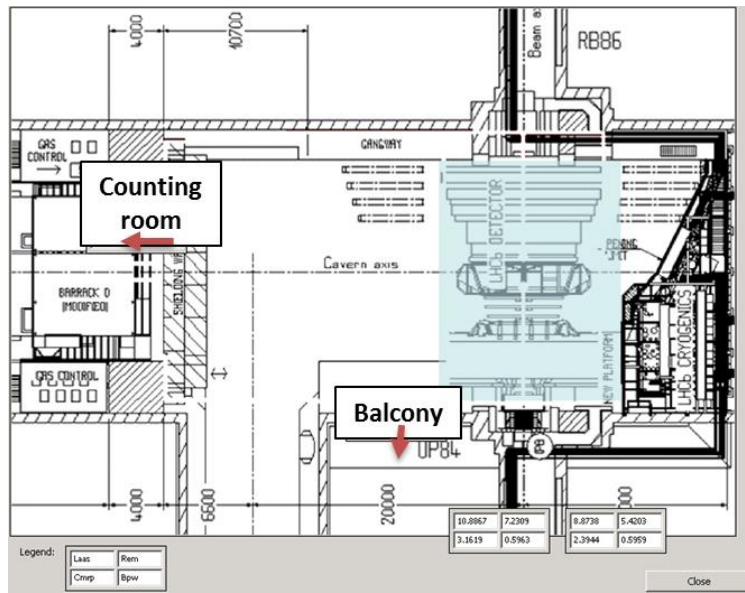


Figure 114: Positions of the active and passive sensor groups described in this section that are not shown in figure 113. One group is located on the balcony next to the experiment, on the top of electronics' racks. The other one called "Counting room" is located behind the shielding wall on the accessible side of the underground area, on the third floor of the container barracks which are housing the LHCb computing farm and data acquisition. The two unlabeled value displays on the bottom of the layout belong to the sensor positions on the ECAL test modules in the upstream tunnel, discussed in the previous section.

5.3.5.1 MEASUREMENT RESULTS (TOTAL IONIZING DOSE)

In this section, active and passive measurements at the various positions distributed mostly around the outside of the LHCb detector close to electronics will be evaluated and compared to each other as well as to simulation estimates. The dose measurements will be analyzed in groups of sensors with similar placements or field properties. With the exception of 4 sensor groups, all of the locations in this section have been exposed to very small amounts of dose and fluence, leaving TLD measurements as the only reliable dosimetry reference. The remaining 4 groups are evaluated based on the corresponding Alanine measurements. Due to the lack of comparable measurements, the active 1 MeV neutron fluence equivalent measurements from active sensors will subsequently be compared to simulation estimates only. Summaries of dose and fluence measurements alongside their descriptors and positions in the LHCb coordinate system are listed in table 17 and table 18. The descriptions and explanations in this section generally follow the order of table 17, while some sensors will be discussed together because of their similar placement.

The highest dose of all the sensors in this section was measured at RICH1 exit, located below the beam pipe on the downstream backside of the RICH1 magnetic shielding box, as shown in figure 115. This location was chosen because the Trigger Tracker (TT) detector has front-end electronics located at several cm distance from the sensors. The RICH1 shielding features a practical ledge where both an active and a passive dosimeter box could be placed without interfering with the access to and movement of the TT detector halves. Since the Alanine measurement has a value of 67.75 Gy as listed in table 17, neither TLD nor LAAS measurements are expected to provide accurate measurements in this case. REM measures around 15% less than Alanine, and gives the same value as the simulation estimate, placing all of them within an acceptable range of agreement. No significant drift correction had to be applied up to this point. However the REM signal history of this sensor does exhibit some irregular behavior, such as large spikes equaling a point measurement of several Gy appearing in almost regular intervals, and a small rise of the signal during long Technical Stops. Technical

problems behind the cause of these irregularities could be partially responsible for the 15% discrepancy versus Alanine, although this disparity is already considered small. The LAAS averaged signal mostly overlapped accurately with the REM curve until they reached 10 Gy. Saturation effects took over for the LAAS curve above that point. The earlier described issues of sub- and supra-linearity of MCP and MTS responses can be observed as expected at this location, where MCP measures almost 16 Gy below Alanine while MTS measures 7 Gy above.

Table 17: Summary of dose measurements and simulation estimates of 17 mostly low-level active and passive sensor groups in the vicinity of the experiment's electronics. Results from passive sensors and simulation from both measurement campaigns are added up to reflect the integrated signal at the start of LS1 representing 3.47 fb^{-1} . Most Alanine measurements did not exceed threshold. Two locations further away from the experiment have not been included in the simulation scoring. Measurements of both ^7Li based TLD types are listed in this table. They are expected to provide very similar measurements in the dose range below 1 Gy, but in some instances a significant discrepancy is observed.

<i>Run1</i> 3.47 fb^{-1}	<i>Coordinates [cm]</i>			<i>Dose [Gy]</i>						
	<i>Description</i>	<i>x</i>	<i>y</i>	<i>z</i>	<i>Alanine</i>	<i>Sim</i>	<i>MCP-7</i>	<i>MTS-7</i>	<i>REM</i>	<i>LAAS av.</i>
	RICH1 exit	0	-80	215	67.75	57.00	52.01	74.73	58.60	25.44
	IT U-support Magnet-side	50	-250	830	NA	2.37	1.33	1.37	1.47	2.93
	ECAL top middle	114	576	1360	NA	0.67	0.15	0.16	0.11	3.14
	Counting house	NA	NA	NA	NA	NA	0.00	0.00	0.18	0.03
	Bunker extension	-600	-450	1000	NA	0.39	0.18	0.32	NA	NA
	Bunker middle	50	-450	1000	NA	0.20	0.18	0.33	0.08	0.04
	Balcony	1200	150	250	NA	NA	0.15	0.28	0.04	0.19
	VELO repeater	75	0	20	38.25	46.10	31.85	34.89	39.70	17.51
	RICH2 HPD bottom A-side	430	0	1030	18.12	13.60	17.58	16.61	15.07	15.48
	IT U-support RICH2-side	50	-250	890	NA	3.25	2.28	2.21	2.76	4.05
	TT service boxes magnet A-side	330	-100	240	NA	2.80	2.47	2.48	2.91	4.55
	ECAL LV powersupplies Q2A01	370	410	1920	NA	0.11	0.69	1.21	0.78	0.09
	ECAL/HCAL racks L3B04	100	400	1290	NA	0.72	0.36	0.37	0.33	0.58
	Muon intermediate board M2A02	-620	110	1650	NA	0.66	0.69	0.68	0.61	0.68
	Muon service board M1A12	620	-140	1650	NA	0.73	0.42	0.40	0.12	0.01
	Close to beam exit at RB86	-380	110	2030	NA	0.12	0.12	0.22	0.17	0.08
	RICH1 HPD bottom A-side	95	-90	112	12.48	12.80	12.04	11.36	14.52	13.28

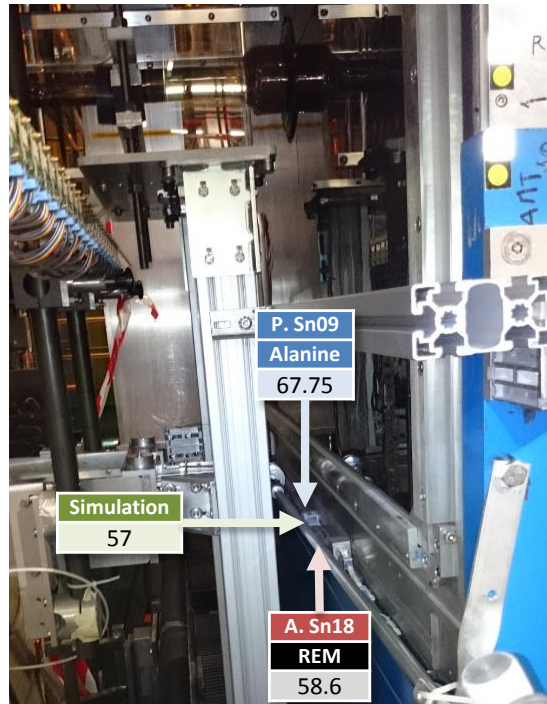


Figure 115: Positions with dose measurements and simulation estimate in [Gy] of active and passive sensors at the “RICH1 exit” on a ledge of the RICH1 magnetic shielding below the beam pipe, which can be seen in the upper half of the picture. The large aluminum support bars in the picture are only present to support the beam pipe protection during a long technical stop and are removed during normal operation when this space is taken by the closed TT. While TLD measurements also agree within their expected linearity deviations, only Alanine and REM measurements are shown in the figure.

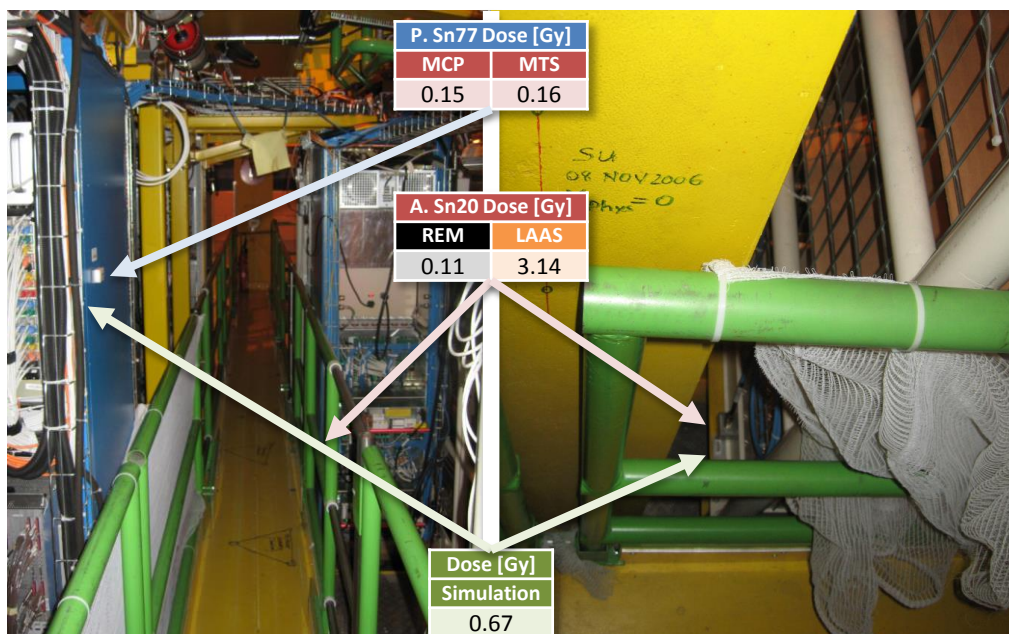


Figure 116: Positions with dose measurements and simulation estimate in [Gy] of active and passive sensors on the walkway on top of the calorimeter detectors. The walkway on the left picture is seen from C-side towards A-side. The passive sensor *Sn77* is glued to the blue rack at eye level (left picture), whereas the active sensor *Sn20* is placed slightly below the other side of the walkway (right picture). While active and passive sensors are located at quite a distance to each other, TLD and REM give almost equal values. The same is true for the simulation, which gives a higher estimate because almost every support structure and electronic rack visible in the pictures is not replicated in the simulation geometry.

Above the calorimeters is a large platform housing several electronics racks and cables, which was mentioned in section 5.1.4.6. It is accessible via a walkway on top of a large iron steel beam that connects A-side and C-side on top of the calorimeter detector. This yellow painted walkway is shown in the left picture of figure 116. In addition to many of the passive boxes all around the platform, two active sensor PCBs are placed on it. Unlike other groups of active and passive sensors, the active box referred to as “ECAL top middle” (*Sn20*) does not have any passive counterpart close by. It is placed on the downstream side of the walkway slightly below the steel beam. The closest passive box is located on the opposite side of the walkway on the side of a blue rack, also visible on the left side in figure 116. Due to the relatively large distance, some discrepancy between active and passive measurements of these sensors is expected. Overall, the dose level on the platform is quite low because of the distance to the beam line on one hand, and the large support structures including this steel beam and the electronics racks themselves on the other, which are able to shield the sensors from a lot of the incoming radiation. According to TLDs, the dose deposited on the walkway was around 0.16 Gy for the whole Run1. Although the active sensors are located at a lower height and therefore closer to the beam line, they are also better shielded by the large steel beam walkway, as well as by the outermost modules of the main HCAL detector itself. With that in mind, the REM readout at 0.11 Gy at the beginning of LS1 does not seem to be far from the truth, although it is yet below its measuring limit. The LAAS sensor on the contrary indicates a much larger dose in this location at 3.14 Gy, but the measurement signal shown in figure 117 before most corrections are applied suggests that it cannot be trusted. While the cleaned signal seems to follow the luminosity, it exhibits an extremely noisy behavior with an unexplainable drop towards the end of the measurement history. Even though the LAAS sensor is failing in this location, REM could take over soon providing accurate measurements. Simulation estimates for both locations are very similar at around 0.67 Gy, which is significantly higher than TLD measurements. As explained earlier, this is a consequence of the missing support and electronic structures on top of the calorimeters in the simulation geometry. Nothing that is visible in figure 116 is represented in the geometry, so a higher, because less attenuated, dose estimate in these locations is absolutely expected.

Another group of active and passive sensors on this platform is called “ECAL/HCAL racks L3B04” in table 17, and it is located more on the A-side on the upstream part of the platform visible on the left in figure 116. Both active and passive boxes are placed within 10 cm on the lower end of another blue rack behind the blue rack visible in the left photo. They are more exposed to radiation from the direction of the IP and therefore would be expected to receive slightly more dose than the active sensor *Sn26* behind the walkway. Indeed, TLD measurements measured more than double than in the “ECAL top middle” position around 0.37 Gy. In this case however, active sensors measured much closer to the dose indicated by TLD. REM in particular again agrees very well with 0.33 Gy, while LAAS measures at least within a factor of 2 with 0.58 Gy. Assuming that the radiation field on the platform is rather dominated by photons and electrons than high energy hadrons, a proper calibration of the LAAS signal could manage to increase its accuracy by a large factor. The simulation estimate is again higher than TLD and REM measurements, in this case by a factor of 2, as expected because of the aforementioned lack of detail in the geometry description.

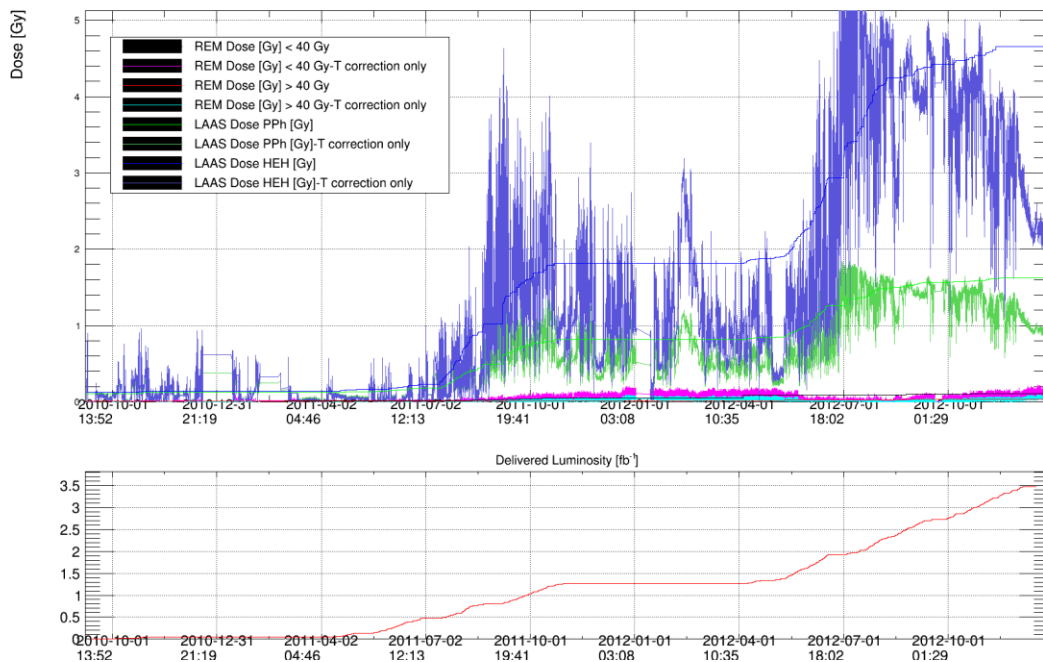


Figure 117: Measurement history of dose sensors on top of the calorimeters of active sensor PCB Sn20. The noisy green and blue signals are only corrected for temperature and then converted, while the straight blue and green lines represent the signals of LAAS after correction. While the very low purple and light blue REM signal on the bottom of the plot agrees quite well with TLD measurements in the vicinity, the LAAS signal exhibits extreme noise and an unexplainable drop of the signal towards the end of the measurement. For comparison, the integrated delivered luminosity curve is plotted in red over the same timespan on the lower canvas.

The “Counting house” labeled sensor is located at the furthest distance from the experiment behind the 3 m thick shielding wall which partitions the underground cavern into an accessible side (also during operation) and the experimental cavern itself, as shown in figure 114. It is placed on the top floor of the barracks which are built of 3 levels of stacked containers and are housing the LHCb computing farm as well as the data acquisition and other Information Technology (IT) infrastructure. The sensors in this location are expected to measure nothing but background radiation, as almost no radiation from the experiment should penetrate the shielding wall even in an event of a full beam loss. None of the sensors of the PCB in this location measured anything above their lower limit with the exception of the LAAS active sensor. With a measurement of 0.03 Gy accumulated over 3 years, the LAAS signal seems to be slightly higher than the expected natural background in this area. In comparison, the close-by TLD measurements did not yield any dose above background, and in this low dose range around a few tens of mGy LAAS sensors have shown rather limited reliability. Considering the very low dose rate over 3 years, it would also be expected that the signal is prone to annealing which would be very hard for the correction algorithm to pick up on, especially if some noise is interfering as well. Nonetheless LAAS picked up on radiation that correlates with the increase in luminosity, as can be seen in figure 118. In view of the TLD measurements, the total value of the LAAS measurement might be questionable, but an overall increase due to small amounts of radiation looks plausible, even though it had to pass through tens of meters of air as well as a 3 m thick concrete shielding wall on the way from the IP. A confirmation on the level of the dose measurement of the LAAS sensors will have to wait until higher luminosity levels in the experiment would be able to induce a measurable dose in the close-by TLD sensors as well. REM sensors picked up 0.18 Gy, but since this is well below its trusted range it is attributed to noise as well. No estimations from simulation are available in this location because of the large distance to the detector.

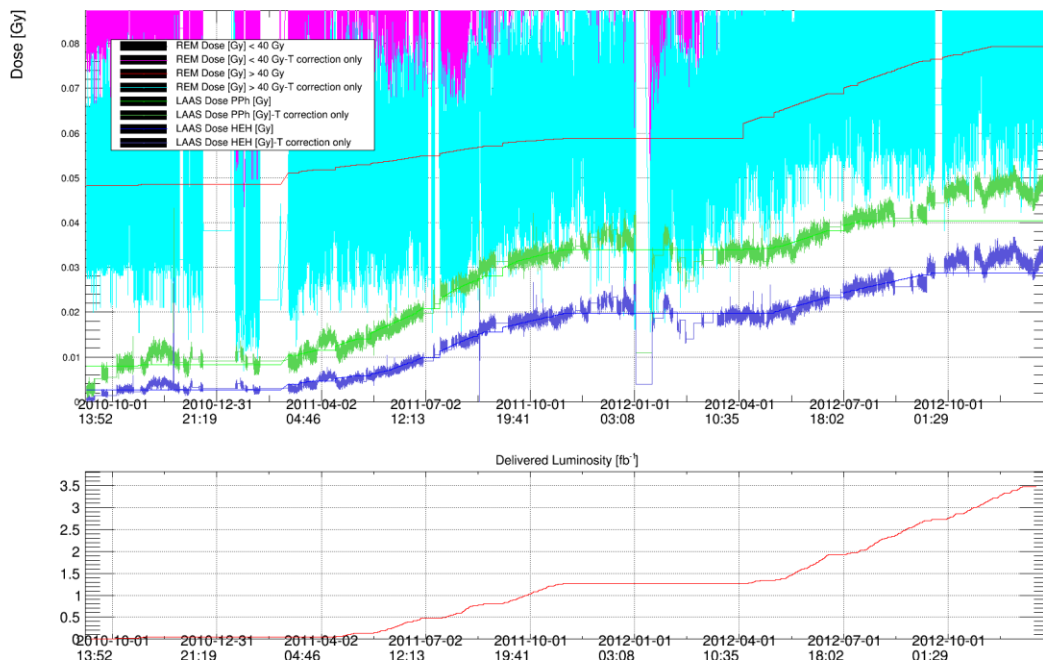


Figure 118: Measurement history of dose sensors in the “Counting house” of active sensor PCB Sn21. The purple and turquoise REM signals are basically mostly noise at this low level. The less noisy LAAS signals in blue and green are only corrected for temperature and then converted, while the straight blue and green lines represent the signals after correction. Although no measurement would be expected in this well shielded area, the LAAS sensor actually picks up radiation corresponding to an increase in luminosity. For comparison, the integrated delivered luminosity curve is plotted in red over the same timespan on the lower canvas.

The “Bunker” is a passageway below RICH2 and the Tracking Stations which allows to cross the experiment from A-side to C-side. It has a reinforced concrete wall on the side of the LHCb dipole and a concrete roof in order to support the detector components above. It is possible to access in between the calorimeters from the middle of the Bunker when the subdetectors’ halves are open. Several electronics racks which are connected to different subdetectors are installed inside the bunker to protect them from radiation. These include for example power supplies for electronics in the muon towers or control and monitoring equipment for some of the active sensor PCBs discussed in this thesis. Because of the large angle to the beam line, the massive yoke of the magnet and the concrete ceiling, all these racks are well shielded from direct radiation from the direction of the IP. As a consequence, both active sensor locations, one on top of the racks in the very center of the Bunker and the other on top of OT gas control systems in the far corner on the C-side, measured very small amounts of dose during all measurement campaigns up to now. The measurement results for the central position in the Bunker are shown in figure 119. TLD MCP sensors suggest a measurement of 0.18 Gy for the whole Run1. MTS measurements from 2012 are exaggerated, because in 2011, both TLD types agreed on a value of 0.05 to 0.06 Gy, but MTS measured double the value of MCP in 2012. This discrepancy is considered a readout error together with a few other examples which have already been exposed in figure 75. Both active sensors do not reflect these measurements, although LAAS sensors are supposed to work in this dose range in contrast to REM. Unfortunately the LAAS signal showed even worse behavior than in figure 117 with extreme noise, bumps early in the measurement history and large drops of the signal during the following 2 years. For this as well as other LAAS sensor positions which are well shielded from radiation, it was assumed at first that the low dose rate in this area might not be high enough to counter the annealing of the sensor over time, as the increase by dose and decrease by annealing could cancel each other out. However the well defined behavior of the “Counting house” sensor which measures at an even lower dose rate is a valid counter example to that hypothesis. It is more likely that the sensor in the Bunker is broken or suffers from connection problems, but further observation is needed for confirmation. The active sensor PCB on the OT Gas system at the far end of the Bunker called “Bunker extension” however is confirmed broken. None of the sensors at this

position provide any signal anymore. TLD dosimeters measured the exact same dose as in the center of the Bunker, although the location is several meters further removed from the beam line. The concrete roof of the Bunker does not stretch far enough to cover the OT Gas rack, therefore some stray radiation keeps the dose on the same level as in the center of the Bunker. Due to the nonetheless very low dose and fluence values, it was decided that this PCB would not be replaced during LS1 and only passive measurements would be used. The simulation estimate in the Bunker center was quite accurate at 0.2 Gy versus a TLD measurement of 0.18 Gy. On the “Bunker extension”, the simulation yields a higher value than the measurement. As with many other locations far from the beam line, the lack of support structures in the simulation geometry leaves more space for stray radiation to find its way into this area, explaining this estimated value.

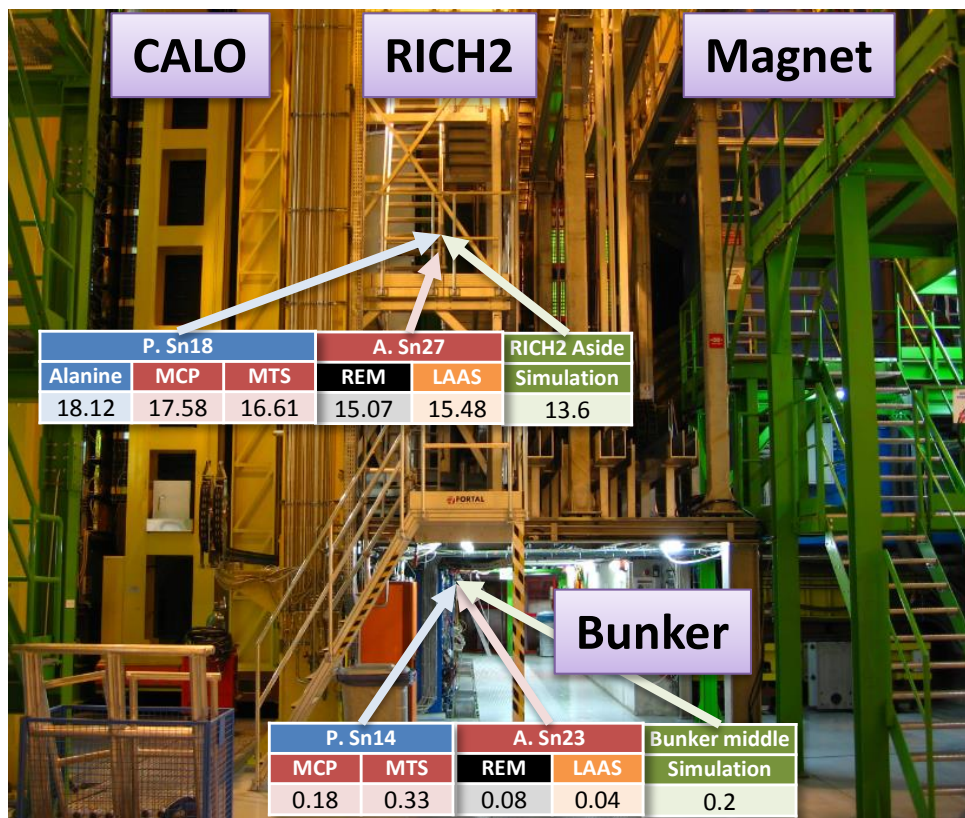


Figure 119: Positions with dose measurements and simulation estimates in [Gy] of active and passive sensors for the position “RICH2 HPD bottom A-side” and the “Bunker middle”. At the side of RICH2, all sensors even including LAAS measure in very good agreement. The simulation estimates a bit lower values than measurements. In the middle of the Bunker that transverses below RICH2 and the Outer Tracker, TLDs are not in full agreement, REM cannot measure such low values and LAAS seems to measure too low. The position “Bunker extension” is located at the far end of the Bunker in this picture, at the same height as “Bunker middle”.

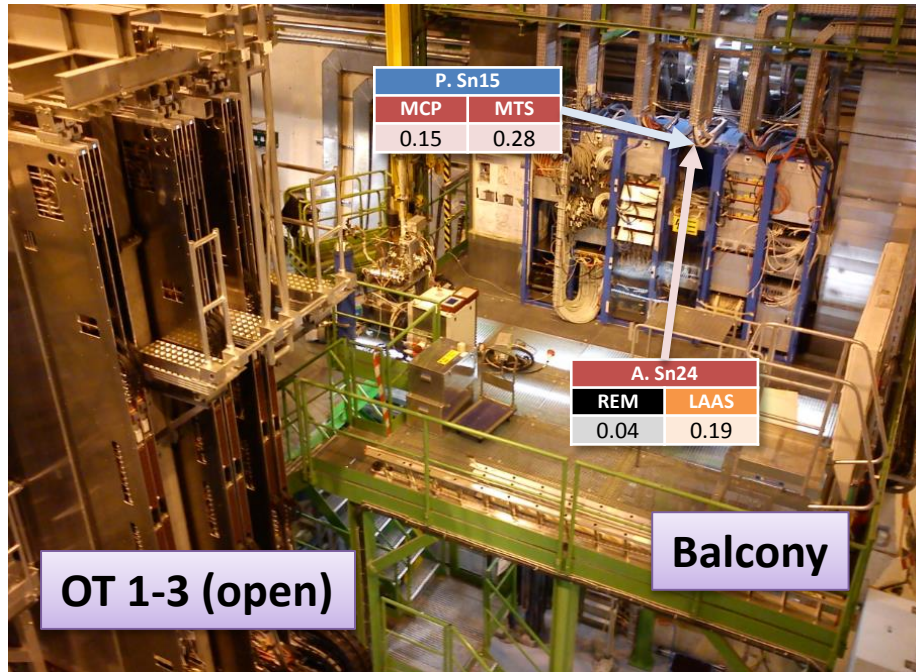


Figure 120: Dose measurements in [Gy] for active and passive sensors at the top of the electronics racks on the balcony. Due to the large distance to the LHCb detector, no simulation estimates have been scored for this location. The fully opened halves of the 3 Outer Tracker Stations can be seen on the left side of the picture.

At several meters distance to the A-side edge of the LHCb dipole, an elevated platform named the “balcony” houses some electronics racks and other equipment. The platform is shown in figure 120, bordered by green railings. On the left side of the picture, the fully opened detector halves of the three Outer Tracker stations can be seen, indicating the large distance of the platform to the LHCb detector itself. One group of active and passive sensors is located on the top of one of the central blue racks pictured in the back to observe the evolution of dose and fluence around the electronics placed within. Because of the large distance and the lack of a direct line of sight to the IP, the measurements are expected to be very low, which is confirmed by TLD MCP measurements of 0.15 Gy. The TLD MTS measurement is again considered a readout error because of the disagreement of the 2012 MTS result with all other TLD measurements. The active REM sensor is not yet able to measure anything but the more sensitive LAAS seems to agree very well with MCP measurements at the end of 2012. Unfortunately, this is an agreement by coincidence because the LAAS signal history does not actually follow the luminosity. The LAAS signal of the balcony sensor jitters as badly as the LAAS signal of Sn23 in the Bunker. In view of the very low expected dose on the balcony even during Run2, no replacement for this active sensor PCB was considered yet, but an eventual need will be reevaluated after LS2. No simulation estimate can be provided for this area because of the large distance to the actual detector. Future simulation attempts will include an extended scoring area and a geometry model which includes more details of the underground structures surrounding the LHCb experiment such as the balcony and the earlier mentioned barracks.

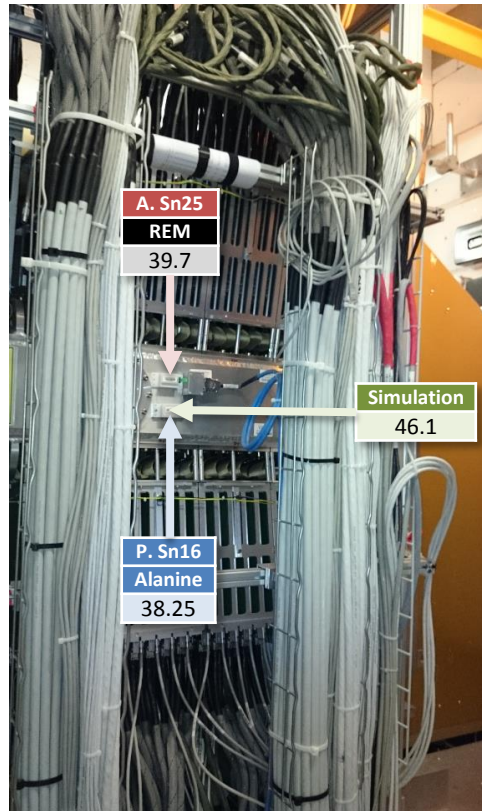


Figure 121: Positions with dose measurements and simulation estimate in [Gy] of active and passive sensors on the outside of the “VELO repeater” electronics on the A-side of the VELO. The VELO hood can be seen as orange cover to the right edge of the picture. While TLD measurements also agree within their expected linearity deviations, only Alanine and REM measurements are pictured.

The position “VELO repeater” is located close to the IP on the outer shell of the electronics around the VELO vacuum vessel as pictured in figure 121, but at an angle of almost 90 degrees to the IP on the beam line. Because of the forward directed radiation field, the dose measured here is the lowest of all locations similarly distanced from the IP. The summarized Alanine measurements for both measurement campaigns resulted in a value of 38.25 Gy. With the exception of LAAS which suffered from saturation effects as expected, all other sensors provided reasonable values, while the REM sensor in particular agrees almost perfectly with Alanine measurements. The simulation estimate is around 20% above that value, which is still considered very useful. The small discrepancy between simulation and Alanine might be caused by details in the geometry description of the electronics around the vacuum vessel, which are represented in a simplified manner compared to other components of the detector.

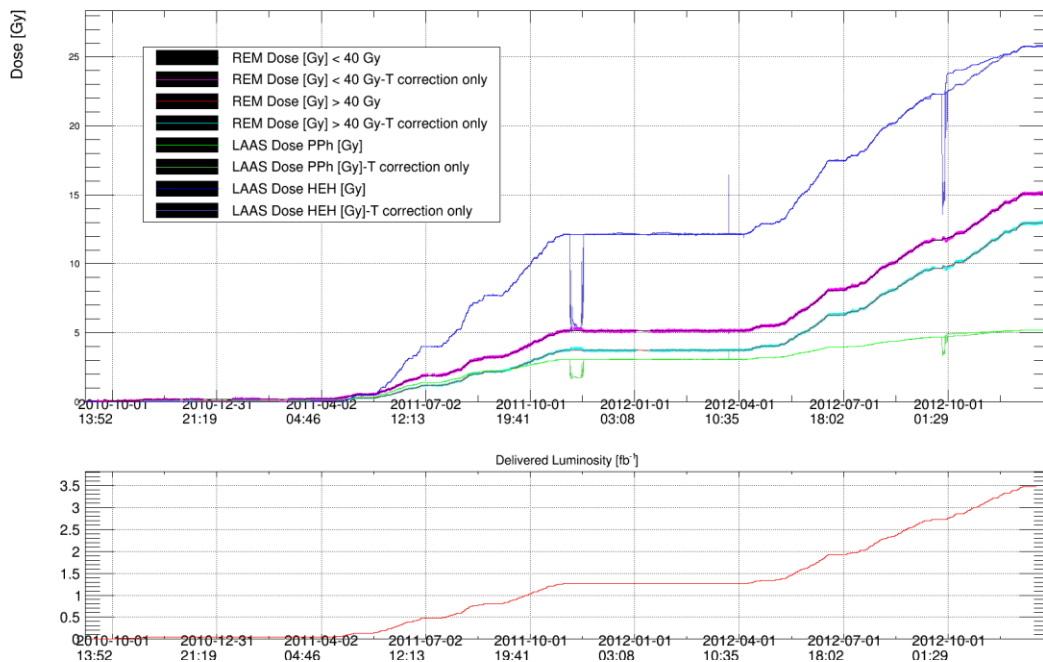


Figure 122: Measurement history of dose sensors at RICH2 A-side of active sensor PCB Sn27. The noisy signals are only corrected for temperature and then converted, while the straight lines represent the signals after correction. Both REM curves lie between the blue LAAS_HEH and the green LAAS PPh curves in closer vicinity of the photon calibration. Both sensors show similar increase of signals in accordance with the luminosity. Short drops of the LAAS signal are corrected for. At the end of the measurement, LAAS shows some unexpected drop followed by a strong hike, however at 23 Gy this happens already well above its upper measurement limit. For comparison, the integrated delivered luminosity curve is plotted in red over the same timespan on the lower canvas.

In order to observe the evolution of dose and fluence around the detector equipment of RICH2, a group of active and passive sensors is placed directly on the plating encapsulating the HPDs on the A-side of the detector. In figure 119, the actual position is hidden by a large aluminum staircase with platforms on 3 levels, which is used to access these HPDs as well as parts of the calorimeter and Outer Tracker detectors when they are opened. The sensors are placed around beam height. Because of the strongly horizontally spread shape of the dose distribution at this point and the almost direct line of sight to the IP, the dose on the outside of the detector enclosure measured around 18 Gy. This measurement is orders of magnitude higher than for example the Bunker middle which has a similar distance to the IP. Coincidentally, all measurements in this location are within a reasonable range of each other. The most reliable of these is Alanine, which measured 18.12 Gy, which is confirmed by TLDs that measured 17.58 and 16.61 Gy. Both active sensors agreed quite well with REM measuring 15.07 Gy and even LAAS measuring 15.48 Gy slightly above its range. The rather well-behaved measurement histories of the active dose sensors are plotted in Figure 122. The simulation estimate is the lowest value with 13.6 Gy. While it still agrees within a factor of 2 with measurements, the exact cause of the discrepancy with measurements is unknown. It is assumed by the author that it is caused by a lack of the RICH-tower support structure which is missing in the simulation description as well as the lack of equipment inside the RICH2 HPD enclosure which is empty in the geometry.

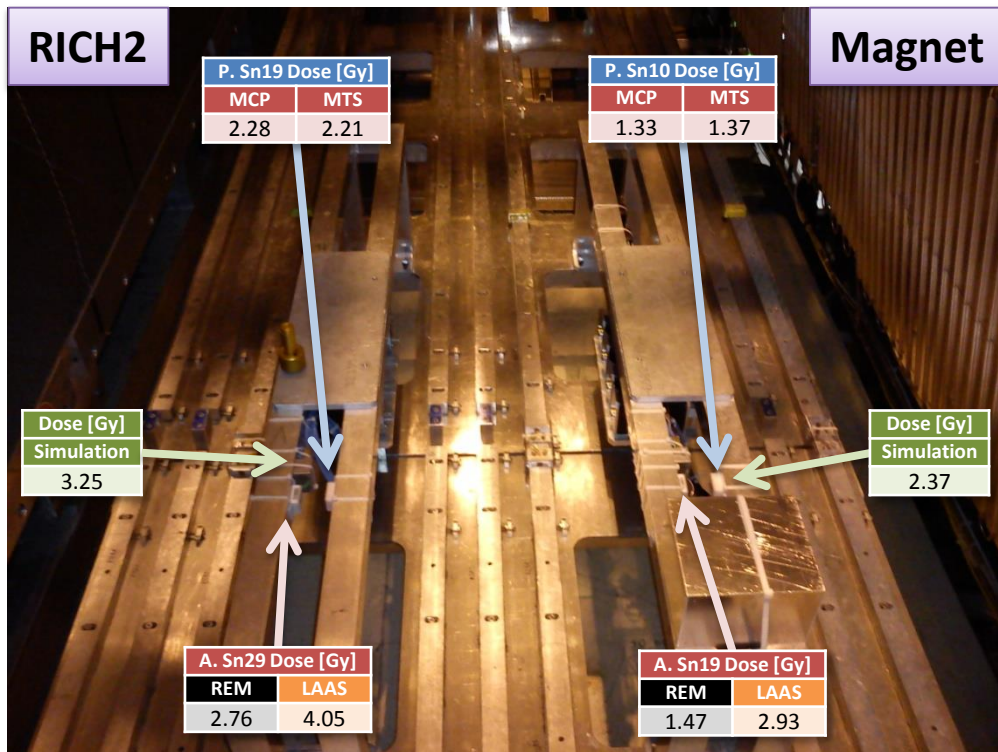


Figure 123: Positions with measurements of active and passive sensors on the IT support U-frames in between the bottom Front End electronics of the OT Stations. They are accessible when the two detector halves are fully opened, as it is the case in this picture. Two pairs of active and passive boxes have been placed in between T1 and T2 and between T2 and T3. Measurements show that the pair close to the magnet is actually shielded partially from radiation coming from the IP.

Two dosimeter positions at the bottom of the Outer Tracker Stations close to their front-end electronics measured quite different values although they are located less than 50 cm from each other. Both groups are called “IT U-support”, whereas “magnet side” means it is located between T1 and T2 and “RICH2 side” means between T2 and T3. The term “U-support” refers to some aluminum bars doubling as support structures for the beam pipe protection during technical stops on which the sensors are attached. A photo of the support, which is accessible when the OT halves are opened, and the corresponding sensor positions is shown in figure 123. The measurements listed in table 17 suggest that even though the group close to RICH2 is further away from the beam, the dose is higher by almost 80%. This is the result of the inner edge of the LHCb magnet yoke and coils shadowing the group on the side of the magnet from the radiation arriving in a direct line from the IP. Despite the overall low dose values, REM agrees well with both TLD measurements in both locations, in contrast to LAAS where the averaged curve gives an exaggerated value. The latter likely disagrees mostly because of a calibration that does not reflect the radiation field at this far distance from the beam line. The active sensor measurement histories show behavior as expected except for the overall elevated LAAS signal. The LAAS PPh calibration still yields lower values than REM. The simulation on the other hand confirms the shape of the distribution and also estimates a larger dose on the side of RICH2, but it always yields larger values than TLD and even REM measurements. Passive sensor boxes are strapped to the inside of the U-support structures visible in figure 123 with the bars possibly shielding them from low-energy radiation from the direction of the IP. Since these bars are not represented in the simulation geometry, they might be partially responsible for the higher simulation values.

The silicon strip based Trigger Tracker (TT) detector adjacent to RICH1 is connected to racks housing its electronics a few meters towards the A- and C-side. These “TT service box” racks are located right in front of the LHCb dipole yoke. The one on the A-side is equipped with active and passive sensors on its upstream-facing front side. In figure 124, only the sensors can be seen on the left edge of the picture, the rack itself is cut off. Because of the very large angle to the IP, the measured dose in Run1 is rather low. TLD measurements

yielding around 2.48 Gy agree very well with REM measuring 2.91 Gy and the simulation estimate at 2.8 Gy. Only the LAAS sensor is giving higher values, although within a factor of 2 at 4.55 Gy. Since both history curves of REM and LAAS seem to have no visible problems, a proper calibration of LAAS oriented towards photon radiation could help to improve its accuracy in this location as it is the case with other sensors.

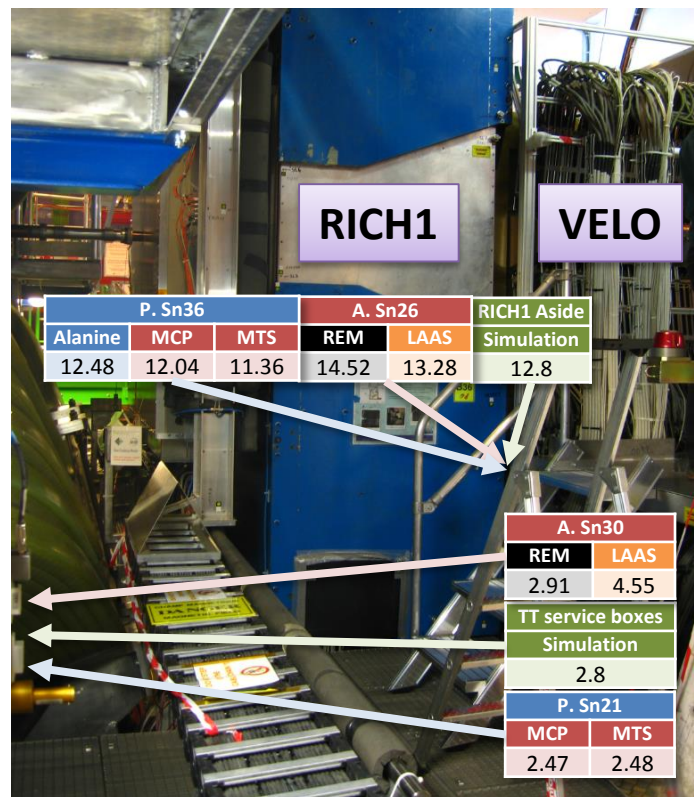


Figure 124: Positions with measurements and simulation estimates in [Gy] of the “RICH1 HPD bottom A-side” and the “TT service boxes”. The TT service box rack is not actually visible, but the sensors that are attached to its front are recognizable on the leftmost edge of the picture. At the side of RICH1, all sensors and simulation agree almost perfectly. At a few m distanced to RICH1, the LAAS sensor on the TT service box is again the single measurement which does not match all others.

Another location of a group of active and passive monitors attached to the side of the blue RICH1 magnetic shielding is visible in figure 124. The “RICH1 HPD bottom A-side” sensors are expected to provide indications of the irradiation of the HPD equipment inside the magnetic enclosure, in a similar way to the sensor outside the RICH2 HPDs. Although the distance of the sensors to the IP is very small, they were not exposed to a very large amount of dose during Run1. The angle of the placement to the IP on the beam line is only slightly smaller than for the group on the VELO repeater boards, but the sensors are protected by additional shielding through the VELO vacuum vessel and the edge of the RICH1 enclosure. These sensors are able to give a lower limit for the exposure of the HPDs inside, while the sensor at RICH1 exit should provide an upper limit. As an exception rather than the norm, all measurements in this location are agreeing extremely well with each other. All passive and active measurements as well as the simulation estimate are within 17% of the Alanine measurement of 12.48 Gy. While REM reasonably measures 14.52 Gy, even LAAS yields 13.28 Gy slightly above its theoretical upper measurement limit. The active measurement history plots accurately follow the shape of the integrated luminosity curve.

On top of the edge of the last muon iron shielding block, which separates the LHCb experimental cavern from the downstream tunnel section RB86, a single rack houses some electronics and is equipped with active and passive sensors on its front. The location is called “ECAL LV power supply” in table 17 and the location of sensors is pictured in figure 125. On the left side of the picture which was taken during LS1, the muon chambers of M5 can be seen. Upstream of M5, three larger walls made of iron shielding blocks are

alternatingly placed in between the other muon detectors until M2. These walls, which are reaching higher than the one on which the rack is placed, are responsible for shielding the rack, as well as the muon detectors upstream of M5, from almost all radiation from the direction of the IP. On the right side of figure 125, an aluminum plated rectangular structure is visible beneath some cable trays. The aluminum plating covers a thick layer of iron bricks which have been installed during LS1 as additional shielding to protect M5 as well as these electronics from radiation which is scattered from LHC machine equipment through a hole in the ceiling of RB86. The hole in the RB86 ceiling is now plugged, but it was open during the whole length of Run1, and some of the stray radiation was impinging on the pictured sensors. This stray radiation was responsible for the greater part of measured dose on the rack. In the simulation geometry, the opening was not modelled and instead the ceiling above RB86 was fully covered by a thick concrete slab. As a consequence, the simulation estimate is significantly lower at 0.11 Gy than actual measurements which point to a measurement of around 0.7 Gy. Due to the installation of the additional shielding, the simulation estimate is expected to be much closer to measurements during Run2 even if the geometry description will not be improved in this location. TLD MTS measurements in 2012 again exhibited a doubling of the signal with respect to 2011 which is considered a readout error. The active REM sensor again agrees very well with TLD measurements near its low range limit despite exhibiting strong noise in the original signal. The LAAS sensor on the other hand appears to be broken on this PCB, as the signal only starts rising very slowly towards the end of 2012 and then drops again. The LAAS end value is almost an order of magnitude below reliable measurements.

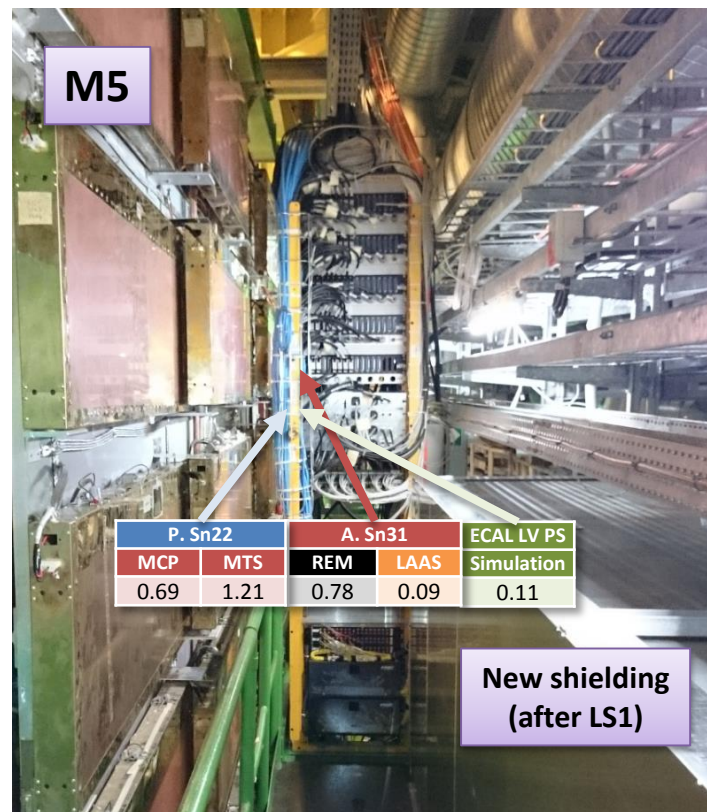


Figure 125: Positions with measurements and simulation estimates in [Gy] at the ECAL LV power supplies Q2A01 behind M5 above the last muon iron shielding. On the lower right side of the picture, the connection to the downstream tunnel section RB86 is covered by an extra layer of iron shielding with aluminum plating. This extra shielding was installed during LS1 and was therefore not present during Run1, explaining the higher measurements compared to the simulation estimate, which was calculated without an opening above RB86.

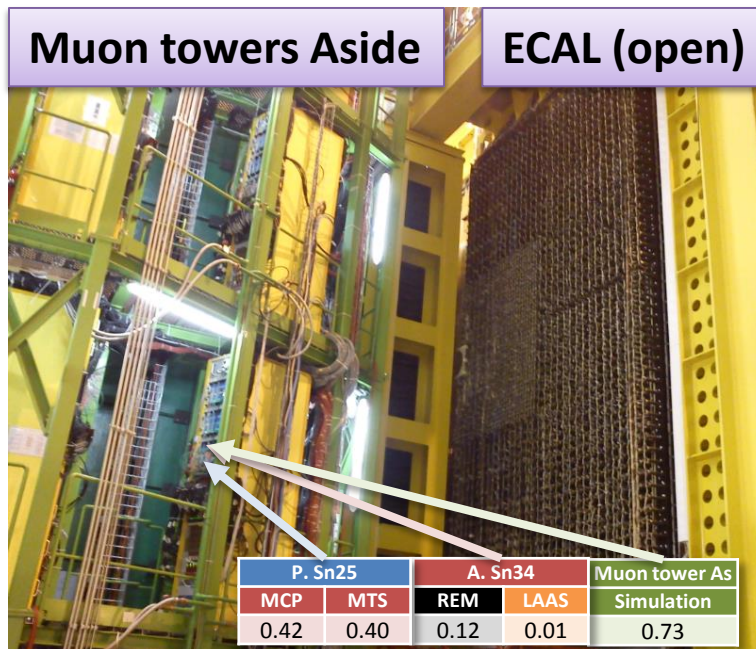
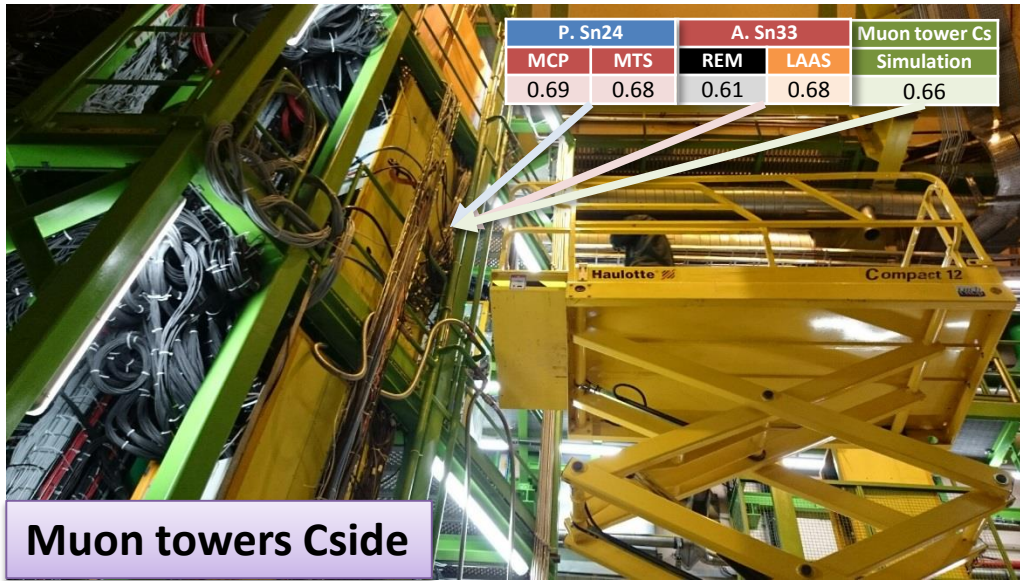


Figure 126: Positions with measurements and simulation estimates in [Gy] for “Muon intermediate board M2A02” (top picture) and “Muon service board M1A12” (bottom picture). While the sensors on the A-side are located on the first of 3 levels of the muon towers, which are symmetrically shaped on both sides of the detector, the sensors on the C-side are placed on racks one level above, in the second of 3 levels.

The muon towers are walk-in support structures symmetrically placed around the muon detectors M2 to M5, housing racks with various electronics as well as gas systems. They feature 3 accessible levels on both A-side and C-side. Dose levels at both towers are expected to be rather equal because of the symmetrical shape in relation to the IP, although the large amount of cryogenic machinery beside the detector on the C-side in contrast to the open space on A-side might induce a slightly increased measurement on the C-side due to stray radiation. Each muon tower was equipped with one set of sensors as it is pictured in figure 126. On the A-side it was placed on the downstream side of a rack on the lower of the 3 levels. On the C-side the group is located on the middle of the 3 levels, also on the downstream side of a rack. Since they are not symmetrically placed with respect to the beam line, small differences in measurement are expected. On the A-side in the group labelled “Muon service board M1A12”, both TLDs measured around 0.42 Gy. The active REM sensor measures only 0.12 Gy, however it might approach the TLD values in the future as the dose measured by TLD is still

below the official range of measurement of REM sensors. The LAAS sensor on the other hand only measured 0.01 Gy, suggesting problems with the sensor itself. The measurement history of this LAAS sensor does not seem to follow the luminosity curve at all and exhibits a very similar behavior to the one behind M5 on the ECAL LV power supply. A replacement of the active PCB will be considered during the next Long Shutdown. The simulation estimate is slightly higher than TLD estimates, which is caused by an issue similar to the one on the platform on top of the calorimeters. The muon towers as a whole are missing from the simulation geometry, therefore the simulation is disregarding any attenuation by support structures or the equipped racks. Consequently, this discrepancy is expected. The sensor group labelled “Muon intermediate board M2A02” on the C-side of the detector shows far better agreement on all levels, as can be seen in figure 126. TLDs measure around 0.69 Gy while both active sensors are agreeing well with REM measuring 0.61 Gy and LAAS pinpointing 0.68 Gy. The active measurement history of both active sensors seems accurate without much need for calibration. Even the simulation value agrees at 0.66 Gy in this location, although this high precision might be accidental due to a slightly inaccurate position in the comparison that was assumed for the sensor group.

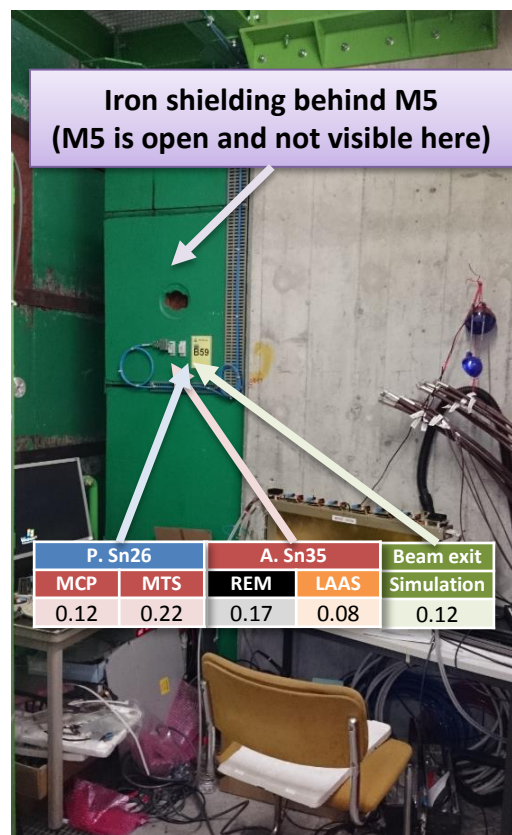


Figure 127: Positions with measurements and simulation estimates in [Gy] “close to the beam exit at RB86”. The green structures are the second-to-last and last muon iron shieldings downstream of the experiment. M5 is in open position, and therefore the detector cannot be seen. The space next to the sensors has been used for temporary workstation during LS1 due to practically non-existent activation levels.

Behind the last muon detector M5, on the side of the last muon iron shielding which divides the LHCb experimental cavern from the RB86 downstream tunnel segment, a group of active and passive sensors called “Close to the beam exit at RB86” is located. This is the same iron shielding on top of which the ECAL LV rack Q2A01 is located, which was discussed before. Although the distance from the beam line is not very large, the measured dose values are very low compared to all other locations in the cavern. The massive iron shielding blocks between the muon detectors M2 to M5 are protecting this opening from almost all the radiation coming directly from the IP, with the exception of muons which are able to pass through these structures. Even though radiation may pass laterally to the beam line in between the iron blocks, the location of the sensors on the side of the last block, shown in figure 127, is also well protected in that direction. Both active

sensors seem to measure reasonably well within this very low dose range when compared to TLD measurements. Unfortunately the measurement histories of both active sensors rather suggest that these agreements are coincidental. While the REM sensor is not expected to be accurate at this level and shows mostly high noise, the LAAS sensor again only rises during 2012. Although it too shows high levels of noise, it might become more accurate as dose levels will increase over the course of Run2. Its performance during Run2 should be observed before a possible replacement of the PCB is considered. The MTS measurement in 2012 seems unusually high at 0.18 Gy, which is double the value of MCP at 0.09 Gy. This is considered a readout error, since MCP and MTS agreed on 0.04 Gy and 0.03 Gy in the year 2011 based on roughly half the delivered luminosity. In this regard, the simulation estimate matches the MCP measurement perfectly. However due to the large distance to the IP with the whole LHCb detector structure in between, this one-point accuracy of the simulation is to be taken with caution.

5.3.5.2 MEASUREMENT RESULTS (1 MEV NEUTRON FLUENCE EQUIVALENT)

With the exception of the sensor in the “Bunker extension” on the OT Gas system, which suffered from a full PCB breakdown during Run1, all CMRP sensors were able to measure fluence levels within their range. In contrast to the earlier discussed variety of dosimetry methods used in these locations, no alternative fluence sensors for the existent levels are available in these locations. None of the measured values reached the sensitive range of BPW sensors, therefore BPW readings have been completely omitted in this section. This includes the passively used BPW diodes as well. In table 18, CMRP measurements are listed for each location alongside simulation estimates summarized for the full length of Run1 corresponding to an integrated delivered luminosity of 3.47 fb^{-1} . For the positions of the “Balcony” and the “Counting house” no simulation estimates are available. None of the signal histories of these CMRP sensors exhibit any particular issues as it was sometimes the case with active dosimetry sensors, particularly of the LAAS type. Most seem to follow the luminosity curve as expected when the fluence increase is discernible.

Similarly to the distribution of dose, the highest fluence values are registered at the “RICH1 exit” and the “VELO repeater” boards’ locations. The increase in fluence at RICH1 exit follows the luminosity curve as expected. However the position at RICH1 exit is also the only one where the CMRP sensor measured more fluence than the simulation estimated. All other measurements are equal or lower than simulation estimates. Apart from a potential error in the assumed position of the sensor, which might be responsible for part of the discrepancy, it is also possible that the sensor started to show early signs of increased response, as it approached its upper limit of sensitivity of $2 \cdot 10^{12} \text{ cm}^{-2}$. In any case a discrepancy of a factor of 1.72 is still considered rather reasonable.

The lowest value of fluence would be expected in the barracks on the accessible side behind the shielding wall of the underground complex. Surprisingly, the fluence measurement in the “Counting house”, which is considered to be at background level, is not very low in comparison with other low-level locations. The sensor close to the beam exit at RB86 in particular even measured less during Run1. Both of these measurement histories indicate that they might be nonetheless valid, since a visible increase of the signal only happens during collisions. The history of the Counting house sensor is shown in figure 128. Its increase does not perfectly correspond to the luminosity, but suggests a measurement within this order of magnitude. This of course means that a measurable amount of neutrons is able to pass the 3 m thick shielding wall and reaches the sensors inside the container barracks housing the LHCb farm equipment. Fortunately for the equipment employed in these barracks, a measurable amount in this case means a still very low amount in general.

Table 18: Summary of 1 MeV neutron fluence equivalent measurements and simulation estimates of 17 mostly low-level active and passive sensor groups in the vicinity of the experiment's electronics. Results from passive sensors and simulation from both measurement campaigns are added up to reflect the integrated signal at the start of LS1 corresponding to a delivered luminosity of 3.47 fb⁻¹. Only CMRP sensors were able to accumulate measurement signals due to the low radiation environment at these locations. Two locations further away from the experiment have not been included in the simulation scoring.

Run1	3.47 fb ⁻¹		Coordinates [cm]			1 MeV n. fl. equ.		
	Passive Box Sn	Active Sn	Description	x	y	z	CMRP	Sim
4IRCERPW000009		Sn18	RICH1 exit	0	-80	215	1.71E+11	9.95E+10
4IRCERPW000010		Sn19	IT U-support Magnet-side	50	-250	830	1.56E+10	4.30E+10
4IRCERPW000077		Sn20	ECAL top middle	114	400	1400	2.02E+09	2.87E+09
4IRCERPW000012		Sn21	Counting house	NA	NA	NA	1.52E+09	NA
4IRCERPW000013		Sn22	Bunker extension	-600	-450	1000	NA	4.02E+09
4IRCERPW000014		Sn23	Bunker middle	50	-450	1000	1.59E+09	2.69E+09
4IRCERPW000015		Sn24	Balcony	1200	150	250	1.99E+09	NA
4IRCERPW000016		Sn25	VELO repeater	75	0	20	1.59E+11	1.73E+11
4IRCERPW000018		Sn27	RICH2 HPD bottom A-side	430	0	1030	1.35E+10	3.54E+10
4IRCERPW000019		Sn29	IT U-support RICH2-side	50	-250	890	2.18E+10	5.03E+10
4IRCERPW000021		Sn30	TT service boxes magnet A-side	330	-100	240	1.49E+10	1.49E+10
4IRCERPW000022		Sn31	ECAL LV powersupplies Q2A01	370	410	1920	8.72E+09	4.40E+08
4IRCERPW000023		Sn32	ECAL/HCAL racks L3B04	100	400	1290	4.29E+09	3.04E+10
4IRCERPW000024		Sn33	Muon intermediate board M2A02	-620	110	1650	1.94E+09	2.05E+09
4IRCERPW000025		Sn34	Muon service board M1A12	620	-140	1650	5.24E+08	1.96E+09
4IRCERPW000026		Sn35	Close to beam exit at RB86	-380	110	2030	1.19E+09	1.71E+09
4IRCERPW000036		Sn26	RICH1 HPD bottom A-side	95	-90	112	6.24E+10	7.25E+10

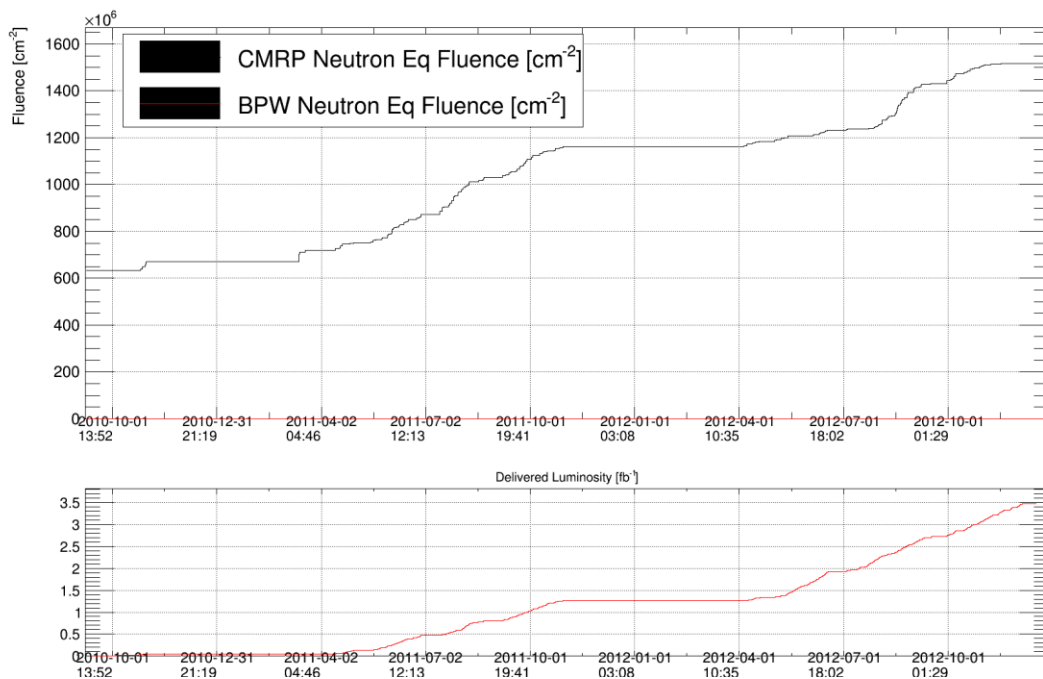


Figure 128: Fully corrected measurement history of 1 MeV neutron fluence equivalent sensors in the Counting house of active sensor PCB Sn21. Only CMRP values are visible as black curve, because the BPW signal stays at 0 as a red line at the bottom of the plot. While the increase fluctuates in ways not fully corresponding to the luminosity curve, the measurement does indicate a measurable amount of neutrons passing through the shielding wall during collisions. For comparison, the integrated delivered luminosity curve is plotted in red over the same timespan on the lower canvas.

The ratio of measurements versus simulation estimates for CMRP sensors, which is plotted in figure 129, does not exhibit any specific behavior. Four of the sensors agree very well within less than 20% difference, another four agree within a factor of two. Five positions measure significantly lower than the simulation predicts. One value is not plotted because its ratio is almost 20. This latter value was measured and estimated for the “ECAL LV power supplies Q2A01”, where the earlier mentioned difference between simulation and reality in the form of an opening in the ceiling above RB86 is responsible for most of this discrepancy. Judging from the distribution in figure 129, none of the discrepancies larger than a factor of 2 can be attributed to a dependency on the fluence rate, as they are distributed over the whole measured range and are interspersed with measurements that appear to be accurate. Some of the discrepancies are likely caused by the lack of detail in the simulation geometry, as it is already the case with dose measurements. For example, measurements on both muon towers show a difference of a factor 1.65 in dose, but a factor of 3.7 in fluence. The difference in measurements could be explained by the larger amount of material in form of several levels of cryogenic equipment on the C-side, which serve as obstacles to scatter neutrons back into the direction of the muon tower. The area on the A-side that would correspond to these cryogenic installations is filled with nothing but air. Both muon towers are not represented at all in the geometry, and neither is the cryogenic area. Consequentially, estimations are quite similar on both sides, but only one side perfectly matches the measurement in the simulation. Although this is a match by coincidence, as the missing attenuation by the muon tower representation is compensated by the added fluence from the cryogenic area. A similar situation presents itself on the top of the calorimeters, where the whole platform on top of the detector is not modelled. The simulation estimate at the “ECAL/HCAL racks L3B04” is higher than the measurement by more than a factor of 5, which might be explained by the lack of neutron-moderating material in the simulation along the way of the particle showers reaching this location. In the close-by position of “ECAL top middle”, the upper edge of the ECAL detector which is modelled accurately in the simulation is attenuating and moderating a large part of these showers, leading to a better agreement between measurement and simulation. The remaining larger discrepancies are observed at the location of the Outer Tracker front end electronics and on the side of the HPD enclosure of RICH2. Apart from the missing HPD equipment in the RICH2 enclosure and the missing details at the bottom of the Tracker Stations in the simulation geometry, which might explain part of but certainly not all of the discrepancies, no important differences could be determined in these cases. Due to the lack of comparison points within short distance of the widely separated locations discussed in this section, some malfunctioning of CMRP sensors which would be responsible at least for part of the discrepancies cannot be fully excluded.

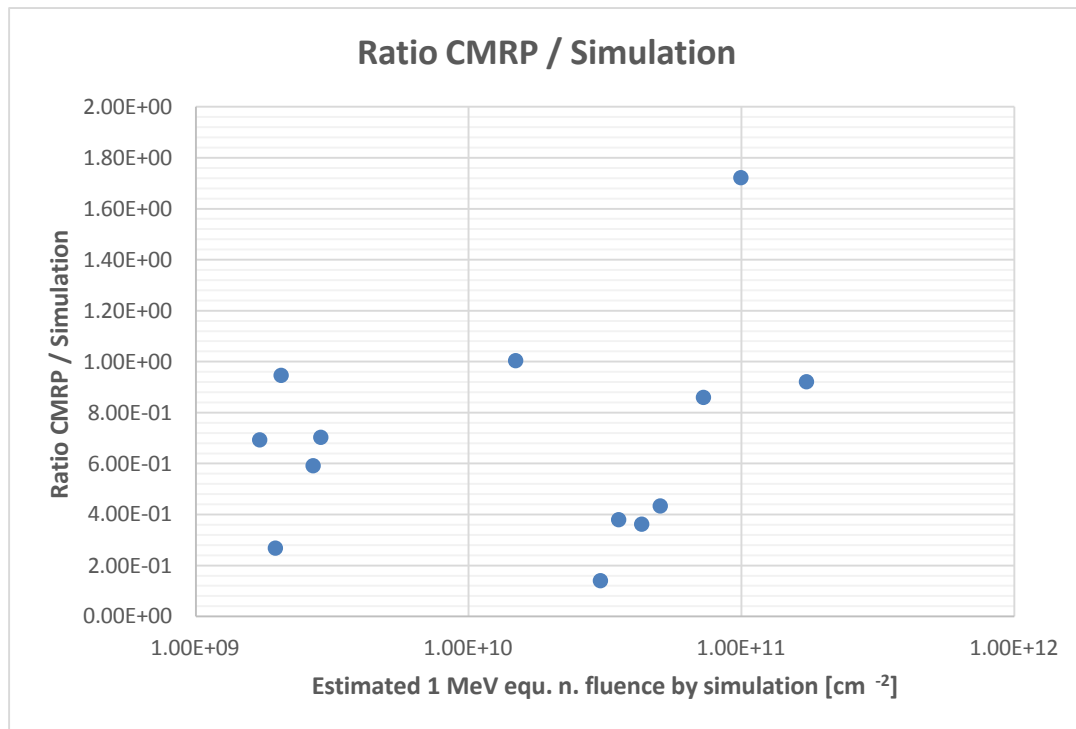


Figure 129: Ratio between 1 MeV neutron fluence equivalent measurements from CMRP sensors versus simulation estimates of the sensor positions around electronics in the LHCb cavern. The values on the abscissa are the corresponding simulation estimates of each location. One ratio of a factor of 20 for the position of the ECAL LV power supply Q2A01 is missing from this plot.

5.3.5.3 SUMMARY OF MEASUREMENTS AROUND ELECTRONICS

In the preceding section, dose and 1 MeV neutron fluence equivalent measurements of active and passive sensors distributed around the outer edges next to the electronics of the LHCb experiment have been analyzed and compared where applicable. Because of the low dose and fluence rates in almost all of the observed locations, TLDs and active CMRP sensors provided the most accurate measurements in most places. For passive measurements, both TLD types MCP-7 and MTS-7 are compared, because in this range they should and mostly do agree. Some of the readout errors of 2012 that have been mentioned in earlier sections and can be seen in figure 75 are related to some of these analyzed positions.

While the performance of LAAS was expected to be accurate in the range of mGy up to 10 Gy, most of the sensors of this type either reached saturation before the beginning of LS1 or suffered from technical problems. Only a handful of LAAS sensors such as *Sn33* at the muon tower C-side or *Sn30* at the TT service box performed well enough to allow for a viable adjustment of their calibration in relation to the two provided photon and hadron calibrations. Many others showed high noise and unexplainable behavior equal or worse than what is displayed in figure 117. The efforts to perform a calibration of LAAS type sensors based on different properties, which will be described in the following section, are held back by many of these technical problems. Without a successful calibration, the LAAS sensors are of rather limited use due to their lack of precision, especially in the range below 1 Gy. Measurements of TLDs remain the preferred reference in areas with low exposure to radiation.

REM sensors on the other hand performed very well even at a lower range than they are supposed to cover. Not only did they measure in good agreement with Alanine at a dose range above 1 Gy, they also mostly reproduced measurements from both TLD types at a few Gy down to at least 0.5 Gy if not lower, again

demonstrated best by the sensor ^{33}Sn at the muon towers. REM signals do show very high noise in this low dose range, and even after all corrections are applied, the shape of the luminosity curve is not fully replicated. Nonetheless they often manage estimate accurately at the beginning of LS1. Above a dose of 1 Gy, they usually appear to be in very good agreement with reliable Alanine measurements as long as signal drift does not become a problem, as it was discussed in section 5.3.4.

On the active sensor PCBs only CMRPs were able to measure 1 MeV neutron fluence equivalent in the locations described in the previous section. Only two of the measured or simulation values barely exceeded the lower measurement limit of BPW at 10^{11} cm^{-2} , one at the exit of RICH1 about 80 cm below the beam line, and one at the VELO repeater boards perpendicular to the IP but very close to the beam. BPW measurements in both locations have not been considered because passive BPW PINs only measured some 10^{10} cm^{-2} and active BPWs showed similar results below their official measuring range. In general, most CMRP measurements agree very well with the simulation within a factor of 2. Some larger discrepancies were found, but could be partially explained by missing details in the simulation geometry. Based on these comparisons of electronics locations, the excellent agreement between simulation and CMRP measurements seen on the front of the M1 detector cannot be safely confirmed for all sensors. Considering the fact that the simulation at M1 is expected to be far more accurate and detailed than at the locations discussed in this section, the accuracy shown in the results from M1 are likely to be true. At the least, when the CMRP measurement history is following the increase of delivered luminosity at the experiment, the corresponding sensors are expected to reliably provide an accurate measurement within an order of magnitude of the real value or better.

In contrast to the dose estimations, the simulation values for 1 MeV neutron fluence equivalent were always higher than measurements, except in two locations. One of these locations, the ECAL LV power supply behind M5, was clearly unfit for comparison due to the large difference in simulation geometry and real conditions. The other at the "RICH1 exit" might be an exception due to either individual sensor behavior or partial misalignment of the assumed positioning of the sensor. If the assumed position is wrong and should actually be closer to the beam line, then the discrepancy in dose between the REM and the Alanine measurement in this location would become smaller as well as the one concerning fluence. An indication for either of these issues is the fact that the REM and Alanine measurements as well as the CMRP measurement and the simulation estimate at the "VELO repeater" boards, which are close to "RICH1 exit" in dose range and location, agree almost perfectly. Although the particle spectra of these two locations are quite different from each other, since the hadrons arriving at the outside of the VELO perpendicular to the beam line have much lower energy than the particles at "RICH1 exit", the REM response should not change much between those fluence distributions as it was pointed out in figure 98.

As mentioned before, measurements from TLD and Alanine are generally reliable except for some readout errors that occurred to a single type of TLDs in 2012. However careful evaluation is necessary when trying to utilize the measurements for predictions on the behavior of the equipment close by. The placement of many of the sensors described in this section, which are usually found on the outside of electronics, racks, HPD enclosures or other equipment is rarely fully representative of the dose received by the equipment they are placed on. Simulation estimates can be used to bridge the gaps which are not covered by actual measurements, but in most of these outlying locations estimates are based on less detailed simulation models unlike the areas within the acceptance of the experiment, where the behavior of the simulation is well known due to the analysis performed earlier in this thesis. If the sensor on a piece of equipment is placed in between the equipment and the IP in an environment of high energy radiation, it is possible that the equipment is exposed to a higher dose than the dosimeter because of the buildup of radiation occurring in the mostly metallic casings. On the other hand, by taking the example of HPD equipment inside the thick metallic enclosure of RICH1, the dose received by those HPDs is difficult to estimate via simulation as the actual equipment is not represented in the simulation geometry, where instead the area is filled with air. Due to buildup, the real dose value inside an HPD array will be higher than the simulation will predict in an empty air

volume in the same location. Therefore the seemingly very precise measurements of the sensor group named “RICH1 HPD bottom A-side” cannot be easily transformed into a prediction of the deposited dose inside the magnetic shielding of RICH1. Instead, it provides a base for evaluating the reliability of the simulation in the vicinity of the region of interest, while predictions for the dose received by the HPDs inside the shielding necessitate taking into account the aforementioned circumstances.

5.3.6 LAAS CALIBRATION EFFORTS

Studies performed in [34] on the more dose-sensitive LAAS sensors have yielded different calibration factors that depend on the composition of the field that they are exposed to. The sensors are less efficient at picking up signals from charged hadron radiation than they are when the radiation field consists purely of photons. The response of LAAS sensors to various types of radiation is plotted in figure 130, where the different reactions to photons from ^{60}Co sources and protons at 23 GeV/c can be clearly seen. The resulting conversion factors from voltage into dose based on either of those radiation types differ by a relatively large amount compared to the maximum sensitivity of the device. As an example plotted earlier in figure 122, the sensor on the RICH2 A-side showed no unexpected or abnormal behavior. Nonetheless when both calibrations are applied, the high energy hadron calibration already gives a dose indicating that the sensor has reached the upper sensitivity limit of 10 Gy, while the photon calibration gives a dose still below 3 Gy, suggesting over 300% of uncertainty. Several attempts have been made to utilize results from FLUKA simulation and other means of measurement to find a reasonable implementation of a weighting factor that is to be applied on the two proposed calibrations in order to accommodate the varying properties of the mixed field at the experiment and improve the accuracy of LAAS sensors. All of the calibration efforts were attempted during summer in 2012 in collaboration with a summer student. While the correction algorithms were applied later on all sensors for the whole dataset of Run1 until December 2012, the calibration efforts were conducted only once during summer 2012 using passive measurements from the end of 2011 [64].

The 2011 results on the front of M1 that were discussed in section 5.3.3 did not yield a lot of hope for a potential calibration for the LAAS sensors which would be based on the ratio between impinging particle types. When compared to REM signals, which measure demonstrably close to reliable passive dosimeters, many LAAS measurements on M1 were seemingly on the wrong side of the expected calibration regarding hadron and photon fluence. Nevertheless several attempts to improve the accuracy of this type of sensors were performed attempting to find a recipe for all LAAS sensors. Only two measurements in 2011 were made below 10 Gy in a field which is comparably richer in photons and electrons than the central areas of M1, and of those two, one sensor (*M1Y Outer*) showed heavy disturbances during the latter measurement campaign, which calls the whole sensor behavior into question. These disturbances were already shown in figure 102. In order to minimize deterring influences from sensors with potential technical problems, or large inaccuracies from simulation input in areas where the geometry is not sufficiently detailed, the calibration efforts concentrated on sensors which measured at least around 1 Gy until the end of 2011. The sensors taken into consideration included the PCBs at *RICH1 exit*, *VELO repeater boards*, *RICH1* and *RICH2 HPD bottom A-side*, *TT service boxes* and all PCBs on the front of M1 except *M1X Center+1*. The latter was exempted because of expected technical issues connected to the *jump*-correction mentioned earlier and a possibly larger than usual offset of V_0 , which in hindsight were not as severe. On the other hand, the sensor *M1Y Outer* was still included, because its abnormal behavior was not recognizable as such before late 2012. Within a certain margin, passive results in 2011 were mostly consistent within themselves for these locations.

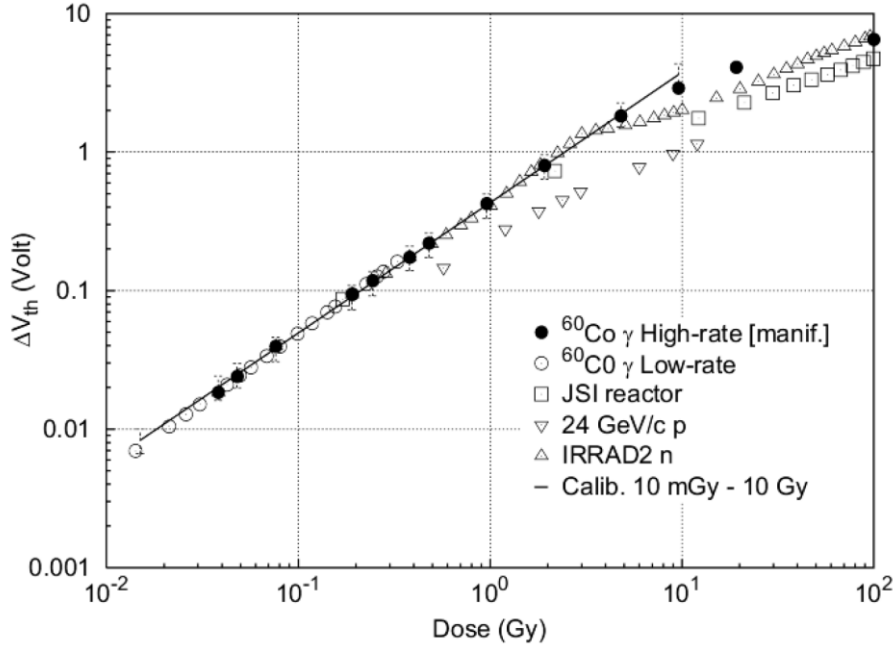


Figure 130: Radiation response of LAAS RadFETs according to [34]. The threshold voltage shift at 100 μ A is plotted versus the TID. The 24 GeV/c proton data was acquired at the IRRAD1 facility at CERN. In contrast to the REM response plotted in figure 98, LAAS sensors exhibit a significantly different response to photons and high energy hadrons. The latter are represented here by 23 GeV/c protons.

All calibration efforts are based on using weighting factors for the different response functions to adjust the curve in between the hadron and photon calibrations. The converted signal from the LAAS sensor is considered as a weighted sum of the response to pure photon (PPh) and high energy hadron (HEH) radiation:

$$LAAS(t) = w_{HEH} * HEH(t) + w_{PPh} * PPh(t) \quad (16)$$

$$w_{HEH} + w_{PPh} = 1 \quad (17)$$

Although LAAS sensors usually continue to have a response above a dose of 10 Gy, the calibration efforts are only applied to converted dose measurements below the limit of reliability at 10 Gy because of the strong saturation effects that usually appear above this limit.

In a first step the LAAS signal is matched to other reliable dosimeters (*REF*) such as Alanine or TLD, resulting in a weighting factor of:

$$w_{PPh} = \frac{REF - HEH}{PPh - HEH} \quad (18)$$

For Alanine and TLD, only measurements below the LAAS limit of 10 Gy are taken to directly match values. Since a measurement <10 Gy was only rarely the case at the end of 2011, another method was used to match values e.g. from the center of M1, which already exceeded 10 Gy. Fully corrected REM signal histories, which did follow the luminosity quite accurately and exhibited only small amounts of noise in this dose range, were rescaled to match the passive measurements at the end of 2011:

$$REM(t) \rightarrow REM(t) \times \frac{REF}{REM_{max}} \quad (19)$$

Subsequently, the LAAS measurements can be matched to the REM signal below 10 Gy. Most of the time, REM measurements matched the Alanine reference values of the YETS 2011 quite well, especially since the signals

of the observed sensors experienced almost no drift at that time. The resulting adjustments by the correction algorithms were generally rather small in these cases. In order to avoid involving saturation effects from LAAS sensors by only adjusting LAAS curves to the 10 Gy point of a REM curve, the LAAS curve was fitted to follow the REM curve in the whole range between 1 and 10 Gy. The fitting procedure aimed to find the combination of weighting factors yielding the smallest average discrepancy between all REM values <10 Gy and the corresponding LAAS values. The shapes of the LAAS and REM curve never fully match due to the different power functions of the conversion from voltage into dose. Hence, small inconsistencies are expected, also in regard to comparing direct matches of passive measurements with rescaled curves. In relation to the large variation between the two LAAS calibrations however, these inconsistencies should not have a large impact. An example of a calibrated LAAS curve which was fitted to the REM <40 Gy signal at the location of *VELO repeater* is shown in figure 131. The REM curve itself was also rescaled to match the 2011 Alanine measurement, but the difference to the original is barely visible in the plot because of the good agreement.

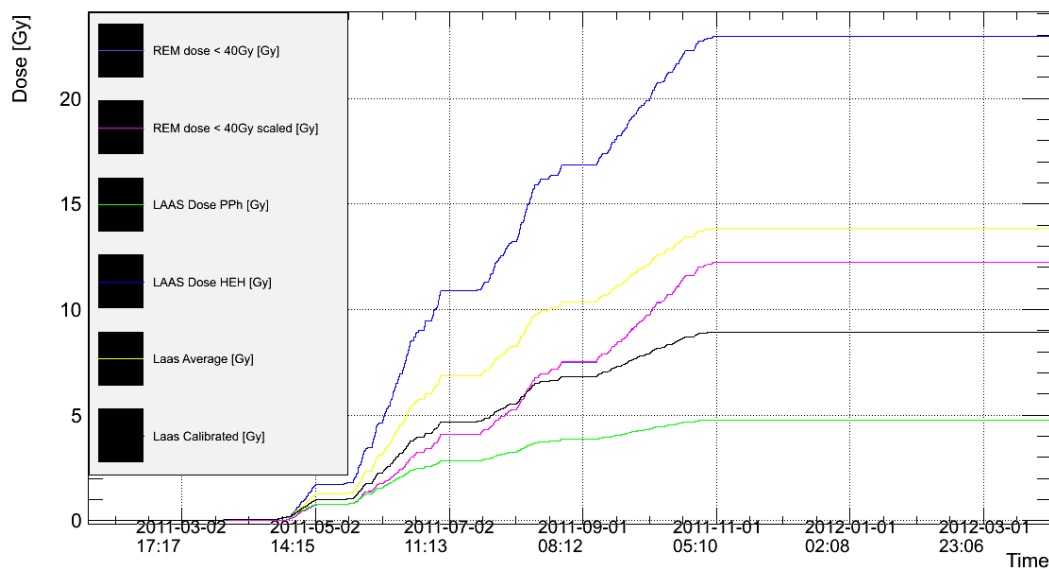


Figure 131: LAAS calibrated curve (black) matched to REM <40 Gy (purple) next to the original LAAS and REM curves for the “VELO repeater” sensor PCB. While the REM curve was also scaled to the Alanine measurement of the end of 2011, the resulting curve matched the original calibration almost perfectly in this case.

The weighting factors w_{HEH} and w_{PPh} of a fitted LAAS curve are calculated during this matching process. Once they have been obtained, they are to be compared to the properties of the radiation field. By using fluence estimators from the simulation, the weighting factors should be matched to changes within the field composition at each location. If the behavior of the sensors in different field compositions can be reproduced by attributing fluence ratios of two main particle types to each location, a generalized calibration for all LAAS type sensors could be established. In order to enable some cross checking, the simulation results for several fluences were taken into account. Among these were of course the photon fluence, and as a counterweight either the fluence of hadrons with an energy above 20 MeV or the fluence of all charged hadrons and neutrons of all energies combined. The simulation results used for these estimations were based on the same input files as the simulation discussed earlier in this thesis, but they were calculated already in 2012 with a lower number of primary collisions, up to a factor of 10 lower than what was used to obtain the current simulation results. Therefore the statistical error for these earlier results was higher, although the locations discussed in this section were not too affected due to the relatively high dose rates and low distance to the beam line and IP. Nonetheless a certain amount of error for the calculated fluence ratios was to be expected as well. The ratio calculated between two of the aforementioned fluence types was plotted versus the values of w_{HEH} obtained for each chosen location. The abscissa of the plot is based on w_{HEH} for comparison reasons, since its scale

always reaches from 0 to 1. If it is possible to find a correlation between the fluence ratio and the LAAS measurements, these plots should show something similar to a linear distribution. Because of the smaller inconsistencies explained before, some amount of deviation was expected for each of the various attempts involving different fluence and sensor types.

The second best correlation between a small collection of 9 signals was found by plotting the fluence ratio between high energy hadrons >20 MeV and photons over w_{HEH} results from Alanine calibration, the result of which is shown in figure 132. The best correlation was found for the same fluence plotted over a TLD (averaged) calibration, which is not visibly different from the one in figure 132. However this calibration is considered slightly inconsistent, for reasons explained in the next paragraph. All other attempts show even worse correlation between individual points. Even though a linear fit was found using an integrated linear Fit() function of ROOT [65] on the small dataset, the individual points are visibly dispersed over the graph. One has to keep in mind that this data only involves the 9 most promising sensors out of 28. None of the sensors suffering from high noise, possibly broken sensors or generally sensors exposed to very low dose levels have been included in this first calibration attempt. It has to be noted that Alanine measurements from 2011 did show a rather high variance below 3-5 Gy, as it can be seen in the bottom plot of figure 74. As a result, no sufficient correlation could be found which allowed for a reliable generalized application on all LAAS sensors.

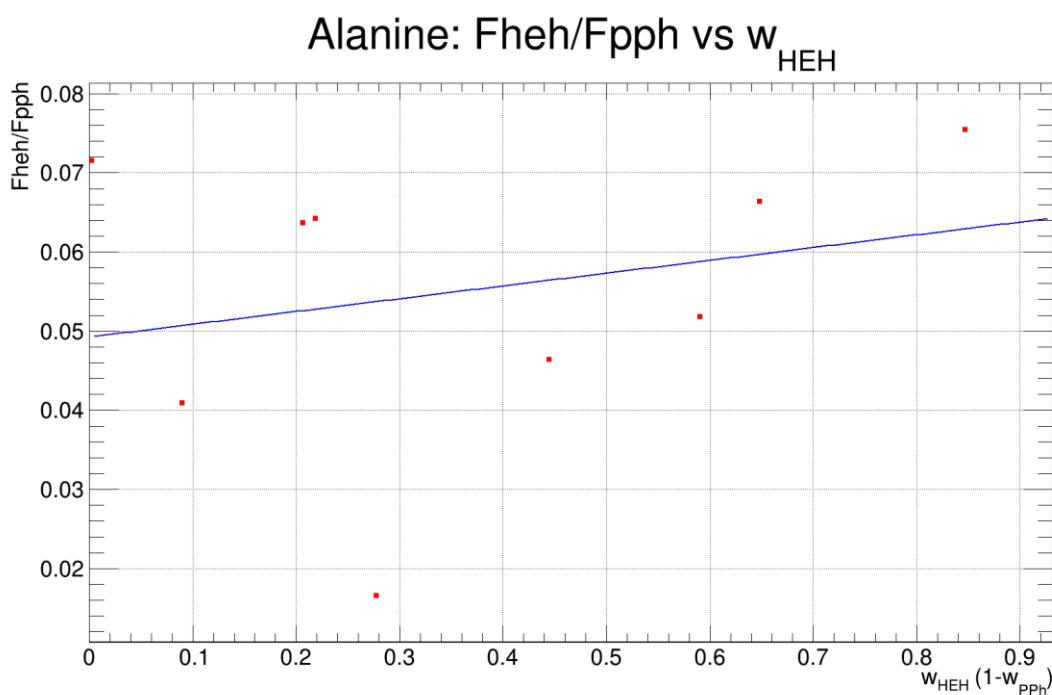


Figure 132: Attempt to find a correlation between fluence ratio and weighting factor for the calibration of LAAS sensors based on matching curves to Alanine measurements for 9 selected sensors. Even though a linear fit (blue line) was found, the individual correlations are too far removed from the fit to deduce a conclusive behavior even for this seemingly well-functioning selection of sensors.

When TLD measurements were used to scale REM curves or match LAAS calibrations, all 4 TLD results were averaged instead of correctly assigning measurements to the different TLD types. However in 2011 the difference between each type and the combined average was less pronounced because of the fact that 2 samples of MCP-7 instead of 1 sample each of MCP-7 and MCP-N were used, and MCP and MTS types agreed even better than in the following year. Therefore the only measurement slightly raising the average value was from a single MTS-N out of 4 sensors. In addition, the knowledge about the extent of the sub- and supra-linear behavior of the sensors in the range between 1 and 10 Gy was not yet known. As a consequence, the

calibration based on this TLD average was unlikely to succeed over an Alanine based one. However, the correlation is about equal to the one shown in figure 132.

It is apparent from these results and from the large amount of trials not shown in this thesis which exhibit even less correlation that no reliable calibration method could be deduced. Lacking a generally applicable recipe, most sensors will have to be calibrated individually by hand based on reliable passive measurements. Many other PCBs would have to be exchanged completely in order to have a chance of obtaining consistent measurements from LAAS sensors. However, an exchange of an active sensor PCB is only considered in rare cases. Apart from the fact that only a very limited number of replacement devices are available, the limited range of LAAS sensors in relation to the dose levels prevalent at the experiment makes their efficient performance less of a priority than that of REM and CMRP sensors, which are much more reliable and less prone to technical issues. A replacement will more likely be considered if one or both of the latter sensor types are not working to specifications anymore.

As many LAAS sensors either already exceed or were about to reach their limit of 10 Gy after which the signals become deterred by saturation effects, the LAAS calibration project was hibernated after the summer of 2012. In 2014, another project related to the active sensors was initiated in the form of a summer student project that focused on porting the offline signal correction scripts into an online environment. Instead of using all available data at once to correct individual measurement histories, the goal was to apply a temporary correction based on several predictions and other measurements, such as delivered luminosity, on each new incoming signal. Afterwards a delay of one or more days is implemented until a large enough batch of data undergoes the full correction cycle and is subsequently saved into new data points. This would allow to provide online available measurements in almost real-time while ensuring that the corrected measurement history stays true to the original signal. This project is still ongoing, because the final version could not be fully tested due to technical problems with the database system it was supposed to be set up on.

Since the calibration attempts were performed using passive measurements from the end of 2011 and simulation results from 2012, the accuracy of Alanine measurements has been improved and the number of reliable measurements until LS1 within the dose range of LAAS has increased. Also the simulation values that were used at the time were reproduced in 2014 with significantly less statistical error, which could possibly improve correlation. Therefore another attempt at the calibration of LAAS sensors should be made with measurements obtained at the start of LS1 and preferably from the first measurement campaign of Run2.

An evaluation of the radiation environment of the LHCb experiment during its first years of operation was performed using various means of measurement and simulation. The period studied in this thesis includes the larger part of Run1 beginning from late 2010 until the start of Long Shutdown 1 in 2013, comprising all but a negligible number of collisions delivered to the experiment during the first year of Run1. The final values measured in LS1 were already reached at the end of 2012, because the LHCb experiment only was exposed to a negligible amount of radiation during collisions of protons with heavy ions in the last months of Run1. Before that, the sensors have been exposed to the radiation fields produced by proton-proton collisions at 7 TeV CM in 2011 and 8 TeV CM in 2012, corresponding to integrated delivered luminosities of 1.26 fb^{-1} and 2.21 fb^{-1} respectively. Various types of active and passive sensors have been used to measure Total Ionizing Dose (TID) and 1 MeV neutron fluence equivalent in silicon. Different sensor types have been evaluated in regard to their suitability and reliability to measure within the diversified mixed fields in and around the LHCb detector. Passive sensors were collected and measured once per year during the Year End Technical Stop (YETS). Only 2 of the conducted measurement campaigns involved the majority of passive sensors installed in the LHCb underground cavern by including those installed in between the calorimeter detectors. Voltage measurements from active sensors were read out electronically within short intervals of around 23 minutes and stored in a database beginning late 2010. A correction of signal noise and errors and the subsequent conversion of these voltage signals into dose and fluence measurements was performed offline after the end of Run1.

FLUKA Monte Carlo simulations have been used to predict various parameters of the radiation field in and around the LHCb detector, some of which are relevant for the performance of electronic components of the detector. The most essential quantities in this context are the TID, the 1 MeV neutron fluence equivalent in Silicon and the high energy hadron (HEH) fluence above an energy of 20 MeV. A wide variety of damage on the equipment can be caused by the TID, depending on the total value and sometimes also on the dose rate. The 1 MeV neutron fluence equivalent is responsible for displacement damage in lattices of silicon crystals, leading to a degradation or even disruption in the performance of semiconductor devices. Both quantities accumulate over time and are able to induce permanent forms of damage in detector components. High Energy Hadrons are linked to a different type of damage that mainly affects electronic components. Their highly localized ionization capabilities are able to induce Single Event Upsets (SEU) which are capable of stopping an electronic device temporarily, and can in rare occasions cause Single Event Latchups (SEL) which might destroy an electronic component. FLUKA estimations for TID and 1 MeV neutron fluence equivalent have been compared to measurements considered accurate where they are available in order to draw conclusions on the reliability of the simulation within the whole detector geometry.

The passive sensors located around the Calorimeter structures of the LHCb experiment have been analyzed separately from other passive sensors. They represent the largest group of systematically placed sensors within a volume which is expected to be accurately and coherently described in the simulation, and are therefore very suited for a comprehensive evaluation. Passive sensors from the calorimeters have also been collected and measurements obtained in two independent campaigns since the start of the experiment: once at the end of 2011, and a second time at the beginning of LS1. Results from Alanine and TLD sensors have been analyzed in detail to understand in depth the discrepancies observed, and to assess their reliability. RPL measurements have been found to generally agree well with Alanine measurements. Nevertheless the observed surface damage on most of the RPL crystals interfered with the readout process, changing the final values in an unpredictable way. For this reason, RPL results were subsequently ignored or omitted during analysis, relying on Alanine to provide measurements in the high dose range.

The highest dose of all locations inside the calorimeters has been measured on the front around the center of the ECAL, as it was predicted by the FLUKA simulation performed with a detailed model of the LHCb geometry. The Alanine dosimeters closest to the beam along the horizontal measured 3594 Gy from the start of

operation until LS1, which corresponds to an integrated luminosity of 3.47 fb^{-1} when adding up all proton-proton collisions at 7 TeV CM and 8 TeV CM. The lead plate sandwiched between the SPD and PS detector panels is a sufficiently large cross sectional area for particles with high energy to transfer part of their energy into secondary particle showers, which are responsible for the deposition of high dose to the sensors in place. The ECAL volume itself, with its thickness of roughly 40 cm, of which about a third is made of lead, is massive enough to shield the biggest part of this incoming radiation dominated by electrons and photons, so that measured dose values at the front of the HCAL are significantly lower than in front of the ECAL. Of course, interactions within the material of the ECAL also lead to the generation of secondary particle cascades. However, many of these are already attenuated inside the detector itself. Only part of these secondaries have enough energy to escape the self-shielding ability of the ECAL and contribute to the dose on the front of the HCAL along with high energy hadrons that arrive there on their way from the IP.

Close to the central calorimeter lead plug on the front of the HCAL, similar to the other calorimeter subdetectors, the total ionizing dose rises steeply with smaller distance to the beam line. No dosimeters have been placed right at the edge of the plug, where the maximum dose on each layer is much higher than what has been measured. In order to estimate these maximum values, simulation studies have to be used in combination with measurements in order to safely extrapolate upper dose limits with some reliability. On the front of the HCAL, the maximum dose on the horizontal inner edge of the detector adjacent to the outer edge of the beam plug is higher than the closest horizontal Alanine measurement by at least a factor of 1.5, according to the simulation. The fact that the simulation estimates inside the acceptance of the detector are usually lower than measurements up to a factor of 2 has to be taken into account. This underestimation is especially pronounced above the beam pipe on the front of the HCAL. The exact cause for this effect in the simulation requires further investigation.

The lowest dose around the calorimeters, around 0.1 Gy, was measured on the back of the HCAL and at other locations far away from the beam pipe, for example the electronic racks on top of the detector. In these places, only measurements performed by TLDs are considered valid, because they show values well below the thresholds of reliability for Alanine sensors. In all other cases, Alanine measurements are deemed to be the most reliable. Simulation estimates in the low dose areas outside of the acceptance of the detector sometimes tend to be higher than measurements. This is mainly caused by a lack of detail in the FLUKA geometry, i.e. the lack of support structures and electronics racks in these locations.

Comparisons of calorimeter measurements from the same dosimeter type between the two collection campaigns have been made for each sensor type. Considering the higher energy of proton-proton collisions of 8 TeV CM versus 7 TeV CM, a small increase in dose per collision was expected. For these comparisons, the values for each energy are normalized to 1 fb^{-1} , in order to focus on the difference due to collision energy. Disregarding discrepancies that can be explained by readout errors or linearity deviations, comparison values of measurements point to an increase of dose per collision between 10% and 20% within 1.5 m from the beam line. Estimates for the simulation for both collision energies differ by a lesser amount. At most locations on all planes, simulation results predict an increase between 5% and 10% at higher collision energy, around 7-8% on average. Although it is more likely that this difference in relation to measurements is caused by issues related to changes in the readout procedure of measurements between campaigns, a potential issue with the behavior of the simulation in this unprecedented high energy region cannot be fully excluded.

In most points within the calorimeter structure, simulation values generally agree quite well with measurements that are deemed reliable by the author, those being Alanine measurements for dose greater than 1 Gy and TLD measurements around and smaller than 1 Gy. Inside the acceptance of the experiment, the simulation estimates always remain within a factor of 2 of the measurements. Most of these values are in better agreement within a factor of 1.5. However, comparisons show that in almost all cases, simulation estimates are systematically lower than Alanine measurements, with the exception of some low dose regions

on the edges of the detector. This underestimation is more pronounced in the central regions of the detector, where issues with binning of the simulation contribute to the discrepancy as well as some potential issues with simulation geometry modelling. As a consequence, the use of a minimum safety factor of 2 is compulsory when simulation results are used for estimations of possible future irradiation scenarios in the experiment. The use of higher safety factors is highly advised, in particular if a partially changed LHCb geometry has to be taken into consideration.

Significant changes in the LHCb geometry for future upgrades will affect the results presented in this thesis much more than any error of the measurement does. Changes in materials can have a large influence on the development of particle cascades along the experiment. As an example, the removal of the SPD/PS subdetectors, as it is envisaged for the LHCb upgrade, will noticeably change the radiation environment in front of the calorimeters. In this case, a safety factor of 2 will not be sufficient anymore, in particular when considering estimations for the front of the ECAL subdetector. Dedicated simulations are needed for these cases.

A safety factor of 2 is advised as well for the locations of the electronic racks on top of the detector, where simulation estimates usually score higher than actual TLD measurements. Uncertainties based on the placement of the sensors have to be taken into account, as electronics inside the racks might be more exposed to incoming radiation than the dosimeters currently are. Nevertheless the dose values in these locations are very low compared to the values inside of the acceptance of the detector. An improvement of the simulation geometry to improve the precision of predictions in these places has very low priority at this moment.

In addition to the dosimeters, passively used BPW PiN diodes have been used in all passive sensors boxes in and around the experiment to measure levels of 1 MeV neutron fluence equivalent. Due to their low sensitivity, many diodes inside the calorimeters and most of the sensors located next to detector electronics have not been able to measure above their lower measurement threshold of 10^{11} cm^{-2} . Those from calorimeter positions could only be compared to simulation estimates, as no other means of measuring the 1 MeV neutron fluence equivalent was available. The cumulative measurements corresponding to an integrated luminosity of 3.47 fb^{-1} were in agreement with the simulation within a factor of 2, with the simulation estimating higher at all times. This stands in contrast to measurements performed at the end of 2011, where simulation values were higher by more than a factor of 2. These measurements already hinted at a potential issue concerning the linearity of the provided BPW calibration curve, which was confirmed later by measurement histories of actively used BPW sensors.

After establishing the reliability of passive dosimeters by analyzing measurement results in between the calorimeter subdetectors, this knowledge was applied to an analysis of the remaining sensor positions of LHCb, which also include actively used sensor PCBs. Measurements of active sensors had to be converted from raw voltage data into dose and fluence values. The conversion was performed offline using time-consuming looping algorithms over the whole dataset of each sensor in order to optimally suppress signal noise and distortions and maximize the precision of the corrected measurements. Temperature corrections based on measurements of an NTC chip mounted on each PCB had to be applied to all sensors, with LAAS dosimeters and CMRP fluence sensors requiring manual adjustment of the calibration factor for each individual sensor. Precise signal offsets had to be determined in order to optimize sensor performance in their foreseen measurement ranges. Signal drifts to lower levels, which are caused by annealing effects and are predominantly seen in sensors exposed to higher dose and fluence levels, were compensated using a drift correction algorithm which relied on an efficiently corrected measurement history exhibiting low noise as well as on the data of the integrated luminosity delivered to LHCb.

The sensors on the front of first muon detector M1 provide valuable information about the evolution of the radiation field within the acceptance of the experiment upstream of the calorimeters. Between the IP and M1, the most defining aspect of the radiation field is the influence from the dipole magnetic field, because an

effort was made to minimize the amount of material in the way of collision products until these impinge on the calorimeters. Active and passive sensor boxes on the front of M1 are placed in mixed groups with small distances between boxes within a group on 4 positions along the horizontal and 4 along the vertical axes that are crossing with the beam line.

Actively used REM sensors measuring in a range of around 1 Gy to several tens of kGy in particular showed very good agreement with Alanine measurement with a difference of up to and around 20%, as it was expected considering their quite uniform response to different types of radiation as outlined in section 5.3.3.2. Smaller discrepancies in the range of 30% between dose measurements and Alanine in the central areas can be attributed to issues concerning the precision of V_0 values. For these sensors, V_0 was calculated based on assumptions made for the time of low exposure, before measurement results were stored in the current database. In addition, some sensors might be subject to systematic errors. The extent of those errors and possibly their cause could be revealed in future measurement campaigns.

The more sensitive LAAS sensors suffered from several complications, including early saturation in the central areas around the beam, technical problems such as extended irregularities in the signals, and a generally low precision of measurements due to calibration issues. Two different calibration curves for photon and hadron radiation are provided for the LAAS sensor, converting the initial voltage signal into two distinct measurements that differ by a factor of around 3. Since the radiation field in LHCb is mixed, an average curve placed halfway in between the two calibrations was assumed for all measurements. This assumption is not valid for the whole LHCb radiation field and only worked for a small number of locations where LAAS sensors were mostly in agreement with other sensors in the overlapping sensitive ranges. Most other locations would require a more sophisticated method of calibration in order to match the corresponding reliable passive measurements.

When measuring 1 MeV neutron fluence equivalent values on the front of the M1 detector, actively used BPW measurements appeared to be in good agreement with CMRP as well as simulation values at the end of Run1 as they start to measure inside their range. When compared to their passive counterparts, active BPW measurements measure higher values within a factor of 2. In this case, the active BPWs are considered to be more accurate because of the generally high temperature sensitivity of BPW PiNs and the fact that the onboard temperature sensor is more reliable than the handmade measurements at a small distance in the laboratory. An additional influence to discrepancies between active and passive sensors by electrical perturbation, seen as noise during measurements of active sensors, cannot be fully excluded. It is recommended that passive PiNs are read out at least 3 times in rapid succession during future measurement campaigns to determine the level of uncertainty.

CMRP measurements on the front of M1 are in exceptionally good agreement with simulation estimates for the majority of locations. Smaller discrepancies close to the beam are explained by the increased sensitivity of the device when integrated fluence levels start to approach its upper measurement limit.

In an effort to improve the precision of estimations in this area by profiting from the well-known environment, the front of M1 has been equipped with a set of additional passive boxes during LS1 in preparation for Run2. These are distributed in a similar layout to those in the calorimeters, increasing the number of comparison options for cross-checking sensor types and evaluating the simulation.

Only three groups of active and passive sensor boxes are located very close to the beam line, where the cumulative dose during Run1 exceeded a few kGy. The group located on the upstream wall directly above the beam pipe at a distance of around 15 cm to the beam line measured the highest dose values of all LHCb sensors at 9871 Gy, while the two active sensor PCBs in the upstream tunnel were exposed to 3350 Gy and 1947 Gy, according to Alanine measurements. At these high dose levels, the active sensors exhibited a visibly strong drift behavior, which manifested in a significant drop of the signal during periods without collisions. Short-term and long-term annealing effects combine to an initially strong drop of the signal which begins to

flatten and stabilize over the course of a few weeks. The drift correction algorithms described in this thesis are only applied during periods without beams, while annealing of course continues during irradiation. As a consequence, the most exposed REM sensor on the upstream wall above the beam pipe is more than factor 2 below Alanine measurements in the same spot at the end of Run1. The other 2 highly exposed sensor groups in the upstream tunnel were less affected because of the lower dose levels, showing excellent agreement with Alanine around a dose of 2 kGy and only 10% discrepancy around 3 kGy. During LS1, these three active sensor PCBs have been replaced using new non irradiated samples in order to measure accurately again during Run2, when the collision energy is increased significantly to 13 TeV CM. The effect of the increased energy on the sensitivity of the sensors will be easier to analyze without the influence of the heavy annealing. Since it is expected that annealing will happen earlier at smaller levels of integrated luminosity in the future, the continued exchange of PCBs after measuring a few kGy will not be an option due to a very limited supply of replacement PCBs and the restricted accessibility of some of the more exposed sensors. If REM sensors are to remain accurate up to dose values of 10 kGy and above, it will be necessary to develop an algorithm to account for annealing effects during irradiation. This method will depend on the currently registered dose level of the device, as well as the correct anticipation of short-term and long-term annealing effects occurring during irradiation, when their effect cannot be directly measured in contrast to periods without collisions.

The 1 MeV neutron fluence equivalent levels at these exposed locations were high enough to reach far into the range of BPW PiN sensors, while exceeding that of CMRP sensors. Consequently, the most exposed CMRP sensor exhibited significantly an exaggerated sensitivity after reaching the upper limit of its range and then ceased functioning in summer 2012, after showing strong drift of the signal towards lower levels during periods without beam. Apart from the exaggerated response, the shape of the luminosity curve was still recognizable for an extended period of time. Hence it might be possible to find a calibration which would improve the usefulness of this type of sensor by extending its measuring range even further. Both active and passive versions of BPW diodes agreed within 20% of each other in the 3 locations which are equipped with both. No drift of the BPW signal caused by annealing effects could be observed until LS1. While the measurement history of the active BPW sensors superficially followed the steps of the integrated luminosity curve, the increase per collision changed significantly in between measurement campaigns of 2011 and 2012. Although the BPW calibration is based on an expected linear behavior of the sensor, the sensor will not fully respond that way until it is exposed to around 10^{13} cm⁻² of fluence equivalent or more. As a consequence, during Run2 the BPW measurements are expected to approach the simulation estimates, which were around 1.5 times higher in LS1 for the location at the upstream wall next to the beam pipe. The earlier mentioned comparison of BPW measurements versus CMRP and simulation on the front of M1 at the end of Run1 would in fact correspond to this nonlinear behavior: in areas close to the beam which are exposed to higher fluence, BPW sensors measure relatively more than in areas with less fluence towards the outside of the detector, resulting in a bump-like shape of BPW ratios in figure 105.

The lowest dose and fluence values of all locations were measured within the group of sensors around the experiments electronics. Apart from some easily identifiable readout errors, the two different basic types of TLD sensors agreed quite well with each other in most of the locations, and exhibited the expected supra- and sublinear behavior when exceeding their reliable range. LAAS sensors, whose measurements should be able to cover an almost identical dose range unfortunately suffered from technical problems as well as a general lack of precision. Many of those issues are likely linked to flawed connections that extend up to several tens of meters. In addition, some LAAS chips are or at least appear to be broken. High amounts of noise at low signal strength make it difficult to ascertain the status of some devices. Only a handful of LAAS sensors provided measurement histories that promised an eventual improvement in precision after additional calibration. An initial theory discussed with the provider of these devices was intended to justify the unresponsive behavior of some of the problematic sensors by ascribing it to annealing effects which act quicker than the accumulation of a measurable signal. However this assumption became highly unlikely after analyzing the results of some of the least exposed sensor PCBs. A surprisingly well-behaved measurement history of the LAAS sensors in the

“Counting house” does not show any significant annealing behavior, indicating the potential for a better performance of this type of sensor. In this location on the accessible side of the LHCb underground area behind the large shielding wall, the LAAS sensor was able to register increments of several mGy which follow the luminosity curve caused by radiation that is able to penetrate the shielding wall. The signal itself exhibits a relatively low amount of noise, most certainly due to the fact that the readout electronics are located close by inside the barracks and the length of the connection to the readout device is the smallest of all installed active sensor PCBs in LHCb. Unfortunately the connection length for the active sensor PCBs in the LHCb cavern, which seems to be one of the factors with the highest impact on sensor performance, cannot be significantly shortened because of the restrictions for possible placements of the related electronics crates.

Overall, REM sensors repeatedly performed better than LAAS even in areas of 0.5 Gy and above. Even at lower levels, REM sometimes pinpointed the dose value indicated by TLD measurements despite showing comparably high signal noise at that stage. These sensors are expected to continue to measure the dose levels during Run2 and beyond at a precision comparable to that of Alanine.

CMRP sensors generally performed well in these low-fluence environments compared to simulation estimates, with only a few exceptions. Most of the discrepancies can be explained by the lack of detail in the simulation geometry, but a malfunction of a few sensors cannot be fully excluded due to the lack of comparable measurement devices. The simulation estimates for 1 MeV neutron fluence equivalent in these areas are always higher than measurements, as long as the CMRP sensors do not approach the upper limit of their range where their response starts exaggerating.

In these locations with relatively low exposure, the need for a precise calibration of LAAS sensors becomes most obvious, since they are otherwise outperformed by other sensors including REM in the dose ranges most relevant for the possible damage of radiation tolerant electronics around 1 Gy and above. Some early plots of the evolution of dose values measured by LAAS sensors in 2011 for the front of the M1 detector looked promising for delivering reliable measurements in the low-dose regions with an online accessible measurement history. Several attempts to calibrate the LAAS sensors within their location specific radiation environment were carried out by utilizing simulation results and reliable measurements from passive sensors. Despite efforts to concentrate on a small selection of the most promising sensor locations, a sufficient correlation which would allow for a reliable generally applied calibration on all LAAS sensors could not be found. While additional accumulated data and a comparison with passive results of the latest measurement campaign might improve correlation in a future calibration attempt, a manual calibration using TLD measurements will likely be required for each individual sensor.

Only LAAS type sensors were subject to calibration attempts as of now, because of their otherwise very limited use due to their lack of precision. Flawed connections to the readout systems and a high susceptibility to other technical problems further narrow their scope of application. For most purposes, it is recommended to rely on appropriately scaled TLD measurements in the range <1 Gy by correlating them to the integrated luminosity levels. A refined calibration as it is needed for LAAS sensors is not required for REM RadFETs. After all corrections are applied, REM sensors provide a sensible way of observing the almost real-time evolution of the dose in locations where the dose exceeds a few Gy per year. Discrepancies between REM and reliable passive measurements usually lie within less than a factor of 1.5. However an improved drift correction algorithm for measurements of cumulative dose above a few kGy will be required to extend the accuracy of the sensor in that range.

In the relatively low-fluence LHCb radiation environment during Run1 in terms of 1 MeV neutron fluence equivalent, BPW sensors appear to be handicapped more by high signal noise and temperature sensitivity rather than by calibration issues. In the most exposed locations, a deviation from the linear calibration in the lower measurement range of the device was observed, which corresponds to its previously evaluated response function. This deviation leads to a small underestimation of the measurement in its lower range when

compared to simulation and the overestimating CMRP signal. In order to improve the performance of the BPW sensors during Run2 and beyond, when radiation levels will increase along with the number of BPWs measuring within their range, an improved calibration curve should be conceived that takes this behavior into account.

On the front of M1 and on several positions next to electronics around the edge of the detector, CMRP diodes showed to be accurate according to simulation estimates until they approached their upper measurement limit of 10^{12} cm^{-2} . Around and above this limit, they exhibited a largely exaggerated response, which nonetheless still seemed to follow the luminosity curve until the sensor either finally saturates or ceases to function. It could be possible to find a calibration that would account for this exaggerated behavior in order to extend the period of application for many of those sensors in LHCb. Due to the lack of reliable comparison opportunities, the accuracy of both CMRP and simulation estimates cannot be fully confirmed, particularly for areas close to the edges of the detector, where the simulation geometry lacks in detail compared to the actual environment. Nevertheless the accuracy of CMRP inside the experiments' acceptance is believed to be within a factor of 2, alongside simulation values. For fully functioning sensors well within their measurement range, no indication of a deviation beyond this factor was given during the analysis of results.

Compared to BPW sensors, CMRP diodes proved to be the more appropriate choice of 1 MeV neutron fluence equivalent measurement device for most monitored locations in LHCb. As a consequence, a possible expansion of utilization of these devices for LHCb was investigated. Unfortunately, CMRP diodes have a very high price point and furthermore their production ceased some years ago. A substitute device called Si-2, which was also evaluated in [34], is currently being deployed on replacement active sensor PCBs as well as in the form of a passive measurement device similar to BPWs. In LS1 about 5 Si-2 diodes per layer were added to selected passive dosimeter boxes in the calorimeters at various distances where the sensors should be able to measure the expected fluence levels. In addition, passive boxes on the front of M1 have been equipped with these sensors as well, allowing for comparisons of the performance of the new diode type in comparison to actively used CMRPs during Run2.

The reliability of simulation predictions for TID with the running conditions of Run1 was evaluated in this thesis based on the measurement of reliable passive dosimeters. Simulation estimates were found to be reasonably accurate within a factor of 2 of reliable measurements in most places. Larger discrepancies in the remaining locations could be explained after additional investigation. In some cases, the assumed positions of sensors within the LHCb coordinate system, which are used for comparisons between measurements and simulation, are suspected to have an influential margin of error. A reevaluation of some of the position data, e.g. on the front of M1, could improve the agreement for some of the analyzed locations. In contrast to the evaluation of deposited dose, only a very limited amount of sensors measuring 1 MeV neutron fluence equivalent were used in LHCb. Nonetheless the simulation predictions for fluence estimators in the examined locations are believed to be reasonably accurate as well. Considering the excellent agreement between CMRP measurements and simulation estimates in rather well known environments such as the front of M1, as well as the acceptable agreement with BPW sensors in a few locations where measurement regions overlap, it is assumed that the simulation is able to predict the 1 MeV neutron fluence equivalent levels reasonably well within the acceptance of the detector. The issue of the underestimation of dose values by the simulation in regions closer to the beam line does not seem to apply as strongly to the fluence. Nonetheless, and because of the comparable lack of reference measurements for 1 MeV neutron fluence equivalent levels in LHCb, the use of a safety factor of at least 2 is recommended when using fluence predictions from the simulation. The fluence of hadrons with an energy $>20 \text{ MeV}$, an estimator which is often used for correlation with the occurrence of Single Event Effects (SEU and SEL) in the experiment, could not be analyzed using available sensors. This is a quantity that has to be estimated purely via simulation. However its quantification only requires the simulation to follow tracks of hadrons above an energy of 20 MeV in contrast to more complicated calculations involving NIEL and TID. Based on the verified accuracy of these latter estimators, which are at least partially based on

the simulation of particle tracks, it is assumed that the predictions of high energy hadron fluence are of equal if not better quality.

The performed evaluation of the simulation using the current LHCb geometry described in this thesis allows for the prediction of the aforementioned radiation-damage-related estimators for a variety of future detector-upgrade scenarios with an assessable reliability. Several subdetector groups have already profited from modified calculations that are based on these results by designing and testing new equipment according to the predicted requirements for the upcoming high-luminosity environment in LHCb.

The analysis of passive dosimeters has shown that Alanine and TLD sensors continue to be useful in the LHCb mixed field within their respective reliable measurement ranges above and below 1 Gy, despite the fact that their calibration is based on irradiation with ^{60}Co . The generally good agreement between most active and passive sensors and their corresponding predictions from the simulation implies that the measurement deviation caused by the influence of the various mixed field compositions should certainly be less than a factor of 1.5 and is likely much lower, as it was stated in previous studies mentioned in the first part of the thesis. A summary of all trusted passive TID measurements for all observed locations totalized for Run1 can be found in the Appendix. However a better understanding of individual dosimeter behavior in high energy mixed fields would help to enhance the precision even more. In view of the upcoming increase of delivered luminosity of the LHC, the selection of appropriate radiation tolerant and radiation hard detector equipment becomes increasingly more difficult. Choice and development of those components would directly profit from an enhanced precision of the predictions of radiation fields of an upgraded detector. Such investigations on dosimeter behavior would admittedly be very elaborate and would require individual studies in well-defined hadron fields reaching the energy levels of LHC collision products. The actual structure and composition of the LHCb experiment is unfortunately too complex to be used as an irradiation facility to calibrate dosimeters beyond an uncertainty of 50% within its mixed field. Despite the high amount of detail inside the acceptance for the current simulation geometry, there are too many uncertainties caused by the large amount of missing cabling and support structures in the simulation, along with the influence of unknown geometries and compositions of electronics between the IP and the dosimeter positions. Considering all those obstacles, establishing a range of reliability within a factor <2 of simulation and certain evaluated types of measurements for the greater part of the LHCb detector and its close surroundings is more than acceptable in regard to its application in current maintenance operations and the prediction of future radiation levels in the LHCb experiment.

7 REFERENCES

- [1] CERN. CERN CDS OPEN Photos. [Online] 2014. <https://cds.cern.ch/record/1708847>.
- [2] The LHCb collaboration. The CERN Large Hadron Collider: Accelerator and Experiments. [ed.] Rüdiger Voss and Amos Breskin. 2008. Vol. 3, pp. S08001 - S08007.
- [3] The LHCb detector at the LHC. Alves, Jr. and others. 2008, JINST, Vol. 3, p. S08005.
- [4] The LHCb Collaboration and Lindner, Rolf. Definition of the Coordinate System. s.l. : CERN, September 2014. EDMS 37264, LHCb-C-EN-001.
- [5] Herr, W. and Muratori, B. Concept of Luminosity. Zeuthen, Germany : s.n., 15-26 September 2003. CERN-2006-002.
- [6] The LHCb Collaboration. Precision Luminosity Measurements at LHCb. 2014. CERN-PH-EP-2014-221, LHCb-PAPER-2014-047.
- [7] LHCb Public Web Page. [Online] <http://lhcb-public.web.cern.ch/lhcb-public/>.
- [8] Alemany-Fernandez, R., Follin, F. and Jacobsson, R. The LHCb Online Luminosity Control and Monitoring. Shanghai : s.n., 2013. IPAC2013. TUPFI010.
- [9] LHCb Operations Plots. [Online] <http://lhcb-operationsplots.web.cern.ch/lhcb-operationsplots/index.htm>.
- [10] The LHCb Collaboration. Status of the LHCb experiment. 2013. CERN-RRB-2013-036, LHCb-PAPER-2014-047.
- [11] International Commission on Radiation Units and Measurements. Fundamental Quantities and Units for Ionizing Radiation. ICRU Report 60.
- [12] Notes on the Fluence Normalisation Based on the NIEL Scaling Hypothesis. Vasilescu, Angela and Lindström, Gunnar. 2000. ROSE/TN/2000-02.
- [13] The NIEL scaling hypothesis applied to neutron spectra of irradiation facilities and in the ATLAS and CMS SCT. Vasilescu, Angela. 1997. ROSE/TN/97-2.
- [14] K.A. Olive et al. (Particle Data Group). Chin. Phys. C. [Online] 2015 update. <http://pdg.lbl.gov/2015/AtomicNuclearProperties/>. 2015090001 (2014).
- [15] Knoll, Glenn F. Radiation Detection and Measurement Third Edition. s.l. : John Wiley & Sons, Inc.
- [16] Krieger, Hanno. Grundlagen der Strahlungsphysik und des Strahlenschutzes. s.l. : Vieweg+Teubner, 2009. 978-3-8348-0801-1.
- [17] Richard, P. M. Neutron interactions with matter, Passive Nondestructive Assay of Nuclear Material. Los Alamos : s.n., 1991. pp. 357-377. NUREG/CR-5550, LA-UR-90-732.
- [18] Bergström, Ida. Private Communication. 2016.
- [19] Cossairt, J. Donald. Radiation physics for personnel and environmental protection. s.l. : Fermilab report, 2007. TM-1834 Revision 9B.
- [20] Vincke, Helmut. Private Communication. 2016.

- [21] Radiation damage by neutrons and photons to silicon detectors. Gill, K. 1992, Nucl. Instr. Meth. A, Vol. 322, pp. 177-188.
- [22] Moll, Michael. Radiation Damage in Silicon Particle Detectors - Microscopic Defects and Macroscopic Properties. University of Hamburg, Germany : s.n., 1999. DESY-THESIS-1999-040, ISSN 1435-8085.
- [23] Computational method to estimate Single Event Upset rates in an accelerator environment. Huhtinen, M. and Faccio, F. s.l. : Nucl. Instr. & Meth. in Physics Research, 2000, Vols. A-450, pp. 155-172.
- [24] Ilgner, Christoph. Private communication. 2010.
- [25] High-Level Dosimetric Methods. Schönbacher, Helmut, Fürstner, Markus and Vincke, Helmut. s.l. : Radiation Protection Dosimetry, 2009.
- [26] BRUKER. [Online] <http://www.bruker.com>.
- [27] First Calibration of Alanine and Radio-Photo-Luminescence Dosimeters to a Hadronic Radiation Environment. Fürstner, Markus, et al. Knoxville, Tennessee : Proceedings of 2005 Particle Accelerator Conference, 2005.
- [28] Response of Alanine and Radio-Photo-Luminescence doseimeters to mixed high-energy radiation fields. Vincke, Helmut, et al. s.l. : Radiation Protection Dosimetry, 2007, Vol. 125, pp. 340-344.
- [29] Lithium Fluoride: from LiF: Mg, Ti to LiF: Mg, Cu, P. Bilski, P. 2002, Radiation Protection Dosimetry, Vol. 100, pp. 199-206.
- [30] Application of Different TL Detectors for the Photon Dosimetry in Mixed Radiation Fields used for BCNT. Burghardt, B., et al. 2006, Radiation Protection Dosimetry, Vol. 120, pp. 83-86.
- [31] Mala, P., et al. Thermoluminescent Detectors in Mixed Fields. 2012. CERN-ATS-Note-2012-086 TECH.
- [32] Method of Thermoluminescent Measurement of Radiation Doses from Micrograys up to a Megagray with a single LiF: Mg, Cu, P Detector. Obryk, Barbara, Bilski, P. and Olko, P. 2011, Radiation Protection Dosimetry, Vol. 144, pp. 543-547.
- [33] Obryk, Barbara. Private Communication.
- [34] Ravotti, Federico. Development and Characterisation of Radiation Monitoring Sensors for the High Energy Physics Experiments of the CERN LHC Accelerator. 2006. CERN-THESIS-2007-013.
- [35] A Beam Loss Scintillator System for Background Monitoring at the LHCb Experiment. Talanov, Vadim and al., et. Protvino : s.n., 2010. RuPAC-2010.
- [36] [Online] Laboratoire d'analyse et d'architecture des systèmes. <https://www.laas.fr>.
- [37] [Online] REM Oxford. <http://www.radfet.com/>.
- [38] Sze, S. M. Semiconductor Devices - Physics and Technology. s.l. : John Wiley & Sons, 1985.
- [39] Ferrari, A., et al. FLUKA: a multi-particle transport code. CERN-2005-10 (2005), INFN/TC_05/11, SLAC-R-773.
- [40] The FLUKA Code: Developments and Challenges for High Energy and Medical Applications. Böhlen, T. T., et al. 2014, Nuclear Data Sheets, Vol. 120, pp. 211-214.

- [41] The Monte Carlo event generator DPMJET-III. Roesler, Stefan, Engel, R. and Ranft, J. [ed.] A. Kling, et al. Lisbon : Springer-Verlag Berlin, 2000. Monte Carlo 2000 Conference. pp. 1033-1038. SLAC-PUB-8740.
- [42] Emmett, M. B. The MORSE Monte Carlo radiation transport system. s.l. : Oak Ridge National Laboratory report, 1984. ORNL-4972/R2.
- [43] FLAIR: A Powerful But User Friendly Graphical Interface For FLUKA. Vlachoudis, V. Saratoga Springs : s.n., 2009. Int. Conf. on Mathematics, Computational Methods & Reactor Physics (M&C 2009).
- [44] Interactive three dimensional visualization and creation of geometries for Monte Carlo calculations. Theis, Chris, et al. 2006, Nuclear Instruments and Methods in Physics Research A, Vol. 562, pp. 827-829.
- [45] Capella, A. and et al. 1994, Phys. Rept., Vol. 236, p. 225.
- [46] The FLUKA Code: Description and Benchmarking. Battistoni, G., et al. [ed.] M. Albrow and R. Raja. Fermilab : AIP Conference Proceeding, 2006. Hadronic Shower Simulation Workshop 2006. Vol. 896, pp. 31-49.
- [47] Corti, Gloria and Shekhtman, Lev. Radiation background in the LHCb experiment. 2003. LHCb-2003-83.
- [48] Corti, Gloria and Shekhtman, Lev. Estimation of induced radioactivity in LHCb to determine the Reference Waste Zoning of the experiment. 2007. LHCb-2007-097, EDMS 850261.
- [49] CERN. Drawing of upstream beam pipe components. LHCVC8B_0043.
- [50] Drawing of Warm Module. LHCVMADA0001.
- [51] Drawing of copper beam pipe. lhcvc8b_0061-v0.
- [52] Drawing of VELO vacuum vessel. lhbtvv__0063-v0.
- [53] Theis, Chris, et al. Assessment of the impact of 110mAg on the activation of electronics boards in the CMS cavern. CERN-DG-2009-104-RP-TN, EDMS 1052205.
- [54] Vincke, Helmut. Monte Carlo Particle Transport Applications in Radiation Protection of High-Energy Proton Accelerators. Habilitationsschrift. s.l. : TU Graz.
- [55] Lindner, Rolf and Roy, Laurent. Zones in UX85 and positioning of racks un UXA85, UXB85 and SG (2870). 2005. EDMS 679336.
- [56] Corti, Gloria, et al. LHCb Calorimeter Module Irradiation in the LHC Tunnel. 2009. LHCb Note. EDMS 1014960.
- [57] Brunner, Isabel, et al. High-Level Dosimetry Results for the CERN High-Energy Accelerators. CERN-SC-2004-094-RP-IR, EDMS 536233.
- [58] Vincke, Helmut and Trummer, Julia. Private Communication.
- [59] The response of different types of TL lithium fluoride detectors to high-energy mixed radiation fields. Obryk, Barbara, et al. 2008, Radiation Measurements, Vol. 43, pp. 1144-1148.
- [60] Roesler, Stefan. Private Communication.
- [61] Sjöstrand, Torbjörn, Mrenna, Stephen and Skands, Peter. PYTHIA 6.4 Physics and Manual. 2006. FERMILAB-PUB-06-052-CD-T, LU TP 06-13.

[62] ETM Professional Control GmbH. SIMATIC WinCC Open Architecture. Eisenstadt : s.n.

[63] Alessio, Federico. Private Communication.

[64] Battista, Vincenzo, Karacson, Matthias and Corti, Gloria. Active Radiation Monitors in LHCb (CERN Summer Student Report). 2012.

[65] CERN. ROOT Data Analysis Framework. [Online] <https://root.cern.ch/>.

[66] LHCb Public Webpage. [Online] <http://lhcb-public.web.cern.ch>.

8.1 MEASUREMENT RESULT TABLES

The ITEM ID names in the following tables are taken directly from their description in the LHCb equipment traceability database. In every case the Equipment ID of the wall mount holder of the passive box is given, which is placed at the coordinates shown right next to the identifier in the tables.

8.1.1 HCAL BACKSIDE

Table 19: Measurement results of dosimeters located on the back of the HCAL on the lower quarter A-side for 2011.

HCAL backside Item ID	Coordinates			Dose (Int. Lum.: 1.26 fb^{-1}), 2011			
	X [mm]	Y [mm]	Z [mm]	Alanine [Gy]	TLD		Simulation [Gy]
					MCP-7 [Gy]	MTS-7 [Gy]	
4CRCERPW000001	390	-325	14970	19.30	9.87	9.58	11.10
4CRCERPW000002	65	-325	14970	29.30	14.03	16.98	18.34
4CRCERPW000003	3705	-3250	14970	Value Too low	0.02	0.02	0.08
4CRCERPW000004	65	325	14970	30.00	16.87	16.41	17.41
4CRCERPW000005	975	-650	14970	4.84	2.00	1.99	3.00
4CRCERPW000006	2145	-1170	14970	Value Too low	0.23	0.23	0.56
4CRCERPW000007	325	-3250	14970	Value Too low	0.07	0.07	0.23
4CRCERPW000008	3705	-130	14970	Value Too low	0.11	0.10	0.23
4CRCERPW000009	565	-1625	14970	Value Too low	0.53	0.57	0.90
4CRCERPW000010	45	-845	14970	4.48	2.34	2.47	4.28
4CRCERPW000011	65	-455	14970	19.60	10.16	11.41	11.96
4CRCERPW000012	390	-65	14970	40.20	23.11	24.95	27.49
4CRCERPW000013	-390	65	14970	39.60	23.72	23.90	29.99
4CRCERPW000014	975	-65	14970	12.60	4.28	3.88	5.48
4CRCERPW000015	455	-455	14970	13.20	6.50	6.68	7.66
4CRCERPW000016	2145	-130	14970	Value Too low	0.50	0.50	0.86
4CRCERPW000017	455	-65	14970	31.20	18.86	21.48	22.64

Table 20: Measurement results of dosimeters located on the back of the HCAL on the lower quarter A-side for 2012/13.

HCAL backside Item ID	Coordinates			Dose (Int. Lum.: 2.21 fb ⁻¹), 2012/13			
	X [mm]	Y [mm]	Z [mm]	Alanine [Gy]	TLD		Simulation [Gy]
					MCP-7 [Gy]	MTS-7 [Gy]	
4CRCERPW000001	390	-325	14970	35.70	20.02	22.50	21.90
4CRCERPW000002	65	-325	14970	57.25	28.71	33.68	32.77
4CRCERPW000003	3705	-3250	14970	0.75	0.04	0.09	0.17
4CRCERPW000004	65	325	14970	58.40	34.37	32.44	30.53
4CRCERPW000005	975	-650	14970	6.80	4.22	4.16	5.22
4CRCERPW000006	2145	-1170	14970	0.80	0.44	0.45	1.04
4CRCERPW000007	325	-3250	14970	0.75	0.14	0.35	0.38
4CRCERPW000008	3705	-130	14970	0.80	0.23	0.23	0.45
4CRCERPW000009	565	-1625	14970	1.50	1.08	1.20	1.68
4CRCERPW000010	45	-845	14970	9.25	4.77	5.10	7.39
4CRCERPW000011	65	-455	14970	38.55	20.17	24.36	24.26
4CRCERPW000012	390	-65	14970	80.20	49.26	48.95	53.76
4CRCERPW000013	-390	65	14970	80.95	50.50	46.35	51.43
4CRCERPW000014	975	-65	14970	13.70	8.47	8.21	9.17
4CRCERPW000015	455	-455	14970	24.35	13.46	15.38	14.49
4CRCERPW000016	2145	-130	14970	1.30	0.94	0.98	1.64
4CRCERPW000017	455	-65	14970	62.15	37.58	38.15	45.77

8.1.2 HCAL FRONT

Table 21: Measurement results of dosimeters located on the front of the HCAL on the lower quarter A-side for 2011.

HCAL front Item ID	Coordinates			Dose (Int. Lum.: 1.26 fb ⁻¹), 2011			Simulation [Gy]
	X [mm]	Y [mm]	Z [mm]	Alanine [Gy]	TLD		
					MCP-7 [Gy]	MTS-7 [Gy]	
4CRCERPW000021	390	-65	13330	333.00	191.10	243.49	285.18
4CRCERPW000022	65	-845	13330	30.00	21.62	23.24	27.60
4CRCERPW000023	4095	-3315	13330	Value Too low	0.22	0.21	0.46
4CRCERPW000024	390	-325	13330	134.00	88.59	82.90	121.70
4CRCERPW000025	65	-435	13330	104.00	67.90	68.22	81.04
4CRCERPW000026	2145	-1235	13330	3.89	2.54	2.70	4.43
4CRCERPW000027	455	-65	13330	270.00	172.36	202.81	248.67
4CRCERPW000028	65	-325	13330	170.00	105.02	98.63	101.01
4CRCERPW000029	65	-1375	13330	11.10	6.56	5.85	10.13
4CRCERPW000030	1105	-715	13330	18.00	13.08	13.25	20.94
4CRCERPW000031	65	325	13330	169.00	87.32	95.34	99.72
4CRCERPW000032	-390	65	13330	374.00	166.44	247.66	317.65
4CRCERPW000033	455	-455	13330	83.90	57.74	52.61	77.70
4CRCERPW000034	1105	-65	13330	54.90	37.24	40.00	48.83
4CRCERPW000035	2145	-65	13330	10.60	7.02	6.32	9.81
4CRCERPW000036	65	-3315	13330	Value Too low	0.58	0.50	1.15
4CRCERPW000037	4095	-65	13330	2.07	2.43	2.10	2.46

Table 22: Measurement results of dosimeters located on the front of the HCAL on the lower quarter A-side for 2012/13.

HCAL front Item ID	Coordinates			Dose (Int. Lum.: 2.21 fb ⁻¹), 2012/13			Simulation [Gy]
	X [mm]	Y [mm]	Z [mm]	Alanine [Gy]	TLD		
					MCP-7 [Gy]	MTS-7 [Gy]	
4CRCERPW000021	390	-65	13330	713.20	383.35	619.87	563.82
4CRCERPW000022	65	-845	13330	62.45	41.77	44.19	52.03
4CRCERPW000023	4095	-3315	13330	1.20	0.43	0.43	0.88
4CRCERPW000024	390	-325	13330	275.30	181.62	195.06	238.01
4CRCERPW000025	65	-435	13330	219.75	133.72	144.31	151.72
4CRCERPW000026	2145	-1235	13330	7.30	5.50	5.27	8.42
4CRCERPW000027	455	-65	13330	565.75	364.31	470.83	492.08
4CRCERPW000028	65	-325	13330	338.00	226.72	214.15	188.97
4CRCERPW000029	65	-1375	13330	18.15	13.98	14.63	18.79
4CRCERPW000030	1105	-715	13330	35.75	27.61	27.87	39.84
4CRCERPW000031	65	325	13330	351.65	176.55	224.60	181.42
4CRCERPW000032	-390	65	13330	783.45	351.78	541.85	558.43
4CRCERPW000033	455	-455	13330	170.50	109.66	109.95	150.98
4CRCERPW000034	1105	-65	13330	111.50	78.55	73.65	93.38
4CRCERPW000035	2145	-65	13330	18.80	14.29	14.70	18.69
4CRCERPW000036	65	-3315	13330	1.35	1.06	1.07	2.14
4CRCERPW000037	4095	-65	13330	5.70	4.79	4.39	4.65

8.1.3 ECAL FRONT

Some MCP sensors from 2011 encountered technical problems due to manipulation errors during the readout, which made the application of the UHTR method impossible. Measurements of dose above 1 kGy were performed only with Alanine in this case. [33]

Table 23: Measurement results of dosimeters located on the front of the ECAL on the lower quarter A-side for 2011.

ECAL front Item ID	Coordinates			Dose (Int. Lum.: $1.26 fb^{-1}$), 2011			
	X [mm]	Y [mm]	Z [mm]	Alanine [Gy]	TLD		Simulation [Gy]
					MCP-7 [Gy]	MTS-7 [Gy]	
4CRCERPW000039	-350	-20	12530	1210.00		1337.17	1001.20
4CRCERPW000040	30	-300	12530	591.00	400.00	505.00	619.77
4CRCERPW000041	30	-390	12530	424.00	207.23	343.22	346.79
4CRCERPW000042	350	30	12530	1140.00		1329.33	926.93
4CRCERPW000043	350	-30	12530	1130.00		1320.55	924.02
4CRCERPW000044	350	-300	12530	393.00	222.95	310.96	321.38
4CRCERPW000045	30	260	12530	829.00	900.00	736.49	1323.70
4CRCERPW000046	460	-390	12530	231.00	135.29	180.12	183.39
4CRCERPW000047	30	-780	12530	83.90	60.14	57.62	80.82
4CRCERPW000048	1010	-30	12530	204.00	144.21	150.20	190.19
4CRCERPW000049	1010	-690	12530	46.10	34.45	36.14	42.09
4CRCERPW000050	30	-1180	12530	27.20	21.93	22.25	35.62
4CRCERPW000051	80	-3120	12530	3.53	2.15	1.84	2.11
4CRCERPW000052	1980	-30	12530	65.40	55.48	51.67	64.57
4CRCERPW000053	1980	-1140	12530	11.70	8.21	7.53	9.95
4CRCERPW000054	3800	-30	12530	24.40	22.25	21.47	20.12
4CRCERPW000055	3800	-3120	12530	Value Too low	0.99	0.82	0.72

Table 24: Measurement results of dosimeters located on the front of the ECAL on the lower quarter A-side for 2012/13. Normally, MTS sensor measurements above 1 kGy are out of Range (OuR).

ECAL front Item ID	Coordinates			Dose (Int. Lum.: 2.21 fb ⁻¹), 2012/13			
	X [mm]	Y [mm]	Z [mm]	Alanine [Gy]	TLD		Simulation [Gy]
					MCP-7 [Gy]	MTS-7 [Gy]	
4CRCERPW000039	-350	-20	12530	2381.00	4600.00	OuR	1812.50
4CRCERPW000040	30	-300	12530	1176.00	2500.00	OuR	1187.20
4CRCERPW000041	30	-390	12530	847.75	491.46	937.81	656.96
4CRCERPW000042	350	30	12530	2380.00	4700.00	OuR	1786.50
4CRCERPW000043	350	-30	12530	2463.50	4700.00	OuR	1805.60
4CRCERPW000044	350	-300	12530	818.30	381.09	810.59	618.89
4CRCERPW000045	30	260	12530	1768.00	3700.00	OuR	2418.40
4CRCERPW000046	460	-390	12530	488.90	319.54	429.50	347.34
4CRCERPW000047	30	-780	12530	170.90	124.57	124.42	151.44
4CRCERPW000048	1010	-30	12530	423.70	278.77	359.03	362.69
4CRCERPW000049	1010	-690	12530	95.00	80.10	68.03	79.12
4CRCERPW000050	30	-1180	12530	53.90	45.80	42.40	66.62
4CRCERPW000051	80	-3120	12530	5.20	4.87	4.16	3.91
4CRCERPW000052	1980	-30	12530	136.80	113.45	105.12	122.14
4CRCERPW000053	1980	-1140	12530	21.20	18.90	17.99	18.74
4CRCERPW000054	3800	-30	12530	49.05	44.81	39.76	37.85
4CRCERPW000055	3800	-3120	12530	2.20	1.87	1.81	1.41

8.1.4 SPD FRONT

Table 25: Measurement results of dosimeters located on the front of the SPD on the lower quarter A-side for 2011.

SPD front Item ID	Coordinates			Dose (Int. Lum.: 1.26 fb ⁻¹), 2011			
	X [mm]	Y [mm]	Z [mm]	Alanine [Gy]	TLD		Simulation [Gy]
					MCP-7 [Gy]	MTS-7 [Gy]	
4CRCERPW000058	60	280	12310	212.00	120.20	149.40	124.69
4CRCERPW000059	-430	90	12310	232.00	132.38	167.76	126.96
4CRCERPW000060	55	-290	12310	179.00	109.95	121.20	106.28
4CRCERPW000061	105	-360	12310	116.00	69.16	75.08	77.82
4CRCERPW000062	60	-960	12310	21.40	15.15	14.91	12.80
4CRCERPW000063	175	-1250	12310	12.00	7.94	7.45	9.41
4CRCERPW000064	60	-2980	12310	2.51	1.51	1.43	1.31
4CRCERPW000065	290	-50	12310	332.00	170.14	223.70	205.22
4CRCERPW000066	410	-100	12310	223.00	139.31	152.86	133.23
4CRCERPW000067	290	-250	12310	150.00	83.41	93.75	96.00
4CRCERPW000068	410	-370	12310	89.30	57.69	60.53	48.50
4CRCERPW000069	1110	-50	12310	74.40	53.63	52.02	40.30
4CRCERPW000070	1110	-555	12310	26.70	20.92	21.30	15.13
4CRCERPW000071	1970	-50	12310	27.80	21.16	22.27	17.40
4CRCERPW000072	1970	-1170	12310	4.99	4.67	4.35	4.28
4CRCERPW000073	3760	-50	12310	11.00	8.30	7.34	7.31
4CRCERPW000074	3650	-2980	12310	Value Too low	0.68	0.65	0.62

Table 26: Measurement results of dosimeters located on the front of the SPD on the lower quarter A-side for 2012/13.

SPD front Item ID	Coordinates			Dose (Int. Lum.: 2.21 fb ⁻¹), 2012/13			
	X [mm]	Y [mm]	Z [mm]	Alanine [Gy]	TLD		Simulation [Gy]
					MCP-7 [Gy]	MTS-7 [Gy]	
4CRCERPW000058	60	280	12310	436.30	303.77	345.10	228.56
4CRCERPW000059	-430	90	12310	471.15	345.32	352.21	229.94
4CRCERPW000060	55	-290	12310	363.80	235.87	267.88	201.04
4CRCERPW000061	105	-360	12310	232.75	151.85	172.95	148.32
4CRCERPW000062	60	-960	12310	41.65	31.38	31.67	22.82
4CRCERPW000063	175	-1250	12310	20.70	16.12	17.89	17.61
4CRCERPW000064	60	-2980	12310	3.55	3.25	2.90	2.51
4CRCERPW000065	290	-50	12310	667.85	319.13	618.74	390.94
4CRCERPW000066	410	-100	12310	455.05	262.45	392.17	253.80
4CRCERPW000067	290	-250	12310	308.75	183.61	220.03	179.51
4CRCERPW000068	410	-370	12310	183.45	121.84	128.96	91.13
4CRCERPW000069	1110	-50	12310	149.75	109.26	107.39	76.06
4CRCERPW000070	1110	-555	12310	53.50	41.40	41.28	28.23
4CRCERPW000071	1970	-50	12310	53.50	44.88	42.78	32.70
4CRCERPW000072	1970	-1170	12310	11.80	9.69	9.15	8.03
4CRCERPW000073	3760	-50	12310	19.50	17.39	17.70	13.74
4CRCERPW000074	3650	-2980	12310	1.80	1.42	1.40	1.18

8.1.5 ECAL TEST MODULES

High Level dosimetry with TLD measurements was attempted, but due to the large inconsistencies of TLD measurements between the two measurement periods, only Alanine measurements are considered reliable in this case. FLUKA simulation results are deemed too unreliable for this scenario because of an insufficiently realistic geometry and were subsequently left out.

Table 27: Measurement results of dosimeters located next to the beam pipe in the upstream tunnel for 2011. Normally, MTS sensor measurements above 1 kGy are out of Range (OuR).

ECAL Tunnel Item ID	Coordinates			Dose (Int. Lum.: 1.26 fb ⁻¹), 2011		
	X [mm]	Y [mm]	Z [mm]	Alanine [Gy]	TLD MCP-7 [Gy] MTS-7 [Gy]	
4CRCERPW000101	-264	0	-8820	235.00	141.06	202.70
4CRCERPW000102	-132	0	-8820	762.00	410.38	652.12
4CRCERPW000103	-264	0	-8380	642.00	354.98	597.14
4CRCERPW000104	-132	0	-8380	1137.00	990.00	1054.37
4CRCERPW000105	-70	60	-8660	3130.00	3360.00	OuR

Table 28: Measurement results of dosimeters located next to the beam pipe in the upstream tunnel for 2012/13. Normally, MTS sensor measurements above 1 kGy are out of Range (OuR).

ECAL Tunnel Item ID	Coordinates			Dose (Int. Lum.: 2.21 fb ⁻¹), 2012/13		
	X [mm]	Y [mm]	Z [mm]	Alanine [Gy]	TLD MCP-7 [Gy] MTS-7 [Gy]	
4CRCERPW000101	-264	0	-8820	451.80	299.16	393.97
4CRCERPW000102	-132	0	-8820	1292.50	3500.00	OuR
4CRCERPW000103	-264	0	-8380	1305.00	3100.00	OuR
4CRCERPW000104	-132	0	-8380	2213.50	4400.00	OuR
4CRCERPW000105	-70	60	-8660	6679.00	10400.00	OuR

8.1.6 CALORIMETER ELECTRONICS

Some dosimeter boxes had to be left in place, because the necessary dismantling of the detector could not be justified for the small benefit of reading them out. Considering their similar placement, these should measure in the same range as the sensors that were collected.

Table 29: Measurement results of dosimeters located on the front of the SPD lower quarter A-side for Run1 (2010-2013).

Electronics Item ID	Coordinates			Dose (Int. Lum.: 3.47 fb^{-1}), 2010-2013			
	X [mm]	Y [mm]	Z [mm]	Alanine [Gy]	TLD		Simulation [Gy]
					MCP-7 [Gy]	MTS-7 [Gy]	
4CRCERPW000078	1140	4530	13600	1	0.25	0.25	0.89
4CRCERPW000079	4330	5660	12580	0.8	0.10	0.10	0.54
4CRCERPW000080	4330	4500	12580	0.8	0.19	0.18	0.70
4CRCERPW000082	3320	4620	14350	1.1	0.10	0.10	0.47
4CRCERPW000084	2010	3840	12280	1.25	1.16	1.07	1.29
4CRCERPW000085	210	3840	12280	2.2	1.48	1.35	1.60
4CRCERPW000086	2210	-3840	12280	1.55	1.15	1.02	1.39
4CRCERPW000087	320	-3840	12280	2.05	1.46	1.38	1.74
4CRCERPW000089	300	-3840	12530	2	1.46	1.36	1.64
4CRCERPW000094	180	-4130	13340	1.2	0.78	0.71	0.89
4CRCERPW000095	2150	-4130	13340	1	0.56	0.54	0.71
4CRCERPW000096	280	5600	12590	0.6	0.15	0.15	0.82
4CRCERPW000097	5060	5180	14970	0.5	0.10	0.10	0.36
4CRCERPW000098	4160	-5180	14970	0.8	0.08	0.08	0.16

8.1.7 SUMMARY TABLES OF RELIABLE MEASUREMENTS

The following tables provide a summary of the most reliable measurements for all observed locations. The entries are comprised of Alanine and TLD values only. The totalized value of the integrated dose collected during Run1 until LS1 is listed along location descriptors and the corresponding position in the LHCb coordinate system. If two measurements with the same type of sensor during the same campaign were made in a location, the value in the table is based on the average of those two measurements. For example, HCAL Alanine measurements during 2012 are averaged from two dosimeters in one box, whereas in 2011 only one dosimeter per box was measured. The value in the table is the sum of the average value from 2012 plus the single measurement from 2011. For TLD measurements, the measurements that are considered readout errors from 2012 are ignored.

Table 30: Summary table of reliable measurements totalized for Run1, corresponding to an integrated luminosity of 3.47 fb⁻¹. The dose values in [Gy] are listed next to the coordinates of the sensor boxes within the LHCb coordinate system in [mm]. Values for the backside of the Hadron Calorimeter.

Summary Run1 (3.47 fb ⁻¹) Location	Coordinates			Dose [Gy]
	x [mm]	y [mm]	z [mm]	
HCAL backside	65	-325	14970	86.55
HCAL backside	65	325	14970	88.40
HCAL backside	390	-65	14970	120.40
HCAL backside	-390	65	14970	120.55
HCAL backside	65	-455	14970	58.15
HCAL backside	455	-65	14970	93.35
HCAL backside	390	-325	14970	55.00
HCAL backside	455	-455	14970	37.55
HCAL backside	45	-845	14970	13.73
HCAL backside	975	-65	14970	26.30
HCAL backside	975	-650	14970	11.64
HCAL backside	565	-1625	14970	1.64
HCAL backside	2145	-130	14970	1.46
HCAL backside	2145	-1170	14970	0.67
HCAL backside	325	-3250	14970	0.22
HCAL backside	3705	-130	14970	0.34
HCAL backside	3705	-3250	14970	0.06

Table 31: Summary table of reliable measurements totalized for Run1, corresponding to an integrated luminosity of 3.47 fb⁻¹. The dose values in [Gy] are listed next to the coordinates of the sensor boxes within the LHCb coordinate system in [mm]. Values for the front of the Hadron Calorimeter.

Summary Run1 (3.47 fb ⁻¹) Location	Coordinates			Dose [Gy]
	x [mm]	y [mm]	z [mm]	
HCAL front	65	-325	13330	508.00
HCAL front	65	325	13330	520.65
HCAL front	390	-65	13330	1046.20
HCAL front	-390	65	13330	1157.45
HCAL front	65	-435	13330	323.75
HCAL front	455	-65	13330	835.75
HCAL front	390	-325	13330	409.30
HCAL front	455	-455	13330	254.40
HCAL front	65	-845	13330	92.45
HCAL front	1105	-65	13330	166.40
HCAL front	1105	-715	13330	53.75
HCAL front	65	-1375	13330	29.25
HCAL front	2145	-65	13330	29.40
HCAL front	2145	-1235	13330	11.19
HCAL front	65	-3315	13330	1.62
HCAL front	4095	-65	13330	7.13
HCAL front	4095	-3315	13330	0.64

Table 32: Summary table of reliable measurements totalized for Run1, corresponding to an integrated luminosity of 3.47 fb⁻¹. The dose values in [Gy] are listed next to the coordinates of the sensor boxes within the LHCb coordinate system in [mm]. Values for the front of the Electromagnetic Calorimeter.

Summary Run1 (3.47 fb ⁻¹) Location	Coordinates			Dose [Gy]
	x [mm]	y [mm]	z [mm]	
ECAL front	30	260	12530	2597.00
ECAL front	30	-300	12530	1767.00
ECAL front	-350	-20	12530	3591.00
ECAL front	350	30	12530	3520.00
ECAL front	350	-30	12530	3593.50
ECAL front	30	-390	12530	1271.75
ECAL front	350	-300	12530	1211.30
ECAL front	460	-390	12530	719.90
ECAL front	30	-780	12530	254.80
ECAL front	1010	-30	12530	627.70
ECAL front	30	-1180	12530	81.10
ECAL front	1010	-690	12530	141.10
ECAL front	1980	-30	12530	202.20
ECAL front	1980	-1140	12530	32.90
ECAL front	80	-3120	12530	8.73
ECAL front	3800	-30	12530	73.45
ECAL front	3800	-3120	12530	2.87

Table 33: Summary table of reliable measurements totalized for Run1, corresponding to an integrated luminosity of 3.47 fb⁻¹. The dose values in [Gy] are listed next to the coordinates of the sensor boxes within the LHCb coordinate system in [mm]. Values for the front of the Scintillating Pad Detector (SPD).

Summary Run1 (3.47 fb⁻¹)	Coordinates			Dose
Location	x [mm]	y [mm]	z [mm]	[Gy]
SPD front	60	280	12310	648.30
SPD front	290	-50	12310	999.85
SPD front	55	-290	12310	542.80
SPD front	105	-360	12310	348.75
SPD front	290	-250	12310	458.75
SPD front	410	-100	12310	678.05
SPD front	-430	90	12310	703.15
SPD front	410	-370	12310	272.75
SPD front	60	-960	12310	63.05
SPD front	1110	-50	12310	224.15
SPD front	1110	-555	12310	80.20
SPD front	175	-1250	12310	32.70
SPD front	1970	-50	12310	81.30
SPD front	1970	-1170	12310	16.79
SPD front	60	-2980	12310	4.78
SPD front	3760	-50	12310	30.50
SPD front	3650	-2980	12310	2.10

Table 34: Summary table of reliable measurements totalized for Run1, corresponding to an integrated luminosity of 3.47 fb⁻¹. The dose values in [Gy] are listed next to the coordinates of the sensor boxes within the LHCb coordinate system in [mm]. Values for the ECAL test modules in the upstream tunnel RB84 and the electronics locations on top and bottom of the calorimeters.

Summary Run1 (3.47 fb ⁻¹) Location	Coordinates			Dose
	x [mm]	y [mm]	z [mm]	[Gy]
ECAL Tunnel modules	-264	0	-8820	686.80
ECAL Tunnel modules	-132	0	-8820	2054.50
ECAL Tunnel modules	-264	0	-8380	1947.00
ECAL Tunnel modules	-132	0	-8380	3350.50
ECAL Tunnel modules	-70	60	-8660	9809.00
CALO racks on platform	1140	4530	13600	0.25
CALO racks on platform	4330	5660	12580	0.10
CALO racks on platform	4330	4500	12580	0.19
CALO racks on platform	3320	4620	14350	0.10
SPD VFE	2010	3840	12280	1.16
SPD VFE	210	3840	12280	1.48
SPD VFE	2210	-3840	12280	1.15
SPD VFE	320	-3840	12280	1.46
PS VFE	300	-3840	12530	1.46
CALO HV_DAQ/Monitoring	180	-4130	13340	0.78
CALO HV_DAQ/Monitoring	2150	-4130	13340	0.56
CALO HV_DAQ/Monitoring	280	5600	12590	0.15
CALO HV_DAQ/Monitoring	5060	5180	14970	0.10
CALO HV_DAQ/Monitoring	4160	-5180	14970	0.08

Table 35: Summary table of reliable measurements totaled for Run1, corresponding to an integrated luminosity of 3.47 fb⁻¹. The dose values in [Gy] are listed next to the coordinates of the sensor boxes within the LHCb coordinate system in [mm]. Values for the locations in the LHCb cavern that are mostly next to electronics, including the sensors on the front of M1 and on the upstream wall close to the beam pipe.

Summary Run1 (3.47 fb ⁻¹) Location	Coordinates			Dose
	x [mm]	y [mm]	z [mm]	[Gy]
M1X Center	780	0	12100	174.50
M1X C+1	1400	0	12100	78.90
M1X C+2	2370	0	12100	39.85
M1X Outer	3370	0	12100	27.22
M1Y Outer	600	-3250	12100	3.37
M1Y C+2	600	-2000	12100	10.85
M1Y C+1	630	-1150	12100	29.06
M1Y Center	780	-400	12100	116.90
RICH1 exit	0	-800	2150	67.75
IT U-support Magnet-side	500	-2500	8300	1.37
ECAL top easy view	1140	5760	13600	0.16
Counting house	NA	NA	NA	0.00
Bunker extension	-6000	-4500	10000	0.18
Bunker middle	500	-4500	10000	0.18
Balcony	12000	1500	2500	0.15
VELO repeater	750	0	200	38.25
RICH2 HPD bottom A-side	4300	0	10300	18.12
IT U-support CALO-side	500	-2500	8900	2.28
IT ST1 on detector panel	0	-2500	8000	2.11
TT service boxes Magnet Aside	3300	-1000	2400	2.47
ECAL LV powersupplies Q2A01	3700	4100	19200	0.69
ECAL/HCAL racks L3B04	1000	4000	12900	0.36
Muon intermediate board M2A02	-6200	1100	16500	0.69
Muon service board M1A12	6200	-1400	16500	0.42
Close to beam exit at RB86	-3800	1100	20300	0.12
above beampipe powersupply wall/pillar next to VELO	1100	900	-2000	36.20
	-2500	-300	450	18.39
RICH1 HPD bottom Aside	950	-900	1120	12.48
BLS beam entrance	0	150	-2150	9871.00
ceiling above VELO	-20	195	-20	16.80
black PATROL box	-2500	-100	-1600	13.87

Curriculum Vitae

- **Contact**

Matthias Karacson
Schützengasse 1/10/50
A-2700 Wiener Neustadt
Austria
Email: m.karacson@gmx.at
Phone Nr.: 0043 676 7365292
Born: November 9th 1980 in Wiener Neustadt

- **Education**

- CERN/CHUV: Completed Training course for Radiation Protection Officers in the field of type B and C working areas, according to Swiss legislation (June 2012)
- CERN: Enrolled in the Doctoral Student program at CERN (2010 – 2013)
Degree from Vienna University of Technology expected in November 2016
- Vienna University of Technology (2000 - 2010): Diplom Ingenieur (DI)
Field of studies: Technical Physics
- Secondary school (1991 - 1999): AHS Bundesgymnasium Zehnergasse Wiener Neustadt, graduation with Matura
- Primary school (1987 - 1991): Volksschule Santa Christiana Wiener Neustadt

- **Work experiences**

- Applied Fellowship at CERN (Assessment of the radiation environment in view of the LHCb upgrade); 2014 – today

In order to make informed choices when considering new technologies in the LHCb experiment, knowledge of the radiation environment after its upgrade is essential. I model new detector configurations in FLUKA Monte Carlo geometry descriptions in collaboration with the detector groups and perform simulations to obtain relevant information on radiation levels for the upgrade running conditions. As an example, this culminated in the design of a large neutron shielding required by the upgrade SciFi Tracker. Meanwhile I maintain and improve the current network of active and passive radiation monitors at the experiment. Together with a WinCC expert I supervised a summer student who adapted the LHCb active radiation monitor system to perform online noise reduction and measurement validation. In addition I perform area classifications and material/equipment clearing work in my function as Radiation Protection Assistant/Expert (RPA/RPE) for LHCb.

- **Work experiences (continued)**

- Doctoral studentship at CERN (Evaluation of the radiation environment of the LHCb experiment); 2010 – 2013

Various active (RADFET, PIN etc.) and passive (Alanine, RPL, TLD etc.) dosimeters are used in the LHCb experiment to examine different aspects of the radiation environment. I compared these measurements with simulation results to achieve a better understanding of the behavior of the monitors, and to provide an overall view on particle fluences and energy deposition in and around the experiment via the simulation. I adopted a FLUKA based Monte Carlo description of LHCb which I extend and optimise on a regular basis, and which I use to perform studies considering various running conditions of the experiment. With the help of my supervisor I oversaw the work of a summer student that analyzed the active dosimeters.

- Technical studentship at CERN (resulting in diploma thesis: Monte Carlo simulation of the activation of air at the MedAustron project); June 2009 – July 2010

The goal of the project was an extensive simulation study contributing to the environmental impact assessment of the radio-oncological center for research and treatment of cancer patients MedAustron. For that purpose, I performed generic simulations with FLUKA to investigate on the strengths and weaknesses of two different methodologies of calculating air activation from proton and ^{12}C ion beams. After applying the appropriate technique to the planned irradiation scenarios, I analyzed the results in reference to Austrian radiation protection law.

- Austrian Research Centers Seibersdorf Health Physics Division:

- Health Physics Studies; July 2001
- Dosimetry (Measurements and Evaluations for Project ITRAP); July 2002
- Laser Safety (resulting in 2 academically credited project works); July and August 2005

As part of the process to acquire an official accreditation as specialized test house for laser safety, the laboratory had to verify the physical pixel size of a commercially available CCD camera, and the validity of the included beam diameter measuring software. I designed an experimental setup to measure the pixel size of the CCD chip with a focused laser beam and a calibrated xy-stage, and wrote a C program to reproduce different beam measurement functions of the supplied proprietary code.

- 12 months of alternative national service at the volunteer fire department Wiener Neustadt from October 1999 to October 2000 including volunteer firefighter training

- **Publications**

- In preparation: LHCb Public Note “Radiation Environment of the LHCb Calorimeters 2010-2013”
- Co-Author of LHCb Public Note “Irradiation of a 2.5 m long SciFi module with 24 GeV/c protons to the dose profile expected in LHCb”, A.B. Cavalcante et al., LHCb-PUB-2016-001, January 2016
- Co-Author of LHCb Internal Note “Viability assessment of a scintillating fibre tracker for the LHCb upgrade”, F.Blanc et al., CERN-LHCb-INT-2013-004, January 2013
- Co-Author of LHCb Internal Note “Radiation studies for the LHCb tracker upgrade”, N. Lopez March, M. Karacson, CERN-LHCb-INT-2013-003, January 2013
- Diploma thesis “Monte Carlo simulation of the activation of air at the MedAustron project”, October 2010
- Co-author of Poster-presentation at the Conference of the Austrian Physical Society “CERN-IH LINAC verification via CERN-DYNAC source code”, September 2005

- **Presentations**

- Presentation at the LHCb week in Orsay “Update on radiation issues for LHCb”, September 2014
- Presentation at the LHCb week in Krakow “Update on prompt radiation levels in the LHCb cavern”, September 2013
- Presentation at the LHCb week in Davos “Prompt radiation levels in the LHCb cavern”, September 2012
- Poster for ESI 2011: EIROforum School on Instrumentation in Grenoble “Evaluation of the Radiation Environment of the LHCb Experiment”, May 2011

- **Interests and Knowledge**

- Languages: German, English, French (basic)
- Hobbies: Playing Piano, E-Guitar; Hiking, Skiing, (Mountain)biking,...